Enhancing Electrical and Heat Transfer Performance of High-Concentrating Photovoltaic Receivers

Submitted by Leonardo Micheli to the University of Exeter
as a thesis for the degree of
Doctor of Philosophy in Renewable Energy
In April 2015.

I certify that all material in this thesis which is not my own work has been identified and that no material has previously been submitted and approved for the award of a degree by this or any other University.

Signature: …………………………………………………..

ΣΤ. ήδη παρά τοϊσι φαρμακοπώλαις τήν λίθον
ταύτην έόρακας, τήν καλήν, τήν διαφανή,
άφ΄ής τό πὺρ άπτουσι;
ΣΩ. τήν ϋαλον λέγεις;
ΣΤ. έγωγε. Φέρε, τί δήτ΄ άν, εί ταυτην λαβών,
όπότε γράφοιτο τήν δίκήν ό γραμματευς,
άπωτέρω στάς ώδε πρός τόν ήλιον
τά γραμματ΄ έκτηξαιμι της έμης δίκης;

Strepsiades: Have you ever seen a beautiful, transparent stone at the druggists, with which you may kindle fire?
Socrates: You mean a crystal lens. Well, what then?
Strepsiades: Yes. If I placed myself with this stone in the sun and a long way off from the clerk, while he was writing out the conviction, I could make all the wax, upon which the words were written, melt.
Aristophanes ("The Clouds", 420 BC)

Abstract

In a world that is constantly in need of a continuous, reliable and sustainable energy supply, concentrating photovoltaic technologies have the potential to become a cost effective solution for large scale power generation. In this light, important progresses have been made in terms of cell's design and efficiency, but the concentrating photovoltaic industry sector still struggles to gain market share and to achieve adequate economic returns.

The work presented in this thesis is focused on the development of innovative solutions for high concentrating photovoltaics receivers. The design, the fabrication and the characterization of a large cell assembly for high concentrations are described. The assembly is designed to accommodate 144 multijunction cells and is rated to supply energy up to $2.6kW_e$ at 500 suns. The original outline of the conductive copper layer limits the Joule losses to the 0.7% of the global power output, by reducing the number of interconnections. All the challenges and the issues faced in the manufacturing stage are accounted for and the reliability of the fabrication has been proven by quality tests and experimental investigations conducted on the prototype. An indoor characterization shows the receiver's potential to supply a short-circuit current of 5.77A and an open circuit voltage per cell of 3.08V at 500×, under standard test conditions, only 4.80% and 2.06% respectively lower than those obtained by a commercial single-cell assembly. An electrical efficiency of 29.4% is expected at 500 suns, under standard conditions. A prototype's cost of $0.91/W_p$, in line with the actual price of CPV systems, has been recorded: a cost breakdown is reported and the way to further reduce the cost have been identified and is accounted.

In a second approach, the design of a natural convective micro-finned array to be integrated in a single cell receiver has been successfully attempted. Passive cooling systems are usually cheaper, simpler and considered more reliable than active ones. After a detailed review of micro-cooling solutions, an experimental investigation on the thermal behaviour of micro-fins has been conducted and has been combined with a multiphysics software model. A micro-finned heat sink shows the potential to keep the CPV temperature below 100°C under standard

conditions and the ability to handle the heat flux when the cell's efficiency drops to zero. Moreover, a micro-finned heat sink demonstrates the potential to introduce significant benefits in terms of material usage and weight reduction: compared to those commercially available, a micro-finned heat sink has a power-to-weight ratio between 6 and 8 times higher, which results in lower costs and reduced loads for the CPV tracker.

Acknowledgments

It's often said that the PhD is a long, lonesome road. This is only half-truth. Partly true because my PhD has been about three-and-half-year and at least 84000-mile long. Despite the length of this journey, I have never felt alone: the PhD is a road that I have been lucky enough to walk with many wonderful people beside me. I feel like everyone I have met has added his own brick to the construction of this work: without them, this thesis would not be the same thesis you are going to read.

First of all, I have to thank **Prof. Tapas Mallick**, for having trusted my candidature in such an important project. Despite my mistakes and oversights, I have always been morally and economically supported. I had countless opportunities in these three years and my work has been the only way to pay them back: I sincerely hope to have at least partially settled my account. I would like to thank **Prof. K. S. Reddy**, for having hosted me in his facilities for almost five months and for having continuously followed my work. I have to thank **Prof. Xichun Luo** and **Dr. Senthilarasu Sundaram** for having been, in different moments, attentive second supervisors.

It has been dramatically important to start this PhD in company of my Cypriot twin, **Marios**. I miss our pints and our barbecues; man, I really hope to meet you again soon! **Nabin** and **Eduardo** have been two essential elder brothers, always ready to assist me and to have a coffee or a pint somewhere. Both of you deserve the positions you have obtained; guys, I am sure our roads will meet again! I cannot forget to mention **Nadia**, who has been essential during the last months of my PhD. Thanks for the nice time spent together, for the laughs and for all you support and your friendship: keep on the sunny side!

I have been lucky enough to study at three different universities and, thus, I shared the labs and the offices with many colleagues. During my whole time in the UK, **Hasan** has always been present, sharing with me the same difficult choice to leave Edinburgh. I wish to thank **Nazmi** for his helpful advices and then **Yiorgios**, **Mandy**, **Rashid**, **Prabhu, Shivangi** and everyone else who joined the two research teams I have been part of. A special mention goes to my colleagues in the Indian Institute of Technology Madras: **Arjun**, **Lokes**, **Nikhil**, **Nithil**, and

List of Contents

List of Tables

List of Illustrations

Nomenclature

Symbol	Definition	Unit
A_{cell}	Cell's active area	m^2
A_{fins}	Area of the finned surface	m^2
A_i	Area of the i-surface of the fins	m^2
CL	Characteristic length	m
c_p	Specific heat capacity	J/K
D	Diameter	m
E_{ref}	AM1.5 reference spectrum	W/m^2nm
FF	Cell's fill factor	
$F_{i,k}$	View factor between the surfaces i and k	
g	Gravitational acceleration	m/s^2
Gr	Grashof number	
h	Heat transfer coefficient	W/m^2K
H	Fin height	m
h_{fins}	Heat transfer coefficient of a micro-finned surface	W/m^2K
h_m	Mass specific heat transfer coefficient	W/kgK
h_{tot}	Average heat transfer coefficient	W/m^2K
I_{DC}	Currant provided by the DC supply	A
I_F	Diode's forward current	A
I_R	Diode's reverse current	A
I_{SC}	Cell's short circuit current	A
J	Current density	A/m^2
k	Thermal conductivity	W/mK
k_B	Boltzmann constant	J/K
Kn	Knudsen number	
L	Length of the micro-fins	m
l	Length	m
L_{max}	Maximum length	m
n	Ideality factor	
N_{cell}	Number of cells	
N_{fins}	Number of fins	
Nu_{loss}	Nusselt number of the insulating case surfaces	
N_w	Number of wires	
Pr	Prandtl number	
Q	Heat power	W
q	Conduction heat flux	W/m^2
q_{el}	Elementary charge	C
Q_{cell}	Waste heat produced by the cell	W

Q_{fins}	Heat dissipated by a micro-finned surface by convection	W
Q_{in}	Heat produced by the heater	W
Q_J	Heat generated because of the Joule losses	W
Q_{loss}	Heat lost by the insulating case	W
Q_r	Heat dissipated by a micro-finned surface by radiation	W
Q'_v	Volumetric heat source	W/m^3
r	Hydraulic radius	m
R	Thermal resistance	K/W
R*	Thermal resistance per unit of surface	Km^2/W
Ra	Rayleigh number	
R_{el}	Electrical resistance	Ω
s	Spacing between the fins	m
SR	Spectral response	A/Wnm
T	Temperature	K
t	Thickness	m
t_b	Fin base thickness	m
T_{back}	Temperature of the back surface of the insulating case	K
T_{cell}	Cell's temperature	K
T_{fins}	Temperature of a micro-finned surface	K
v_{air}	Kinematic viscosity of the air	m^2/s
V_{DC}	Voltage provided by the DC supply	V
V_F	Diode's forward voltage drop	V
V_{fins}	Volume of the fins array	m^3
V_{OC}	Cell's open circuit voltage	V
V_{OCS}	Subcell's open circuit voltage	V
V_R	Diode's reverse voltage drop	V
w	Electrical conductor's width	m
W	Fin array's width	m
x	Concentrations	suns
z	Electrical conductor's thickness	m

Greek symbols

α	Coefficient of linear thermal expansion	1/K
$α_D$	Thermal diffusivity	m^2/s
β	Coefficient of volumetric thermal expansion	1/K
$ΔL_{max}$	Maximum expected deformation	m
ΔT	Temperature difference	K
ε	Material's emissivity	
$ε_{fins}$	Fin effectiveness	

θ	Tilt angle	rad
μ_G	Mean of the Gaussian distribution	
v	Kinematic viscosity	m^2/s
ρ	Electrical resistivity	Ωm
ρ_D	Density	kg/m^3
σ	Stefan-Boltzmann constant	W/m^2K^4
σ_{el}	Electrical conductivity	S/m
σ_G	Standard deviation	

Subscripts

air	Air
amb	ambient
c	Convective
d	Layer below the thin resistive layer
d	Power dissipated
fins	Micro-fins
flat	Flat silicon wafer
g	Power generated
HP	Heat path between the cell and the ambient
loss	Losses happening on the insulating case
OC	Open circuit
p	Peak power (under standard test conditions)
r	Radiative
S	Surface
SC	Short-circuit
Syl	Sylgard
Tot	Combination of radiation and convection
trl	thin resistive layer
u	Layer over the thin resistive layer
w	Wire
Ω	Ohmic losses

Prefixes

U	Uncertainty

Abbreviations

ASTM	American Society for Testing and Materials International (USA)
CNT	Carbon nano-tubes
CPC	Compound Parabolic Concentrators
CPV	Concentrating Photovoltaics (or Concentrator Photovoltaics)
CR	Concentration Ratio
CSTCs	Concentrator Standard Test Conditions
CTE	Coefficient of Thermal Expansion
CVD	Chemical Vapour Deposition
DBC	Direct Bonded Copper
DC	Direct current
DNI	Direct normal irradiance
DRIE	Deep Reactive Ion Etching
DST	Department of Science and Technology (India)
DWCNT	Double-walled carbon nano-tubes
ENEPIG	Electroless Nickel/Electroless Palladium/Immersion Gold
EPSRC	Engineering and Physical Sciences Research Council (UK)
EVA	Ethylene-Vinyl Acetate
FF	Fill factor
FR4	Flame Retardant, type 4
HCPV	High Concentrating Photovoltaics
HiPco	High pressure carbon monoxide
HS	Heat Sink
IEC	International Electrotechnical Commission (Switzerland)
IEEE	Institute of Electrical and Electronics Engineers (USA)
IMM	Inverted Metamorphic Multijunction
IMS	Insulated Metal Substrate
IPC	Association Connecting Electronics Industries
IR	Infrared
LCPV	Low Concentrating Photovoltaics
LED	Light Emitting Diode
LM	Lattice-matched
MCHS	Microchannel heat sink
MCPV	Medium Concentrating Photovoltaics
m-EDWM	Micro-electro discharge wire machining
MEMS	Microelectromechanical systems
MHP	Micro-heat pipes
MJ	Multijunction
MPP	Maximum Power Point

MWCNT	Multi-walled carbon nano-tubes
NREL	National Renewable Energy Laboratory (USA)
PCB	Printed Circuit Board
PDMS	Polydimethylsiloxane
PMMA	Poly(methyl methacrylate)
PPMS	Poly(p-methylstyrene)
PV	Photovoltaics
PV/T	Photovoltaic/Thermal collectors
RIE	Reactive Ion Etching
SEM	Scanning Electron Microscope
SWCNT	Single-walled carbon nano-tubes
TIM	Thermal interface material
UHCPV	Ultra-High Concentrating Photovoltaics
UV	Ultraviolet

List of publications

Publications included in the thesis

Book chapters

- Pedro Rodrigo, **Leonardo Micheli**, Florencia Almonacid, The High Concentrator Photovoltaic Module, In: High Concentrator Photovoltaics: Fundamentals, Engineering and Power Plants, Springer, 2015.

Journal papers

1. **Leonardo Micheli**, Nabin Sarmah, Xichun Luo, K.S. Reddy, Tapas K Mallick, Opportunities and challenges in micro- and nano-technologies for concentrating photovoltaic cooling: A review, Renewable and Sustainable Energy Reviews, Volume 20, April 2013, Pages 595-610, ISSN 1364-0321.

2. **Leonardo Micheli**, Nabin Sarmah, Xichun Luo, K.S. Reddy, Tapas K. Mallick, Design of A 16-Cell Densely-packed Receiver for High Concentrating Photovoltaic Applications, Energy Procedia, Volume 54, 2014, Pages 185-198, ISSN 1876-6102.

3. **Leonardo Micheli**, Nabin Sarmah, Xichun Luo, K S Reddy, Tapas K Mallick, Design and Production of a 2.5 kW$_e$ Insulated Metal Substrate-based Densely Packed CPV Assembly, AIP Conf. Proc., Volume 1616, Issue 196, 2014, ISSN 0094-243X.

4. **Leonardo Micheli**, S. Senthilarasu, K.S. Reddy, Tapas K Mallick, Applicability of silicon micro-finned heat sinks for 500✕ Concentrating Photovoltaics Systems, Journal of Material Science, Volume 50, Issue 16, 2015, ISSN 0022-2461.

5. **Leonardo Micheli**, Nabin Sarmah, Xichun Luo, K.S. Reddy, Tapas K Mallick, Development of a Novel 2.65kWe Densely Packed 500✕ Concentrating Photovoltaic Assembly on Insulated Metal Substrate, International Journal of Photoenergy, Issue 2015, 2015, ISSN 1687-529X.

6. **Leonardo Micheli**, K.S. Reddy, Tapas K Mallick, General correlations among geometry, orientation and thermal performance of natural convective

micro-finned heat sinks, International Journal of Heat and Mass Transfer, Volume 91, 2015, ISSN 0017-9310.

Submitted

1. **Leonardo Micheli**, K.S. Reddy, Tapas K Mallick, Thermal Effectiveness and Mass Usage of Horizontal Micro-Fins in Natural Convection, Applied Thermal Engineering (Accepted).
2. **Leonardo Micheli**, Eduardo F. Fernandez, Nabin Sarmah, S. Senthilarasu, K.S. Reddy, Tapas K Mallick, Small-Volume Fabrication of 144-Cell Assemblies for High-Concentrating Photovoltaic Receivers, Journal of Solar Energy Engineering.

In preparation

1. **Leonardo Micheli**, Francesco Donat, K.S. Reddy, Tapas K Mallick, Experimental Correlations for tilted micro-finned heat sinks in natural convection, Journal of Heat Transfer
2. David Benson, **Leonardo Micheli**, S. Senthilarasu, Tapas K Mallick, Assessing social impacts in photovoltaic technology development

Conference papers

1. **Leonardo Micheli**, Nabin Sarmah, Xichun Luo, K S Reddy, Tapas K Mallick "Thermal effects of micro-fins geometry on a silicon receiver for a CPV cooling purpose." In: Conference proceeding of 27th EU PVSEC, Paris, France, 2013.
2. **Leonardo Micheli**, Nabin Sarmah, Xichun Luo, K S Reddy, Tapas K Mallick "Development of a novel 16-cell densely packed 500× CPV assembly on insulated metal substrate" In: Conference proceeding of ICAER 2013, IIT-Bombay, India, 2013.
3. **Leonardo Micheli**, Nabin Sarmah, Eduardo F. Fernandez, K S Reddy, Tapas K Mallick "Technical Issues and Challenges in the Fabrication of a Large High-Concentrating Photovoltaic Receiver." In: 40th IEEE Photovoltaic Specialists Conference, Denver, USA, 2014.

4. **Leonardo Micheli**, S. Senthilarasu, K S Reddy, Tapas K Mallick "500✕ CPV receiver with integrated micro-finned heat sink" In: 11th Photovoltaic Science Application and Technology (PVSAT-11), Leeds, UK, 2015.

Publications not included in the thesis

1. **Leonardo Micheli**, Nabin Sarmah, Xichun Luo, K S Reddy, Tapas K Mallick, "Infrared reflecting coverglass for multijunction cells in a terrestrial high -concentrating photovoltaic system", In: Conference proceedings of 27th EU PVSEC, Germany, 2012.

2. Nabin Sarmah, Katie Shanks, **Leonardo Micheli**, KS Reddy, Tapas K Mallick, "Design and optical performance analysis of a reflective type high concentrating photovoltaic system." In: CPV-9 Conference, 15-17 April 2013.

3. Tapas Mallick, Nabin Sarmah, Sambhu Banerjee, **Leonardo Micheli**, K S Reddy, Prakash Ghosh, Gavin Walker, Shibani Choudhury, Mohamed Pourkashanian, Joel Hamilton, Donald Giddings, Mark Walker, Kandavel Manickam, Amit Hazara, S Balachandran, S Lokeswaran, David Grant, William Nimmo, Anil Mathew, "Design concept and configuration of a hybrid renewable energy system for rural electrification in India through BioCPV project", In: International Conference on Advances in Energy Research (ICAER), 10-12 December, 2013, Mumbai.

4. Eduardo F. Fernandez, Florencia Almonacid, **Leonardo Micheli**, Tapas K Mallick, "Comparison of Methods for Estimating the Solar Cell Temperature and their Influence in the Calculation of the Electrical Parameters in a HCPV Module." In: CPV-10, Albuquerque, USA, 2014.

5. **Leonardo Micheli**, Eduardo F. Fernandez, Florencia Almonacid, K S Reddy, Tapas K Mallick "Enhancing Ultra-high CPV Passive Cooling Using Least-material Finned Heat Sink" In: CPV-11, Aix-les-Bains, France, 2015.

6. **Leonardo Micheli**, Eduardo F. Fernandez, Florencia Almonacid, K S Reddy, Tapas K Mallick "Least-Material Approach for Passive Ultra-High CPV Cooling: an Experimental Investigation" In: 42nd IEEE Photovoltaic Specialists Conference, New Orleans, USA, 2015.

Chapter 1: **Introduction**

The Sun is the predominant source of energy for our planet and in one hour radiates on Earth much more energy than that consumed by humankind in one year. Despite that, the deployment of solar energy for power generation is still limited because it is not yet cost-competitive if compared to the conventional energy sources. In particular, photovoltaics, a method to directly convert the sunlight into electricity, had to benefit from national feed-in-tariffs to find application in the energy market worldwide. Concentrating photovoltaics has been proposed as a solution to lower the cost of this technology, but it is still in a deployment stage and the companies investing in this field are still struggling to achieve adequate earnings. This section gives an overview of concentrating photovoltaics, describing the limits and the recent progresses of this solution. Furthermore, a record of the concentrators' geometries and a list of the most globally important installations and companies are reported, along with some comments on the potentials of this technology and the challenges that the concentrating photovoltaics community need to face.

1.1 Introduction

Energy represents one of the key issues for social and economic development of any country. Compared to 2012, the global consumption of primary energy increased by 2.3% in 2013 [1], driven by the emerging economies, whose energy demand accounted for 80% of growth. Nowadays, the most of the primary energy is supplied through fossils fuels [2], and, in developing countries, through fuelwood, still commonly used for heating and cooking [3]. Although continuing to lose market share, oil is still the dominant fuel, used for 32.9% of the global energy consumption [1].

In 2013, more than $1600 billion were invested in the energy sector, and, out of that, $250 billion were directed to the renewable sources [4], which accounted for a record 5.3% of the global power generation [1]. In the same year, more than half of the yearly net addition to global power capacity was due to renewables [5]. As stated by the International Energy Agency, energy is considered "renewable" when

it derives from natural processes replenished at a faster rate than they are consumed. This definition falls within the concept of sustainable development, intended as "that development that meets the needs of the present without compromising the ability of future generations to meet their own needs" [6]. Moreover, the use of renewable energy is expected to provide the benefit of reducing the emissions of air pollutants and greenhouse gases [7]. The renewable energy's market share is currently lead by hydropower, but, between 2009 and 2013, solar photovoltaics grew at a higher rate than any energy technology, and wind achieved the highest volume of power capacity added among renewables [5].

The Sun is the most powerful energy source for our planet [8], and solar power generation is expected to become competitive with fossil-fuel power generation within the next decade [9]. Among several applications, the most common solar power generation solutions are the photovoltaics (PV) and the concentrating solar power technologies [10]. So far, PV has obtained the widest attention because of the modularity, the low operating costs, the high building integrability, the lack of moving parts, and the excellent safety record [11].

1.2 Photovoltaics

The term "photovoltaics" refers to the direct conversion of solar radiation into electricity, firstly noted by Henri Becquerel in 1839 [11]. Despite the fact that the first silicon solar cell was developed at Bell Laboratories in 1954 [12], 98% of the current global PV capacity has been installed only after the 2004 [5]. Supported by strong national feed-in tariff policies, the PV technology has spread in the last decade, finding application both in on-grid and off-grid installations, and almost half of the current worldwide PV capacity has been installed after 2012 [5]. Since 1980, the photovoltaic market has grown by 37% per year [13] and, in 2013, for the first time, the new installed PV capacity was larger than that of wind [5], reaching a global installed capacity of $139GW_p$ worldwide[i] [3]. This capacity is expected to grow up to $320GW_p$, or, in the most optimistic scenario, up to $430GW_p$ by the end of 2018. Despite this impressive development, Peter Lund [13] reported a decline

---

[i] The peak power is the maximum power that a PV module would produce under standard conditions: $1000W/m^2$ and $25°C$ [11]. It is expressed in Watt-peak, W_p.

of the economic returns for photovoltaic companies in recent years and defined as "poor or negligible" the prospects of initiating new investments in this market. Lund concluded that reducing the price of the technology and the manufacturing costs are keys to raise the profitability of this business. Along with that, in the last years, many countries have stopped or heavily reduced the feed-in tariffs [14], increasing the difficulties to have economic returns for the investors.

1.3 Concentrating photovoltaics

Despite the dramatic reduction of 75% in the cost of crystalline-silicon modules registered since 2011 [15], PV is not yet cost-competitive as compared to other conventional and renewable power generation sources, such as coal, natural gas, nuclear and wind [16]. The cost of a photovoltaic system is still strongly affected by the price of the semiconductor materials: according to the British Department of Energy & Climate Change [17], the module represents between 30% and 50% of the whole cost of the system. One strategy to decrease PV costs is reducing the amount of employed semiconductor material. Some companies are thinning the silicon wafer [18], whereas others use lenses or mirrors to concentrate sunlight onto smaller cells: the replacement of part of the semiconductor area with cheaper concentrating mirrors or lenses is a way to lower the cost of solar electricity. This solution, first proposed in the early 1970's [19], is called *Concentrating Photovoltaics*[i] (CPV) and has already shown the ability to reduce the contribution of the semiconductor to less than 10% of the whole system's cost [20,21].

In 2014, the CPV installed capacity was reported to be 357.9MW [22] and almost 70% of it was shared between the USA and China. In 2012, plants for a cumulative capacity of 471MW were under development in the USA [23]. China is currently holding the record for the largest operational CPV plant in the world: a 50MW plant was opened in 2013 [24]. According to *GlobalData* [22], the worldwide installed capacity is expected to reach $1GW_p$ by 2020.

---

[i] In literature, both the terms *Concentrating Photovoltaics* [18] and *Concentrator Photovoltaics* [25] have been extensively used and are commonly accepted.

One of the most important parameter for CPV is the geometric *concentration ratio* (CR), expressed as the ratio between the concentrating area and the cell's active area. This ratio indicates the number of times that the solar light is concentrated and is generally expressed in *Suns* (1 Sun = 1× = 1000W/m^2). The maximum theoretical concentration ratio achievable on Earth is 46,200× [25], and this is usually set to estimate the limit efficiencies for different types of solar cells. Unfortunately, the effective concentration (or intensity concentration [11]) is actually lower than the geometric CR. This reduction is due to the optic efficiency and to the fact that CPV uses only direct beam radiation, instead of the global radiation (used by flat-PV). Thus, if the concentrator has an optical efficiency of 0.85 and, out of a conventional global radiation of 1000W/m^2, the direct beam radiation accounts for 900 W/m^2, the effective concentration would be 0.85 × 900Wm^{-2}/ 1000Wm^{-2} = 0.765 of the geometric concentration [11].

The most common way for classifying CPV systems is based on the concentration ratio. Although the ranges of concentration for each category have been differently defined in literature [18,26–29], CPV systems can be grouped as follow [30]:

- Low Concentration (LCPV): concentration ratio varies between 1 and 10 suns (1-10×);
- Medium Concentration (MCPV): concentration ratio varies between 10 and 100 suns (10-100×);
- High Concentration (HCPV): concentration ratio is higher than 100 suns (>100×).

Low concentration devices generally use traditional silicon cells and do not require a tracking system [18]. By reducing instead the semiconductive surface by hundreds of time, the use of high cost and high efficiency cells becomes beneficial, because the cell represents only a small fraction of the HCPV total cost. For this reason, the high concentration devices generally use more expensive, record-efficiency multijunction cells. These cells are more sensitive to a wider spectrum of sunlight, thanks to the implementation of several layers of different semiconductors. Most of the CPV companies are investing in HCPV systems

[18,29], because of the best prospects in terms of efficiency enhancement and cost reduction: at the end of 2014, more than the 90% of the installed CPV capacity was designed for concentrations higher than 300× [31].

A new range of concentrations has recently attracted the attention of the research community. Ultra-High CPV (UHCPV) refers to systems with CR>1000×, which have the potential to further decrease the cost of CPV [26,32]. However, the maximum cell's efficiency at ultra-high concentrations is still limited by factors such as series resistance losses and tunnel junctions breakdown [33]. Currently, the cells commercially available are optimized for concentrations up to 500× and, in some circumstances, to 1000×, and a limited number of studies are available on UHCPV.

1.4 Concentrators: an overview

The main challenges for concentrators are minimizing the losses and avoiding any variation of the solar spectrum. Moreover, concentrators are required to prevent non-uniformities in the focal plane, because an irregular distribution of the sunlight would generate mismatches between cells and dangerous hot spots [34,35]. Several different concentrating geometries have been proposed in the last decades [30,36,37] and, among all the potential designs, Fresnel lenses have been so far the most common concentrators [38]. Conventional lenses over 5 cm are too thick and costly to be practical [11], whereas Fresnel lenses have been preferred because of the small volume, light-weight, and low cost [38]. Fresnel lenses are optical elements with step-profiled surfaces, consisting of a series of concentric prismatic grooves designed to direct incident light into a common focus (Figure 1). Fresnel lenses are lighter and thinner and they have lower absorption losses than conventional lenses [39]. They are usually made of acrylic plastic, but Rumyantsev [40] reported that "a tendency exists to replace the 'traditional' acrylic material with more environmentally stable polymers". The main drawback of linear Fresnel lenses is the low concentration ratio that can be achieved [41]. Doubts about the durability of Fresnel lenses have been raised [42]: the poly(methyl methacrylate) material (PMMA) they are usually made of has one of the highest optical durabilities among polymeric materials, but its optical and mechanical durability

under the harsh CPV conditions has not been investigated yet. Alternatively to PMMA, the more expensive silicon-on-glass lenses are expected to provide better performance and longer durability.
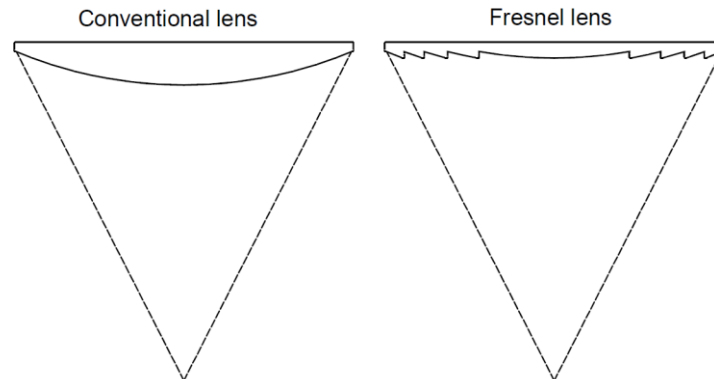
Figure 1 - Comparison between conventional and Fresnel lenses, adapted from [36]**.**

Parabolic mirrors represent an alternative to refractive lenses, because of the potential of being cheaper and reaching higher concentrations than a refractive setup [18]. In particular, by rotating a parabola around its axis, a point-focus configuration is obtained (*parabolic dish*), whereas by translating the parabola perpendicularly to its axis leads to a line-focus configuration (*linear parabolic trough*) [10]. These two schemes require different cells distributions: parabolic dishes are designed for single-cell configurations or for densely packed cells, whereas parabolic troughs are used to focus the light onto a row of cells. CPV systems often include both a primary and a secondary optics in series to increase tracking and alignment tolerance [18]. The secondary optics devices are sometimes exposed to high light intensities: they must be able to withstand high temperatures and to maintain the highest possible optical efficiency.

1.5 CPV technologies: current trends and future perspectives

One of the key drivers for HCPV is the high efficiency of the components, shown in Figure 2: since 2002, the multijunction (MJ) cell's efficiency has increased by 0.9% per year [31]. Today 46.0% is the record efficiency for a solar cell [43], and an efficiency of 46.5% has already been announced [44], but not yet certified in a calibration laboratory [31]. The MJ cells are expected to achieve efficiencies over 50% in the near future [32]. The theoretical maximum efficiencies are limited by the impossibility of fully matching the solar spectrum and by the radiative

recombination taking place in the cells [45]. Nowadays, MJ cells available in the market have efficiencies ranging between 37% and 42% [31].
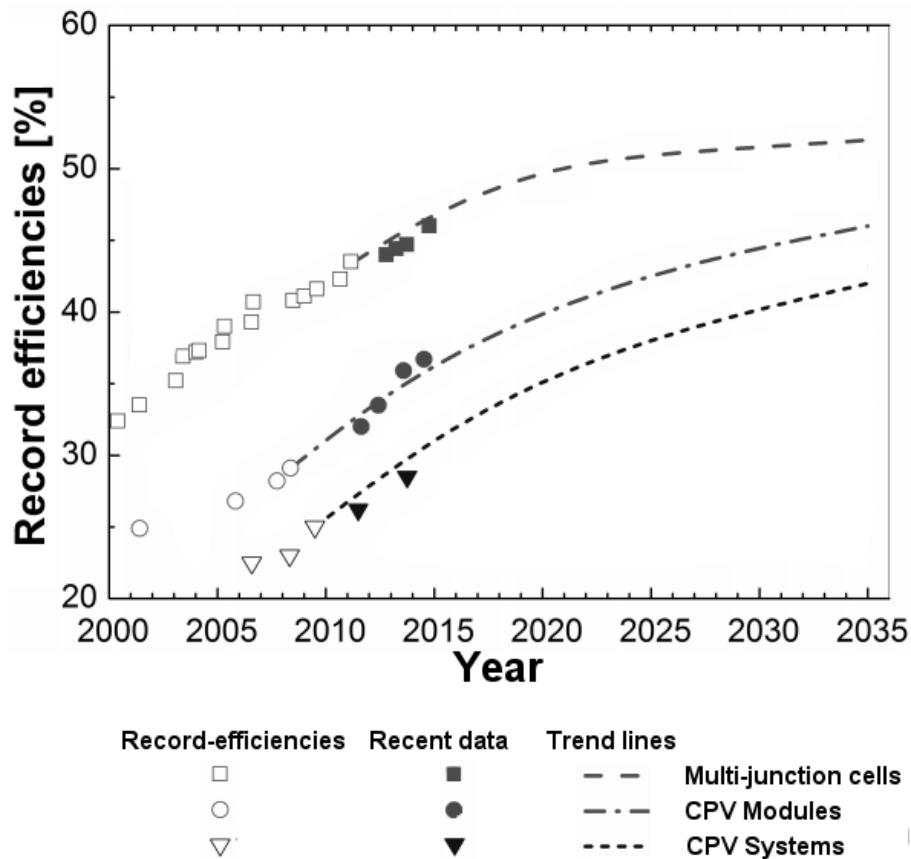
Figure 2 - Record efficiencies of multijunction cells, CPV modules and CPV systems, adapted from [31,46]**. The record efficiency data and the trend lines are reported by** [46]**, whereas the recent data are reported by** [31]**.**

Several companies are working on CPV and each one of them has developed different concentrating technologies. In November 2014, a novel-concept module, equipped with both triple-junction and silicon cells achieved a certified efficiency of 40.4% in outdoor testing at 365× [47]. The record for the module efficiency was previously owned by *Fraunhofer ISE* [48]: an efficiency of 36.7% has been registered for a module consisting of 52 four-junction solar cells provided by *Soitec* and Fresnel lenses achieving a concentration of 230×. *Amonix* [43], an American company currently owned by *Arzon Solar*, has modules equipped with triple-junction cells and Fresnel lens, that reached an efficiency of 35.9% under standard conditions. Among the commercially available modules, in 2013, *Semprius* announced a record efficiency of 35.5%, using Frensel lenses in a 1100× module

[49]. The Japanese *Daido Steel* uses a dome-shaped Fresnel lenses for its 25.8% efficient CPV module [50].

The largest CPV installation is currently located in China, and is owned by *Suncore,* a joint venture between the Chinese *San'an Optoelctronics Co* and the American *EMCORE Corporation*. The DDM-1090X module is used in this power plant: it has a peak efficiency of 28% under standard conditions and uses Fresnel lenses to achieve a concentration of 1090×. In 2013, *Suncore* acquired *ZenithSolar*, an Israeli solar energy company, which owned the patent of a combined heat and power system called Z20. It is composed of two $11m^2$-sized semi-parabolic collectors, mounted on a dual axis tracker that concentrates incoming solar power onto a receiver. The receiver consists of a CPV coupled to a heat exchanger and is able to achieve a combined efficiency of 72% [51]. In this case, multiple small flat mirrors are used to concentrate the sunlight on the receiver (Figure 3).

This image has been removed by the author of this thesis/dissertation for copyright reasons
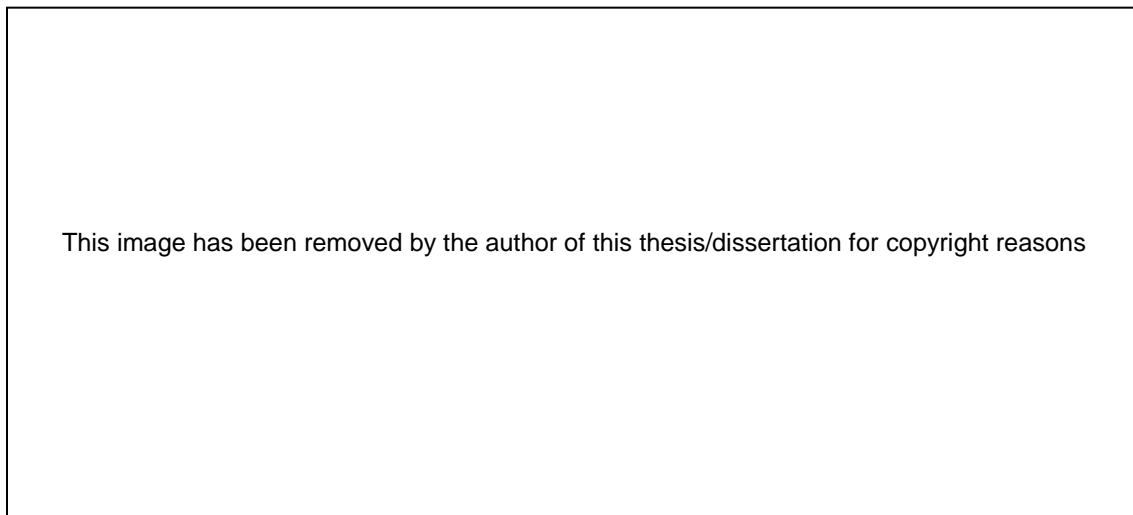
Figure 3 - The ZenithSolar semi-parabolic systems [51]**.**

Reflective concentrators are used by the American *SolFocus* too: primary and secondary mirrors concentrate sunlight 650 times onto the high-efficiency MJ solar cells [18]. Also *Solar Systems,* now *Silex*, an Australian based company, uses parabolic dishes, because of the highest performances and the highest maintainability [19].

This image has been removed by the author of this thesis/dissertation for copyright reasons
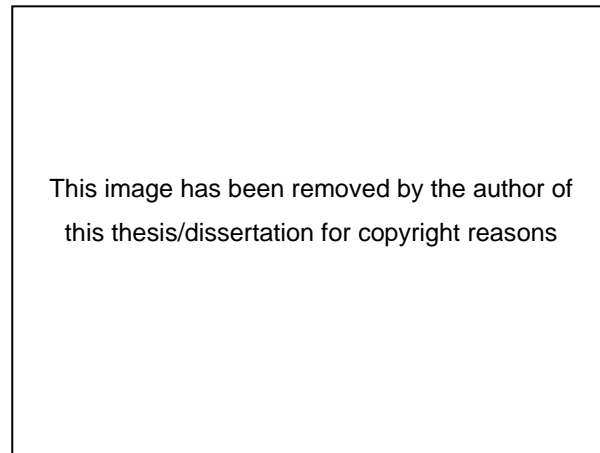
Figure 4 - A CPV plant built by Solar Systems [19]**.**

1.6 Conclusions

The recent progresses of high CPV technology forecast attractive short-term enhancements in terms of efficiency and costs reduction [29]. However, although the number of publications has constantly increased from 2004 to 2013 (Figure 5), with an exception in 2008 and a dramatic rise in 2010, the concentrating photovoltaic technology has not been able yet to prove its competitiveness in the energy generation market. A number of PV and CPV companies have closed or have stopped their solar-related businesses in recent years [52]. In 2013, *SolFocus*, one of the leaders and owner of 18MW of CPV installed worldwide, went bankrupt [53], after having announced, in 2012, the plan of building a record 50MW CPV plant in Mexico [54]. In early 2015, *Soitec*, an international semiconductor manufacturer owing CPV installations for 31MW in 28 countries and deploying a 44MW project in South Africa [55], announced the intention to exit the solar industry [56]. The delaying, the modification and the cancellation of contracts for up to 305MW to be purchased by solar power plants that would use Soitec's CPV technology forced the company to abandon the market. Despite the closure of key companies, a consolidation in module and system suppliers and new strategic partnerships have been registered in the last years [5]. New CPV projects and small pilot plants have been completed or are under way worldwide [57–61].
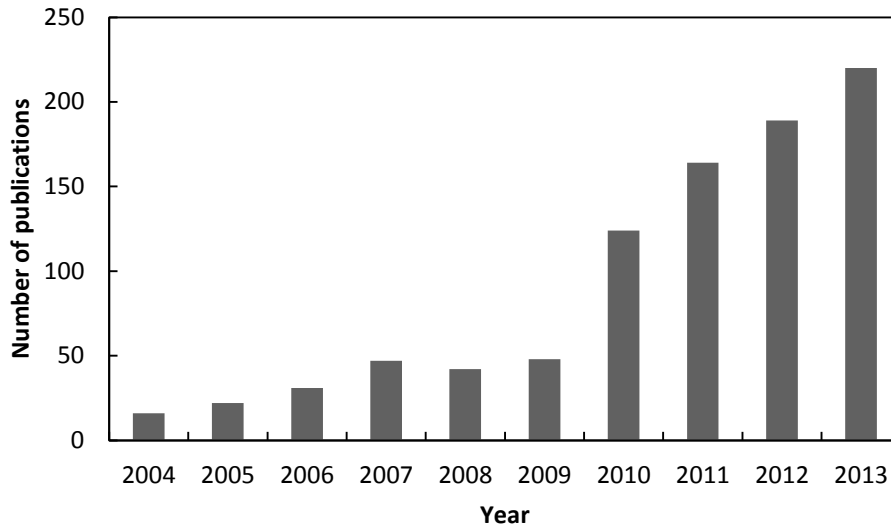
Figure 5 - Number of publications per year classified within the topics "concentrating photovoltaic", "concentrating photovoltaics", "concentrator photovoltaic", or "concentrator photovoltaics". Data sourced from Web of Science[TM], 2014.

As proven by the impressive advancements registered in recent years in terms of cell efficiency and module reliability, concentrating the sunlight on high-efficient solar cells has still the potential to become a cost-effective way to supply energy in a large-scale and sustainable way. Moreover, the reduction in land occupancy and in usage of semiconductive material, still difficult to recycle or to sustainably dispose of, makes the CPV a fundamental player in the future energy market.

In competition with common flat-PV technologies, CPV has particularly suffered the price drop of silicon-based PV, because of the high-cost and high-precision components that CPV is composed of. The CPV community has yet to work in the directions of price reduction, reliability and bankability in order to allow this technology to achieve a complete commercialization and to increase its market share. For these reasons, the goal of this research has been the investigation of innovative solutions able to enhance the performance of concentrating photovoltaics. The work has mainly focused on the receiver, the ultimate component of the system that converts the concentrated sunlight into electricity. Both the current extraction and the heat dissipation mechanisms are located in the receiver and will be reviewed in the next chapter.

Chapter 2: **CPV receivers: state of the art**

This chapter gives an overview of the CPV technologies, reporting the most widely accepted definitions and resuming the most commonly employed components and materials. Moreover, it reviews the state-of-the-art of the cooling systems used to maintain the temperatures of concentrating photovoltaic systems within the acceptable operating range. Particular attention is dedicated to the passive cooling systems and to the micro-technologies, considered able to enhance the thermal behaviour of CPV systems, and, at the same time, to lower both costs and material usage.

2.1 Introduction

High Concentrating Photovoltaic (HCPV) systems achieve concentrations higher than 100 suns and are considered suitable solutions for the future energy market [29]. Despite the recognized potentials, concentrating sunlight onto a small surface introduces some criticisms that influence the design, the fabrication and the operation of CPV systems. The power outputs, the current densities and the heat fluxes have to be maximized, whereas the cost, the size and the weight of the systems need to be reduced. All these concerns make a CPV system much more complex than conventional flat-PV. In any CPV application, the choice of materials and components plays a fundamental role in terms of electrical performance and thermal management.

Considering an optical efficiency of 85% and a cell with a record efficiency of 46.0%, a 500× system operating under a direct normal irradiance (DNI) of 900W/m^2, as for the Concentrating Standard Operating Conditions [62], is expected to produce at least 20W/cm^2 of waste heat. This energy has to be removed from the cell as rapidly as possible, since reduction of about 0.13% in efficiency per Kelvin degree has been registered in GaInP/GaAs/Ge cells at 500× [63,64]. Along with the performance drop, the temperature can lead to cell's degradation and failures. Both active and passive cooling systems have been tested and can be applied in HCPV [65] and, in some cases, the recovered heat has been exploited for other purposes [66,67], increasing the overall efficiency.

In this chapter, the definition of solar receiver is reported and the materials and the components employed in CPV systems are described. The issues related to the cell's temperature are then illustrated and, in conclusion, a review of the present and future potential CPV cooling mechanisms is presented.

2.2 Receivers and cell assemblies

2.2.1 Definitions

The IEEE defines a CPV receiver as "an assembly of one or more PV cells that accepts concentrated sunlight and incorporate the means for thermal and electric energy removal" [68]. According to the IEC 62108 [69], a CPV receiver is made of an assembly of one or more solar cells, a secondary optics and a mechanisms for current extraction, for by-passing in shading conditions and for heat dissipation. The cells are allocated on an electrical substrate, called a *cell assembly*, along with the by-pass diodes, used to minimize electrical losses and damage when the cells are shaded. A complete system, able to convert the unconcentrated solar radiation into heat, is called a module [70] and is represented in Figure 6. The modules are usually mounted on a tracking system that continuously moves them, in order to optimize the incident angle of the sunlight on the cell.
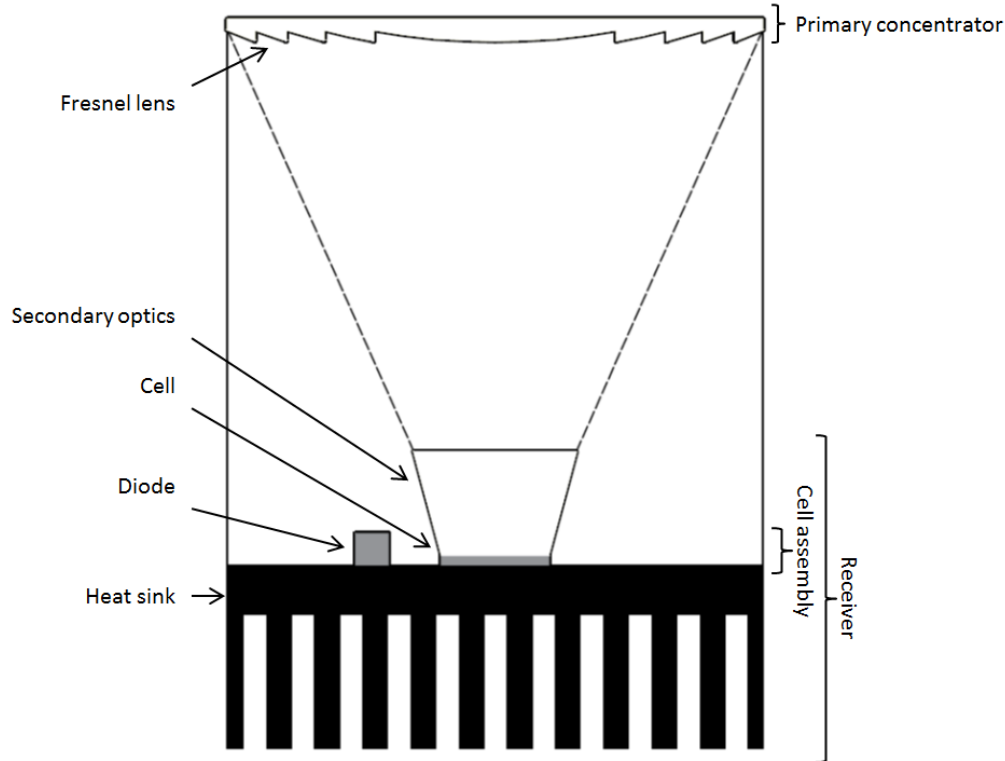
Figure 6 - Structure of a CPV module, composed by primary and secondary concentrators, cells, diodes and heat sinks. Adapted from [13].

2.2.2 Materials and components

2.2.2.1 Substrates

CPV assemblies are usually made of three layers: a conductive layer, a heat spreader and a heat sink. The conductive layer is required to move the current photogenerated by the cell to the extraction mechanism minimizing the electrical losses. The heat spreader has to efficiently transfer the waste heat from the cell to the heat sink, which has then to dissipate it in the surrounding media.

The electrically conductive layer is usually not self-supporting so it has to be placed over a dielectric surface that provides both mechanical support and electric insulation. Copper is the most convenient conductive material, due to its good compromise between cost and performance. Materials such as silver have better performances but, at the same time, higher cost.

The most common substrates in electronics are the Printed Circuit Boards (PCB), laminated materials bonded with heat cured flame retardant epoxy resin and clad

on either one or both sides with copper. PCBs are widely used in electronics, because of their high flexibility and relatively low cost. The laminate materials are primarily chosen to grant a structural strength to the board, but electrical properties (*i.e.* dielectric constant and electrical strength) and environmental properties (thermal expansion, glass transition) also have to be taken into account, especially in CPV applications. Usually the laminated material is a low thermal conductive fiberglass, such as FR4 (Flame Retardant, type 4), a glass-reinforced epoxy resin, but it can be replaced with a metal baseplate. This way the thermal management of the system can be enhanced and the board is referred to as Insulated Metal Substrate (IMS). An IMS consists of a copper foil bonded to a metal base using a dielectric preimpregnated bonding layer. IMSs have been firstly developed for being used in LED (Light Emitting Diodes) applications, and they show a heat transfer management similar to that needed by concentrating photovoltaic technologies [71]. IMSs are considered the best choice in those applications where specific designs are needed, independently of the required quantity [72]. For these reasons, CPV assembly manufacturers' interest in IMS technology is increasing [71,73–75]. Mabille and his group [73] have demonstrated that, when exposed to accelerated aging tests, IMSs behave similarly to the Direct Bonded Copper (DBC) boards, the most expensive [76,77] and most used substrates in CPV applications to date [78–81]. Normally, DBC boards have two layers of copper that are directly bonded onto an aluminum-oxide (also called *alumina*, Al_2O_3) or aluminum-nitride (AlN) ceramic base. Beryllium oxide (BeO) has been widely used in past because of the excellent electrical insulating properties and the high thermal conductivity. Despite that, the high toxicity of the beryllium oxide and the high cost of the raw material have now limited its use to those applications that specifically require its singular properties. According to Arenas *et al.* [82] alumina substrates provide excellent dielectric properties, good thermal properties and high rigidity to the assembly. Although AlN shows an higher thermal conductivity than Al_2O_3 (160-170W/mK versus 24.5-26.8W/mK), alumina still results the most common dielectric for DBC, because of the lower costs, the excellent dielectric properties, and the good rigidity [81,82].

An alternative substrate is represented by a silicon wafer: silicon has a similar thermal expansion coefficient to that of the materials used for the solar cells, it is easy to machine and the dielectric and the conductive layers can be directly sputtered on the substrate. Moreover, the silicon wafer can be easily adapted to work as a heat sink: fins or channel can be machined in it [83,84]. On the other hand, silicon is quite fragile and most expensive than the other substrates.

2.2.2.2 *Surface Mounted Components*

A solar cell assembly is composed of one or more cells, the by-pass diodes, the secondary optics, the encapsulant, the cooling system and the terminal tabs. Differently from well-established packaging technologies for back contact silicon solar cells, CPV requires more consideration in terms of reliability and durability, due to the high experienced fluxes. An initial investigation of components and materials has been conducted in order to build the solar cell assemblies presented in this work in the most appropriate way and is reported in the following paragraphs.

2.2.2.2.1 Multijunction cells

Photovoltaic cells are designed to capture the photons of the solar spectrum. When a photon hits a PV cell [11]:

- If the photon has less energy than the band gap, it is not collected and passes through the cell;
- If the photon has more energy than needed, the extra energy is lost as heat;
- If the photon has the same energy of the band gap, the energy conversion works at the maximum efficiency.

Silicon has been the most used material for photovoltaic cells because it is inexpensive and relatively well understood. The bandgap of silicon is estimated to be 1.1eV[i], whereas the solar spectrum contains energy in the range between 0 and 4eV, with 2.5eV at the peak of the spectrum [85]. This means that most of the infrared spectrum is not collected by silicon cells, limiting the maximum achievable efficiency. In order to increase the conversion rate, the solar spectrum can be

---

[i] $1eV \approx 1.6 * 10^{-19} J$

instead divided into several regions: rather than converting the photon energies with a single cell exploiting a single band gap only, solar energy can be converted by several cells, each one tuned for a different region of the spectrum.

The spectrum can be split across various semiconductors through two approaches: a spatial-configuration (Figure 7a) or a stacked-configuration (Figure 7b) [11]. In the first case, an optical device distributes photons with different energies into different locations, where they hit the "most appropriate" subcell [86]. This approach has recently shown high efficiency potentials for unconcentrated or low concentration PV applications [87–90], but it is still considered complex to be applied in a tracked HCPV [91]. The preferred approach in CPV is to arrange the cells in a stacked configuration, where different layers of semiconductors are piled. Due to this geometry, these cells are usually called multijunction (MJ) cells. The band gaps must decrease from the top to the bottom of the cell: this way, considering the light hitting the top of the cell, the top subcells act as low-pass photon energy filters, transmitting to the subcells below only the sub-bandgap photons. Larger wavelengths (with lower energy) pass through the upper subcells and are absorbed below.

(a) spatial-configuration   (b) stacked -configuration

Figure 7 - Configurations for multijunction spectrum splitting, adapted from [91]**.**

Initially multijunction cells have been used for space applications, where high efficiencies are needed, extra costs are acceptable and high radiation-resistance is required [28,92]. They are still too expensive for flat-PV applications, but they have become desirable for CPV, where the required cell area is smaller [93].

Burnett [91] stated that "alloys of Group III and Group V elements lend themselves well to the design of multijunction cells. By carefully adjusting the compositions, a range of bandgap energies can be achieved. Such selections are usually made in conjunction with lattice-constant constraints". The lattice constant measures the distance between atom locations in a crystal pattern. Lattice mismatches create defects and dislocations, increasing PV conversion losses. For this reason, the most common MJ cells are made of *lattice-matched* (LM) semiconductors (Figure 8).

Figure 8 - Semiconductors lattice constants [94].

Lattice-matched GaInP/GaAs/Ge triple-junction cells are the most common MJ cells nowadays [43]. From top to bottom, they are composed by the following layers, represented in Figure 9:

- **GaInP** is a semiconductor composed of indium, gallium, and phosphorus. It is used as high energy junction. It absorbs the ultraviolet and visible part of the solar spectrum (band gap ≈ 1.85eV);
- **GaAs** is a III-V semiconductor composed of gallium and arsenic. It absorbs in the near infrared spectrum (band gap ≈ 1.42eV);
- **Ge** absorbs lower photon energies in the infrared spectrum (band gap ≈ 0.67eV).
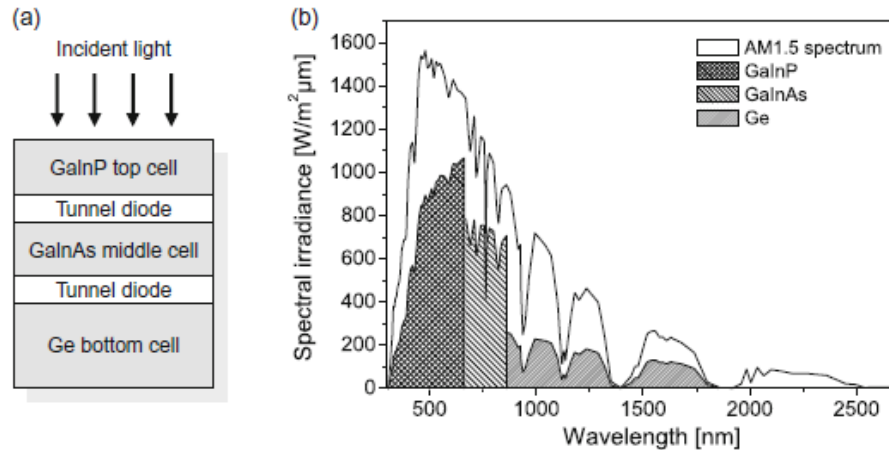
Figure 9 - Spectral irradiance of the AM1.5 spectrum together with the parts of the spectrum that can be used by a triple-junction solar cell [94]**.**

An additional optimization characteristic for MJ cells is the *current matching*. Due to the series-connected configuration, the output current of a MJ cell is equal to the smallest one among the currents produced by any subcell. Thus, it is important to design each junction to produce the same amount of photocurrent [91] and each layer's thickness is selected to best match the currents of the other two subcells. The absorption coefficient for solar cell materials is not infinite: a cell of finite thickness will not absorb all the incident light above band gap [11] and a fraction of that light will be transmitted. The thinner the cell, the greater the transmission: thinning a subcell will decrease its current, increasing instead the current in the lower subcell. For this reason, a correct subcell sizing is important to obtain the current-matching. The terrestrial sun spectrum contains less high-energy light than the AM0[i] spectrum and, thus, in order to satisfy the current matching requirements, the thickness of the terrestrial top subcell has to be greater than that of a space cell [11].

Multijunction cells' efficiencies have recently increased at a rate of about 0.5-1% per year [18]. At the end of 2014, the highest efficiencies were demonstrated as 27.6% and 46.0% for silicon single-junction cells and for multijunction cells respectively [43] under concentrated sunlight. In 1980, C. H. Henry [45] reported

---

[i] *Airmass* (AM) indicates the amount of atmosphere that light must pass to reach the ground. It is a ratio between the optical path length and the optical path length when the sun is at zenith. AM1 occurs if the sun is at zenith, whereas AM0 corresponds to the solar irradiance in space. The most used standard spectrum distribution for comparing the terrestrial solar cell performance is the AM1.5 spectrum normalized to a total power density of 1000W/m^2 [11].

that the efficiency limit for ideal 1-, 2-, 3-, and 36-junction cells would have been 37%, 50%, 56%, and 72%, respectively, at 1000 suns concentration and with the solar cell held at room temperature. In the same year, A. De Vos [95] reported that under 1 sun irradiance, an ideal 1-, 2-, and 3-junction solar cell could covert up to the 30%, 42% and 49% of the solar energy. Under the highest possible light concentration, instead, these efficiencies were set at 40%, 55%, and 63% respectively. The same author [95] then calculated an ideal efficiency of 68% and 86.8% for an infinite-junction cell at 1 sun and at extreme concentration respectively. Cells with 4, 5, and 6 junctions have been recently grown and have the potential to replace the triple-junction cells in future [96]: ideal conversion efficiencies of over 59% for the 4-junction cells, and over 60% for the 5- or 6-junction terrestrial concentrator cells are expected [97].

Traditional GaInP/GaAs/Ge cells are fabricated to have the same lattice constant in all the subcells. The semiconductors used in these cells can be grown with very high-quality [18], but the band-gap combination of the lattice-matched triple-junction cells leads to large excess current in the Ge layer: a different set of semiconductors, would grant a better band-gap combination. A wide range of MJ cells other than the GaInP/GaAs/Ge ones are being investigated and might find application in the near future [98], such as the metamorphic and inverted metamorphic (IMM) cells. In contrast to LM cells, subcells of a metamorphic cell do not have the same lattice constant [99]. The monolithic growth of materials with different lattice constants leads to misfit dislocations that deteriorate the material quality: the introduction of buffer structures between the Ge bottom cell and the GaInAs middle cell is required to reduce the effects of the dislocations [94]. In the IMM cells instead, the top subcell is grown first on a lattice-matched substrate and, then, is followed by the other subcells [28]. This way, the material quality of the upper subcells is enhanced compared to the conventional MJ cells [94]. Alternatively, the subcells can be separately fabricated and then mechanically stacked [100]. Despite the high efficiencies [101], the high costs of mechanically stacked cells have limited their diffusion so far [94].

In a different approach, silicon subcells can be used to replace the more expensive Ge subcells. But silicon introduces some problems [94]: a 4.1% difference in lattice constant and a difference in thermal expansion coefficients compared of GaAs (Table 1). Moreover, so far, GaInP/GaAs/Si triple junction cells have demonstrated lower efficiencies than GaInP/GaAs/Ge triple junction cells [43,94].

Table 1 - Semiconductors' properties comparison.

	Bandgap	Linear thermal expansion at 25°C	Lattice constant at 300K [siliconfareast.com]
GaAs	1.4 eV	$5.7 * 10^{-6}$ °C^{-1}	5.653 Å
Ge	0.7 eV	$5.9 * 10^{-6}$ °C^{-1}	5.646 Å
Si	1.1 eV	$2.6 * 10^{-6}$ °C^{-1}	5.431 Å

2.2.2.2.2 By-pass diodes

Shading is an important matter to take into account when designing photovoltaic systems, since it has been identified as one of the main causes affecting the energy yield of grid-connected photovoltaic systems [102]. A shaded cell is not truly an open circuit, but it acts as an impedance added to the solar array. When reverse biased, the shaded cell dissipates power and generates heat. Thus, hot spots can then occur and damage the cell and the devices connected to it.

Shading of a complete row of series-connected cells causes a power loss of almost 100% and, for this reason, it can be treated as an open circuit [103]. Several models to calculate the power losses have been presented in literature [104–107]. The amount of power loss depends on the size and the shape of the shadow, the geometrical and electrical layout of the cells in the array, as well as on the number of shaded cells [104]. The ratio between the shaded semiconductive surface and the total surface is defined *shading factor* [108]: it has been demonstrated that, in stable ambient conditions, the CPV system power decreases linearly with the shading factor [109].

By-pass diodes (also known as *shadow diodes* or *shunt diodes*) can be used to prevent both the power dissipation and the hot spots in shading conditions of work. The basic function of by-pass diodes is protecting solar cells against hot spots and damage when the photovoltaic module is partially shaded. In regular operation, the

diode is reverse biased and, in this condition, only a small amount of leakage current flows through it (Figure 10). The device turns on when the cell is shaded (Figure 11) and, then, the current flows through the diode, by-passing the shaded cell.
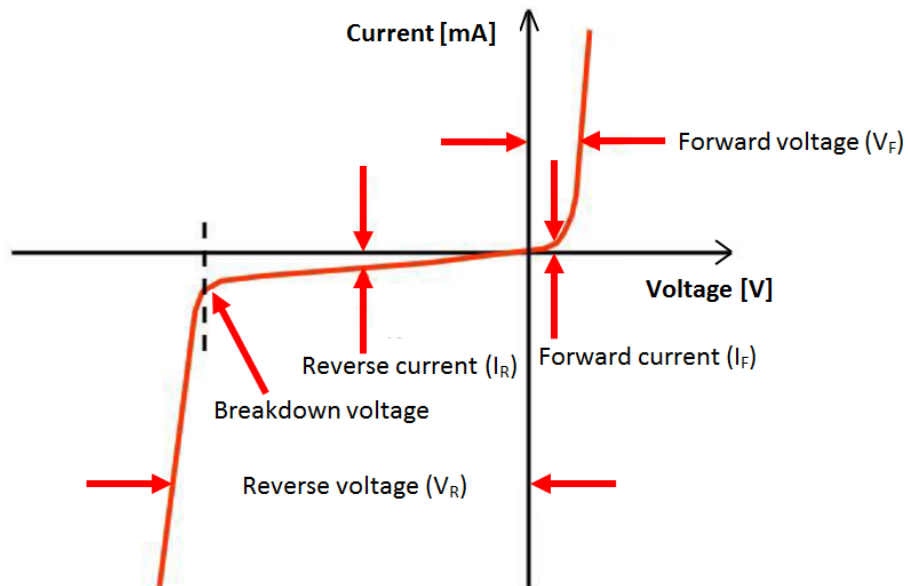
Figure 10 - Voltage-to-current curve of diode, adapted from [110]**.**
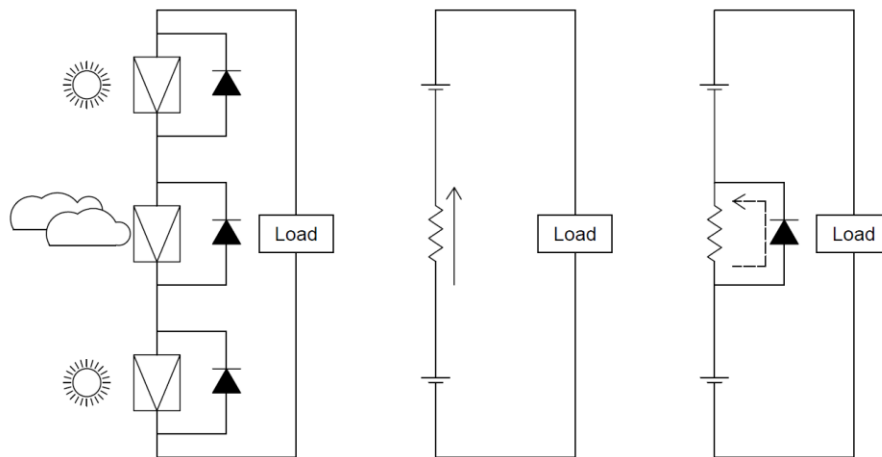
Figure 11 - By-pass operation, adapted from [110]**.**

Vorster and Van Dyk [111] analysed the current-voltage (I-V) characteristic of two series-connected point-focusing 335× HCPV modules. Each module consisted of sixteen series connected cells. Modules' normal operation voltage varied between 12V and 14V, while the maximum power point voltage was 11V. Initially a by-pass diode was connected across each eight-cell string. The authors changed the layout and installed one by-pass diode per cell: even if the maximum power remained the

same, the energy produced by the cells significantly increased. One bypass diode per cell limited the effects of the current mismatches and, since the mismatched cells were no longer reverse-biased, the resistive heating was limited and the module was found to operate at lower temperatures.

The key parameters to take into account to select an appropriate by-pass diode are:

- Physical size of diode compatible with the solar cell layout and the available space;
- Lowest possible reverse leakage current;
- Lowest possible forward voltage drop;
- Lowest possible diode series resistance;
- Capability to withstand temperature cycling without electrical failures.

According to Janssen *et al.* [112] the application of common p-n junction diodes as by-pass results in high losses and is not practical. On the other hand, the application of Schottky by-pass diodes is considered economical and more efficient. Schottky diodes have a lower forward voltage drop and, therefore, lower losses and lower temperature while in by-pass operation. Usually they switch faster and are able to work with higher currents than the normal diodes. Schottky devices have been previously used in CPV [78,82].

As already stated, Schottky diodes show a small forward voltage drop (V_F), even in case of high currents (I_F). However, they do not perform so well when reverse biased: the reverse voltage drop (V_R) across the diode strongly increases when increasing the reverse current (I_R) flowing there-through. This is highlighted by the initial slope of the reverse characteristic curve, more enhanced than that of conventional diodes, as highlighted in Figure 12. In order to limit the enhancement in reverse voltage, oversized Schottky diodes have to be used. Moreover, it is known that diodes break more easily if they are working closer to the maximum rating [113]. So, over-dimensioned diodes are generally considered more durable and reliable, and are, thus, preferred.
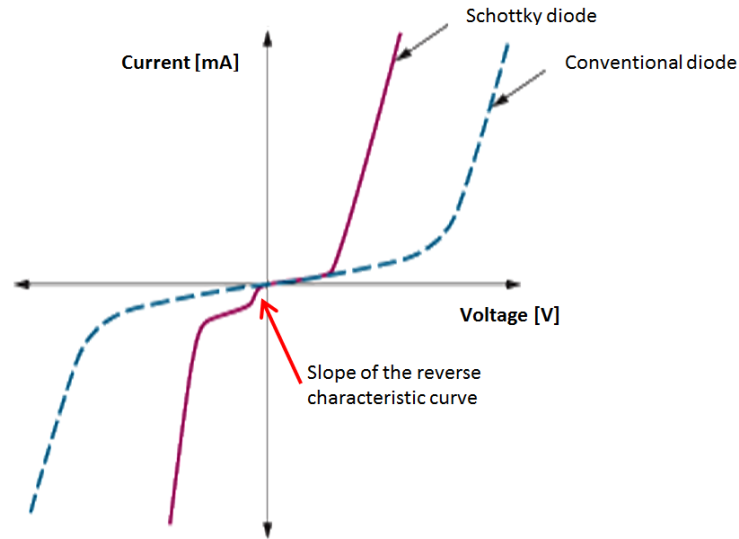
Figure 12 - The characteristic curve of Schottky diode compared to a p–n diode, adapted from [114]**.**

A promising alternative to Schottky diodes is represented by the so-called *lossless diodes* (or *cool by-pass switches*). These devices are composed by a diode, a charge pump, a capacitor and a trigger [115]. Compared to Schottky diodes, cool by-pass switches reduce the electrical losses both in reverse and direct bias conditions. The average forward voltage drop for the 10A SPV1001 cool by-pass switch produced by STMicroelectronics is 2-3 times lower than the one of a comparable 10A Schottky diode. The reverse leakage can drop up to 1000 times lower. The drop in electrical losses has a second benefit too: while operating under the same conditions, they have been found to work at lower temperatures than Schottky diodes [115]. Although the better performances, these devices are more complex, expensive and larger than common by-pass devices [112]. Moreover, the literature is still limited and their reliability in CPV applications has yet to be demonstrated.

2.2.2.2.3 Die attaches

Solderings and adhesives play an important role in the assembly, especially in terms of electrical and thermal resistances [116]. Soldering is usually recommended by the solar cell manufacturers because of the high thermal and electrical conductivities [117]. A uniform distribution of the solder paste below the cells is essential to optimize the cell's performance and to avoid catastrophic failures [118,119].

In some applications a thermally conductive adhesive can be used to replace solder paste. Adhesives help preventing delamination and maintaining good surface contact between substrates with different coefficients of thermal expansion, limiting the stresses [120]. However, thermal adhesives and pastes usually result in poor thermal conductivity, creating an interface with thermal resistance in the order of 20mm^{2}K/W [121], and do not survive a large number of thermal cycles. Duckham and He [121] demonstrated that a high conductivity epoxy bond did not survive past 400 cycles, while a low conductivity epoxy bond was found to be more reliable, although showing signs of degradation with thermal resistance values increasing with the number of thermal cycles. The same result was reported by Ross *et al.* [122] for Epo-Tek, an electrically conductive epoxy developed by *Epoxy Technology*. Cao *et al.* [123] tested the durability of epoxies used as bonded material in a CPV cell and discovered that, at temperatures lower than 70°C, the material started to break, causing the failure of the CPV module.

A possible alternative solution to solder pastes and adhesives can be represented by NanoFoil®, produced by *Indium Corporation* and made of thousands of alternating nanoscale layers of aluminum (Al) and nickel (Ni). The solder is quickly realized at room temperature through a small pulse and can operate at high temperatures. It is electrically conductive, has high thermal conductivity (35 to 50 W/mK) as compared to epoxy resins and has already demonstrated to be able to survive more cycles than other adhesives [121].

2.2.2.3 Interconnectors

The triple junction cells used in this work have the positive terminal on the bottom Ag/Au alloy-finished surface, suitable for soldering, which grant at the same time the mechanical support and the required thermal and electrical conductivities. The negative terminal consists of two thin metallic tabs symmetrically placed on two edges of the active area on the front of the cells. The interconnectors link the front tabs of multijunction cells with the conductive layers and are expected to allow the current extraction only. Because of the reduced size of the tabs, usually less than 0.5mm wide, micro-electronics process are required to achieve the high-quality expected for CPV systems. Micro-welding is the procedure generally exploited by

commercial companies to interconnect the front of the cell with the conductive layer [78], due to its high mechanical strength. It consists of a thin silver tab welded on the cell's sides and soldered on the conductive layer. Wire bonding represents an alternative, lower cost solution: it has become a standard microelectronics technology, widely available and has already been exploited in CPV [124]. It is considered extremely reliable after the introduction of automatic wire bonding, low temperature bonding processes and effective pad cleaning methods [125]. Either gold or aluminium wires are generally used. High-conductive copper wires have been recently developed and are gaining much attention, but are not yet capillary available. A summary of the different materials properties is reported in Table 2.

Table 2 - Properties of wire bonding materials, adapted from [126]**.**

Material	Properties	Application
Aluminium	Best mechanical properties; High corrosion resistance; Applied at room temperature; Excellent bondability; Good loop stability.	Automotive components; IC cards; Power components.
Copper	High conductivity High tensile strength; Good loop stability; Require inert atmosphere to bond.	Discrete components; Semiconductor components.
Gold	High conductivity; High corrosion resistance; High cost; High temperature required to bond.	High power components; High frequency applications; Opto-electric applications Integrated circuits.

2.2.2.4 Encapsulation

The encapsulation materials are used to protect the cells from environmental corrosion and mechanical damages and to provide electrical insulation. Encapsulants are exposed to high optical flux, including ultraviolet (UV) and infrared (IR) wavelengths. The light intensity and wavelength distribution are important considerations to take into account when choosing the most suitable encapsulant material. Another important criterion in the selection is the durability under the harsh CPV conditions. The cell encapsulant must remain optically stable over several years: it must not delaminate, discolour or crack. The industry generally requires a minimum of 20-year lifetime with minimal reduction of efficiency.

Ethylene-Vinyl Acetate (EVA) has traditionally dominated the flat panel PV application, due to the low cost and the proven durability [127]. In low and medium CPV applications, EVA and other hydrocarbon-based encapsulants should be capable of performing well for the whole service lifetime [127]. At high concentrations, instead, siloxane-based encapsulants, such as *poly(dimethylsiloxane)* (PDMS), have been predominantly used, because of the extreme high resistance to thermal and light-induced degradations.

The US National Renewable Energy Laboratory (NREL) published several papers on this topic. As shown in Figure 13, Miller and al. [128] reported that PDMS, *Poly(p-methylstyrene)* (PPMS) and *Poly(methyl methacrylate)* (PMMA) were the materials providing the most efficient power production, because of the low-absorptance in the PV specific wavelengths' range. Kempe *et al.* [129] investigated the durability of some CPV encapsulant materials, exposing them to about 42 suns of UV radiation and found that PDMS materials did not show any sign of degradation after 4000 hours of exposure.

This image has been removed by the author of this thesis/dissertation for copyright reasons

Figure 13 - Optical absorptance for CPV encapsulant materials [128]

In 2011, Miller and al. [130] tested the durability of polymeric encapsulation materials. They observed material decomposition, as well as fractures and haze formations, in CPV modules if no homogenizing optic was applied. The authors

tried adding soil, aluminium fillings, polymer fillings or voids to separate sets of EVA and PDMS and reported that:

- Soil, aluminium and polyethylene facilitated the thermal decomposition of EVA;
- Polyethylene facilitated the thermal decomposition of PDMS;
- The soil and the aluminium filled sample became cracked within 2 days in the field;
- The specimens with bubbles did not appear changed after 116 consecutive days, but voids reduced the optical transmittance.

McIntosh *et al.* [131] found that the optical properties of the PDMS remained quite stable after exposures to a 30× concentration, while EVA had the highest tendency to absorb moisture, which resulted in scattering.

Silicone has been used in PV modules on satellites and in LEDs. It has high optical transparency and aids in providing stress relief during thermal cycling, thanks to the low coefficient of thermal expansion (CTE). Norris and al. [132] stated that silicone is an ideal candidate for PV encapsulations, thanks to its high transparency in the UV-visible wavelength regions, very low ionic impurities, low moisture absorption, low dielectric constant and broad temperature use range. Moreover silicone shows excellent adhesion to the glass and cell substrates. The authors marked silicones as an excellent material for PV encapsulant. According to them, silicones will increase the module efficiency of about 0.5-2.5% as compared to equivalents modules encapsulated with EVA, due to higher transparency in the low-wavelength region. McIntosh *et al.* [131] stated that silicone showed very little degradation after 232 days on the 30× concentration, while EVA was reduced to char after 43 days.

In 2011, Velderrain [133] investigated the benefits and the risks associated with using phenyl containing silicones versus non-phenyl silicones. Phenyl silicones demonstrated higher chemical resistance than non-phenyl silicone but, despite increasing the photon flux to the cell, it is more affected by external factors, such as dry heat or UV, than non-phenyl silicones.

Encapsulants and coverglasses can play an important role in CPV cooling. In fact, IR photons with energies below the lowest bandgap of multijunction cells cannot be used to produce energy and are converted into waste heat, increasing the cell temperature. Moreover, the Ge subcell in traditional multijunction GaInP/GaAs/Ge cells produces a significantly higher current than the other two subcells connected in series [134]. For these reasons, part of the near-infrared light can be reflected to reduce the amount of heat produced by the cells, and, thus, to contribute maintaining the cell's temperature in the operating range [135]. Works presented in literature refer to inverted metamorphic cells [136,137] and space applications [134,138,139], whereas no previous research was found about terrestrial application of infrared reflecting encapsulant in triple junction cells.

2.2.2.5   Considerations

In HCPV, series-connected cells arrangement should be preferred because it would limit the current flowing into the connectors and, thus, minimize the Ohmic losses. This configuration requires a uniform sunlight over the cells, in order to avoid current mismatch: otherwise, the current value will be limited by the worst performing cell. Series-connected designs have been used both in several flat-plane PV modules and in some multijunction applications [140,141]. However, the receiver shape and the cell distribution on it are important parameters to take into account before deciding connections layout.

By-pass diodes are used to minimize output losses and to protect cells when they become shadowed. In strings of silicon cells, one by-pass diode may be connected to several cells. On the other hand, multijunction cells are particularly susceptible to damage when subjected to a reverse bias condition. Thus, in multijunction cell applications, the use of one by-pass diode per cell is generally recommended.

Despite its application in common PV, all the researchers agree that EVA is not a convenient encapsulation material for CPV applications. For a 500× plant, the best solution seems to be the application of a silicone material, such as PDMS, which showed highest performance and longest degradation time.

2.3 Concentrating photovoltaic cooling

Only a fraction of the incoming sunlight is used by the cell to generate electrical energy. The remaining part of the absorbed energy is converted into thermal energy [65] and increases the temperature if not removed. The cell temperature strongly influences the electrical performance. The efficiency of any photovoltaic cell decreases when the temperature increases and when the temperature is not uniform across its volume [11]. Martinelli and Stefancich [116] stated that "this fact can be viewed as a consequence of the second principle of thermodynamics imposing a limit on the conversion efficiency of energy coming from a source at a given temperature by a converter/sink having a finite temperature". Moreover, the cells also exhibit long-term degradation if the temperature exceeds certain limits [65]. For these reasons, the solar cells employed in HCPV systems are generally kept at temperatures ranging between 50°C and 80°C [142,143] while in operation. Temperatures should not overtake 150°C [117]: this temperature is considered the maximum allowed limit in case of exceptional conditions (such as inverter's or cooler's failures). Long exposure to extreme temperatures can melt the solder paste and damage the circuitry. Higher temperatures are tolerable for short time periods only during the module's fabrication.

Cooling usually is not required in common flat PV systems, because of the large module surface and the limited irradiance. On the contrary, cooling becomes an important aspect in CPV systems, due to the reduction of the receiver surface and the rise in sunlight concentration. This section is intended to describe the effects of the temperature on the cells and will give an overview of the CPV cooling latest state of the art.

2.3.1 The effects of the temperature

The *open circuit voltage*[i] (V_{oc}) of PV cells decreases with temperature [116]. Because of the stacked configuration, the V_{oc} of a multijunction cell is the sum of the open circuit voltages of each subcell (V_{ocs}). Thus, the temperature coefficient dV_{oc}/dT_{cell} can be obtained as the sum of the dV_{ocs}/dT_{cell} [11]. According to the

---

[i] Open circuit voltage: the output voltage of a solar cell with no current flowing from it [91].

datasheet [144], the latest GaInP/GaAs/Ge cell released by *AZUR SPACE Solar Power*, faces a reduction in open circuit voltage of 0.135% per Celsius degree at 500✕, which corresponds to a drop of 4.2mV/°C. Higher concentrations reduce the percentage V_{oc} drop, because V_{oc} increases with the concentration [11].

The *short circuit current*[i] of the system is positively influenced by the temperature. The subcell that gives the smallest output limits the current (I_{sc}): usually the top and the middle subcells produce lower currents than the Germanium bottom one. Moreover, the subcells do not have the same temperature coefficients. The increase in cell temperature normally causes a red shift in the spectral response (Figure 14) and, consequently, a change to the current mismatch between the top and the bottom subcells [145]. The redshift increases the current of the top and the middle subcells, so the overall current is expected to increase. In particular, the short circuit current of a commercial cell increase by the 0.080% per Celsius degree at 500✕ [144]. Studying the space applications, Aiken *et al.* [146] concluded that solar cells are fairly insensitive to temperature in terms of current matching: a III-V cell designed to be current-matched at 28°C is current-mismatched by only 3.3% at 100°C.
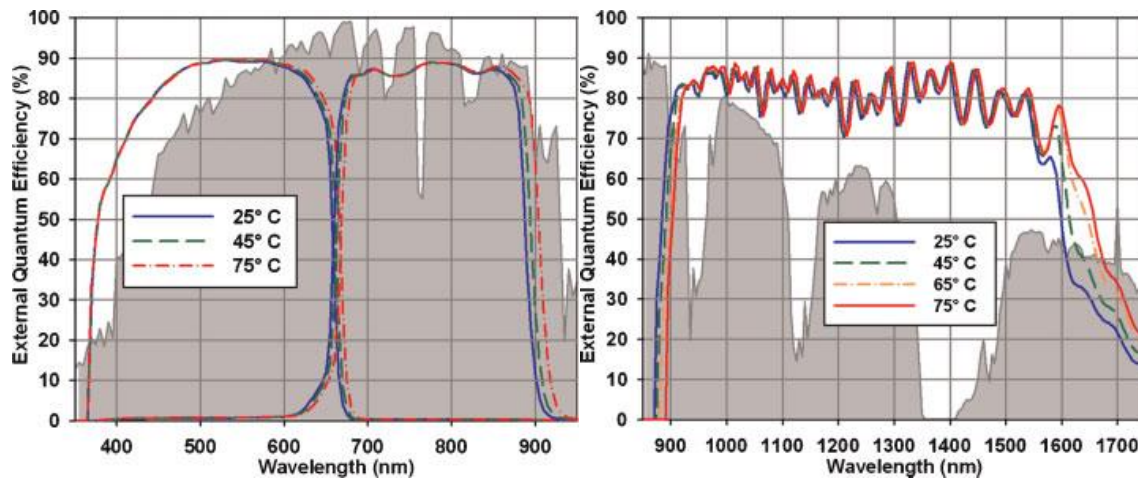
Figure 14 - The red shift in the spectral response of a GaInP/GaAs/Ge cell [142]**.**

---

[i] Short circuit current: the current produces by the cell when a zero-resistance is placed across its terminal [91].

The fill factor[i] (FF) is strongly influenced by current-limiting subcells [11], similarly to the current output. A reduction of 0.106% in fill factor is registered for each degree at 500× by the AZUR SPACE MJ cell [144]. The efficiency depends on the product $V_{oc} \times I_{sc} \times FF$: it decreases almost linearly when temperature increases [11]. An average relative drop of 0.106% in efficiency is registered per each degree in a MJ cell working at 500× [144].

Along with the drop in the electrical performance, overheating can introduce some mechanical issues in CPV systems. Long term degradation has been demonstrated for cells exposed to high temperatures [142]. The temperature rising can also lead to mechanical failures such as deformation on the cell surface, delamination of the transparent layer and development of micro-cracks on the cell. The difference in thermal expansion coefficients among the several materials that compose the cells and the assemblies can even cause immediate or fatigue failures of cells and fragile components.

The cell temperature is a key parameter to be taken into account in any operating CPV system, but it is difficult to directly measure [70]. Moreover, it can be up to 30°C higher than that of the heat sink [147] and depends on different factors, including the heat sink design, the thermal attachment, the location, the irradiance, and the wind speed. For this reason, many indirect methods to determine the temperature of the cell have been presented in literature and are based on:

- meteorological data [143,148],
- the electrical outputs [149],
- the heat sink temperature [143],
- the photo-luminesce emissions [150,151].

The most suitable method is usually chosen depending on the application, the available data and the required accuracy [70].

---

[i] Fill factor is a performance parameter, commonly used to describe the degree to which V_{MPP} (voltage at maximum power point) matches V_{oc} and I_{MPP} (current at maximum power point) matches I_{sc}. It can be expressed as:
$FF = (I_{MPP} \cdot V_{MPP})/(I_{sc} \cdot V_{oc}) = P_{MPP}/(I_{sc} \cdot V_{oc})$ [91]

2.3.1.1   An experimental investigation

A preliminary investigation on the temperature rising in HCPV was experimentally carried out. A 166× system was built, using a PMMA Fresnel lens to concentrate the AM1.5 light generated by a solar simulator on a commercial assembly equipped with a 37.2%-peak efficiency MJ cell [117]. The room was constantly kept at 25°C. A thermocouple was placed in contact with the side of the cell to measure the temperature and the temperature was recorded every 0.2 seconds.

During the experiments, several setups were tested, using different heat sinks under the same conditions. The relevance of the heat sink for the thermal management of CPV can be noted in Figure 15. In the first case, no heat sink was added to the cell. The temperature quickly increased, going over 150°C in less than a minute. The test was repeated twice. In the second attempt, the test was not stopped at 150°C: the solder paste started melting and the assembly was damaged. In the second case, a 0.5 mm-thick copper plate (dimensions: 12cm×12cm) was stuck to the backplate of the receiver through a thermally conductive adhesive. This way, the temperature raising was slower, reaching a temperature about 120°C in 10 minutes. In the third setup, a commercial 10-fin aluminum heat sink was used: in this case, after 600 seconds the temperature was about 50°C lower than the copper plate case.
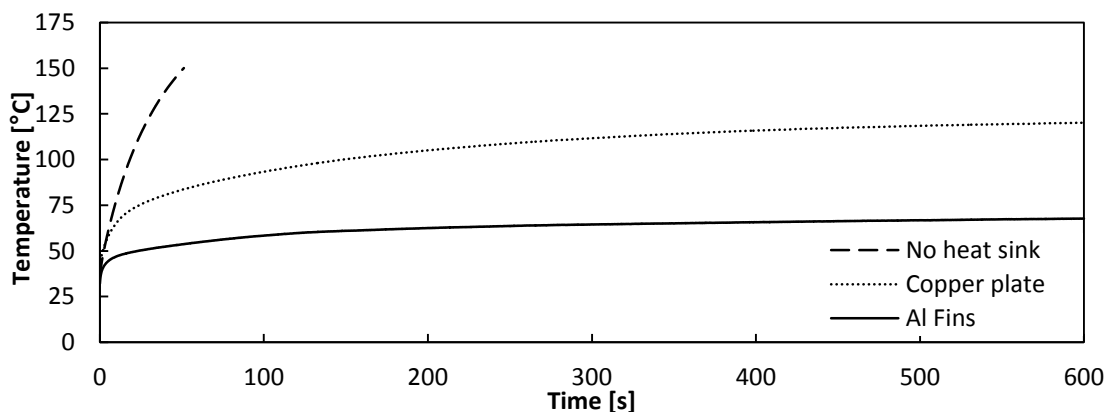
Figure 15 - Temperature rising with different heat sinks

This investigation was useful to understand the variation in performance due to the temperature rising. An I-V tracer was used to measure the performance every time a 5°C growth in temperature was registered. As reported in Figure 16, a difference

of about 10% was registered between the power output at 40°C and the power output at 70°C.
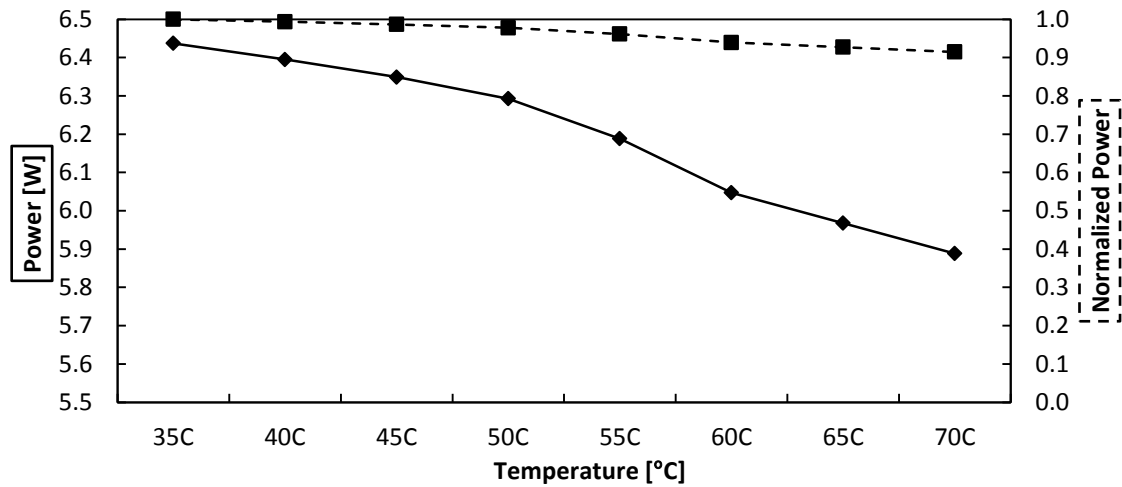
Figure 16 - Power vs. temperature.

2.3.2 Passive and active cooling

Usually cooling systems are classified as *passive* or *active*. Passive cooling does not require input of mechanical or electrical power because it acts through the exploitation of natural laws. Active cooling instead is obtained using a fraction of the cell power output and is usually independent of the work conditions and easily controllable. The use of part of the energy output reduces the overall system efficiency.

In 2005, Royne *et al.* [65] published a complete review on the cooling system for photovoltaic cells under concentrated illumination. At the end of the report, the authors stated that passive cooling was not feasible for any densely packed cells or for linear concentrators with concentration ratios above 20 suns. They concluded that micro-channel heat sink or impinging jets, both active cooling systems, were found to be the most promising technologies for CPV cooling. In 2008, Yeom and Shannon [152] wrote a review about micro-coolers, but only few among the reported technologies were passive. In 2007, Tseng *et al.* [153] applied Taguchi's statistical method to optimize the passive cooling systems for electronic devices: they stated that passive cooling is more reliable than active cooling and reduces the damage probability caused by cooling failures.

Some references use a different definition for passive and active cooling. In [154], active cooling referred only to the so-called *photovoltaic/thermal* (PV/T) technology, where the PV waste heat is reused for other purposes. In this concept, technologies such as micro-channels or fluid jets impingement are not necessarily included. In this work, the terms "active" and "passive" are used according to the first reported meaning.

2.3.3 Key features for CPV cooling

The design of a CPV cooler depends on many factors, which are not limited to the concentration and the outdoor conditions. Firstly, the geometry of the optics plays a fundamental role. The most typical optical configurations in HCPV systems are shown in Figure 17. In those reflecting systems where no reflective secondary is applied, the receiver is usually located between the sun and the mirrors (Figure 17a). This means that the receiver needs to be as compact as possible, to reduce the shading. Due to their higher thermal exchange coefficients, active coolers can achieve better performances while limiting the volume and, for this reason, are preferred. If, instead, a secondary reflector is present (Figure 17b) or the concentration is achieved through lenses (Figure 17c), the cooler would not create any risk of shading and larger surface would be available for cooling. In these cases, passive cooling may be preferred.
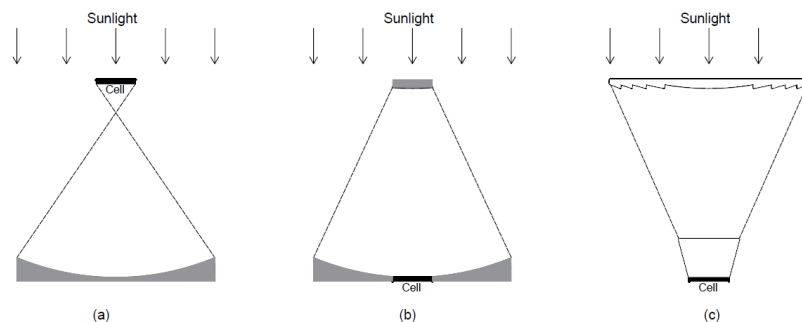
Figure 17 - Typical optical configurations for HCPV devices: only primary reflecting optics (a), primary and secondary reflective optics (b) and refractive optics(c). In (a), the cooler must be compact to reduce shading, so that active cooling is usually preferred. In (b) and (c), a larger area is available for the cooler, so that passive cooling can easily operate.

Secondly, the number of cells and their distribution on the receiver are key issues to be taken into account: cells are usually grouped either in single-cell, linear or densely-packed geometries [65]. In single cell geometries, concentrators focus the

sunlight onto an individual cell. This is a favourable configuration for cooling: ideally, an area equal to the surface of concentrators is available for heat exchanging purposes. In linear geometries two sides of each cell are in contact with the adjacent cells, reducing the available cooling surface. In densely-packed geometries, each cell is surrounded by cells on each side (excluding the cells on the side): the reduced surface available for cooling and the high thermal power densities make the application of passive cooling systems difficult.

Thirdly, the choice of the fluid may depend on its availability. High thermally conductive fluids might be too expensive or not easy to provide in remote locations. Unfortunately water is not yet easy to access in many locations, especially in those areas, such as the desert lands, where irradiance is particularly high. For these reasons, in some applications, air can result the best fluid to be exploited, both for active or passive systems.

Lastly, the inclination angle of the receiver changes continuously, since HCPV systems are usually tracked. Heat sinks in natural convection are particularly affected by the inclination angle and, in particular, a downward facing heat sink is the worst orientation for passive cooling. In spite of that, CPV systems may require such disadvantageous orientations for their cooling devices [155,156].

2.3.4 State of the art

The simplest passive way to increase the thermal transfer of any surface is the addition of fins [157]. The performance of the fins in HCPV systems are not only dependant on the number, the spacing and the length [158], but are affected as well by the inclination angle and the temperature difference [155]. The heat management of any heat sink can be enhanced by a forced air flow. Due to the low heat capacity of air, water cooling has been applied in many high concentrating systems: impinging jets [159], water-immersion [160] and heat pipes [161]. Beyond all these proven technologies, more solutions, such as thermoelectric devices [162] or two-phase flows [163], can arise as a feasible way for efficient HCPV cooling. Due to the high power densities and the small volumes involved, micro and nano technologies can play an important role in HCPV cooling. Micro-channels have

already been successfully applied in CPV [164]. The suspension of high thermally conductive particles smaller than 100 nm into a fluid can be a way to enhance the performances of any system. Nanofluids have already been used in many applications [165], including PV/T cooling [166], but, despite their potential, the research on their application for heat transfer purposes seems to have lost appeal [167]. Among the emerging passive micro-technologies, carbon nanotubes and micro-fins are the most promising solutions [168]. More technologies, such as nano-wires or miniature heat pipes and thermosyphons may soon become suitable for HCPV. The integration of different technologies can lead to innovative and high-performing solutions: hybrid schemes, such as hybridizations of jet impingement and micro-channels [169,170], have shown the capability of reaching high heat transfer coefficients and of improving the temperature uniformity [171]. Nowadays, the ratio of solar energy converted into heat is still higher in percentage than that converted into electricity. The re-use of the waste heat produced by HCPV represents already an opportunity to improve the overall system efficiency and, thus, to reduce the costs of the technology. According to Kribus *et al.* [172], adding a heat-recovery system to an actively-cooled or a passively-cooled HCPV system would increase the installation costs by no more than 5% and 10% respectively. Cogeneration is able to provide both electricity and heat at medium rather than low temperatures [173]. The recovered heat can be used in many domestic and industrial processes, such as air conditioning, water desalination or water heating.

A detailed review of the CPV cooling systems presented so far in literature is reported in the following sections, according to the categorizations proposed by [65], and the main features of each technology are summarized in Table 3.

Table 3 - Main characteristics of different cooling system, adapted from [36]**.**

Type	Description		Ref.
Microchannels	(i)	Low thermal resistance;	[36]
	(ii)	Low power requirement;	
	(iii)	Ability to remove a large amount of heat from a small area.	
Impinging jets	(i)	Low thermal resistance.	[65]
Hybrid jet impingement/microchannel	(i)	High uniformity of temperature;	[170,174]
	(ii)	Reduced pressure drops;	
	(iii)	High heat flux dissipation.	
Two-phase forced convection	(i)	High heat transfer coefficient.	[65]
Water immersion	(i)	Minimized contact thermal resistance;	[175]
	(ii)	Uniform.	
Heat pipe	(i)	Simple;	[36]
	(ii)	Reliable;	
	(iii)	Uniform;	
	(iv)	Costless;	
	(v)	Passive.	
Heat spreader	(iii)	Simple;	[176]
	(iv)	Passive.	
Cooling fins	(i)	Well known;	[155,158]
	(ii)	Simple;	
	(iii)	Reliable;	
	(iv)	Passive;	
	(v)	Costless.	

2.3.4.1   *Microchannels*

A microchannel heat sink (MCHS) suits well many electronics applications, because of its ability to remove a large amount of heat from a small area. As already remarked, Royne *et al.* [65] stated that this technology is the best performing active cooling system for HCPV.

A MCHS cooling system is composed of many parallel micro-channels, with hydraulic diameters ranging from 10 to 1000nm. Coolant is forced to pass through these channels to carry the heat away [177]. In a MCHS the coolant flows close to the heat source and, this way, the contact area between the coolant and the cooling structure is enlarged. Convective heat transfer in microchannels has been found to be significantly higher than in conventional sized channels [178]. According to Karathanassis *et al.* [164], MCHS are particularly suitable for the high heat flux dissipations and can achieve thermal resistance values as low as 0.0082K/W. In 2011, Mu̇ller *et al.* [179] investigated the micro-channels performances in a ultra-high CPV. They showed that the system remained fully functional up to 4930 suns, registering drop of 1% in photovoltaic efficiency per each 100 suns concentration increasing.
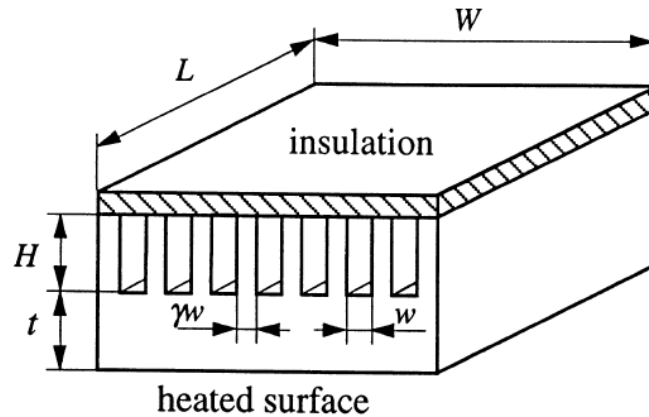
Figure 18 - Schematic of a microchannel cooling system [180]

One way to enhance the heat transfer in MCHS devices is the application of *nanofluids*, traditional heat transfer fluids - such as water or oil - containing suspended nano-particles (average size below 100nm) [181]. The use of metallic particles enhances the thermal behaviour of fluids: the addition of a small amount of nano-particles (less than 1% in volume) has been found to double the thermal conductivity of the fluid [181].

2.3.4.2   Impinging jets

Thermal resistances as low as $10^{-6}m^2K/W$ can be achieved through the use of impinging liquid jets [65]. This is an active cooling solution, where high velocity liquid is forced onto the surface to be cooled. The number of nozzles per unit of area affects the performance of the system: a high number of jets would enhance both the overall performance and the uniformity of the cooling effect.
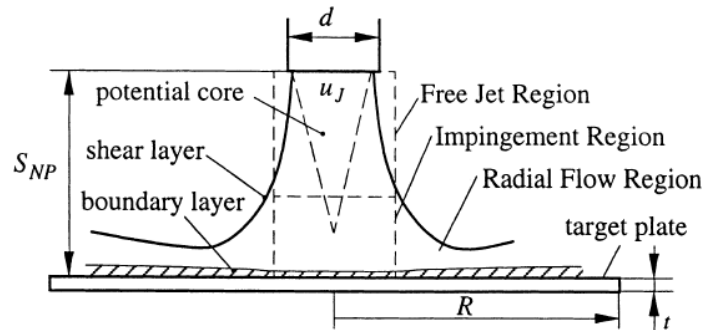
Figure 19 - Schematic of a typical jet impingement arrangement [180].

2.3.4.3 Hybrid jet impingement/micro-channel cooling

Lee and Vafai [180] compared the performances of jet impingement and micro-channel cooling systems. Jet impingement cooling usually required a very large coolant flow rate with a comparatively small pressure drop, whereas micro-channel cooling was subject to a large pressure drop even for a comparatively small flow rate. The authors stated that "the microchannel cooling is preferable for a target dimension smaller than 0.07m×0.07m, while the jet impingement is comparable or better than the microchannel cooling for a larger target plate if a proper treatment is applied for the spent flow after the impingement".

The successful applications of micro-channels and jet impingements leaded to the investigation of a hybrid solution [170,174], because "both technologies provide very high flux removal" but "do not offer adequate temperature uniformity on the receiver". The combination of both solutions, shown in Figure 20, made it possible to maintain higher temperature uniformity across the cell's surface. The efficiency of the hybrid system was found to be 48.5% higher than that achieved applying a classical micro-channel design, with pressure losses reduced by 90.5%.
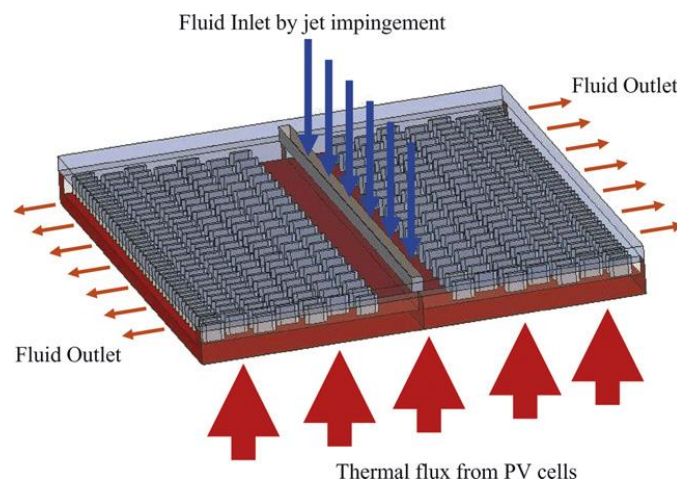
Figure 20 - Principle of operation of the hybrid cooling device [170]**.**

2.3.4.4 Two-phase forced convection cooling

By allowing the coolant to boil, the heat capacity of a fluid can accommodate a significantly larger heat flux [65]. The main advantage of this solution resides in the possibility of achieving high heat transfer coefficients using low coolant flow rates, requiring a reduced pumping power [182]. Royne *et al.* [65] proposed the two-

phase forced convection as a viable active cooling alternative to micro-channels and impinging jets.

2.3.4.5 Water immersion cooling

Water immersion cooling is an active cooling solution, schematized in Figure 21: the solar cells are immersed in a circulating dielectric liquid. This way, the heat is transferred from two cells surfaces, rather than from the cell's back surface only as for conventional CPV systems. Moreover, the contact thermal resistance between the cell and the cooling system is minimized [175].
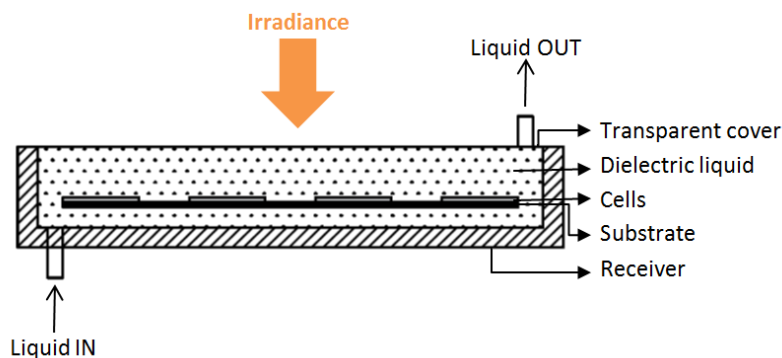
Figure 21 - Design concept schematic of liquid immersed solar receiver, adapted from [183]**.**

Zhu *et al.* [160] reported that the cell temperature under high concentrations could be maintained below 45°C and the convective heat transfer coefficient could be higher than 3000W/m^{2}K. They demonstrated that at 250 suns the overall convective heat transfer coefficient could reach a value as high as 6000W/m^{2}K. An analytical investigation by Han *et al.* [184] showed that a uniform temperature could be maintained in a liquid-immersed CPV receiver. Among the suitable fluids, Victoria *et al.* [185] found that the most appropriate fluids were paraffin and silicone oils, because the transmittance was only slightly affected by the UV radiation at AM1.5.

2.3.4.6 Heat pipe

A heat pipe is a vacuum tight device consisting of a working fluid and a wick structure (Figure 22). The heat input vaporizes the liquid working fluid inside the wick. Then, the vapour condenses and gives up its latent heat. The condensed liquid returns to the evaporator through the wick structure by capillary action [186].
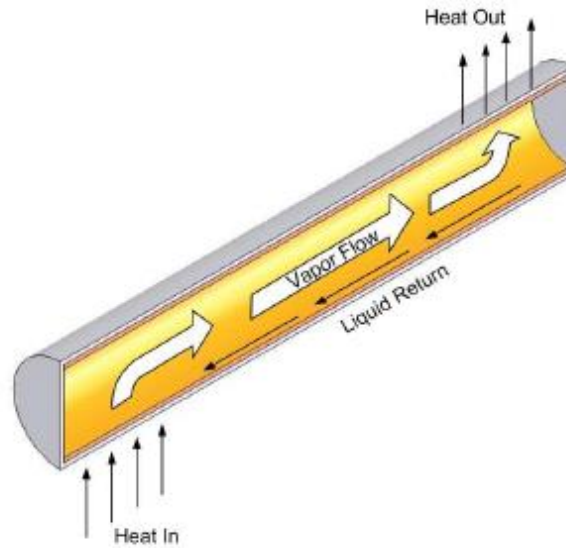
Figure 22 - Heat pipe crossing section, © 2008 IEEE [161]**.**

Anderson *et al.* [161] placed an array of fins around the heat pipe, as shown in Figure 23. The heat was distributed by the heat pipe to a series of fins, where it was removed by natural convection. This way, the heat pipe was suitable for single cell arrays at high concentration ratios (up to 1000 suns), and for linear concentrators at lower concentration ratios (up to 30 suns).
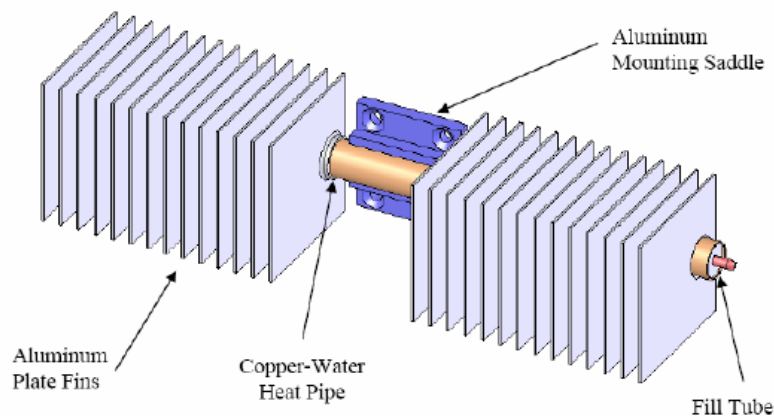
Figure 23 - Heat pipe 3D representation, © 2008 IEEE [161]**.**

2.3.4.7   *Heat spreading*

One of the simplest approaches for passive cooling can be obtained using a heat spreader: in this case, heat is exchanged by a metal plate. Araki *et al.* [176] used a 3mm-thick aluminium plate, represented in Figure 24, as large as the concentrator,

to cool a solar cell under 500× and demonstrated that the cell temperature would be only 18 degrees higher than ambient.
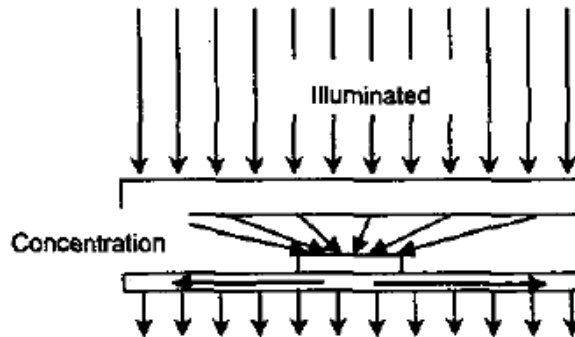
Figure 24 - Araki *et al.* cooling device representation, © 2002 IEEE [176]**.**

2.3.4.8   Cooling fins

Natarajan *et al.* [158] investigated the use of cooling fins in a LCPV. The authors firstly observed that the thermal conductivity of the back plate of the receiver was important for reducing the solar cell temperature: the higher the conductivity, the lower the solar cell temperature. Moreover, the authors defined a maximum number of fins that appeared to be effectively convenient in the considered case. On the other hand, Natarajan and his colleagues found that the thickness of fins did not significantly influence the cell temperature: "use of larger fin thickness, increases the conduction heat loss, but at the same time suppresses the convection heat loss in between the fins". The best configuration they tested was found to reduce the cell temperature by 35% compared to the worst case. A correlation between the fin spacing, the inclination angle and the temperature difference for a CPV setup cooled by a plate-fin heat sink was developed and reported by Do *et al.* [155] after a detailed investigation on the relationship among the thermal resistance, inclination angle and power input.

2.3.5 Micro-and nano-technologies for cooling CPV systems

Aluminum is generally used to fabricate heat sink and, according to [21], can contribute to more than 60% of the module's weight. For this reason, reducing the weight of the heat sink would benefit in terms of both system's efficiency and emissions' drop. In this light, the development of micro-and nano-technologies offers new perspectives for CPV cooling. Due to the small dimensions and the

promising performances, micro-and nano-technologies can play an important role in CPV cooling. This section gives a critical overview of the potential technologies that could find application in the thermal management of concentrating photovoltaic systems.

2.3.5.1 Principles

The concentration of sunlight leads to a reduction of the irradiated surface. Mesoscale cooling device could be not appropriate to remove a great amount of heat from small surfaces. Micro-and nano-technologies, intended as technologies on a micro- or nano-scale that have application in the real world [187], can assure faster performance, requiring both less space and less material than common devices. On the other hand, when sizes drop below 100nm important changes in material properties can occur. Additionally, in the nano-meter domain there are new unique effects due to quantum phenomena and enhanced surface to volume ratios that have to be considered [188]. A lot of research has been focused on micro- and nano-cooling technologies, due to their growing importance in electronics: micro- and nano-scaled electronic devices have already been proven able to manage heat fluxes exceeding one thousand watts per centimetre square [152,188].

2.3.5.2 Micro-and nano-cooling technologies

Several papers were published on micro-cooling, but no one strictly focusing on passive micro-cooling and its application to CPV systems. In 1998, Gromoll [189] published a review of micro-cooling systems based on forced air cooling for high density packaging. Nano-scale thermal transport advances were reported in 2003 by Cahill *et al.* [190] and in 2006 by Shakouri [188]. In 2008, Yeom and Shannon [152] wrote a review on micro-coolers, where nano-technologies, such as carbon nano-tubes and nano-wires, were not explored in detail.

2.3.5.3 Micro-and nano-cooling manufacturing

The nanotechnology manufacturing techniques can be divided into conventional and unconventional processes. The first, such as photolithography and electron beam lithography use light or electrons to generate patterns and are the most

widely used techniques. According to Gates *et al.* [191], the cost of purchasing, installing, and maintaining the tools they require limits their application in areas other than microelectronics. A summary of the conventional nanofabrication techniques are given in Table 4. The unconventional techniques are reminiscent of macroscopic molding, embossing, printing and skiving technologies, and are indicated as the ultimate, low cost solutions [192]. They are usually developed to overtake the technical or financial limitations of conventional methods.

Table 4 - Comparison of conventional nanofabrication techniques, adapted by [192]**.**

Technique	Cost
Contact lithography	$
Proximity lithography	$
Projection lithography	$$$
Extreme Ultraviolet lithography	$$$

2.3.5.4   Coolers

A list of micro- and nano-technologies for passive cooling electronic devices will be reported in this section. The cooling technologies are summarized based on the working fluid [152]:

- **Air cooling**: heat spreaders, natural convection in micro-channels, carbon nano-tubes, micro-fins, nano-wires;
- **Liquid cooling**: natural convection of nano-fluids, micro-heat pipes, miniature thermosyphons.

2.3.5.4.1 Micro-heat spreaders

Micro-heat spreaders are thin layers of high thermally conductive, dielectric materials, with a high specific heat [193]. A good heat spreader should show a coefficient of thermal expansion (CTE) close to those characteristic for semiconductors, stability under thermal cycling in the operating temperature, low specific weight, easy manufacturability and low cost [194]. According to Bar-Cohen and Wang [195], due to the high thermal conductivity of silicon (~150W/mK), only modest spreading improvements can be obtained from the use of traditional spreading materials, such as copper (390W/mK), beryllia (250W/mK), aluminum nitride (220W/mK). Aluminum and copper are good heat conductors, but their

coefficients of thermal expansion are higher than those of germanium or silicon. Composite materials such as Cu-W or Al-SiC are less expensive, but the thermal conduction is usually lower than 250W/mK. No common composite materials show thermal conductivity higher than 400W/mK (Figure 25). Higher thermal conductions can be obtained with pyrographite and diamond composites. Pyrographites plates are strongly anisotropic and thus cannot be easily applied [194]. Carbon nanotubes have been considered for composite materials, due to their high conductivity. Unfortunately, while showing important enhancements in mechanical proprieties, CNT composites cannot be considered a promising option yet [194].
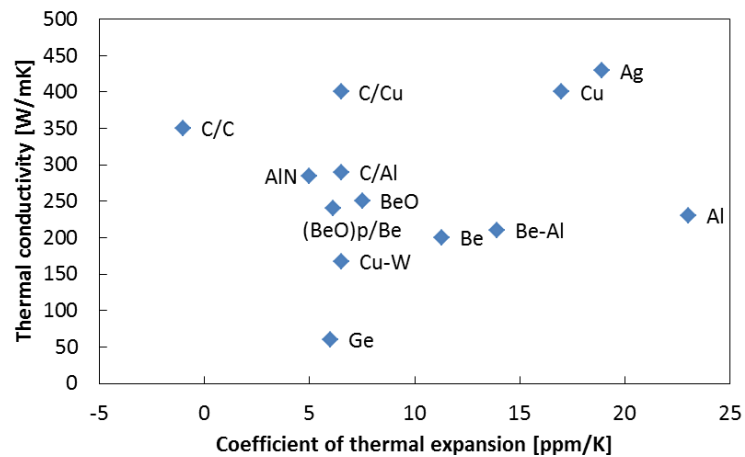
Figure 25 - Thermal conductivities vs CTEs of different materials.

Diamond is indicated as a very good material for electronic heat spreading [193,195,196] due to its extremely high thermal conductivity (500-2100W/mK, the highest values among all the known materials) and its very high electrical resistance ($\sim10^8\Omega$m). Bar-Cohen and Wang [195] defined the deposition of diamond on substrates, such as silicon, as a "reasonably mature technology" able to assure good results. This was also confirmed by Zhang *et al.* [197] and Twitchen and al. [198], who stated that the thermal conductivity of the best quality synthetic diamond grown by Chemical Vapour Deposition (CVD) is identical to that of high purity natural type diamond at room temperature (2200W/mK). Due to its important qualities, the deposition of a diamond layer on the receiver seems to be a good solution for CPV cooling.

Jagannadham *et al.* [193] noted that the low molar heat capacity of diamond made it good for distribution of energy rather than dissipation. For this reason, they suggested that the low heat capacity of the diamond could be compensated through a higher heat capacity substrate on which the diamond is then deposited. In their heat spreader design, the authors used an intermediate layer of aluminum nitride under a continuous layer of diamond. They obtained an increase in heat spreader characteristic and life compared to a single layer diamond and a molybdenum heat spreader. On the other hand, Zhang *et al.* [197] simulating in COMSOL the performances of a polycrystalline CVD diamond thermal substrate as a part of active cooling for power devices, observed that there was no improvement in cooling by replacing the aluminum nitride with diamond in a direct bonded copper, because of the higher value of the thermal convection resistance than that of the thermal conduction resistance. Once all the redundant layers were removed, they demonstrated an increase in power dissipation of the systems by two times by replacing the ceramic with the diamond. A further increase in performances was then obtained by depositing a layer of copper micro-pillars onto the backside of the diamond substrate.

Diamond deposition is obviously an expensive process which is the main commercial limitation of this technology. The cost of the thermal diamond substrate can be within €1-10 per mm^3 as reported by Zhang *et al.* [197]. Recently Abyzov *et al.* [194] reported the cost to be within \$3 and \$6 per mm^3 for CVD diamond plates with a thermal conductivity of 1000 and 1800W/mK respectively. Hence diamond composite is still an expensive option compared to copper (a 99.9wt% purity copper plate costs about \$0.06 per cm^3) [194]. Sung *et al.* [199] addressed the high diamond film cost as well and obtained cheaper spreaders infiltrated with copper or aluminum with thermal conductivities respectively increased by factors of 2 and 1.5 times compared to the copper one. Composites of diamond particles can be a good compromise between costs and performances. The cost of diamond-copper composite material with a thermal conductivity between 800 and 1200W/mK is less than 1/20 the cost of a CVD-diamond [194]. Reported analytical calculations estimated a price between \$1-10 per cm^3 for a copper material with

63% in volume fraction of diamond particles. This estimation did not take into account the production costs, however, underlined the differences in costs among copper, diamond-copper composite and CVD-diamond (Table 5).

Table 5 - Cost comparison among copper, diamond/copper composites and diamond.

Copper	Cu/D composites	Diamond
~400 W/mK	800-1200 W/mK	1000-1800 W/mK
\$0.06 per cm^3	\$1-10 per cm^3	\$3000 and \$6000 per cm^3

Cu/Dia is the most promising diamond composite because of the low cost and high thermal performances of the copper. Composites with diamond filler and metal binder can be made by sintering or infiltration process. These operations can be run at ultrahigh pressures (>1GPa) or at a pressure between 1 to 100MPa, depending on the materials [194]. Diamond composites' production process is crucially important because the manufacturing process affects the thermal conductivity of the product [200]. In the worst case it can lead to a thermal conductivity of the composite lower than expected as reported by Nishiyabu *et al.* [200]. The diamond powder in air is thermally deteriorated at the conventional copper powder's sintering temperature: this means that diamond powders can be thermally damaged when sintered with copper powders. Furthermore, the presence of small-sized pores between copper and diamond powders can negatively affect the thermal conductivity. The authors concluded their work stating that further studies to improve thermal conductivity were necessary.

In the last years, graphene, a two-dimensional crystal, has gained lot of interest for its extra-ordinary properties [201]. Many experimentally measured graphene characteristics have exceeded those obtained by any other material, in terms of room-temperature electron mobility, Young's modulus, and intrinsic strength [202]. In particular, the thermal conductivity was found to reach values up to 6600W/mK [203], making it interesting for heat spreading and dissipation purposes. In the near future, graphene is expected to find wide application, from electronics to energy generation and photonics.

2.3.5.4.2 Natural convection in micro-channels

As previously reported, micro-channels are composed of many parallel micro-cavities, have been extensively investigated for active cooling applications and have been considered the best systems for HCPV cooling [65]. On the other hand, natural convective gas flows in micro-channels have not received much attention yet [204].

In 2005, Chen and Weng [205] analytically investigated the natural convection in micro-channels and reported that the volume flow rate at micro-scale was higher than that at macro-scale, while the heat transfer rate was lower. In 2010, Buonomo and Manca [206] carried out an investigation on natural convection in vertical micro-channels. They observed that the highest mass flow rate was obtained at the highest Knudsen number (Kn)[i] while no significant changes in the average Nusselt number[ii] was detected in terms of the heat flux ratio. In 2012, the same researchers [204] further investigated the natural convection in a vertical micro-channel. They showed that wall temperature profiles increased with increasing Kn and the differences between wall temperature profiles, for different Kn values, decreased with increasing the channel height. Furthermore, mass flow rate increased with increasing Kn, whereas Nusselt number decreased with increasing Kn. Haddad *et al.* [207] studied laminar free-convection flow in open-ended micro-channels filled with a porous medium and found that heat transfer decreased when increasing the Knudsen number and the thermal conductivity ratio.

2.3.5.4.3 Micro-channels fabrication

The fabrication approaches for micro-channels have been reported in several papers. In 1997, Tjerkstra *et al.* [208] listed four ways to fabricate micro-channels by etching: wet anisotropic, wet isotropic, dry anisotropic and dry isotropic. The basic approach for constructing channels in silicon is depicted in Figure 26. The silicon is first covered with a mask material which is patterned and then etched. The channels in Figure 26 are etched (a) isotropically, (b) anisotropically using

---

[i] Kn is a dimensionless parameter defined as the ratio between the mean free path and a characteristic length.
[ii] The Nusselt number compares the heat transfer due to natural convection and that due to conduction in a fluid layer.

Reactive Ion Etching (RIE), and (c) anisotropically in a KOH solution. Furthermore, Tjerkstra *et al.* [208] classified micro-channel machining methods in two groups: technologies involving bonding and not involving bonding. In 2000, Dwivedi *et al.* [209] presented a new wet anisotropic method to fabricate long and deep micro-channels in silicon with really smooth sidewalls.
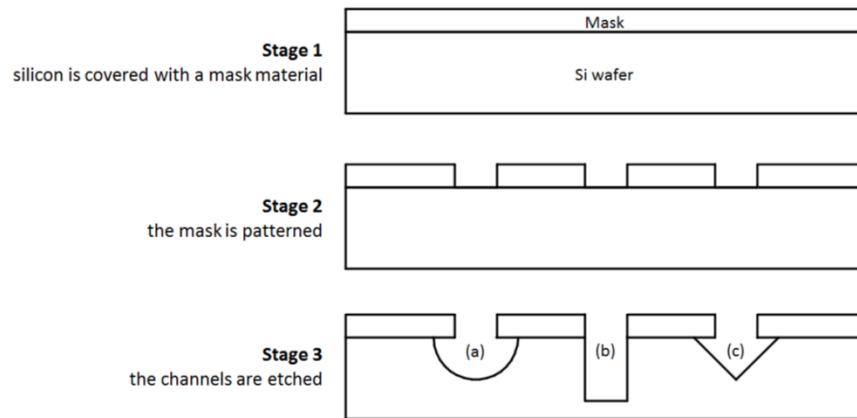
Figure 26 - Schematic of making a channel in silicon, adapted from [208]**: isotropical etching (a), anitropical RIE (b), anitropical in a KOH solution (c).**

Dry etching can be obtained using laser micro-machining. Alavi *et al.* [210] used laser melting and anisotropic etching to fabricate micro-channels with high aspect ratio. Kam *et al.* [211] developed a flexible and fast femtosecond laser ablation of micro-channels in silicon to develop branching networks to serve gas exchangers. Chen *et al.* [212] used this technique to produce 5µm diameter micro-channels in a silicon substrate by femtosecond laser with 800nm wavelength, which is in the absorption region of silicon.

2.3.5.4.4 Carbon nano-tubes

In 1991 Sumio Iijima [213] announced the synthesis "of a new type of finite carbon structure consisting of needle-like tubes". Later literature referred to that paper as the first on Carbon nano-tubes (CNTs). CNTs consist of hollow cylinders made of graphite sheets, with diameters and lengths in the order of nm and µm, respectively. CNTs have high mechanical strength and good thermal conductivity. They are usually classified into two categories, shown in Figure 27, differing both in diameter and in thermal proprieties:

- *Single-walled carbon nano-tubes* (SWCNT): individual cylinders 1-2nm in diameter, consisting of a single rolled graphene sheet. SWCNTs have important electric proprieties, but are still very expensive to produce [214].

- *Multi-walled carbon nano-tubes* (MWCNT): nested graphene cylinders coaxially arranged around a central hollow core and held together by interlayer van der Wall's forces. Diameters range from a few nm to hundreds of nm and the length can be as high as 100nm.

Sometimes CNTs with only two layers are grouped in a category other than MWCNT: they are called *Double-walled carbon nano-tubes* (DWCNT) [215].
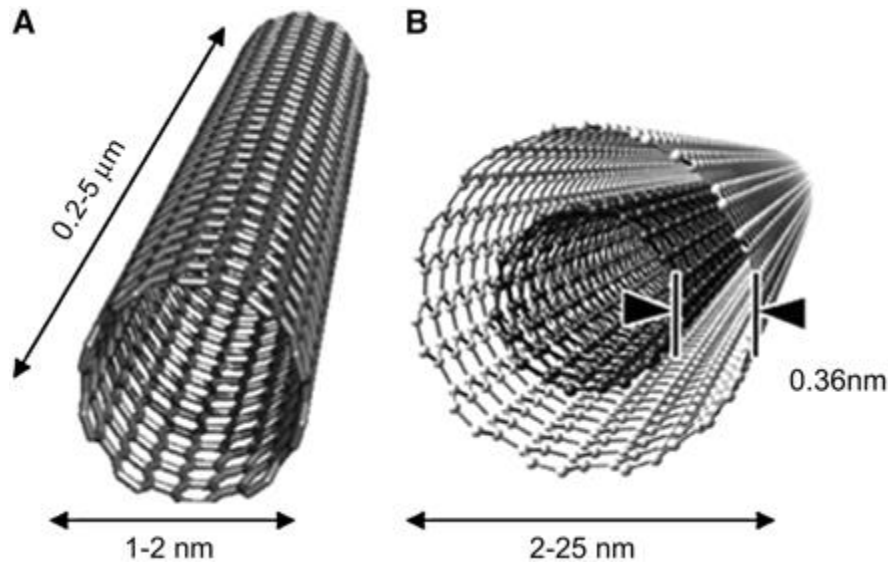
Figure 27 - Conceptual diagram of a SWCNT (A) and a DWCNT (B) [216]

CNTs attracted significant attention due to their important thermal and mechanical properties and several studies were conducted on their application for cooling. The potential uses of CNTs have been investigated in several fields, such as medicine, electronics, aerospace, field emission and lighting [217,218].

In 2010, two reviews on carbon nano-tubes were published [214,219]. Shakouri [188] reported that upper bound for CNTs thermal conductance could be set at $4 \cdot 10^9 W/m^2K$ at room temperature. An increase of 400% in the heat transfer coefficient was demonstrated by using CNT arrays on a chip surface [152]. In 2011 Chiavazzo and Asinari [220] investigated CNTs as alternatives to nano-fluids in heat transfer.

Kim *et al.* [221] measured a thermal conductivity of 3000W/mK for a single carbon nano-tube. On the other hand, Jakubinek *et al.* [222] reported that "the heat dissipation ability of CNTs has not translated to bulk CNT materials". Tong *et al.* [223] determined a thermal conductivity of 250W/mK for a MWCNT array, grown on Si wafer by chemical vapour deposition (CVD) process with transition-metal iron (Fe) as catalyst. As reported by the authors, taking into account an estimated fill-in ratio of 10%, this result matched the first one.

Jakubinek *et al.* [222] used vertically aligned MWCNT arrays, grown by water-assisted CVD to investigate thermal and electrical conductivities of CNTs. Nano-tubes had a diameter of 10-20nm and were approximately spaced 70-100nm. The authors measured a thermal conductivity in the range of 0.5-1.2W/mK at 300K, with the shortest array having the highest values. Moreover, scaling the arrays' values, they determined the thermal conductivity ranging between 18 and 42W/mK for an individual MWCNT.

Berber *et al.* [224] conducted a simulation to determine the CNTs thermal conductivity and their dependence on temperature. Combining equilibrium and non-equilibrium molecular dynamics simulations with accurate carbon potentials, the authors obtained a value of 6600W/mK for an isolated nano-tube at room temperature. Their calculations suggested that at T=100K, carbon nano-tubes would show an unusually high thermal conductivity value of 37000W/mK. As highlighted by Han and Fina [219], this trend was in strong disagreement with the experimental results obtained by other works, regardless of temperature.
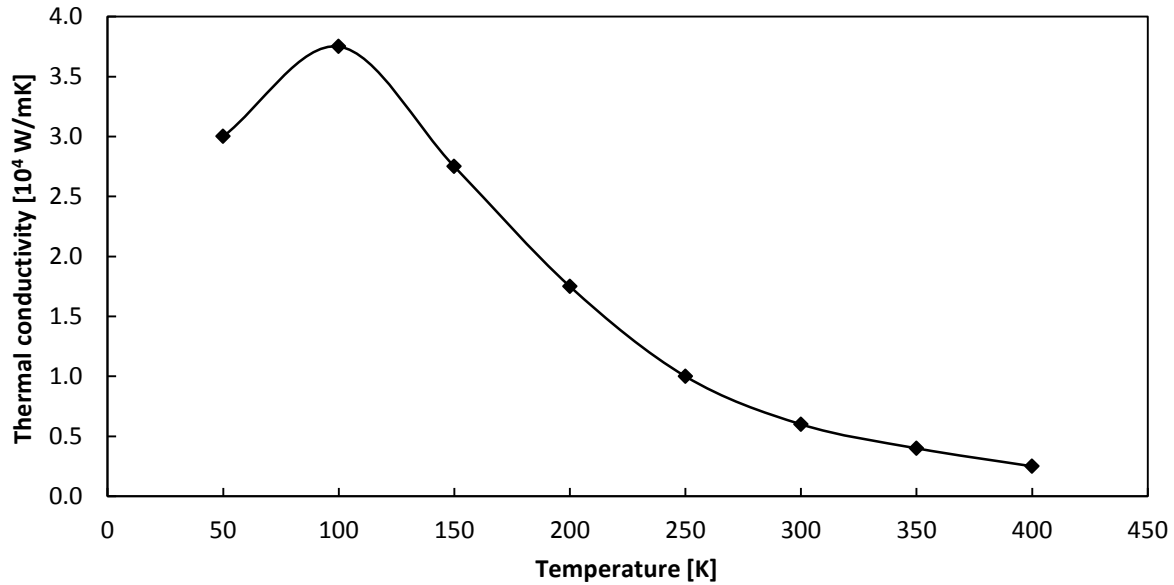
Figure 28 - Example of temperature dependence for a carbon nano-tube for temperatures below 400 K; adapted from [224]

Kordas *et al.* [225] tested a 1.2mm long laser patterned CNTs on a 1mm^2 silicon chip. Tests took place with various thermal loads (up to 7W) and cooling gas (N$_2$) flow rates. The authors discovered that the application of the nano-structure allowed the dissipation of 30 to 100W/cm^2 more power at 100ºC from a hot chip than that obtained by respectively natural and forced convections. According to the reported data, CNTs have been found to be one of the most interesting solutions for CPV passive cooling due to their high heat transfer proprieties.

CNTs manufacturing

There are four common methods for synthesizing CNTs: arc discharge, chemical vapour deposition, laser ablation and high pressure carbon monoxide (HiPco). The most important characteristics of these methods are reported in Table 6.

Arc discharge

In this method, CNTs self-assemble from a carbon vapour created by an arc discharge between two carbon electrodes. Arc discharge method was used by Iijima [213] in the first CNTs synthesis. Keidar [226] stated that CNTs produced by the arc discharge technique have fewer structural defects than those obtained by low temperature techniques, whereas Aqel *et al.* [214] wrote that arc discharge

method produced large quantities of impure material. Every year, several works are published on CNTs grown by arc discharge technique.

Chemical Vapor Deposition synthesis

Chemical Vapor Deposition (CVD) is the most used method to produce CNTs. In this method CNTs are grown using catalysis, which involves decomposition of a hydrocarbon gas over a transition metal catalyst and the initiation of CNT synthesis by some of the resulting carbon atoms. CVD generally results in MWCNTs or poor quality SWNCTs [214]. The growth of individual single-walled carbon nano-tubes by chemical vapour deposition have been tested on several elements [51, 52].

Laser ablation

In this process, a high power laser beam impinges on a volume of carbon containing feedstock gas. The CNTs formed by the laser ablation method are of a higher quality than those produced by the arc discharge method. However, the production rate is low, and the pulsed laser vaporization or laser ablation method is both capital and energy intensive [229]. In 2002, laser ablation techniques were reviewed by Maser *et al.* [230], which concluded that these methods were not compatible with large scale production. Furthermore, they added that a large potential in using different lasers and combination of lasers was still unexplored and that cheaper feedstock materials and more efficient processes were the milestones for low cost production.

High Pressure Carbon Monoxide

The high pressure carbon monoxide is a low-cost gas-phase catalytic process developed in 1999 at Rice University by Richard E. Smalley and his co-workers [231] to grow SWCNTs. It consists of the decomposition of $Fe(CO)_5$ in CO at high pressure and temperature. According to the authors, the HiPco process can run continuously. In some works, it is reported as a CVD process ("via the decomposition of volatile metallo-organic compounds within the reactor, without the use of a substrate") [232]. Other authors reported it by itself [233].

Table 6 - Comparison of the established techniques for CNT Synthesis, adapted from [57].

Method	Arc discharge	Chemical vapour deposition	Laser ablation	High pressure carbon monoxide
Description	Arc evaporation of graphite in the presence of inert gas; CNT formed on electrodes, during quenching	Decomposition of hydrocarbons over transition metal catalyst to form CNT	Vaporization of graphite target by laser; CNTs formed on receiver during quenching	Nucleation surface for the growing of CNT provided by the reaction of Fe(C0)2 and CO
Operating temperature	>3000°C	<1200°C	>3000°C	<1200°C
Operating pressure	50-7600Torr generally under vacuum	760-7600Torr	200-750Torr	7600Torr
Advantages	Good quality CNTs	Easy scale up; synthesis on templates possible	Good quality CNTs; single conformation SWNT formed (10,10)	High-quality SWCNTs, run continuously
Disadvantages	Difficult to scale up	Quality of CNT not as good	Difficult to scale up; expensive	N.A.

Alternative processes

Apart from the above methods, other CNT synthesis processes can be found in literature, such as plasma torch method [234–236], electrolysis [237], and flame synthesis, which is one of the most extensively researched alternative method [53, 60–62]. Unfortunately, although these methods can produce large quantities of CNTs, the cost is generally still too high to make any large-scale applications. Continuous synthesis of CNTs allows growing large quantities of CNTs effortlessly. According to Ying *et al.* [215], which published a review of continuous synthesizing methods in 2011, research in the continuous synthesizing processes has made some progresses in both arc discharge and CVD.

CNTs usually contain impurities whose type and amount depend on the synthesis process. These impurities influence CNT properties and limit their applications. Several purification processes have been proposed, such as oxidation [241–243], acid treatments [244] and filtration [245]. Different techniques can be combined to improve purification [246].

Some groups investigated high purity synthesis methods to avoid the purification processes, which usually cause changes in CNTs proprieties. In 2006 Hong *et al.* [247] firstly proposed a high purity CNTs production process. Through the catalytic decomposition of methane with NiO/TiO2 as a catalyst, they obtained MWCNTs with 99.9wt% purity. In 2007, Dasgupta *et al.* [248] fabricated high-purity CNTs by

a catalytic chemical vapour deposition of acetylene diluted with nitrogen. Cobalt formate supported on carbon black was used as the catalyst. The purity of the obtained nano-tubes was as high as 96%. In 2012, a model to determine and compare the cost of the SWCNT synthesized by arc discharge, CVD and HiPco was developed by Isaacs *et al.* [233]. Their results showed a cost per gram respectively of $1906, $1706 and $485. According to the authors, the HiPco method resulted in the lowest cost because it was able to re-circulate CO in a continuous process [233]. Fleury *et al.* [249] noted that the prices of CNT-polymer nanocomposite could rise if safety costs for CNT polymer nanocomposites production, such as safe process design, workplace organization, personal protective equipment and safety management during the maintenance procedures, were considered. Starting from the data exposed by Isaacs *et al.* [233], Ok *et al.* [250] estimated the costs for SWCNT manufacturing using a Monte Carlo model they developed. The results confirmed the cheapness of the HiPco process, when compared to the arc discharge and CVD. Furthermore, they predicted the variation in prices due to a voluntary implementation of higher EHS standards by the industries.

2.3.5.4.5 Micro-fins

Heat transfer around macro-fin arrays has been extensively researched. Fins increase the heat transfer of a surface by extending the heat exchanging surface. Macro-fins are widely used, from radiators to printed circuits boards, and they have been used for CPV cooling too [158].

Although many papers focused on macro-fins in natural convection conditions, only few researches on micro-fins arrays [251–253] were found. Kim *et al.* [251] demonstrated that the heat transfer correlations used for macro-finned arrays could not be applied in micro-scaled systems. Moreover, the authors found an enhancement in heat transfer up to 10% after the introduction of micro-fins and concluded that the orientation had no effects at micro-scales. Mahmoud *et al.* [252] carried out an experiment to investigate the effects of micro-fin geometry on natural convection heat transfer of horizontal micro-fins on a copper surface. The authors discovered that the values of convective heat transfer coefficient increased when

the fin height decreased or the fin spacing increased (Figure 29). The effect of fins thickness on the thermal exchange was not considered by any of the previous studies.
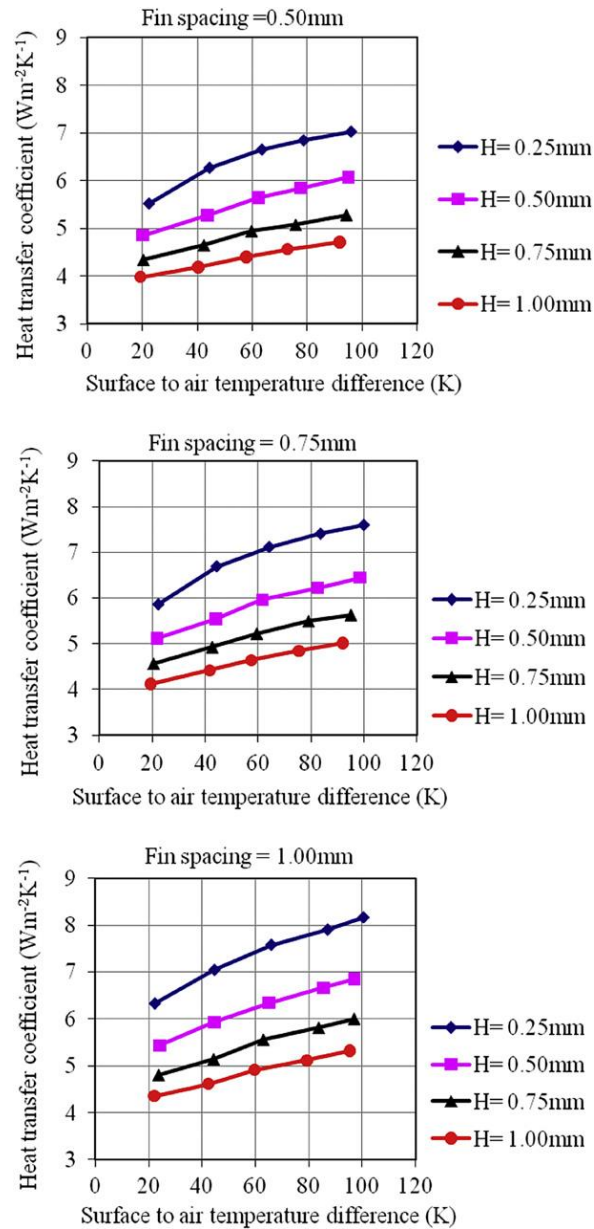
Figure 29 - Effect of fin height and spacing on the heat transfer coefficient [252]**.**

Shokouhmand *et al.* [253] conducted a numerical investigation on natural convection and radiation heat transfer from micro-fin array heat sinks, taking into account temperatures ranging between 80 ℃ and 100℃. They discovered that the contribution of radiative exchange could not be neglected, and that it should be included in the studies on natural convective micro-fin heat sinks.

Overall, micro-fins look like a simple and reliable solution to improve the cooling of a CPV system, even if their performance seems to be lower than CNTs. More studies on naturally convective micro-finned heat sinks are required in order to find out the optimized geometries for a HCPV application.

Micro-fins fabrication

Micro-fins are usually obtained through standard subtracting manufacturing methods such as wet or dry etching. Mahmoud *et al.* [252] used a micro-electro discharge wire machining (m-EDWM) process to fabricate their prototypes. Kim *et al.* [251] fabricated micro-fin arrays with fin heights of 100 and 200μm in a bulk silicon wafer using microelectromechanical systems (MEMS) process. The procedure was divided into two major steps: the metal deposition process for the electric heater, and the deep etching process for fin geometries. The second step was realized through Deep Reactive Ion Etching (DRIE, from (f) to (h) in Figure 30). DRIE is a widely used process for deep trench etching of a silicon wafer. The most common DRIE technique is the Bosch process, patented by Robert Bosh GmbH in 1994 [254] and based on alternating multiple steps of etching and sidewall passivation. Even Peles *et al.* [255] used DRIE process to evaluate the forced convective heat transfer across a bank of micro-fins. In 2009 Bopp *et al.* [256] presented a new DRIE process to obtain different micro-and nano-structures, *i.e.* fins and nano-wires, arranged on two or more levels in bulk silicon.
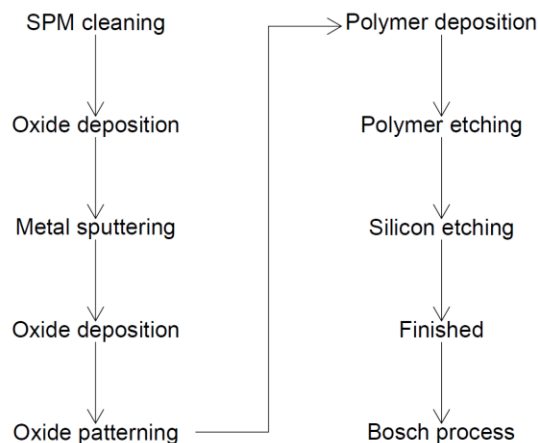
Figure 30 - Fabrication procedure of Kim *et al.* micro-fin arrays, adapted from [251]**.**

Dry etching techniques, also known as Reactive Ion Etching (RIE), are processes that combine physical and chemicals effects to remove material from the wafer surface [257]. Wet etching should be faster than dry etching, but has some disadvantages which were reported by Murakami *et al.* [258]. Required structures could not always be fabricated by wet etching process because the etched geometry depended on the crystalline orientation. In addition, micro-structures were often stuck together during dry up after the wet procedure because of the surface tension force of liquid. On the other hand, the authors stated that dry etching procedure could solve these problems. A cryogenic RIE process was used to fabricate 3-dimensional silicon micro-structures with high aspect ratio. According to Laermer *et al.* [257], the most important feature of RIE, compared to wet etching, was the capability of directional (anisotropic) etching without relying on crystal planes of the material. DRIE is considered an extension of the RIE and grant higher-rate etching of deep and narrow structures. Furthermore, DRIE usually allows better selectivity and process controllability than RIE. Koşar *et al.* [259] used RIE process to remove oxide in wafer places not protected by the resist and then DRIE process to etch silicon and to fabricate their low aspect ratio micro-pin fins. In 2008, Abdolvand and Ayazi [260] developed a new DRIE method, modifying the Bosch process. Adding an argon/oxygen plasma pulse between the passivation and etching steps and a short oxygen clean step at the end of each cycle, the authors obtained very high aspect-ratio sub-micron trenches in silicon.

2.3.5.4.6 Nano-wires

A nano-wire is a one-dimensional nano-structure: its length is much greater than its diameter, which is constrained to tens of nano-meters. According to Zhang [261], in the last decade nano-wires have been applied in several fields, such as biosensors and electronic devices. In addition, in 2009, Li *et al.* [262] designed a PV module made of periodic Si nano-wire arrays. The authors found that silicon nano-wire arrays can reach the same efficiency than Si films with the same thickness.

Nano-wires are usually used as thermoelectric devices [263], due to the high electrical conductivity and low thermal conductivity [84, 85]: they are used to

directly convert heat into electricity. Due to their low thermal conductivity, they are not suitable for passive cooling.

2.3.5.4.7 Natural convection of nano-fluids

One of the most important problems in the development of energy-efficient heat transfer systems is the low thermal conductivity of fluids. In 1993, Masuda *et al.* [266] firstly investigated the thermal conductivity of water containing Al_2O_3 nanoparticles. Choi and Eastman [267] in 1995 proposed the concept of nano-fluids: fluids with nano-particles suspended in them. Nano-particles are generally expected to have at least one of the principal dimensions smaller than 100nm. The choice of nano-particle in nano-fluids is crucial to achieve good thermal properties. The following criteria, reported by Rafati *et al.* [268], can be the benchmark to choose nano-particles for different applications:

- High stability in selected base fluid and lower tendency to agglomeration and settling;
- High thermal performance in suspension even at low concentration;
- Availability and reasonable price;
- Non-toxicity and environmental friendliness.

Even if nano-fluids nowadays find application in several fields, from biomedical to heat transfer applications [165], limited and contradictory experimental results have been reported on their performance in natural convection conditions [269,270]. Significant discrepancies among the characteristics measurements (*i.e.* thermal conductivity and viscosity) have been reported: this is possibly due to the lack of standards for nano-fluid preparation, to the different nanoparticle manufacturing processes employed, to the various stabilization methods and to the different time durations between the preparation and the measurement.

Ouelasti and Bennacer [271] numerically studied and compared the heat transfer performances of three nano-fluids in natural convection in a differentially heated square cavity. They reported that Cu nano-particles yield better results than Al_2O_3 and TiO_2 nano-particles. Hwang *et al.* [272] investigated theoretically the thermal characteristics of natural convection in a rectangular cavity heated from below with

water-based nano-fluids containing alumina (Al_2O_3). The authors found that the stability of natural convection in the nanofluid was enhanced when the volume fraction of the nano-particles increased, the size of the nano-particles decreased, the average temperature of nano-fluids increased. Differently, the heat transfer coefficient was found to be positively affected when the size of nanoparticles was reduced, or the average temperature of nanofluids was increased.

In 2003, Putra *et al.* [273] took into account the suspensions of Al_2O_3 and CuO nano-particles in water. They reported a systematic and definite deterioration in natural convective heat transfer. This deterioration was not present in case of forced convection. In another study [274], the convective performance of nano-fluids has been even tested on an electronic heat sink by using CuO/water nano-fluids to actively cool down an aluminum block heated by a 150W-cartridge heater: a maximum increase of 29.63% in convective heat transfer was achieved for a nano-fluid with a volume fraction of 0.2% compared to deionized water at a fixed volume flow rate [274].

In 2009 Nieto de Castro's group presented the concept of *ionanofluids* [275]: these are a specific type of nano-fluids made of nanomaterials suspended in ionic liquids. Ionic fluids have good heat transport and storage capabilities and very good solvent proprieties. In 2010, the same group [276] obtained an enhancement in thermal conductivity ranging between 2 and 9%, with a weak dependence on temperature by comparing several ionic fluids with a 0.01 mass fraction of suspended MWCNTs. In 2012, Nieto de Castro's group [275] investigated the effect of temperature and concentration of MWCNT on the effective thermal conductivity and specific heat capacity of several ionanofluids. They demonstrated that the higher the concentration of MWCNTs, the higher the enhancement in thermal conductivity, while the temperature effect seemed to be negligible.

Further investigations are required on natural convection of nano-fluids, in order to understand their thermal effectiveness and to prove their durability. Moreover, the development of a design able to fit the requirements of a tracked CPV system is needed.

Nano-fluid fabrication

The preparation of nano-fluids requires a correct dispersion of nano-particles. Two methods are commonly used to produce nano-fluids: a one-step method and a two-step method. According to Yu and Xie [277] the two-step method is the most widely used for nano-fluids preparation. In this method, the nano-particles production and dispersion are different operations. Nano-particles are first produced as dry powder, and then dispersed in the fluid. The two-step method is a quite cheap process, because nano-particles are already produced by several companies and commercially available. The main problem in this procedure is the low-stability of the synthesized nano-fluid.

On the other hand, the one-step process consists of simultaneously making and dispersing the particles in the fluid. This process leads to the production of high-stability and uniform nano-fluid. According to Li *et al.* [270], only low vapour pressure fluids can be used in this process. This fact limits the application of the one-step method. In addition, other techniques, such as a continuous-flow micro-fluidic micro-reactor for Cu nano-fluid developed by Wei and Wang [278], have been presented [277], but they are not as popular as the one-step and the two step methods.

Carbon Nano-tube based nano-fluids

The use of CNTs as particles for nano-fluids has been found to be very effective to obtain fluids with high thermal conductivity. Amrollahi *et al.* [279] measured an enhancement of 20% by adding a 2.5vol% of CNTs to ethylene glycol in thermal conductivity and demonstrated that traditional macro suspensions models, such as Maxwell and Hamilton-Crosser ones, could not foresee the behaviour of CNT nano-fluids. In 2008, Venkata Satry *et al.* [280] presented a new model to predict the heat transfer in nano-fluids. In particular, they investigated the formation of extensive three-dimensional CNT chains in the liquid. They discovered that it depended on the CNT length, the volume fraction, the thermal conductivity of the base liquid, and the technique deployed to prepare the nano-fluid. Finally, the authors suggested the introduction of a new dimensionless number, termed as $\prod$, which represents the ratio of thermal resistance of the liquid to that of the CNT

chains and that was able to characterize the thermal conductivity of the MWCNT nano-fluid suspension within an accuracy of ±5%. With a 1vol% MWCNT loading, the thermal conductivities of poly-alpha-olefin oil, water and ethylene glycol were enhanced by more than 150% [281], 40% [282], and 30% [283] respectively. In another study Kumaresan *et al.* [284] reported the increase in thermal conductivity and heat transfer co-efficient of CNT based nano-fluids to optimize the ratio of the CNT in nano-fluids. They suspended MWCNTs in a mixture of 70vol% de-ionized water and 30vol% ethylene glycol, obtaining a high enhancement in performances with a concentration of CNT in the base liquid of 0.45vol%. An enhancement of 19.73% and 159.3% in thermal conductivity and average heat transfer coefficient respectively were reported. The same group of researchers [285] demonstrated that 0.45vol% of CNT was the optimal concentration when using ethylene glycol as base liquid. Other thermo-physical proprieties of the nano-fluids were also found to be changed, such as the density that increased with the MWCNTs concentration, whereas the specific heat decreased with an increase in the MWCNTs concentration. Carbon nano-tubes based nano-fluids have been used both in micro-heat pipe and in thermosyphon. In spite of enhanced thermal conductivity of the CNT based nano-fluids, the stability and the lifetime are still major concerns.

Nasiri *et al.* [286] carried out an investigation on the stability of CNT based nano-fluids by comparing the performances of SWCNTs, DWCNTs and MWCNTs suspended in water. While all the suspensions were found to be stable for months, SWCNT suspension demonstrated the best stability and the higher improvements in thermal conductivity. The thermal conductivity of all suspensions decreased with time due to agglomeration. Similarly, also the reduction rates of thermal conductivity decreased with the time. However, the researchers reported an enhancement in thermal conductivity with the increase in temperature. Meibodi *et al.* [287] reported the optimum conditions for CNT/water nano-fluids production and operation to attain a better stability. However, it was mentioned that the more stable nano-fluids did not necessarily have the higher enhancement in thermal conductivity.

Several reviews underlined the lack of agreements among the data [269,288,289]. Some papers showed that more stable fluids were not necessarily best performing [287,289]. More works are needed on nano-fluids and the standardization of the measurement procedures is necessary to avoid discrepancies in data. Nano-fluids have certainly shown their potential as heat transfer solution and they look a promising solution for devices requiring high heat removal power. Nevertheless, further investigations are required on natural convection of nano-fluids in particular. The application of CNTs in nano-fluids has shown interesting results. Finally, the development of a design able to fit the requirements of a tracked CPV system is needed.

2.3.5.4.8 Micro-heat pipes

The use of micro-heat pipes (MHP) can provide a good transfer of heat flux and can then reduce the thermal resistance between the cell and the cooler. Cotter [290] defined a micro-heat pipe as a heat pipe "so small that the mean curvature of the vapour-liquid interface is necessarily comparable in magnitude to the reciprocal of the hydraulic radius of the total flow channel". In scientific literature, micro-heat pipes have been found both in active and in passive configurations [291]. Yeom and Shannon [152] summarized the efforts on MHPs from 1996 to 2007, reporting that the heat fluxes removed by the MHPs ranged from a few to over 300W/cm^2. Taking into account this wide extent of thermal performance, micro-heat pipes can be considered as a feasible solution for passive CPV cooling.

Cross sections

As reported by Hung and Sang [292], the thermal performances of micro-heat pipe is intimately related to the cross-sectional geometry. Different cross sections have been designed and tested in order to enhance the backflow of working liquid.

As shown in Figure 31, Peterson *et al.* [293] demonstrated that the performance of a triangular micro-heat pipe was better than that of the rectangular one, due to the higher capillary pumping effect. Moon *et al.* [294] confirmed this result, using MHP with curved sections. Suman and Kumar [295] developed an analytical model to study MHP performances. They considered MHPs with two different cross

sections: an equilateral triangular heat pipe with side equal to 400μm and a 400μm×800μm rectangular heat pipe. Pentane was used as working fluid and silicon was employed as substrate. Suman and Kumar [295] demonstrated that the performance of a heat pipe degrades when the number of sides increases.
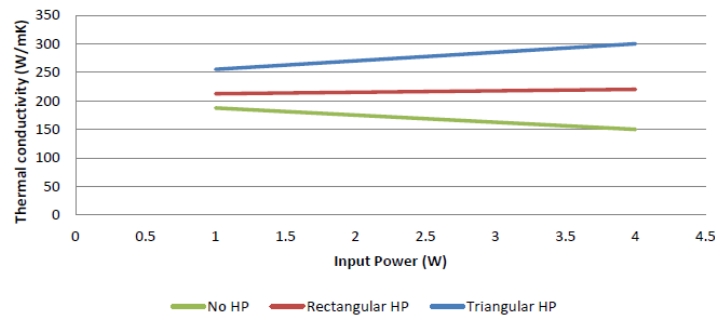
Figure 31 - Thermal conductivities of a silicon wafer with a rectangular heat pipe array, with a triangular heat pipe array and withouth heat pipe array, adapted from [293]

Kang and Huang [296] fabricated a star grooved MHP and a rhombus grooved MHP. They reported an increase in thermal conductivity of 33.6% for the star grooved MHP and of 39.1% for the rhombus grooved MHP when compared with a traditional triangular MHP. The authors stated that better capillarity action was provided by more acute angles and micro-gaps in the star- and rhombus-groove devices.

As reported by Hung and Seng [292], the acuteness and the number of sharp corners are two important basic geometrical factors that govern the capillarity pumping ability and hence the performance of a micro-heat pipe. For regular polygonal shapes, the acuteness of the corner and the number of corners are dependent: the corner apex angle decreases when the number of corners increases. In star-grooved MHP, number of corners and corner apex angles do not affect each other. For these reasons, Hung and Seng [292] stated that star-grooved micro-heat pipes rendered higher capillary pumping power and hence higher heat transport capacity compared to those of regular polygonal micro-heat pipes. Furthermore, they discovered that the increase in total length of the micro-heat pipe resulted in decrease in its heat transport capacity.

Wang and Peterson [297] proposed a wire-bonded aluminum-acetone micro-heat pipe, obtained by sandwiching an array of cylindrical wires between two flat plates.

The authors discovered that the maximum heat transfer capacity increased when the wire diameter and the operating temperature were increased. Moreover they demonstrated that increasing the spacing between wires could increase the maximum heat transport capacity. In their following work, Wang and Peterson [298] confirmed this statement, but added that there was a spacing value where this improvement was overshadowed by the decrease in the number of heat pipes in the array, and the maximum heat transfer capacity became limited. The optimum spacing distance was found to vary with the diameter.

MHP with arteries

This design consists of one vein channel which is the traditional MHP and two neighbour arterial channels distributed on both side of the vein and connected together at both ends. In the vein, vapour carries the latent heat flowing to the cold end where it condenses. In the arteries, the liquid is transported to the hot end by the capillary force applied by the V-grooves in the micro-triangle pipes. Due to the liquid pressure difference between the cold end of the artery and the MHP, the liquid accumulated at the condenser section can be transported back to the evaporator sections.
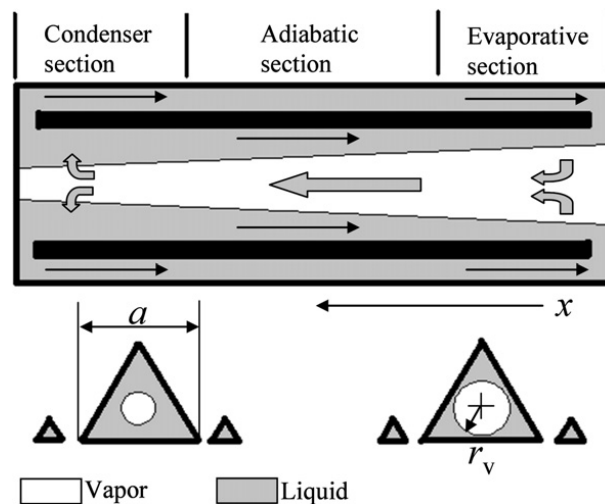
Figure 32 - Working principle of MHP with arteries [299]

Liu *et al.* [299] compared MHPs with and without arteries, concluding that implanted arteries could effectively enhance the capillary force, improve the capability to transport the liquid from the cold end back to the hot end, and limit the propagation of the dry-out region.

Working fluids

The working fluid is an important aspect for the efficiency of micro-heat pipes, which are two-phase cooling devices. In 2003, Chien *et al.* [300] proposed the use of nano-fluids into the micro-heat pipes. Using nano-gold particles suspended in water, instead of pure water, the authors obtained an average decrease of 40% in the MHP thermal resistance. Over 30 papers on the application of nano-fluids into heat pipes had been published at the time this investigation was conducted [301]. For the purposes of this review, only the works on micro-grooved heat pipes have been considered. A summary of the results is reported in Table 7: each research showed an enhancement in MHP thermal exchange due to the use of nano-fluids. Liu Z.-H. and Li Y.-Y. [301] reported three main reasons for these enhancements in thermal transfer: the effective thermal conductivity of nano-fluids increased; the physical proprieties of nano-fluids changed, increasing the capillary force in the HP and making the liquid extending in the micro-grooves; nano-particles formed a thin porous layer on the wall, which increased the capillary force.

Table 7 - Nano-fluids in micro-grooved heat pipes publications, adapted from [301]**.**

Shape of micro-grooved heat pipe	Best performing working liquid type (nanoparticle size and optimal concentration	Maximum reduction in thermal resistance (fluid compared with)	Researchers
Disk-shaped	Au/Water (17 nm)	Average of 40% (DI water)	Chien *et al.* [300]
Cylindrical	Ag/Water (10nm) Ag/Water (35nm)	50% (water) 80% (water)	Kang *et al.* [302]
Cylindrical	Ag/Water (10nm)	44% (water)	Wei *et al.* [303]
Cylindrical	CuO-water (50nm, 1.0wt%)	39% (water)	Yang *et al.* [304]
Flat	Al2O3-water (38.4 nm, 0.8wt%)	47.7% (DI water)	Do K.H. and Jang S.P. [305]
Flat-shape	TiO2-water (20nm, 4.0wt%)	27% (water)	Shafahi *et al.* [306]
Cylindrical	TiO2-water (10nm, 4.0wt%)	25% (water)	Shafahi *et al.* [307]
Cylindrical	CuO-water (50nm, 1.0wt%)	About 50% (water)	Liu *et al.* [308]
Cylindrical	CuO-water (50nm, 1.0wt%)	50% (water)	Wang *et al.* [309]

MHP Fabrication

Micro-heat pipes fabrication usually involves standard micro-systems technologies. Ivanova *et al.* [310] fabricated a silicon/water MHP using two silicon wafers. Deep plasma etching was used to obtain the micro-capillary wick. On one wafer, small diameter holes were laser-drilled for filling. The two wafers were assembled through a silicon direct bonding technique. Finally, a thermal annealing under inert

gas leaded to irreversible bonding due to the formation of covalent bonds between the two surfaces

In 2002 Le Berre *et al.* [311] fabricated and tested two types of silicon micro-heat pipes. The first one (shown in Figure 33a) consisted of a series of 55 parallel triangular shaped, 230µm-wide, 170µm-deep and 20mm-long channels, that were micro-machined into a silicon wafer with a spacing of 130µm. A second wafer was then sealed to the first one to hermetically close the device. For the second design (Figure 33b), arteries were added for the liquid transport: the liquid independently returned via etched channels to the evaporator. In this case, the first wafer consisted of 25 triangular 500µm-wide and 320µm-deep grooves, etched throughout the wafer. The second wafer contained 25 triangular grooves too. The fabrication started with thermal growth of a 1.5µm oxide layer on the device wafer. The oxide on both sides of the device wafer was patterned in order to be used as an etching mask. Triangular grooves were etched by using a 40wt% aqueous KOH solution at 60°C. Plain silicon wafers were used to seal the MHP arrays (*Si-Si direct bonding*).
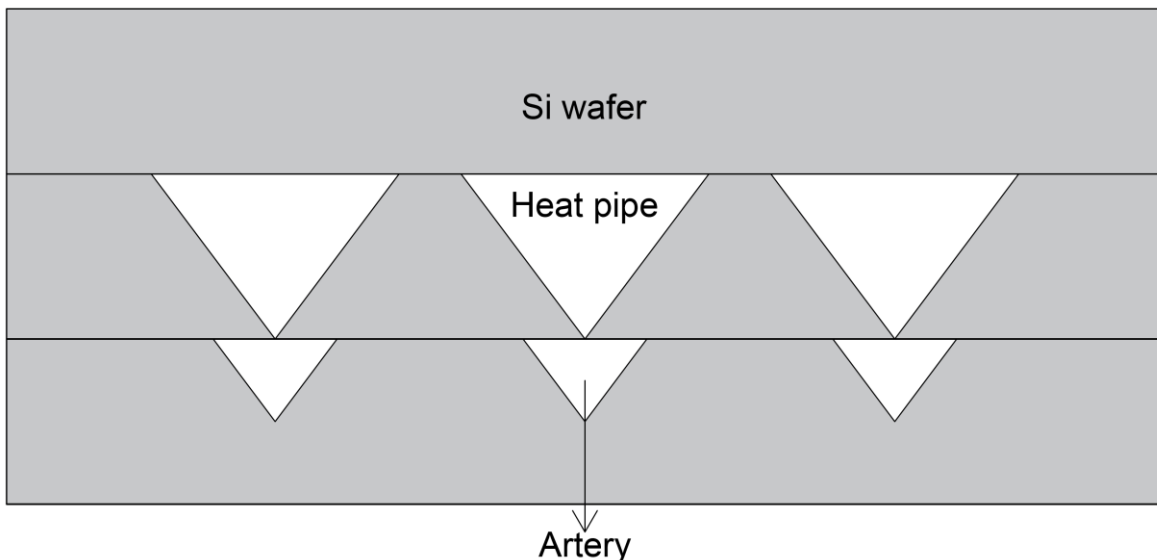
Figure 33 - Transverse cross-sections of a MHP developed by Le Berre *et al.* MHP, adapted by [311]

Kang and Huang [296] fabricated a star grooved MHP formed by three silicon wafers. They used photolithography wet etching technology, to produce a series of

31 parallel V-grooves. Then the three layers of the wafers were eutectic bonded to form the MHP. The whole process is represented in Figure 34.
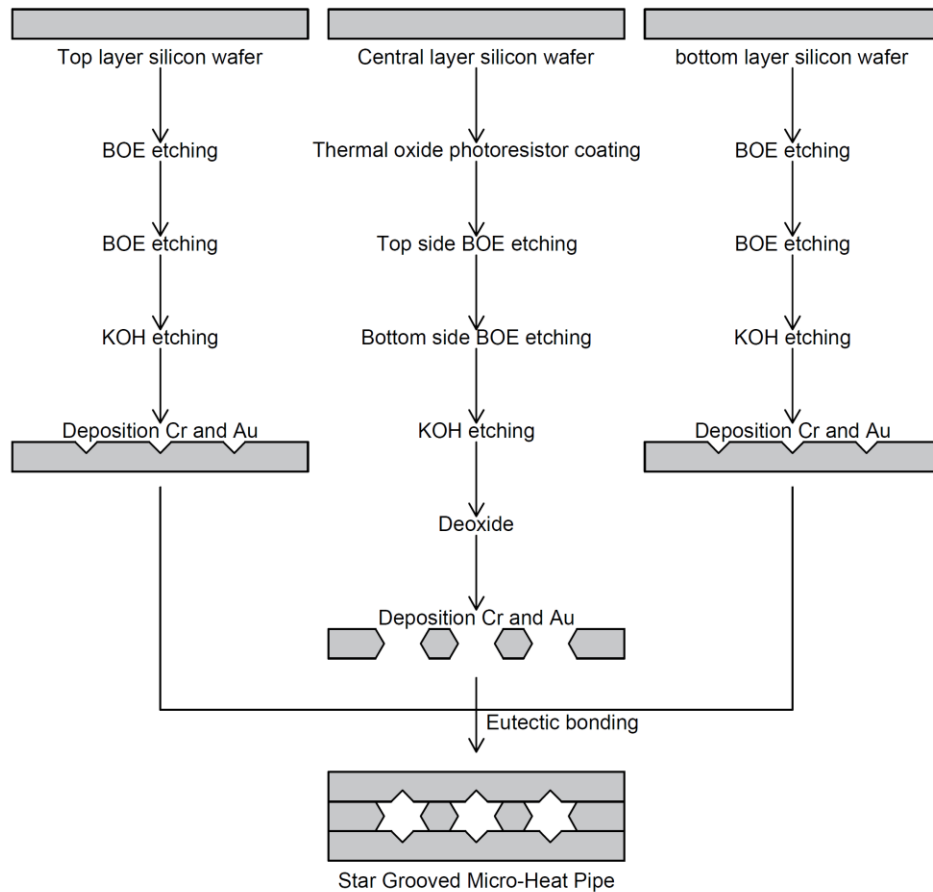
Figure 34 - Fabrication process of the star grooved MHP, adapted from [296]

2.3.5.4.9   Miniature two phase closed thermosyphon

Two phase closed thermosyphons are also known as *wickless heat pipes* (Figure 35). Lee [312] defined them as the heat pipes which do not use the capillary force. Thermosyphons exploit gravitational laws: so, they cannot be used in orientation-dependent applications. Thus, they cannot be easily applied to CPV, where tracking systems are usually employed.
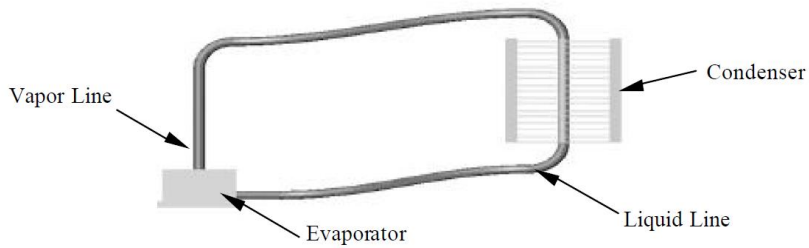
Figure 35 - Conceptual Design of the Loop Thermosyphon, © 2002 IEEE [313]

Wickless micro-heat pipes were conceived first in 1984, by Cotter [290]. He investigated a cooling system "for applications calling for close temperature control, but having only modest cooling requirements". In 1998, Gromoll [189] stated that thermosyphons could be used for power loss densities up to 30W/cm^2: at higher temperatures the film began to boil, decreasing cooling efficiency. On the other hand, in 2007, Yeom and Shannon [152] reported a maximum heat flux of 200W/cm^2.

Pal *et al.* [313] tested two working fluids: deionized ultra-filtered water and PF5060, a dielectric liquid. They stated that water was a better working fluid, because of its better thermal properties than those of PF5060. However, they proposed the exploitation of a proper degassing procedure to improve the performance of the PF5060 charged system. Several works have been published on the exploitation of nano-fluids in closed two-phase thermosyphons [301], but only the few of them focusing on miniature thermosyphons and are reported in this work. Presenting the considerations of Liu Z.-H. and Li Y.-Y. [301] about the reliability of nano-fluids in thermosyphons is interesting for the aims of this review. The authors realized that the nanoparticles generally proved to be able to increase the heat transfer in the majority of the experiments, but that few works reported the opposite results. This discrepancy should depend on several factors: the porous sediment in the boiling process, the impact of the operating temperature on the thermal performance, the preparation of the nano-fluids. The same group [314,315] carried out two experiments to discover the performance of an active miniature thermosyphon using a water-CuO nano-fluid or a carbon nano-tube based nano-fluid. Firstly, they demonstrated that the heat transfer performance of the miniature thermosyphon

could evidently be strengthened by using water-CuO nano-fluid [314]. In the second work [315], the researchers obtained a lower thermal resistance and a more uniform temperature distribution in the micro-thermosyphon using carbon nano-tube suspension instead of deionized water. Furthermore they stated that mass concentration of 2.0% corresponded to the optimal heat transfer enhancement.

Ramaswamy *et al.* [316] investigated the effect of channel width on the miniature thermosyphon performance. The authors discovered an increase in heat dissipation when increasing the pore size.

Thermosyphon fabrication

Ramaswamy *et al.* [316] tested several micro-fabrication techniques to fabricate a silicon thermosyphon. Wafer dicing, laser milling and wet etching were used to etch the channels into the silicon wafer. According to them, wet etching seemed to be the most promising method for bulk fabrication and resulted in very clean channels. Furthermore several bonding techniques were tried, including direct wafer bonding, eutectic bonding, and epoxy bonding. The authors stated that very good bonding was attained with an aluminum-silicon eutectic and cyanate ester epoxy.

2.3.5.5 Considerations

This review investigated micro- and nano-technologies which could be used for passive CPV cooling. The fabrication processes have also been covered. Among the reported solutions, carbon nano-tubes have been found able to offer the best cooling performances, as described in Table 8, whereas micro-fins looked like the most suitable technology for CPV applications because of the low-cost and the intrinsic simplicity.

Table 8 - Comparison of different micro- and nano-technologies

Cooling technologies	Manufacturability	References	Remarks
Heat spreaders	Chemical vapour deposition	[193,195,198]	Mature technology, able to assure extremely high thermal conductivity.
Natural convection in micro-channels	Wet etching; Dry etching	[204–206]	Further investigations on material specifications are required.
Carbon Nano-tubes	Arc discharge; Chemical Vapour Deposition; Laser ablation	[188,214,219]	Highest heat transfer performances among reported technologies. Material stability is an issue that needs to be addressed.
Micro-fins	Dry etching (DRIE, RIE)	[158,252,253]	Simple solution, suitable for CPV.
Nano-wires		[261–263]	Not suitable for passive cooling, due to low thermal conductivity.
Natural convection of nano-fluids	One-step method; Two-step method.	[267,269,277]	Further investigations are required. Suitable for active cooling.
Micro-heat pipes	Standard etching technologies	[291,296,310]	High heat removing capacity. Suitable for passive CPV cooling.
Miniature thermosyphons	Standard micro-fabrication techniques	[189,312,316]	Not suitable for orientation-dependent applications.

A lot of research was carried out on CNTs in the last two decades, due to their important thermal and mechanical proprieties. High thermal conductance and high performance improvements have been demonstrated in several papers using carbon nano-tubes. CNTs fabrication processes are mature techniques: several synthesizing methods have been developed and tested. High-purity carbon nano-tubes have been obtained by different groups without the application of a purification process.

Micro-fins represent a reliable, simple solution, with the potential of increasing the thermal performance of CPV without affecting the cost, even if more studies are needed on their natural convection application. Another promising technology is the high-conductive coating: a diamond layer can be fabricated through a well-known chemical vapour deposition process. However to overcome the high costs and, at the same time, to maintain high performances, the exploitation of composite materials has to be taken into account. Micro-heat pipes can also be considered as plausible solutions for passive CPV cooling. Further investigations are required on nano-fluid in natural convection to understand the real potentials of these solutions.

Only in a limited number of cases, micro-and nano-technologies were applied to concentrating photovoltaic systems. More experimental researches are needed to investigate the applicability and the performances of these technologies to CPV, but the present comparisons may provide a good background.

2.4 Conclusions

In the present section, an investigation on the materials and components of CPV system has been reported. Along with that, a detailed review of macro- and micro-scaled cooling systems has been presented.

The CPV receiver, intended as the assembly of PV cells that accepts concentrated sunlight and incorporates the means for thermal and electric energy removal, has been the main subject of the presented research work. The cells are mounted on a substrate that gives the mechanical support to the structure and is expected to collect the generated current with minimized electrical losses and to efficiently favour the transfer of waste heat from the cell to the heat sink. Direct bonded copper boards have been the most common substrate employed so far in HCPV, but insulated metal substrates are gaining attention due to their lower costs and good performance. Due to the dramatic reduction in semiconductive surface associated with HCPV, the more expensive multijunction cells are generally employed to replace the lower-efficiency silicon solar cells for concentrations higher than 300 suns. Record efficiencies of 46.0% have already been achieved by multi-junction cells and further progresses are expected in the near future. The cells are electrically connected to the circuitry by soldering, which also confers bonding strength to the connections, and by metallic wires bonded on the front tabs. Schottky by-pass diodes are generally used in CPV applications to reduce the electrical losses and the risk of damages in case of shading: installing one diode per cell has been shown to be the most convenient configuration. The components and the interconnectors are generally protected by a clear encapsulating material: so far, silicone materials have been reported to be the best performing in terms of optical transmittance and durability.

The high concentrations achieved in HCPV lead to the generation of high amounts of waste heat that need to be removed from the cells. High temperatures deteriorate the performance of any photovoltaic cells and can cause mechanical failures in the receiver: for this reason, the CPV cells are usually kept in a 50°C to 80°C temperature range. Many cooling approaches have been attempted in the recent years and, among the different systems, micro-channels and jet-impingements have been reported to be the most effective, achieving thermal resistances as low as $10^{-6}m^2K/W$. Due to the lack of moving parts and external inputs, passive cooling is likely to increase the reliability of CPV systems and, at the same time, to reduce the costs. Moreover, micro- and nano-technologies have the potential to offer innovative solutions for a reliable CPV cooling. In this light, a review of passive micro-and nano-cooling technologies has been reported in the chapter: micro-fins in natural convection conditions have been found to be a simple solution, suitable for CPV, but further investigation on the thermal performance are needed.

The aim of the present thesis is to investigate novel solutions to enhance the performance of HCPV receivers: in this light, two different approaches have been attempted. Firstly, a large, high-efficiency, 144-cell cell assembly for HCPV has been designed and fabricated. It is part of a 500× CPV system developed in partnership with the Indian Institute of Technology Madras (India) within the scope of the EPSRC/DST-funded BioCPV project. The aim of this research is to develop an innovative design for HCPV installations and, at the same time, to guide the future researchers and industrials across the issues and the challenges that can occur while producing a high CPV receiver. Secondly, the performance of a passive micro-cooling system for HCPV is investigated. So far, the research on micro-technologies for CPV cooling has been limited and only few examples of CPV micro-cooling systems have been found in literature.

After reporting in Chapter 3 the materials, the instruments and the procedures used in the research, the initial thermal simulations conducted for the selection of the components are reported in Chapter 4. Chapter 5 and Chapter 6 focus, instead, on the development of the large active-cooled receiver: in the first, the design of the

electrical circuitry, the selection of the components and the fabrication processes are explained, whereas, in the second one, the results of the quality tests and the electrical characterizations are reported. Chapter 7 describes the investigation on a micro-passive cooling system for HCPV: it starts from an experimental research on the heat transfer at micro-scale, and ends with the development of a model to predict the performance of a micro-finned CPV receiver in natural convection.

Chapter 3: **Materials and Methods**

This chapter lists the equipment employed to carry out the present work, including the software packages used for modelling and designing, and describes the specifications and the operated practices. The most common laboratory materials are illustrated as well: the featured specifications are reported along with the recommended processing methods. Lastly, the procedures adopted during the experimental investigations and the prototype's fabrication are detailed.

3.1 Components and experimental materials

3.1.1 The solar cell

The 3C40C triple-junction cells developed by the German company *AZUR SPACE Solar Power* were employed in this work. These cells were rated to a peak efficiency of 37.2% and a power of 18.6W at maximum power point (MPP) under standard conditions at 500×. They were chosen because, despite the lowest peak efficiency (Table 9), they were the most cost convenient among those available in 2012 [317].

Table 9 - Cell's cost and performance comparison [317]**. Cost refers to orders for more than 2000 cells in 2011. Data are reported for AM1.5, 1000 W/m² DNI, T= 25°C conditions at 500×.**

Supplier	Cost (£/cell)	Efficiency (%)	Short circuit current (A)	Open circuit Voltage (V)	Power at MPP (W)	Fill factor
AZUR SPACE	5.70	37.2	6.587	3.17	18.6	89.1
Spectrolab	7.17	39.2	7.19	3.21	19.6	85.1
Cyrium	9.35	38.0	7.2	3.0	19.0	88.0
Emcore	9.68	38.5	7.06	3.15	19.03	85.5

These GaInP/GaAs/Ge cells had an active area of 100mm^2 and a thickness of 190μm. The GaInP top subcell and the GaAs middle subcell were current-matched and produced currents of 14.5mA/cm^2, whereas the bottom subcell generated at least 40% of current in excess. The effects of the temperature on the cell's efficiency are shown in Table 10 and Figure 36.

Table 10 - 500× temperature coefficients (25 - 80°C, Beginning of life) [117]**.**

Parameter	Value
$\Delta I_{sc}/\Delta T$	1,596mA/°C
$\Delta V_{oc}/\Delta T$	-4,130mV/°C
$\Delta P_{MPP}/\Delta T$	-6,194mW/°C
$\Delta \eta/\Delta T$	- 0,034 %(abs.)/°C
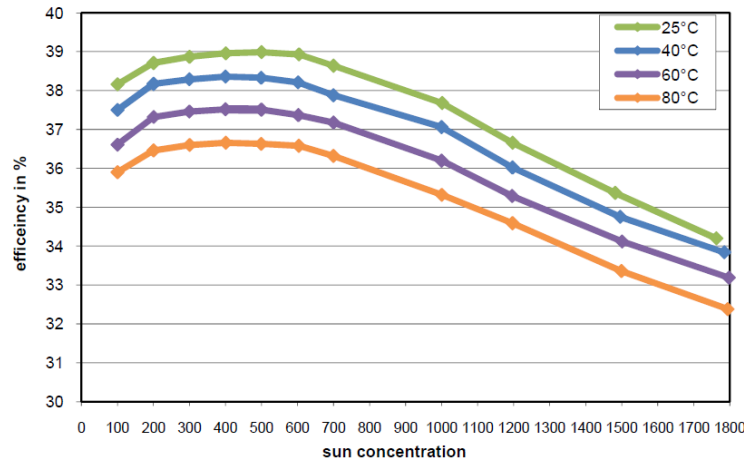
Figure 36 - Efficiency as function of Sun concentration and temperature [117]**.**

3.1.2 The solar assembly

The commercial solar assembly employed in this work was the 3C40A, supplied by AZUR SPACE. It used a 3C40C multijunction cell, attached to a direct bonded copper (DBC) substrate using a $Sn_{96,5}Ag_{3,5}$ solder paste. The DBC was made of an upper 0.25mm-thick copper layer, a 0.63mm-thick Al_2O_3 layer and a lower 0.25mm-thick copper layer. The middle ceramic plate had dimensions of 3.7cm and 3.2cm, while the two layers of copper were about 0.3cm shorter on each side. The assembly was equipped with two parallel 10A Schottky surface mounted diodes.

3.1.3 Sylgard 184

Sylgard® 184 is a clear silicone resin solution produced by Dow Corning. It is a Polydimethylsiloxane elastomer suited for the protection of electrical and electronic components and had been already used in CPV because of its high optical transmittance and its wide operating temperature range (-45°C to 200°C). A summary of the typical properties is reported in Table 11.

Table 11 - Sylgard's datasheet properties

Mix Ratio	Thermal Conductivity	Linear Coefficient of Thermal Expansion	Dielectric Strength	Volume Resistivity	Operating Temperature
10:1	0.2 W/mK	$3.1 \cdot 10^{-4} K^{-1}$	21kW/mm	1.2×1014 Ω·cm	-45 to 200°C

The optical transmittance was measured using the spectrometer: a comparison between the transmissivity of a bare 2mm-thick Borofloat glass and that of the same glass covered with a 3mm-thick layer of Sylgard is reported in Figure 37. Borofloat® is a borosilicate high-quality clear glass manufactured by Schott. It is commonly used for solar applications due to its high transparency and low specific weight.
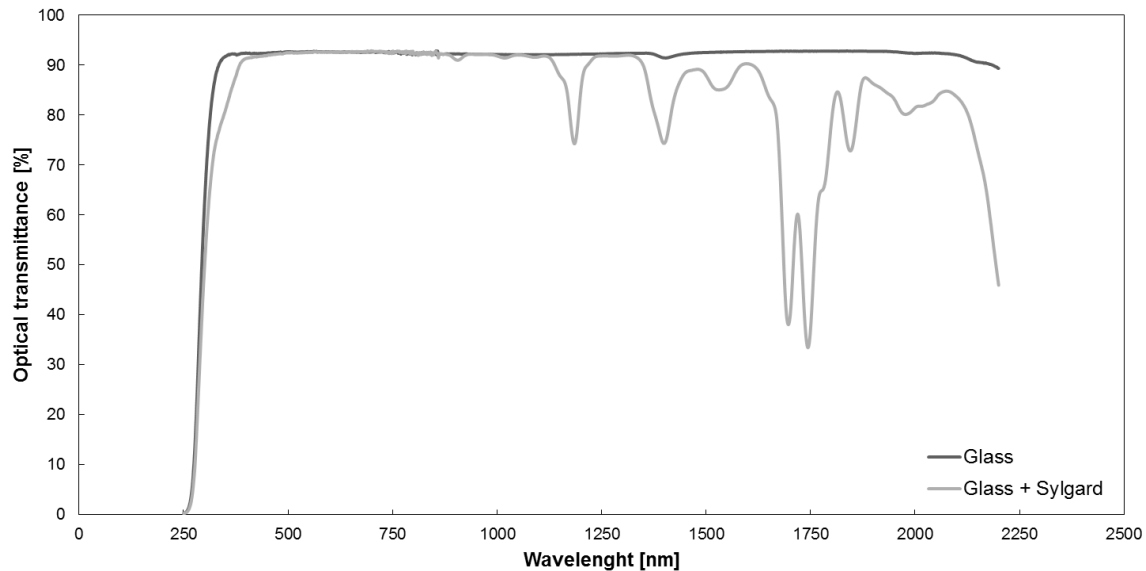
Figure 37 - Optical transmittance of 3mm-thick thick Sylgard poured on a 2mm-thick Borofloat glass between 250 and 2200nm. It is compared with the transmittance of the bare 2mm-thick Borofloat glass.

Sylgard 184 was provided as two-part liquid component. The base and the curing agent have to be mixed in a 10:1 ratio by weight. After mixing, they were manually stirred for about 10 minutes and the solution was left for 10 minutes resting for allowing any air bubbles to be expelled from the liquid. In order to remove any remaining air bubbles, the solution was placed in a vacuum chamber and the process was repeated 2 to 4 times, until bubbles were no longer visible. The pre-pouring treatment was generally completed within one hour.

Sylgard was then dispensed directly onto the encapsulating surface, taking care not to damage fragile components (*i.e.* cells or interconnectors) and trying to spread it as uniformly as possible. Depending on the application, Sylgard could then be cured at room temperature for 48 hours, at 100°C for 45 minutes or at 150°C for 10 minutes.

3.1.4 Silver-loaded epoxy

The silver-loaded epoxy was a two-part solution, provided by RS Components (RS Stock No. 186-3616). It was used for bonding different electrical components if soldering was not suitable. It granted high mechanical strength, excellent electrical conductivity and good thermal conductivity. The operating temperature range (-55 to 150°C) matched the CPV requirements. A summary of the properties is reported in Table 12.

Table 12 - Silver loaded epoxy's datasheet properties

Mix Ratio	Volume Resistivity	Thermal Conductivity	Operating Temperature	Typical Thickness
1:1	0.005 ohm-cm	1.59 W/mK	-55 to 150°C	0.127 mm

The two parts, an adhesive and a hardener, needed to be mixed with a 1:1 ratio, either by weight or volume. The solution was stirred for about 5 minutes, until it appeared homogeneously coloured and was then spread using a small brush within one hour, the maximum recommended pot life. The epoxy could be cured either at room temperature for 36 hours, or at 100°C for 15 minutes. The maximum conductivity and bond strength were usually achieved in 36 hours, so room temperature curing is generally preferred.

3.2 Instruments

3.2.1 Spectrometer

The optical properties were measured through a Perkin Elmer Lambda 1050, which could scan a material's transmittance, reflectance and absorbance in the range between 175nm and 3300nm, with a resolution that could be set down to 0.5nm. A deuterium and tungsten halogen lamp was used as light source: the light passed

through a monochromator and some filters before reaching the sample. The sample was placed in a sample holder: transmittance and absorbance were measured with reference to air, whereas the reflectivity with reference to a calibrated reflective white surface (Labsphere SRS-99-020 AS-01161-060, certificate reflectance between 250-2500nm: 99%). The Perkin Elmer Lambda 1050 used a PMT, InGaAs and PbS 3-detector module.

3.2.2 Solar simulator

Two different solar simulators were used for those experiments that required a controlled light source.

An Abet Technologies Sun 2000 Solar Simulator was employed in Heriot-Watt University for the initial tests on the effects of temperature. It was equipped with Xenon Arc Lamps and its AM1.5G spectral match was grouped as Class A. The 15cm×15cm wide illuminated area had a non-uniformity lower than 5% from a working distance of 200mm. Through the introduction of a filter, the solar simulator was used to reproduce an AM1.5 spectra (Figure 38).
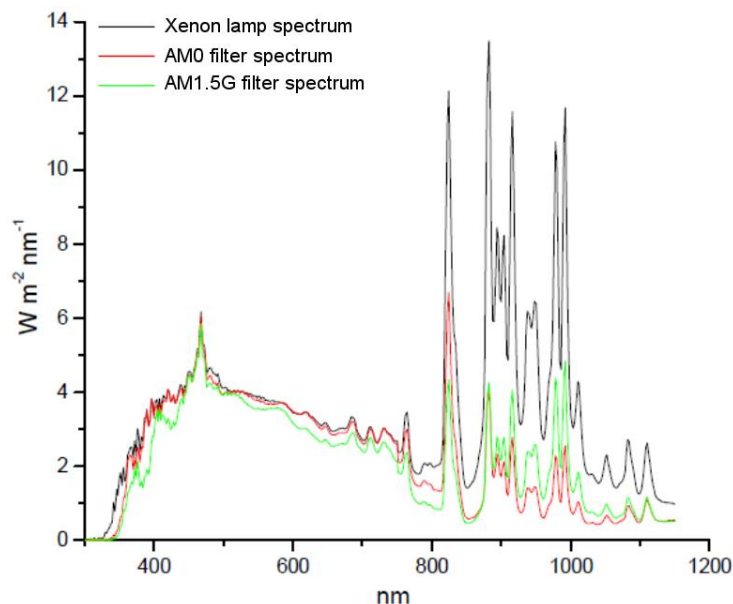
Figure 38 - Solar spectrum of the ABET solar simulator: the original Xenon lamps irradiance, the irradiances after the AM0 and the AM1.5G filters.

A WACOM WXS-300S-50 AM1.5G solar simulator was used instead for the characterization of the receivers in the University of Exeter. The continuous simulator is equipped with a 5000W DC Xenon Lamp, which yielded a high non-

uniformity and a temporal instability lower than 2% on an irradiated surface of 300mm×300mm. This device achieved a Class AAA spectral match (Figure 39).
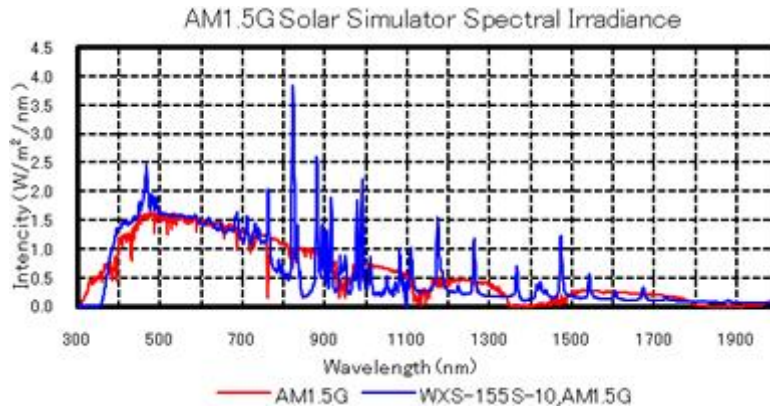
Figure 39 - Solar spectrum of the WACOM solar simulator: comparison between AM1.5G spectrum and the AM1.5G irradiance sourced by the simulator.

All the tests were conducted at Concentrator Standard Test Conditions (CSTCs): AM1.5G, 1000W/m^2, 25°C. The lamps used in the simulators needed time after being switched on to reach a steady energy flux. For this reason, after switching the simulators on, a one hour delay was used before starting the calibration.

A calibrated silicon photo-diode was used to tune the solar simulator before each test: the current flowing into the photodiode was the trusted parameter to calibrate the instrument. In particular, the irradiance of the solar simulator was tuned in order to get in the illuminated photodiode a current of 37.2±0.2uA, measured with the sourcemeter. A temperature controller kept the diode's temperature at 20°C. The temperature-controlled photodiode was placed at the centre of the light flux, at the same distance from the light source.

3.2.3 Sourcemeter

The performances of the PV cells tested in the solar simulator were measured using a Siemens 2440-C 5A Sourcemeter. This instrument could measure voltages up to 6V and currents up to 5.25A. All the values of current and voltage accuracy are reported in Table 13 and Table 14.

Table 13 - Current programming accuracy

Range	Programming resolution	Accuracy (1 year) at 22 °C (±5 °C)
10µA	50pA	0.033% + 2nA
100µA	5nA	0.031% + 20nA
1mA	50nA	0.034% + 200nA
10mA	500nA	0.045% + 2uA
100mA	5µA	0.066% + 20µA
1A	50µA	0.067% + 900µA
5A	50uA	0.10 % + 5.4mA

Table 14 - Voltage measurement accuracy

Range	Default resolution	Input resistance	Accuracy (1 year) at 22 °C (±5 °C)
200.000mV	1µV	>10GΩ	0.012%+300µV
2.00000V	10µV	>10GΩ	0.012%+300µV
10.0000V	100µV	>10GΩ	0.015%+750µV
40.0000V	1mV	>10GΩ	0.015%+3mV

3.2.4 I-V tracer

An EKO MP-160 I-V tracer was used for the characterization of the solar assemblies. This instrument operated in the range between 0.5V and 300V and 0.005A and 10A, as shown in Figure 40, with a maximum power of 300W [318]. A four-wire configuration was used to extract the electrical outputs from the cell. It was coupled to a software tool able to calculate several parameters, such as the open-circuit voltage, the short circuit current, the maximum power and the fill factor. Moreover, the system gave in output the I-V curve of the cell.
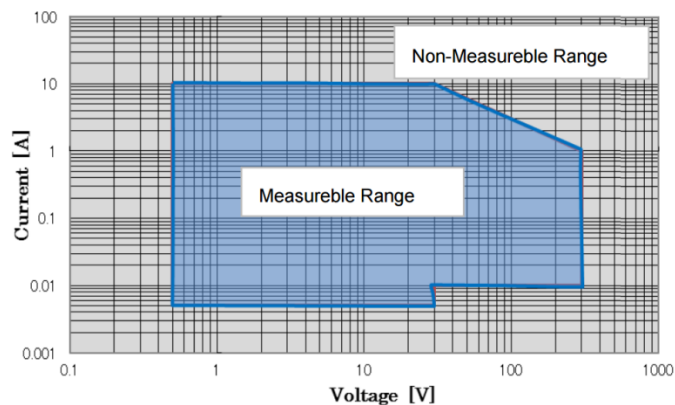
Figure 40 - EKO MP-160 I-V tracer measurable range [318]**.**

3.2.5 Vacuum oven

The EQ-DZF-6210 oven was used for material curing and for investigations about the coefficient of thermal expansion. It was a high temperature vacuum and atmosphere oven, able to work at temperatures up to 270ºC and equipped with three temperature controllers.

3.2.6 Infrared Camera

The FLIR T425 was a thermal imaging infrared camera able to measure temperatures between -20ºC and 1200ºC with a resolution of 0.05ºC. It provided a ±2% accuracy and it was equipped with a built-in 3.1Mp digital camera. For an accurate output, the thermocamera required in input the emissivity of the target, the distance from it and the ambient temperature.

3.2.7 Thermocouples and temperature recorder

Type K thermocouples were used in this work. The outputs were logged using an Omega RDXL12SD Temperature Recorder. This device could record data from 12 thermocouples at the same time, with 0.4% accuracy, and store them in SD memory cards of up to 16GB capacity. The thermocouples were calibrated according to the temperature of melting ice at atmospheric pressure (0°C).

3.3 Software packages

3.3.1 COMSOL Multiphysics

COMSOL Multiphysics is a graphic simulation software platform that can be exploited for different applications. Versions 4.3, 4.4, and 5.0 have been used. The module "Heat Transfer" was employed for modelling natural convective cooling and to understand the effects of the light non-uniformity on the performance of the receiver. The module "AC/DC" was, instead, exploited to analyse the electrical behaviour of the components and to predict the effects of the Joule losses.

The simulations were conducted in a three dimensional environment and in stationary modes. The modelled geometries were reproduced in the graphic window, generally using millimetres and degrees as length and angular units respectively. Each volume was modelled as a solid or a fluid material and,

depending on the studied physics, nodes and boundary conditions were opportunely added. The geometry was automatically discretized into a large number of small elements. Once the model was developed, COMSOL automatically generated the solver sequence and computed the solution. The results were plotted in the graphic window and can be personalized, in terms of analysed points, surfaces or volumes, considered ranges of values, employed units and visualized scales.

3.3.2 AutoCAD

AutoCAD is a 2D Computer Assisted Design software tool developed by Autodesk. The freeware student versions released in 2010 and 2015 were used for designing and dimensioning of solar receivers, heat sinks, and experimental setups. The artworks produced in AutoCAD could be easily integrated or used with other software platforms.

Both basic shapes and complex designs could be replicated in AutoCAD, whose successful features were the large number of functions available to modify the drawings and the user-friendly interface. The length and the angles of the components could be reproduced with high accuracy at any scale.

3.3.3 DesignSpark PCB

DesignSpark PCB is an electronics design freeware platform, developed by RS Components. The versions 5.1 and 6.0 were used. DesignSpark PCB was employed to design the electrical circuitry and the layers of the solar cell receivers.

The different layers of any PCB and IMS were reproduced using this software tool: the aluminium substrate, the conductive pattern, and the paste and the solder masks. Moreover, the holes to be drilled were drawn and the sizes and the specifications of each component were reported. DesignSpark PCB plotted the Gerber files of each layer, which were then processed by the supplier to produce the substrates.

3.4 Measuring the cell's temperature

For the preliminary studies of the effects of the temperature on the cell performance, a thermocouple was placed in contact with the side of the cell. Indeed, the backplate of the assembly is not a good point to measure the temperature: Figure 41 shows that an important temperature difference between the cell and the backplate can occur in CPV receivers and it usually ranges between 10°C and 30°C [147]. Moreover, the thermocouple was not placed over the cell to avoid any shading. All the tests were conducted respecting the CSTCs: AM1.5 spectrum, with a direct normal irradiance of 1000W/m^2 and an ambient temperature of 25°C. The temperature was measured and recorded every 0.2 seconds.
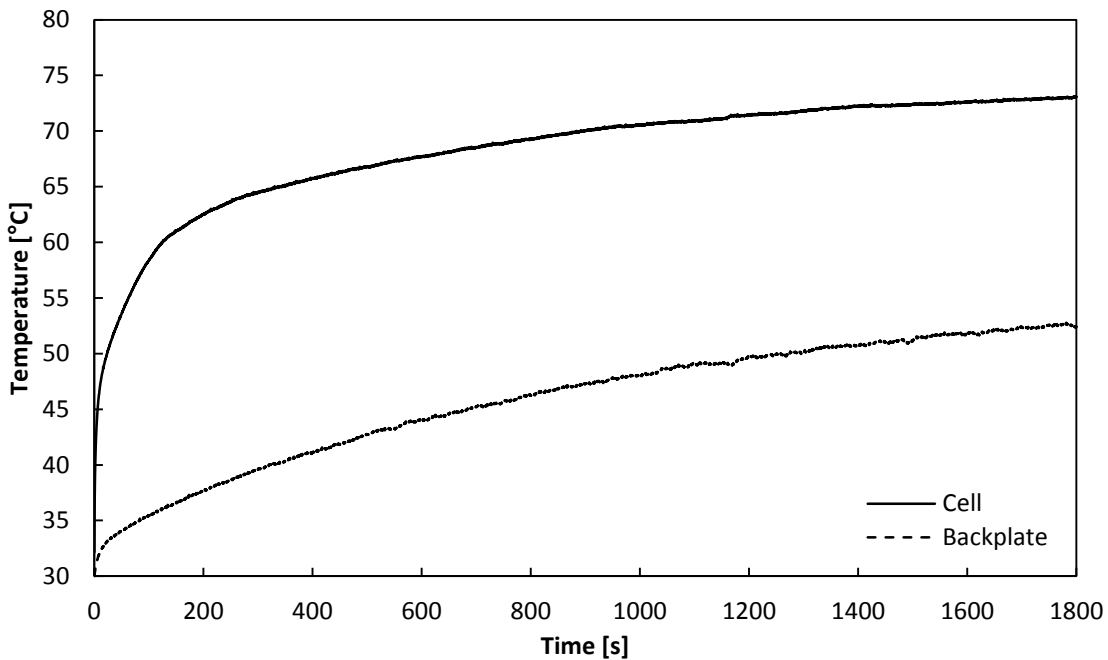
Figure 41 - Differences between cell's and backplate's temperatures under the same conditions

A resistor was connected in series with the cell to allow current to flow. During the measurements, the circuit was kept closed, otherwise all the sunlight would have been converted into heat. When a CPV cell was correctly working, a part of the sunlight was converted into electricity and, thus, the heat produced was lower than that produced by a cell in open circuit conditions. The difference can be seen in Figure 42, where after 20 minutes the open circuit temperature of a 1cm^2-sized cell at 166× was found to be higher than that of the close circuit case.
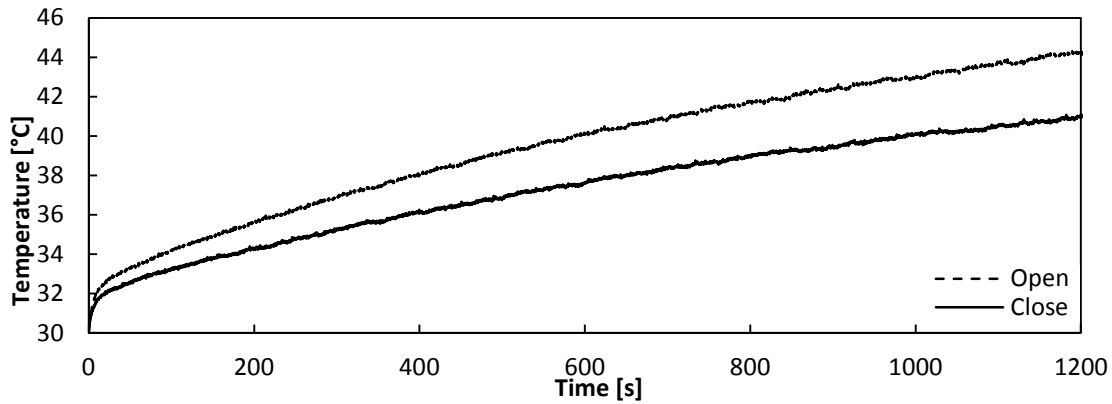
Figure 42 - Difference in temperature between open and close circuit

3.5 Production of the PCB and IMS

The conductive pattern of a PCB or an IMS is usually produced through a subtractive method: either chemical etching or mechanical milling. The quality of the chemical process mainly relies on the accuracy of the photomasking and on the feature of the chemicals. On the other hand, the quality of the mechanical process depends on the size, the sharpness, the speed and the control of the milling devices.

In the present work, the chemical etching process was employed, because generally cheaper and less time-consuming than mechanical milling. Although the same process could be applied to both the substrates, the chemical etching was carried out in a local workshop for the PCBs and outsourced for the IMSs used in the cell assembly development. This way, an enhancement in quality of the IMS-based final receivers was achieved. Both the processes are described in the following sections. The selection and the design of the substrates will be reported in section 4.4 and chapter 5 respectively.

3.5.1 In-house PCB development

The PCB fabrication was carried out using the facilities of the Concept Shed workshop, in Falmouth (UK). Due to the toxic chemicals involved in the process, safety equipment (gloves, protection glasses and lab coat) was used and an adequate waste disposal was managed.

3.5.1.1   Printing the PCB

3.5.1.1.1 Artwork

The copper circuity was designed in AutoCAD and the 1:1 scaled artwork was printed in black and white onto an A3 tracing paper using a laser printer.

3.5.1.1.2 Exposure

The board was then exposed for a variable period under UV lamps (Figure 43), using the previously-printed artwork as a mask (Figure 44). An optimal contact between the mask and the board was ensured to avoid a bad edge definition.
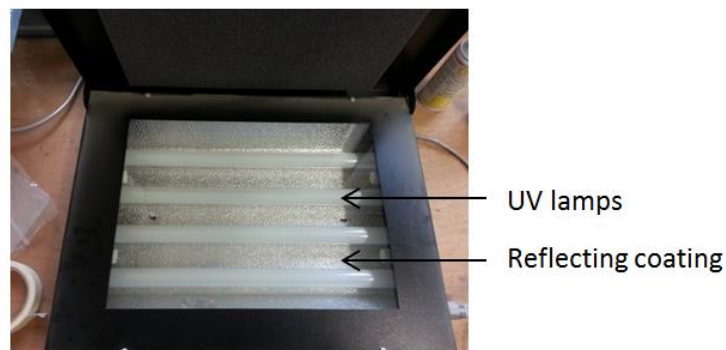
Figure 43 - The high resolutions UV lamps
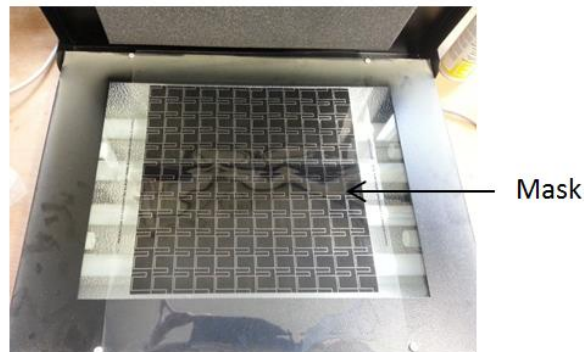
Figure 44 - The mask placed over the lamps

The exposure time was determined by exposing some samples to different times. A short exposure time could lead to an incomplete development, while a long exposure time could cause holes or flaws in the final circuit.

3.5.1.1.3 Development

Immediately after the exposure, the laminate was immersed into a developer. In this device, the previously exposed photosensitive resin was removed by the developer solution.

3.5.1.1.4 Etching

The laminate was then moved into the etching tank (Figure 45), in which the pre-heated etchant solution removed the copper which was no longer protected by the resin. The solution was made by mixing 50ºC water with Fine Etch Crystals supplied by Mega Electronics. The etching period was set by checking periodically the laminate during the process. If the etching time was too short the solution would have not correctly removed the copper, whereas over etching could cause a bad edge definition.
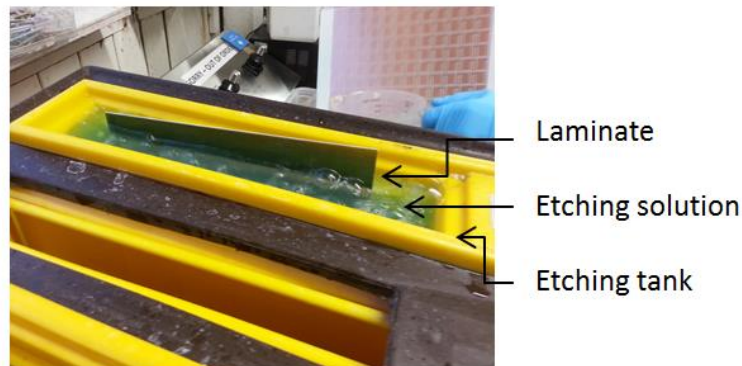
Figure 45 - The laminate into the etching solution

3.5.1.1.5 Resin removal

The laminate was re-exposed under the UV lamp and then immersed into the developer solution (Seno 4006 Liquid Photoresist Developer Concentrate, Figure 46): the resin was then removed and the etching process was complete. The exposure time was the same used in the first step.
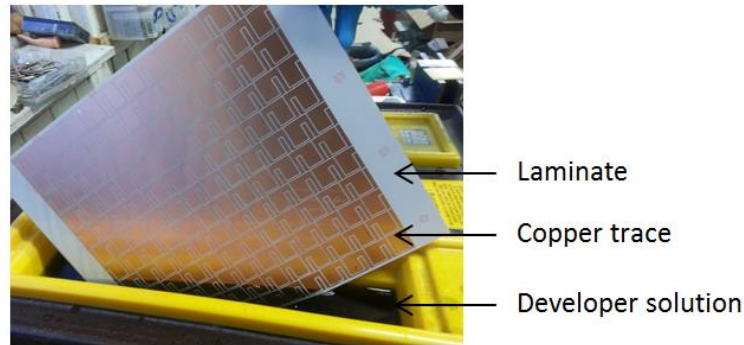
Figure 46 - The PCB board removed from the developer solution at the end of the process

3.5.1.2 Populating and interconnecting the PCB

PCBs of different dimensions were printed. As a first approach, few cells were manually soldered on the printed substrates using a $Sn_{96,4}Ag_{3,6}$ lead-free solder paste (Figure 47 a and b). A small paste mask was fabricated by milling the footprints of the diode and the cell on a thin 2mm×2mm silicone rubber sheet, shown in Figure 47c.
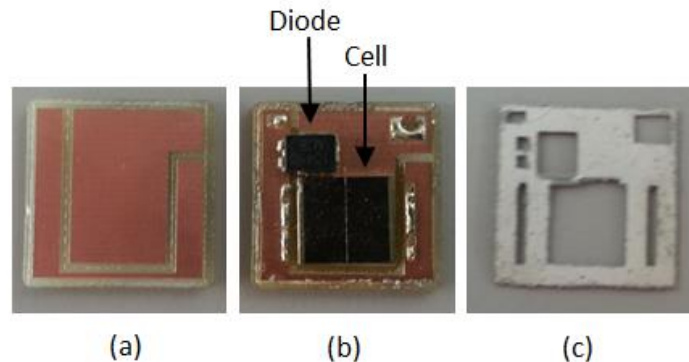
Figure 47 - A bare PCB (a), a populated PCB (b) and the paste mask (c).

The interconnections were firstly made of 3mm-wide tinned copper flat wires soldered on the cell's tabs (Figure 48), but they exhibited low reliability for this application: part of the ribbon covered portions of the cell's active area and, in some regions, the cell seemed to be damaged by the high temperatures required for the wire's soldering. Overall, the quality of the soldering and connections was quite poor, with a high solder paste contamination left on the surfaces and a non-negligible risk of causing short-circuiting.
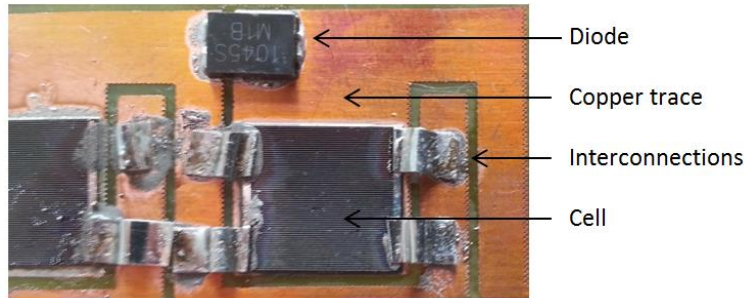
Figure 48 - Manually picked, placed and soldered components

In a different approach, the interconnectors were ultrasonic soldered (Figure 49). As for the previous experience, the solder paste could not be placed with the required accuracy, and part of the paste covered the active area of the cell.
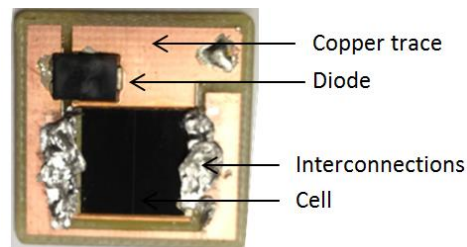
Figure 49 - Ultrasonic soldered cell's interconnections

In a last attempt, realized by Custom Interconnect Ltd. in Andover (UK), a silver epoxy (Loctite Ablebond 84-1LMI) was used to make the interconnections between the cell and the electric circuitry. A bead of non-conductive epoxy (Emerson & Cumin Stycast 50400-1) was applied between the cell's tabs and the copper pads to avoid short-circuiting the top and the bottom of the cells. Once cured, the silver epoxy was dispensed to create the electrical connection. This approach had some drawbacks, because of the low electrical conductivity of the silver epoxy and because it tended to deteriorate with prolonged exposure to UV. Moreover, this method showed a low repeatability: a large number of the interconnected cells were found to be short-circuited. For these reasons, this solution could not be applied in the full scale cell assembly and, so, the wire bonding technology was preferred for interconnecting the cells.
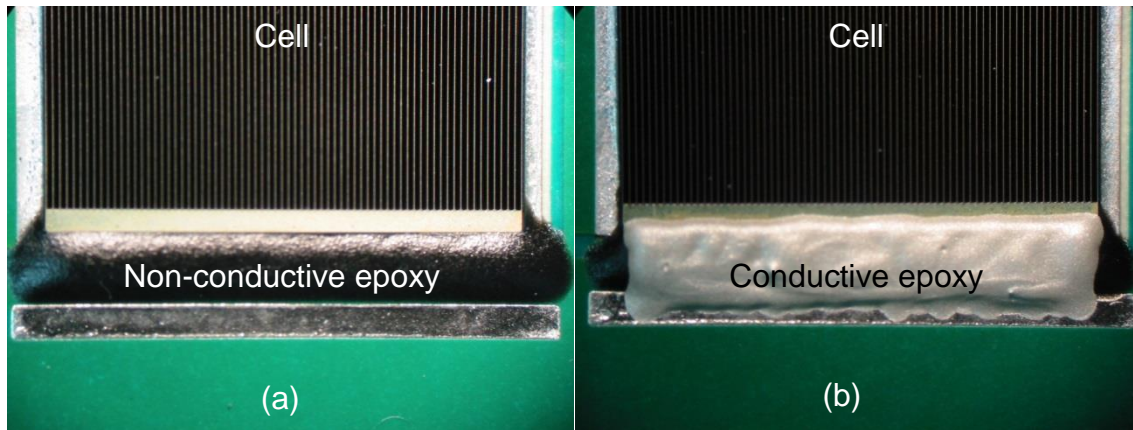
Figure 50 - The interconnected cell: the dispensed non-conductive epoxy (a), then covered by the conductive epoxy (b).

3.5.2 Outsourced IMS printing

In order to achieve a higher quality of the substrate, the insulated metal substrates were outsourced. The IMS was populated in the Cubik Innovation workshop and the wire bonding performed by Custom Interconnect Ltd.

3.5.2.1 Production of the IMS

In this case, a Gerber file was made by using DesignSpark PCB. In the Gerber file, the designs of the different layers of the IMS were reproduced, such as the copper pattern, the solder mask and the paste mask. The size and the materials were specified, as well as the size and the position of the holes to drill, the surface's finishing and the tolerances.

The surface of the copper conductive layer was finished with an Electroless Nickel/Electroless Palladium/Immersion Gold (ENEPIG). This finish, introduced in mid-90s, had already gained much attention among the Pb-free applications. Sn-Ag-Cu/ENEPIG solder joints had already proven a high mechanical robustness [319] and a strong wire bondability [320]. Moreover, the surface mounted components benefitted from the extreme planar surface granted by ENEPIG [321].

The insulated metal substrate, shown in Figure 51, was covered by a thin green resistive layer, called solder mask, in order to electrically insulate and to protect the conductive layer. The same coating prevented the solder paste from spreading out of its planned places. The resistive coating needed to be appropriately designed to accommodate the surface mounted components. The cell's mounting pad layout

(Figure 52a) was increased by 1mm per side compared to the cell surface, in order to take into account the tolerances. The diode's mounting pad layout (Figure 52b) was designed according to the datasheet.

The paste mask was used to produce the metallic stencil employed to dispense the solder paste on the substrate. The solder footprints of the components were accurately reproduced on the mask to assure a homogenous distribution of solder paste under the components:

- The cell's solder footprint was split into 9 parts (Figure 52c), to facilitate the uniform solder paste distribution under the cell's weight;
- The diode's solder footprint (Figure 52d) was designed according to the guidelines provided in the datasheet: one large surface for allocating the cathode and two smaller apertures for the anodes.
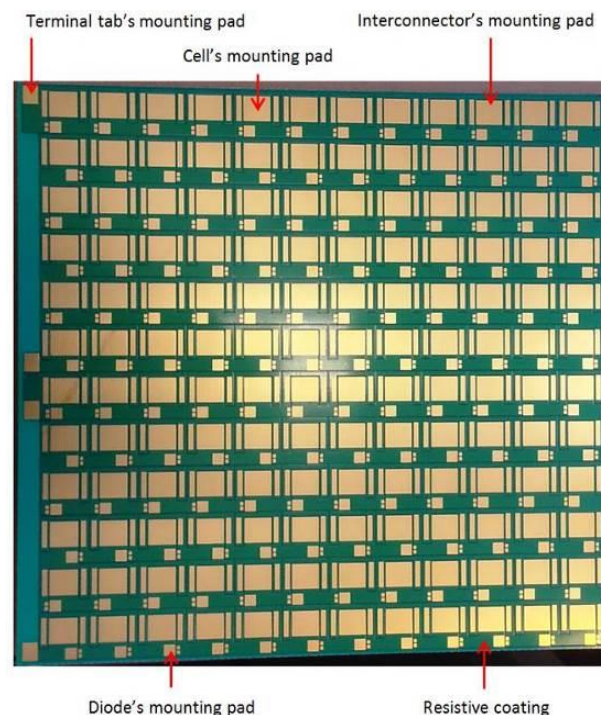
Figure 51 - The bare insulated metal substrate, covered by a thin green electric resistive layer.
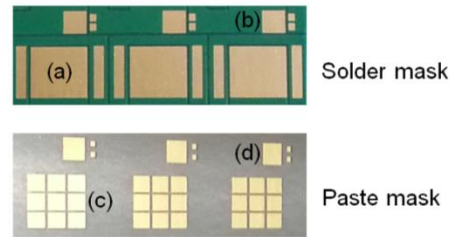
Figure 52 - Particulars of solder mask and paste mask. The mounting pads of cells and diodes are respectively shown in (a) and (b). The solder footprints of cells and diodes are respectively shown in (c) and (d).

3.5.2.2 Populating the IMS

The population of the IMS took place through a few steps, described in the following subsections. It was realized using the Cubik Innovation's facilities, in Bristol (UK).

3.5.2.2.1 Solder paste dispensing

Considering the AZUR SPACE's recommendation to use 3% silver content solder paste for III-V cells in order to enhance the joining strength, the $Sn_{96.2}Ag_{3.2}Cu_{0.6}$ solder paste was employed to paste the surface mounted components on the board. The solder paste was dispensed onto the board by using the paste mask, a 0.125mm-thick stainless steel stencil where the footprints of the surface mount components were reproduced (Figure 53). The past mask was accurately positioned over the board, and both the elements were then held by an external frame. Using a paste squeegee, the solder paste was spread until the entire stencil was uniformly covered. The paste mask was then removed by using a mechanical arm to avoid any solder paste misplacing.

Figure 53 - Image of the paste mask used for the population of the 144-cell assembly.

3.5.2.2.2 Pick and Place

The surface mounted components were manually placed onto the plate (Figure 54), by using a vacuum pick-up system. The dimensions of the board, the low number of boards to be produced and the cells delivered in a diced wafer and mounted on a tape made it impossible to use an automatic pick-and-place machine. Hand-placing did not affect the correct positioning of the components, because any small offset was naturally corrected due to a phenomenon known as "self-alignment" [116]. The wetting force of the liquid-state solder paste moved the components to the correct position, according to the corresponding solder footprint.
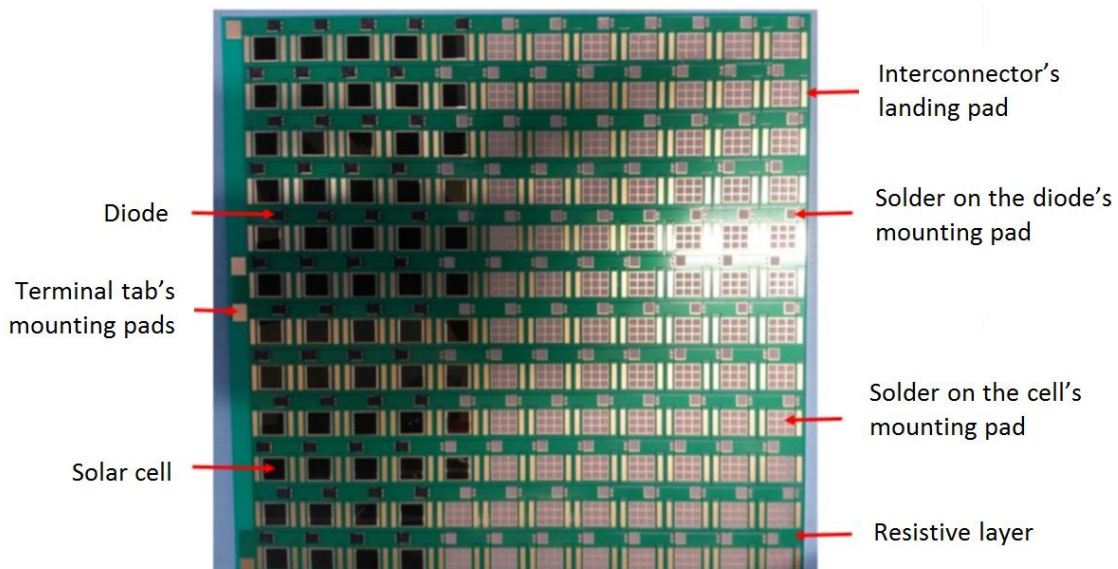
Figure 54 - The 144-cell board being populated.

3.5.2.2.3 Soldering

After the placement of the surface mounted components, the whole setup was moved into a reflow oven to allow the solder paste curing (Figure 55). The use of a reflow oven improved the action of the self-alignment effect [322]. The oven was set at a temperature of 217°C, the melting point of the solder paste. When the oven's atmosphere reached that temperature, moisture was automatically evacuated and the plate was actively cooled through water jets on the rear surface.
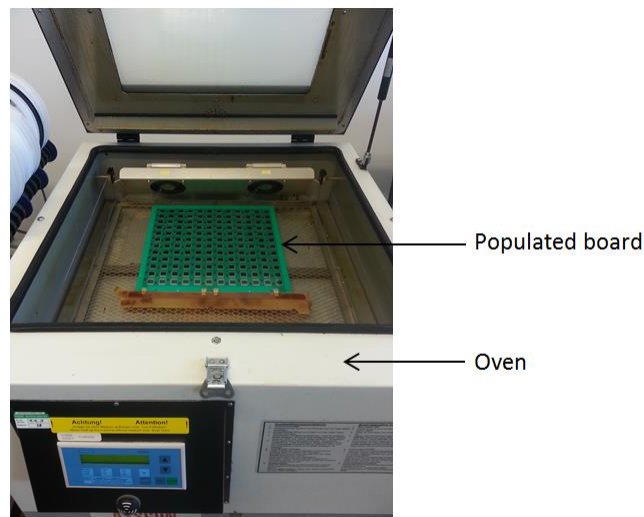
Figure 55 - The populated board placed in the reflow oven

3.5.2.2.4 IMS cleaning

At the end of the population process, a first visual inspection was conducted and some solder paste contamination was found on the surface of the plate (Figure 56a). Soiling can affect the strength of the wires and enhance the risk of failures during the wire bonding: it has been previously demonstrated that cleaning improves the strength of the bonds [323]. For this reason, a cleaning process was undertaken: the substrate was immerged firstly in deionized water, secondly in water and thirdly in a solution of water and deionized water. During the whole cleaning the plate was kept in the dark in order to prevent any potential short-circuiting that could have occurred among the subcells when in contact with water. The plate was then dried in a 135°C oven for short time. The effects of the cleaning are clearly shown in Figure 56b. Once cleaned, the metallic wires could be bonded on the cell's front tabs.
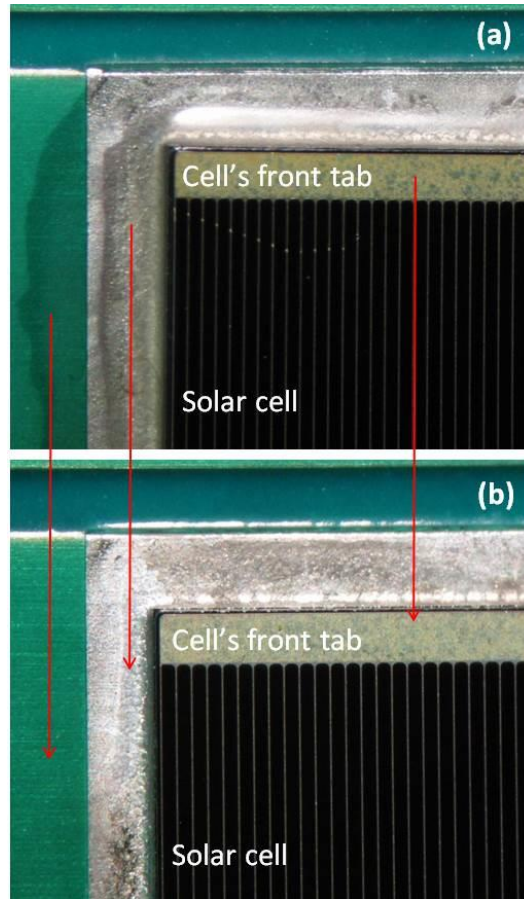
Figure 56 - Comparison between particulars of the pre-cleaning plate (a) and the post-cleaning plate (b).

3.6 Investigation on heat transfer at micro-scale

3.6.1 Experimental apparatus

The experimental investigations on micro-scaled, natural convective heat transfer reported in this work were conducted by using the setup reproduced in Figure 57. Micro-fin arrays were mechanically diced on different 5cm×5cm squared silicon wafers. Each array was heated using 10W flexible heater (Omega KHLV-202/2.5), bonded through a conductive adhesive (3M tape 966, 0.18 W/mK). Each sample was placed in a 1.5cm-thick case made of fibre thermal material (0.05W/mK), back-covered with a 1cm-thick polystyrene block (0.03 W/mK), to minimize the heat losses from the surfaces other than the fins.
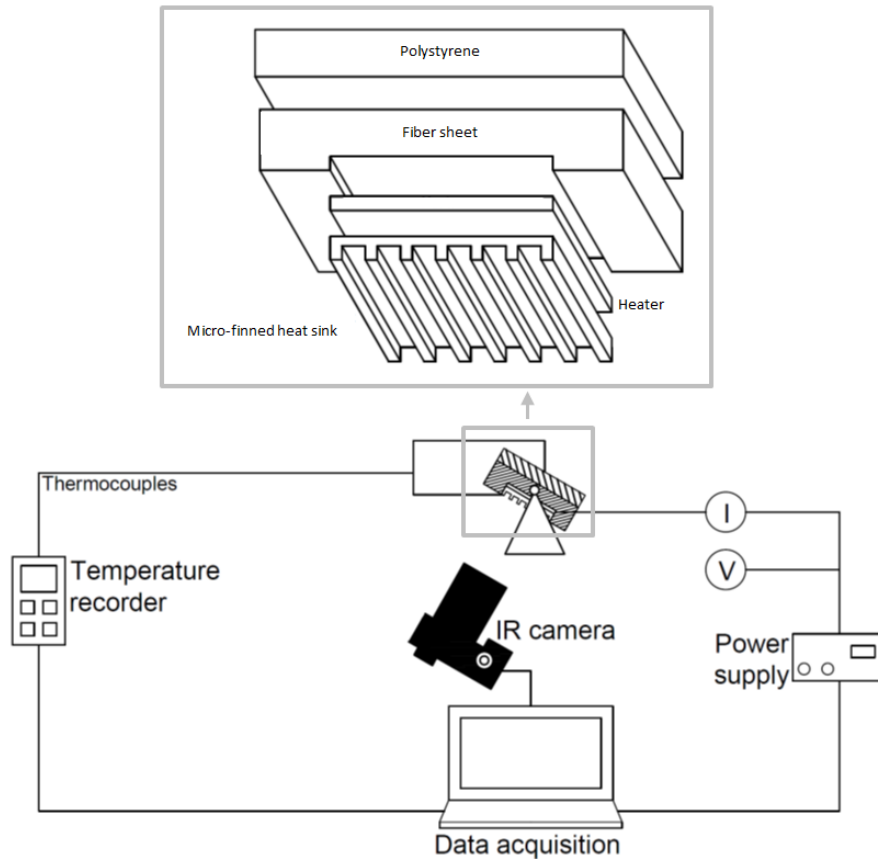
Figure 57 - Schematic of the experimental setup and of the exploded structure of the sample case.

The power input to the heater was controlled through a DC power supply (Weir 413D, Figure 58a), whose output ranged between 0 and 10W. The voltage was manually set through the analogical control of the power supply and both voltage and current were measured respectively using a Fluke 8050A (Figure 58b) and a Fluke 115 (Figure 58c) digital multimeters.

The maximum temperature of the silicon arrays was measured through an infrared camera (FLIR T425, Figure 58d), perpendicularly placed 30cm away from the sample. The emissivity of the silicon wafer, required as an input to the thermocamera, was set to 0.72: it was calculated by measuring the reflectance in a Perkimeter Lambda 1050 spectrometer and then applying Kirchhoff's law. The emissivity used for the infrared imaging was obtained by the average emissivity across the wavelength range the thermocamera works (750µm to 1300µm). Three K type thermocouples were placed on the sides of the fins. The contact between thermocouples and sample's walls was assured using a high temperature Kapton

adhesive tape (Tesa 51408). A fourth and a fifth K type thermocouples were placed in proximity of the samples: the average of their measurements was used to calculate the ambient temperature. One more thermocouple was placed at the centre of the back surface of the insulating material. A 12-Channel Temperature Recorder (Omega RDXL12SD, Figure 58e) was used to record the thermocouples measurements. The room temperature was kept constant at 25°C and measured through a digital thermohygrometer (Testo 608-H1).
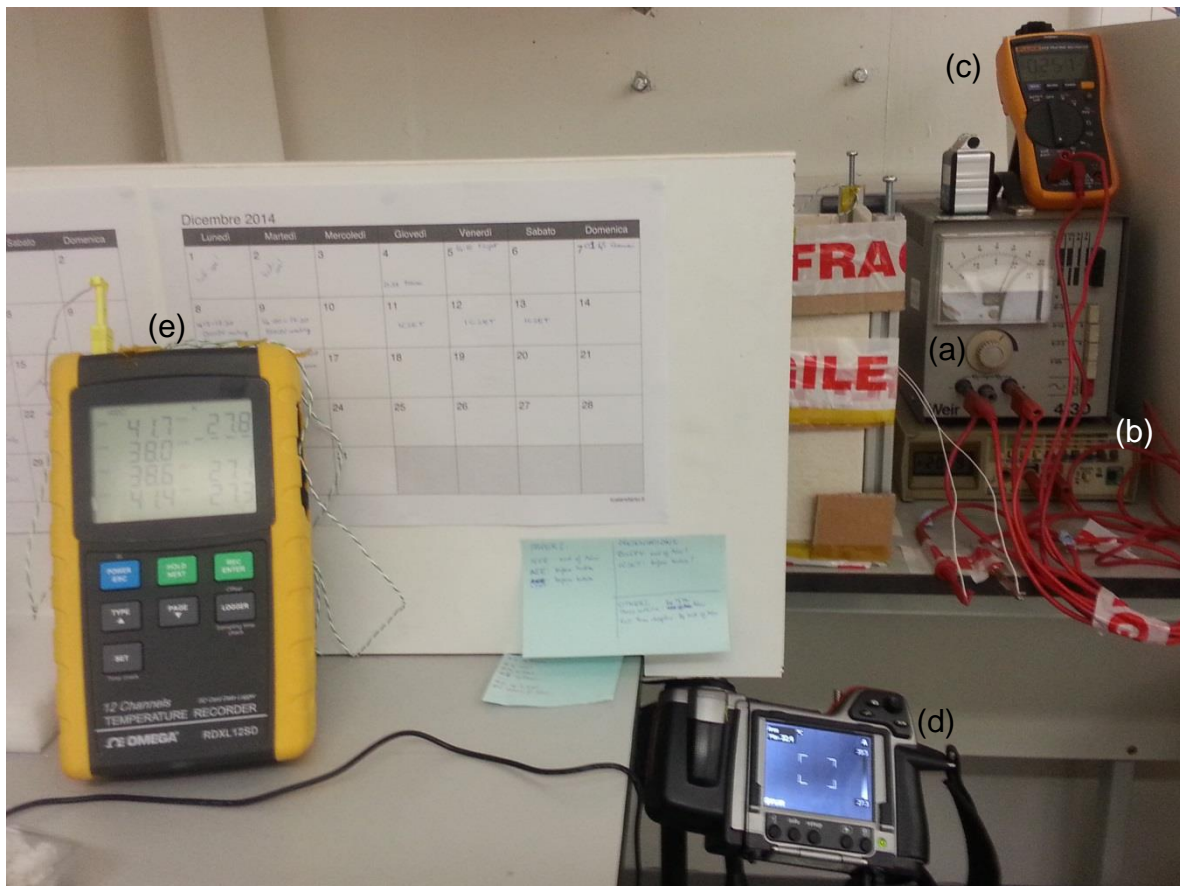
Figure 58 - Picture of the experimental apparatus: (a) the DC power supply, (b) the voltmeter, (c) the ampere-meter, (d) the IR camera, (e) the temperature recorder.

In order to isolate the fins array from any external interferences, the sample was placed inside a 25cm×25cm×25cm box open on top [251] and made of fibre thermal insulating sheet (Figure 59f). On one side of the box, a 10cm×10cm removable opening was placed (Figure 59g): while under test, it was keep closed, and it was opened for only few seconds to let the infrared camera focus on the fins array at steady state, reached in about 20 minutes. The thermocouples data were recorded every two seconds and stored in a database.

Figure 59 - Picture of the experimental apparatus: (a) the DC power supply, (b) the voltmeter, (c) the ampere-meter, (d) the IR camera, (f) the 25cm×25cm×25cm box, (g) the 10 cm×10 cm removable opening.

The heat sink was mounted on an inclinable holder. The inclination angle (θ) was defined according to [155] as the angle between the heat sink base plate and the vertical orientation, as shown in Figure 60. Zero degree described the heat sink in vertical position and 90° the horizontal fin array facing downward, whereas negative values indicated an upwards facing orientation. The tilt angle was varied using a screw on the heat sink holder and measured using an angle gauge with an accuracy of ±0.1°. Seven tilt angles were considered for each sample: -90°, 0°, 30°, 50°, 60°, 70°, 80° and 90°. Each sample was tested at variable power inputs

from 2.5W to 10W. Each test was conducted three times and the average value of the outputs was considered.
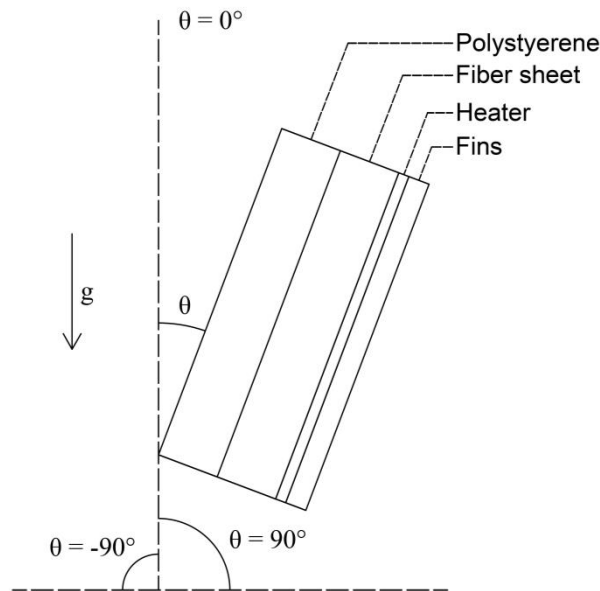
Figure 60 - Definition of the inclination angle (θ)

The nomenclature used to describe the fin arrays is shown in Figure 61. Two fin types were investigated: parallel rectangular plate fins (Figure 61a) and square pin fins (Figure 61b).
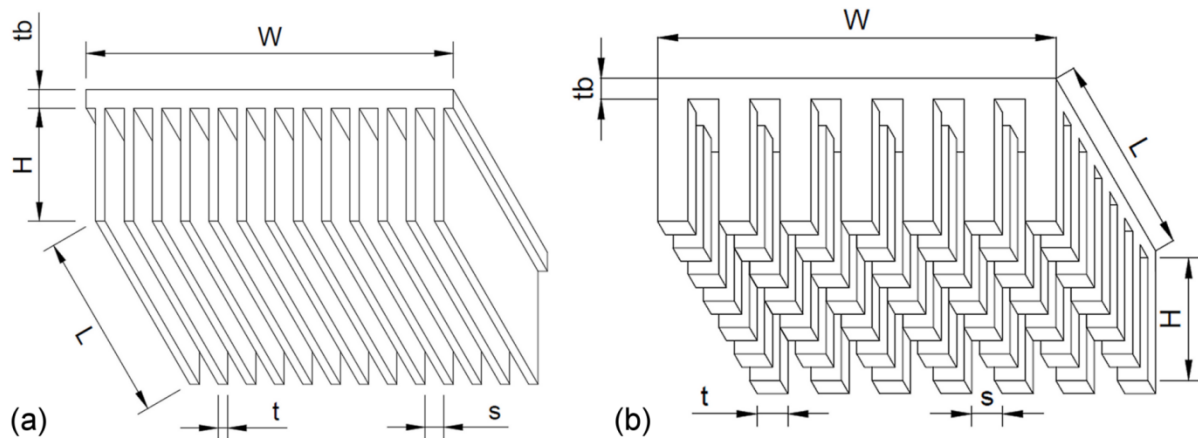
Figure 61 - Description of the parameters: (a) plate fin array, and (b) pin fin array.
L is the length of the fins, W the width of the fin array, H the height of the fin, t the thickness of the fin, s the spacing between two adjacent fins, tb the thickness of the base.

3.6.2 Thermal losses

The aim of this work was to investigate, in different conditions, the heat transfer coefficients of micro-fins arrays (h_{fins}), defined as:

$$h_{fins} = \frac{Q_{fins}}{A_{fins} \cdot (T_{fins} - T_{amb})} \tag{1}$$

where Q_{fins} is the heat dissipated through the fins by convection, A_{fins} is the area of the finned surface, T_{fins} corresponds to the fins temperature, measured by the thermocamera and considered uniform across the fins, and T_{amb} is the ambient temperature, registered by the thermocouples. The heat transfer coefficients were considered as constant for the whole finned surface.

The power load convectively dissipated by the fins (Q_{fins}) was taken into account after the radiated heat transfer (Q_r) and the losses happening on the back and the sides of the samples (Q_{loss}), in order to estimate the heat transfer coefficient of the fins in the most accurate way. It was thus expressed as:

$$Q_{fins} = Q_{in} - Q_r - Q_{loss} \tag{2}$$

where Q_{in} represents the heat produced by the heating film, calculated by multiplying the voltage (V_{DC}) and the current (I_{DC}) provided by the power supply:

$$Q_{in} = V_{DC} \cdot I_{DC} \tag{3}$$

The heat dissipated by the flat plate (Q_{flat}) was calculated similarly to Q_{fins}. The total heat transferred by radiation from the fin array was expressed by the Stefan-Boltzmann equation as the sum of the radiative heat transfers happening in the different fin surfaces (top, side, face and base):

$$Q_r = \sum_i \varepsilon \cdot \sigma \cdot A_i \cdot F_{i,k} \cdot (T_{fins}^4 - T_{amb}^4) \tag{4}$$

where ε is the emissivity of silicon, σ is the Stefan-Boltzmann constant ($5.67 \cdot 10^{-8} W/m^2K^4$), A_i is the area of the correspondent i-surface of the fins, $F_{i,k}$ are the view factors between the surfaces *i* and *k*. In this case, an average emissivity of 0.78 was considered. The view factors depended on the geometry of the fins and were different for each fin surface. They were calculated using the model presented by [324]. The fin wall (Figure 62a) exchanged radiative heat with the base (Figure 62b), the side wall of the adjacent fin (Figure 62c) and the ambient (Figure 62d).
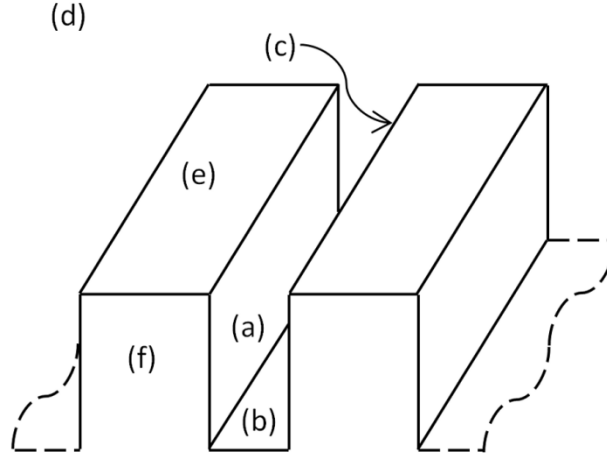
Figure 62 - Schematic of the micro-fin array: the fin walls (a), (c), (e), (f); the base (b); and the ambient (d).

The view factor between the fin wall and the base ($F_{a,b}$) was estimated as [324]:

$$F_{a,b} = \frac{1}{\pi \cdot y} \left\{ y \cdot \tan^{-1}\left(\frac{1}{y}\right) + x \cdot \tan^{-1}\left(\frac{1}{x}\right) - (x^2 + y^2)^{0.5} \cdot \tan^{-1}\left(\frac{1}{(x^2+y^2)^{0.5}}\right) \right.$$
$$\left. + \frac{1}{4}\ln\left(\frac{(1+x^2)\cdot(1+y^2)}{1+x^2+y^2}\left(\frac{y^2\cdot(1+x^2+y^2)}{(x^2+y^2)\cdot(1+y^2)}\right)^{y^2}\left(\frac{x^2\cdot(1+x^2+y^2)}{(x^2+y^2)\cdot(1+x^2)}\right)^{x^2}\right) \right\}$$

(5)

where x=s/L and y=H/L.

The view factor between two adjacent fins' walls ($F_{a,c}$) was estimated as [324]:

$$F_{a,c} = \frac{2}{\pi \cdot x \cdot y} \cdot \left\{ \ln\left(\frac{(1+x^2)\cdot(1+y^2)}{1+x^2+y^2}\right)^{0.5} + x\cdot(1+y^2)^{0.5} \right.$$
$$\left. \cdot \tan^{-1}\left(\frac{x}{(1+y^2)^{0.5}}\right) + y\cdot(1+x^2)^{0.5}\cdot\tan^{-1}\left(\frac{y}{(1+x^2)^{0.5}}\right) - x\cdot\tan^{-1}x - y\cdot\tan^{-1}y \right\}$$

(6)

where x=H/s and y=L/s.

The view factor between the fin wall and the ambient ($F_{a,d}$) was then estimated by using the equation for an enclosure with four surfaces [325]:

$$F_{a,b} + F_{a,c} + F_{a,d} = 1$$

(7)

The view factor between the fin's base and the fin's wall ($F_{a,b}$) was obtained by exploiting the reciprocity relation [325]:

$$A_a \cdot F_{a,b} = A_b \cdot F_{b,a}$$

(8)

The view factors of the surfaces "e" and "f" were set equal to 1. The contribution of the radiative exchange increased with the power input. Out of a maximum 10W

power input supplied to the heater, a percentage ranging between 35% and 42% was found to be dissipated because of radiative exchange of the fins.

The Q_{loss} were due to the heat dissipation happening on the unfinned surfaces of the assembly: these were the radiative and the convective thermal exchanges taking place on the sides and on the back of the structure. The radiative component was estimated considering the emissivity of polystyrene (0.60) and fibre sheet (0.85) and a view factor of 1. The convective exchange happening on the back surface of the insulator was calculated considering the equations reported in [326]:

$$h_{loss} = \frac{k_{air}}{L} \cdot Nu_{loss} \tag{9}$$

where k_{air} is the thermal conductivity of the air and Nu_{loss} the Nusselt number, which was calculated according to the orientation of the surface [326]:

$$Nu_{loss} = 0.13 \cdot (Ra)^{1/3} \text{ if the surface is horizontal and faces upwards;} \tag{10}$$

$$Nu_{loss} = 0.59 \cdot (Ra)^{1/4} \text{ if the surface is vertical;} \tag{11}$$

$$Nu_{loss} = 0.58 \cdot (Ra)^{1/5} \text{ if the surface is horizontal and faces downwards.} \tag{12}$$

Ra is the Rayleigh number, defined as:

$$Ra = \frac{g \cdot \beta_{air} \cdot Pr \cdot s^4 \cdot (T_{back} - T_{amb})}{L \cdot v_{air}^2} \tag{13}$$

where g is the gravitational acceleration, β_{air} is the volumetric thermal expansion of the air, Pr is the number of Prandtl, v_{air} is kinematic viscosity of the air and T_{back} is the temperature measure by the thermocouple placed on the back surface of the insulator. All the properties were evaluated for an air temperature of $(T_{back}+T_{amb})/2$, with the exception of the thermal expansion, estimated at ambient temperature [324].

All the tests were conducted for $Ra>10^6$, condition needed for applying the reported equations of convective heat transfer. The losses averagely account for 26% of the total power input, with comparable contributions from the convective and the radiative heat transfers.

3.6.3 Experimental uncertainty

Any experimental investigation is affected by an uncertainty due to the accuracy of the instruments and to the non-ideal working conditions. In this case, the related overall uncertainty was calculated according to the propagation of error for independent variables [327]:

$$\frac{Uh_{fins}}{h_{fins}} = \sqrt{\left(\frac{UQ_{fins}}{Q_{fins}}\right)^2 + \left(\frac{UA_{fins}}{A_{fins}}\right)^2 + \left(\frac{UT_{fins}}{T_{fins} - T_{amb}}\right)^2 + \left(\frac{UT_{amb}}{T_{fins} - T_{amb}}\right)^2} \qquad (14)$$

where the uncertainties are indicated with the prefix "U". The area of the fin array was calculated with an uncertainty of ±4%. T_{fins} was measured with the thermocamera, which had an uncertainty of measurement of ±0.2%. The uncertainty on the emissivity could not be neglected [251], and was considered equal to ±0.2. This value corresponded to an additional fin temperature uncertainty of ±3.5°C. T_{amb} is obtained as an average of the thermocouples' measurements, read from the temperature recorder (accuracy: ±0.4%). The thermocouple data were adjusted according to the offset measured in a preliminary investigation: an uncertainty of ±1.0°C was considered. The maximum uncertainty was found to be ±8.25%, and occurred at low power inputs. This value fell within the range reported by similar studies [251,252].

3.6.3.1 Data extraction and digitization

Some of the results analysed in the work were obtained by processing the data available in graphical format in [252]. Whereas not explicitly mentioned, the data were extracted by using *Engauge Digitizer 4.1* (M. Mitchell, Engauge Digitizer, http://digitizer.sourceforge.net), an open source software platform that allows converting graphs into numbers. The authors of [252] reported an experimental uncertainty of ±9.4%. Repeating the digitization twice, a repeatability uncertainty of ±1.0% was found. Moreover, the size of the markers introduced an additional uncertainty of ±3.1%. Overall, the uncertainty on the digitalized heat transfer coefficients was found to rise up to ±9.9%.

3.6.4 Experimental validation

3.6.4.1   The thermal model

In order to verify the reliability of the experimental setup, a computation analysis was carried out using the "Heat Transfer" module of COMSOL Multiphysics 4.4. The flat plate sample was modelled and the outputs of the simulation were compared with the experimental results. The setup was validated for the two conditions studied in the present work: horizontal and tilted orientations.

In both cases, the heater was modelled as a 0.254-mm thick copper plate, bonded to the 1.4mm thick silicon sample (Figure 63a.3) through the adhesive, represented as a thermal resistive layer (0.06mm-thick, 0.18W/mK). Both the heater and the silicon sample size 5cm×5cm and built-in silicon and copper materials were chosen (130W/mK and 400W/mK respectively). The insulating structure was reproduced around samples: it was composed of a 1cm-thick fibre sheet (0.05W/mK, 1900kg/m^3, 1369J/kgK; Figure 63a.2), back-covered by a 1cm-thick polystyrene block (0.33W/mK, 960kg/m^3; Figure 63a.1). The heater was set as a "Heat Source", which required the total thermal power in input. The interface contact between the heater and the insulator was considered as a 0.5mm-thick air layer.

The "Convective Heat Flux" function was applied to all the external surfaces: the heat transfer coefficient was automatically defined by COMSOL for each surface according to its orientation and geometry. COMSOL considered the material properties at temperature of $(T_s+T_{amb})/2$, where T_s is the temperature of the closest surface. All the external surfaces were set to exchange radiative heat with the environment. The emissivities were fixed to 0.78 for silicon, 0.85 for the fibre sheet and 0.60 for the polystyrene. The automatic "physics-controlled" mesh generator was chosen and a "finer" size was selected. The simulator solved 242803 degrees of freedom (Figure 63), converging to solution in 1 minute.
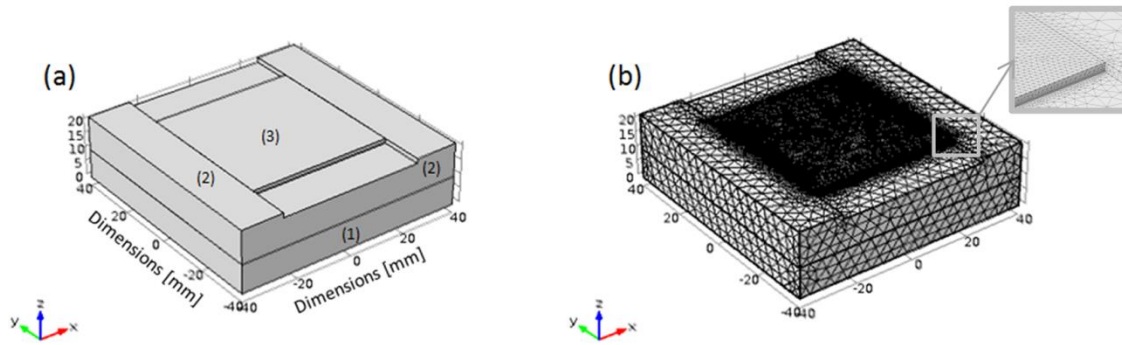
Figure 63 - The geometry of the experimental setup modelled in COMSOL (a): the polystyrene block (1), the fibre sheet case (2), and the flat plane sample (3). In (b), the tetrahedral mesh is reported.

The maximum temperature of sample's external surface predicted by COMSOL was then compared with that measured by the IR camera, as shown in Figure 64. All the tests were carried out in stationary mode.
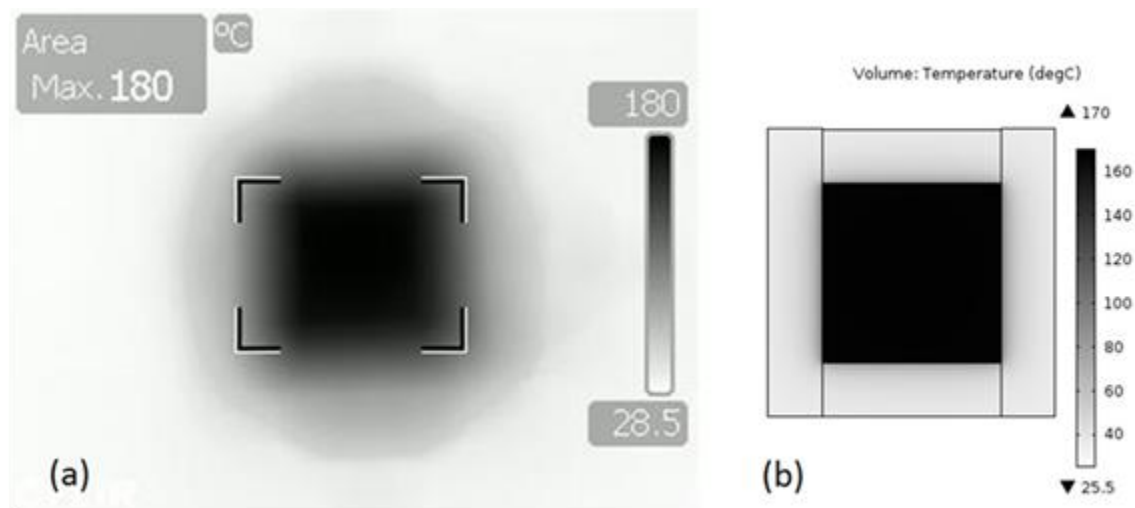
Figure 64 - Comparison between the top view of the sample taken from the IR camera (a) and the COMSOL model results (b). Conditions: sample facing upwards, heat power imput 10W.

3.6.4.2   *Horizontally orientated fins*

The thermal behaviour of horizontally orientated fins was studied in both facing upwards and facing downwards conditions. Power inputs of 2.5W, 5W, 7.5W and 10W were considered. The difference between the experimental and the simulated data ranged between 2°C (for the lowest power) and 8°C (for the highest power). These results were in line with the one reported by [252]: the discrepancies were due to a number of factors. In particular, the model took into account fixed values of the materials' properties (*e.g.* thermal conductivity, and density), whereas these

properties, in the real case scenario, strongly depended on the temperature. Moreover, some divergences between the thermal contact resistance modelled by COMSOL and those recorded in the experimental setup might have contributed to this discrepancy.

In order to understand the reliability of the experimental setup, the experimentally and numerically obtained heat transfer coefficients were compared. The heat transfer coefficients were determined as follows, by removing the heat transferred by radiation and the thermal losses:

$$h_{flat} = \frac{Q_{in} - Q_r - Q_{loss}}{A_{flat} \cdot (T_{flat} - T_{amb})} \tag{15}$$

As shown in Figure 65, the heat transfer coefficients were found to increase with the power input. As expected, the increasing rate lowered at high power input: this was due to the contribution of the radiative heat transfer, which, at constant ambient temperature, increased with the forth power of the surface temperature. The COMSOL model consistently overestimated the heat transfer in downward facing conditions, with an average discrepancy of 6.07% and a maximum of 7.18%. In the upward facing conditions, the average difference dropped to 2.84%, with a maximum of 4.66%. All these discrepancies fell within the uncertainty expected for this experimental setup (8.25%) and could be considered as acceptable values for an experimental investigation on natural convection [328].
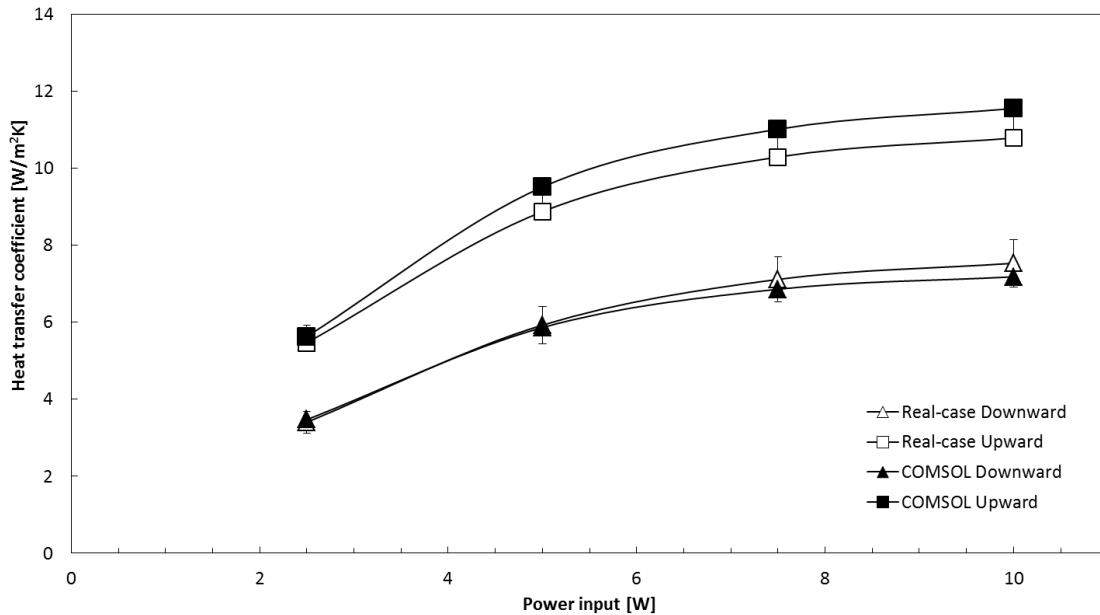
Figure 65 - Comparison between the COMSOL simulation outputs and the experimental real-case measurements

3.6.4.3   *Tilted fins*

The behaviour of the tilted setup was validated through both analytical and numerical processes. The measured heat transfer coefficients were compared with those obtained according to the natural convection correlations summarized in [324]. A wide range of tilt angles were considered: 0°, 30°, 50°, 60° and 90°. No correlations to predict the behaviour of a naturally-convective flat surface for angles of 70° and 80° had been found. The Rayleigh number (*Ra*), product of the two dimensionless Grashof and Prandtl numbers (respectively *Gr* and *Pr*), was calculated as:

$$Ra = Gr \cdot Pr = \frac{g \cdot \beta_{air} \cdot Pr \cdot \left(T_{flat} - T_{amb}\right) \cdot CL^3}{v_{air}^2} \tag{16}$$

The properties of air reported in [329] were used and they were considered for temperatures of $(T_s + T_{amb})/2$. CL was the characteristic length of the sample: for vertical and inclined surfaces it corresponded to L, whereas for horizontal surfaces it was equal to the ratio between the area and the perimeter.

Based on the equation proposed by [330], the Nusselt number (Nu) was obtained as [324]:

$$Nu = 0.68 + \frac{0.67 \cdot (Ra \cdot \cos\theta)^{0.25}}{[1+(0.492/Pr)^{0.5625}]^{0.4}} \text{ for } 0°\leq\theta\leq60° \tag{17}$$

$$Nu = 0.27 \cdot Ra^{0.25} \text{ for } \theta=90° \tag{18}$$

The heat transfer coefficient (h_{flat}) depended on the thermal conduction of air (k_{air}):

$$h_{flat} = Nu \cdot \frac{k_{air}}{CL} \tag{19}$$

Comparing the results of the numerical investigation and the outputs (Figure 66), an average discrepancy of 3.0% for all the experimented tilt angles was found at 10W power input, with a maximum difference of 6.8% at 0°. This divergence fell within the uncertainty range: the setup was considered as reliable for the planned experimental investigation.
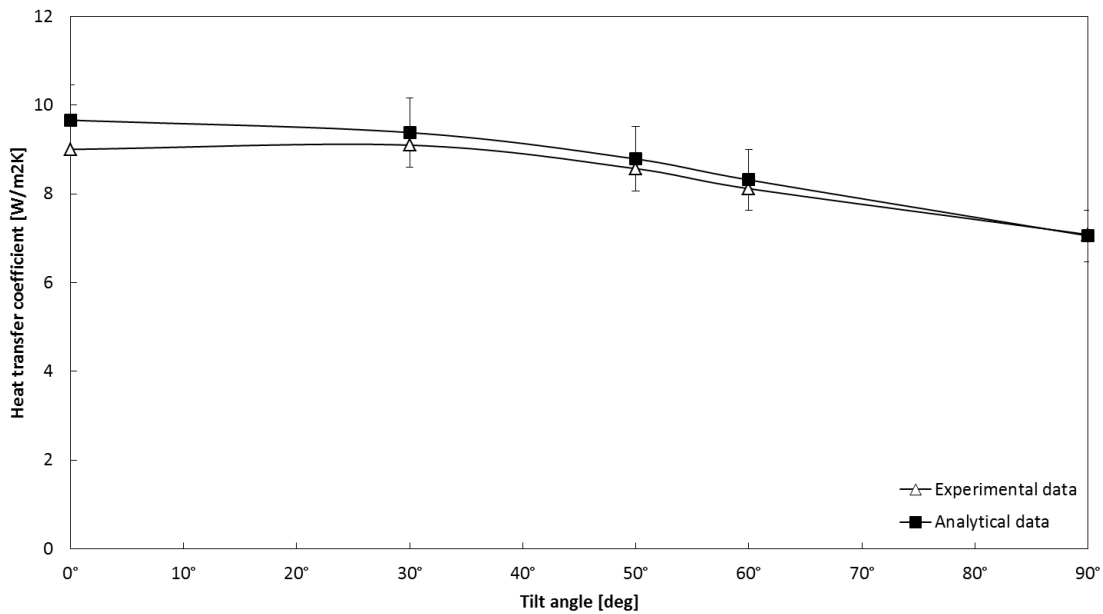
Figure 66 - Comparison of heat transfer coefficients for tilted flat surfaces, according to the experimental data and the analytical calculations. Power input: 10W.

Due to the some limitations in the thermal equations of the COMSOL model, the behaviour of the fins could be modelled at few representative tilt angles only: 0° (vertically oriented fins), 30°, and 90° (horizontally downward facing fins). In order to reproduce the heat transfer coefficients in the most accurate way, the orientation and the characteristic length of each surface were specified in COMSOL (Table 15).

Table 15 - Methods used for solving the Convective heat flux functions for the various surfaces at different tilt angles; in bracket the characteristic length is reported. The surface number refers to the nomenclature in Figure 67.

Tilt\Surface	(1)	(2)	(3)	(4)	(5)	(6)
0°	Vertical wall (5cm)	Vertical wall (8cm)	Vertical wall (1.5cm)	Horizontal plate, downside (0.6cm)	Vertical wall (8cm)	Vertical wall (8cm)
30°	Inclined wall (5cm)	Inclined wall (8cm)	Inclined wall (1.5cm)	Inclined wall (2cm)	Vertical wall (2cm)	Inclined wall (8cm)
90°	Horizontal plate, downside (0.125cm)	Horizontal plate, downside (0.6cm)	Horizontal plate, downside (0.6cm)	Vertical wall (2cm)	Vertical wall (2cm)	Horizontal plate, upside (0.2cm)
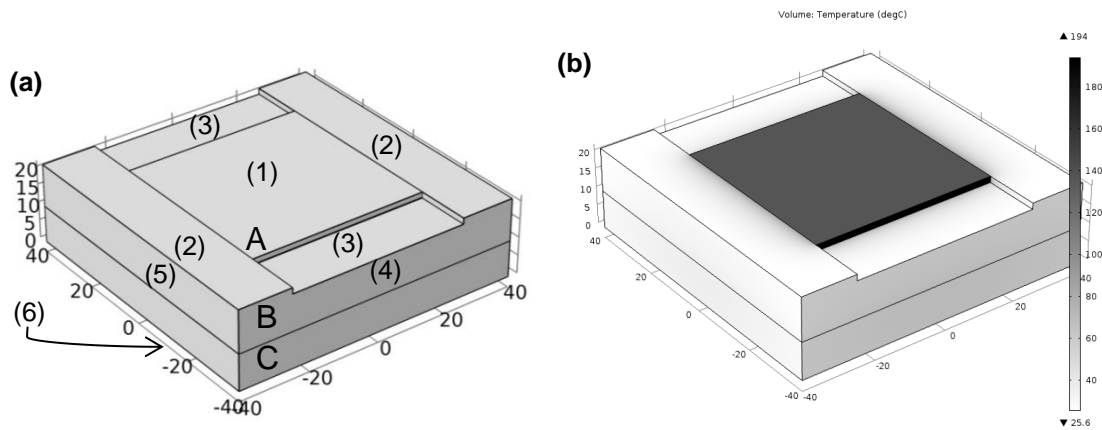
Figure 67 - (a) Geometry of the experimental setup reproduced in COMSOL: the sample (A), the fibre sheet case (B) and the polystyrene block (C). (b) The results of the simulation for θ=90°, Q_{input}=10W.

The COMSOL model underestimated the maximum temperature of the sample, with a maximum difference of 4°C compared to the IR camera measurements. These results were in line with those reported by [252] and obtained in the previously-considered conditions. Moreover, the thermal behaviour predicted by the model appeared similar to the experimental one. The deviations in heat transfer coefficient were found to vary from 0.08% to 6.63%, with an acceptable average of 2.38%. For these reasons, the experimental setup was considered reliable for the conducted investigations.

3.7 Conclusions

The different materials and components, along with the instruments and the calibration processes used in the present research work had been listed in this chapter. The solar cell and the solar assembly were purchased from AZUR

SPACE, a German company specialized in multijunction cells and CPV systems. The $1cm^2$-sized triple-junction cells considered for this application have a peak efficiency of 37.2% at 500× under standard testing conditions. A clear PDMS was used for encapsulation purposes and a silver-loaded epoxy was employed for bonding surfaces when soldering was not available. Both the materials were cured using a vacuum oven.

The characterization of the materials and the assemblies were conducted using the instruments of the solar laboratory. The spectrometer was used to measure the transmissivity and the reflectivity of different materials, such as the encapsulant and the silicon wafers. Two solar simulators were used for the indoor characterization of the cell assembly, whose performances were monitored through an I-V tracer and a sourcemeter. A photodiode was used to calibrate the light flux of the simulators. The thermal measurements were conducted using an infrared camera and K-type thermocouples, connected to a temperature recorder. Different software platforms were used: COMSOL Multiphysics was used for thermal modelling, whereas AutoCAD and DesignSpark PCB were employed for the design of the components.

Different-sized prototypes were manufactured during the work: the printed circuit boards were produced by chemical etching and the whole fabrication process has been described. The population of the boards has been detailed as well: the solder paste was dispensed through specially made paste masks and the components were manually picked-and-placed.

In section 3.6, the chapter reports the methodology followed for the experimental investigation on the micro-scaled heat transfer. The experimental apparatus has been described and the thermal losses were calculated using referenced procedures. A prediction of the uncertainty was reported as well: a maximum uncertainty of 8.25% was expected, in agreement with the previous studies. The whole experimental setup, whose structure was based on similar investigations presented in literature, had been validated through both analytical and numerical studies.

Chapter 4: **Thermal management of CPV receivers**

The largest part of the waste heat is removed from the cell through thermal conduction. For this reason, the substrates and all the materials composing the receivers have to be adequately selected to enhance heat transfer. This chapter describes the assumptions made and the simulations conducted to choose the most appropriate substrate for each application and to predict the thermal behaviour of the CPV receivers presented in this thesis. The densely packed and the single cell receivers have distinct geometries and, thus, need to be designed taking into account different priorities and solutions. The investigations presented in this chapter compare the thermal behaviours, the geometries and the costs of the potential receivers' designs, in order to understand the most adequate solution for each application.

4.1 Introduction

The CPV receivers are designed to maximize the extraction of electrical energy, to enhance the transfer of thermal energy and to assure adequate mechanical support. Several CPV receivers geometries have been already proposed [21,78,116,331,332]: the choice of the geometry and the selection of the materials depend on many factors, such as the concentration and the cost, as well as the thermal management. The structure of the receiver and the order of the materials in the stack are primary topics for heat dissipation, because most of the heat removed by the HCPV cells is transferred by thermal conduction [333]. So, the thermal behaviour of the receiver, which mainly depends on the employed substrate, is one of the major issues to take into account when designing a CPV device and, for this reason, is investigated in this chapter.

In this work two different receiver geometries were developed: an actively-cooled, densely packed receiver and a passively-cooled, single cell version. In this chapter an overview of the thermal conductivities of the CPV receivers layers is firstly reported, in order to highlight the strengths and the weaknesses to be addressed when designing it. This initial analytical investigation was essential to understand the priorities that needed to be taken into account to choose the most adequate

substrate. Secondly, three-dimensional models were developed to optimize the design of the receivers according to the different operating conditions. The geometries were reproduced and tested in COMSOL. The results of the simulations predicted the thermal behaviour of each substrate under the CPV operating conditions. The chapter ends with the description of the substrates chosen for the two different applications: the structure and the materials reported are then used in Chapters 5, 6 and 7 to design and develop the CPV systems.

4.2 Thermal conductivity of the receiver

It had already been demonstrated that the steady-state heat conduction in homogenous materials behaves analogously to steady-state electrical conduction [328]. Using this thermo-electrical analogy, the thermal behaviour of a CPV receiver could be described through a simple one-dimensional thermal model. In this approach, the difference in temperature between the cell and ambient corresponded to the driving potential for the heat flow, as the voltage was the driving potential for current [334]. The aim of any model was to represent a real case in the most appropriate way, but some approximations needed to be taken into account. This model assumed a uniform illumination on the cell and constant isotropic properties in any material. Moreover, each layer was assumed to have a constant temperature throughout its volume.

The present equivalent thermal circuit was developed in one dimension, perpendicularly to the widest surfaces of each layer. A traditional 1cm^2-sized triple junction cell (represented in Figure 68) was generally 190µm-thick. The three visible surfaces were named A, B and C: considering the heat to be generated at the centre of the cell's volume, it had to travel a distance 50 times shorter to reach A than needed to reach B or C. For this reason, the largest portion of the generated heat flew along the low-resistance path to A and the heat dissipation occurring on the thinnest surfaces could be neglected with only a small resultant error.
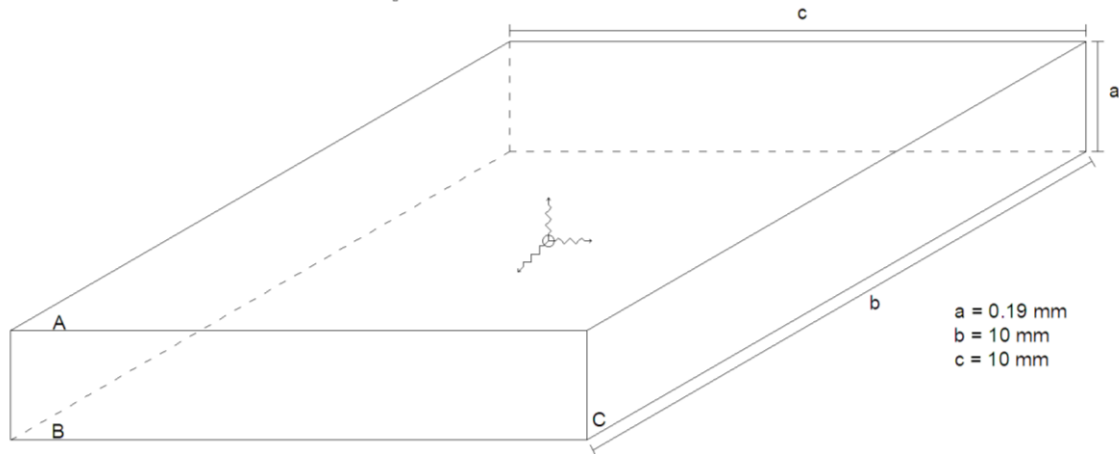
Figure 68 - Thermal circuit of a cell. The heat source is placed in the centre of the volume and heat can follow the three paths, long a/2, b/2 or c/2, to reach one of the three surfaces, respectively named A, B, C.

The equivalent thermal circuit for a general CPV assembly is shown in Figure 69. Since it is a one dimensional model, all the resistances are reported here per unit area and will be referred to as surface specific resistance (R*). It is important to highlight that neglecting the conduction on the other two dimensions and the thermal exchanges taking place in all the layers other than the coverglass and the heat sink is a limitative assumption. Despite this approximation, this approach, which had already been used in literature [65], helped to estimate the performance that the cooling system has to achieve.
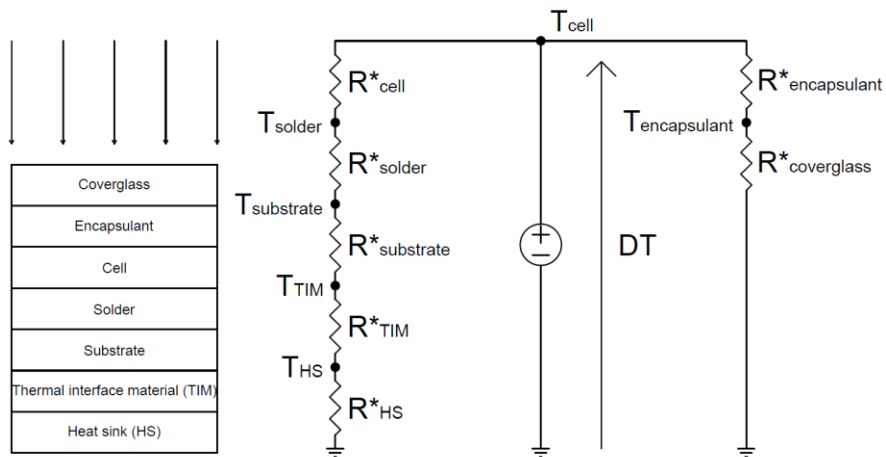
Figure 69 - One dimension equivalent thermal circuit.

Each layer of the assembly introduced a thermal resistance to the path between the cell and the environment, which respectively represented the source and the ground. The overall thermal resistance of the heat path (R^*_{HP}) was expressed as:

$$R_{HP}^* = \frac{T_{cell} - T_{amb}}{q_{cell}} \cdot A_{cell} \qquad\qquad (20)$$

where T_{cell} and T_{amb} are the cell's and the ambient temperatures, q_{cell} is the waste heat produced by the cell and A_{cell} corresponds to the cell's surface. Taking into account the 20W/cm^2 of waste heat produced by a 46%-efficient cell at 500×, a maximum cell's operating temperature of 100°C and an ambient temperature of 25°C, a cooling system with an overall resistance lower than 3.75·10^{-4}Km^2/W had to be designed. Whatever the concentration, the maximum cell's operating temperature was expected not to exceed 100°C under CSTCs: since the cell's efficiency was not linearly increasing with the concentration, higher concentrations required lower thermal resistances. In Figure 70, the maximum values of surface specific resistance were reported for concentrations up to 1500×, assuming a constant record cell efficiency of 46%. Any point below the line would let the cell work at a temperature lower than 100°C. In particular, at constant concentration, the further the point is from the line, the lower the temperature, and, then, the higher the cell's efficiency.
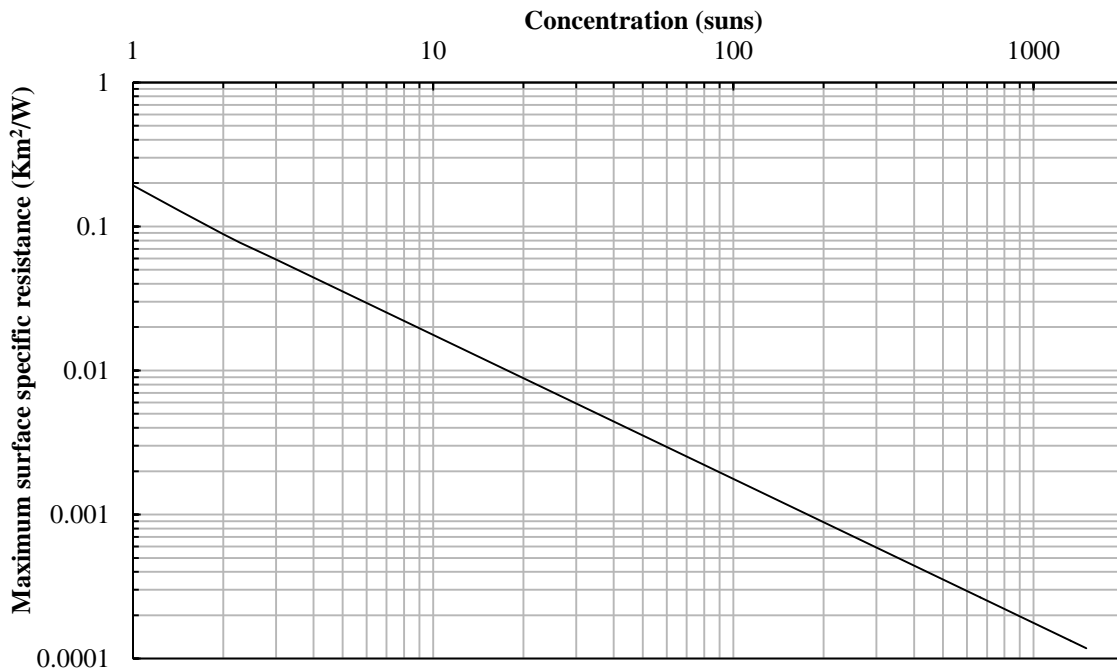
Figure 70 - Maximum surface specific thermal resistance per different concentrations

As shown in Figure 69, the heat was removed by the cell by conduction across the different layers of the receiver first and then dissipated in the ambient. There were

two main conductive directions that the heat can follow: moving from the cell to the heat sink, or moving up to the coverglass. Once at the bottom of the heat sink or at the top of the coverglass, the heat was transmitted to the environment through radiation and convection. In the present chapter, only an analysis of the conductive heat exchange, the main mechanism responsible for heat removal from the cell, was analysed. The radiative and convective heat exchanges were modelled here as dissipative heat fluxes only and have been further investigated in chapter 7.

The cover glass and the encapsulant are not usually required to perform high thermal conductivity: the thermal conductivity of a clear silicone encapsulant (0.27W/mK) is much lower than that of the substrate's materials. For this reason, the heat dissipated by these layers is limited and the present section only focuses on the layers placed below the cell (assuming the light hitting the cell from the top), where the largest amount of heat flows. Taking into account a cell assembly developed on a Cu-AlN-Cu direct bonded copper substrate [116], a more detailed model of the thermal transmission from the cell to the heat sink is reproduced in Figure 71. The assembly was considered to be attached to a flat 1.5mm-thick aluminium heat sink (HS) through a thermal interface material (TIM).
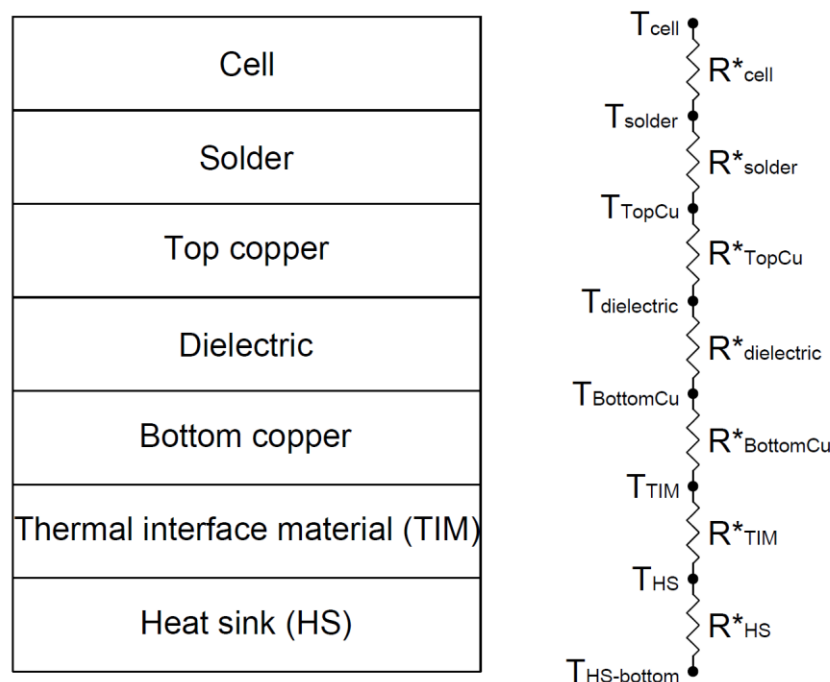
Figure 71 - One dimension equivalent thermal circuit of the layers below the cell.

The GaInP/GaAs/Ge cell was composed of multiple layers of different materials: a widely accepted procedure allows modelling it as a single block of germanium [335,336]. The same approach has been used in all the simulations presented in this thesis. The equivalent surface specific thermal resistance of the receiver ($R^*_{receiver}$) was calculated as the sum of the individual layer resistances.

$$R^*_{receiver} = R^*_{cell} + R^*_{solder} + R^*_{TopCu} + R^*_{dielectric} + R^*_{BottomCu} + R^*_{TIM} + R^*_{HS} \qquad \textbf{(21)}$$

where each resistance could be estimated through the thickness and the thermal conductivity of each layer (Table 16). An overall thermal resistance of $3.35 \cdot 10^{-5} Km^2/W$ was calculated for the considered receiver.

Table 16 - Materials considered in the model of the receiver

Layer	Material	Thickness [mm]	Thermal conductivity at 25°C [W/mK]	Surface specific resistance [K·m²/W]	Ref
Cell	Germanium	0.190	60	$3.167 \cdot 10^{-6}$	[337]
Solder paste	Sn–Ag–Cu	0.125	78	$1.602 \cdot 10^{-6}$	[338]
Substrate	Top Copper	0.3	400	$7.500 \cdot 10^{-7}$	[337]
	Aluminium Nitride	0.63	285	$2.210 \cdot 10^{-6}$	[337]
	Bottom Copper	0.3	400	$7.500 \cdot 10^{-7}$	[337]
Thermal interface material (TIM)	Epo-tek	0.050	2.83	$1.767 \cdot 10^{-5}$	
Heat Sink	Aluminium	1.5	160	$9.375 \cdot 10^{-6}$	[337]
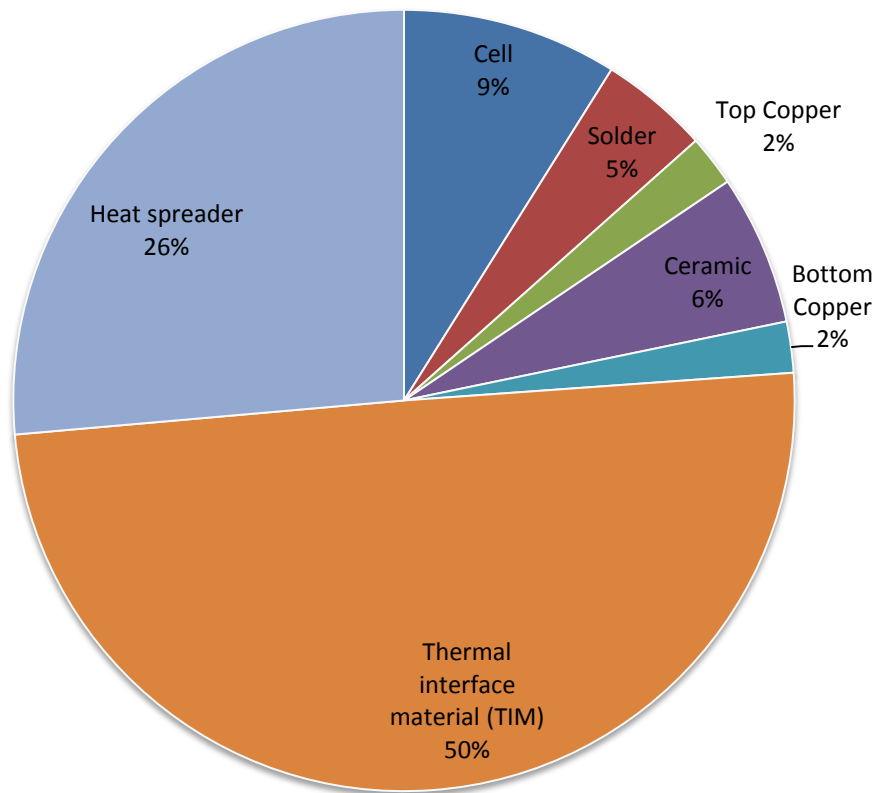
Figure 72 - Breakdown of the layers' surface specific thermal resistances

Figure 72 shows the contribution of each layer to the thermal resistance of the considered receiver. The thermal interface material placed between the substrate and the heat spreader was the largest challenge for heat dissipation, representing, despite the limited thickness, 50% of the overall thermal resistance. This issue

could not be neglected, especially when a passive cooling system was designed. For this reason, two different approaches were chosen for the two receivers to be designed.

The densely packed receiver was coupled to a water-based, active cooling system [339], which was designed by a research team of the Indian Institute of Technology Madras in Chennai (India) to recover the waste heat produced by the 144 solar cells. The employment of an active cooling system limited the concerns related to the thermal behaviour of the receiver. Moreover, the large dimensions of the board made it essential to give the same consideration to the electrical and thermal performance as well as to the cost of the whole CPV system. On the other hand, the single-cell receiver was conceived to be applied in natural convective conditions. In this case, the thermal behaviour of the receiver was the key factor for the system's reliability and it was prioritised over the costs. In order to limit the thermal resistance of the receiver, the passive system was integrated in it, in order to avoid the employment of a thermal interface material. In this chapter, the thermal model used in this chapter is described and the results of the simulations are reported and commented upon.

4.3 The thermal model: equations and conditions

The following simulations were conducted taking into account the CSTCs: a $1000W/m^2$ DNI and an ambient temperature of 25°C. The cell was modelled as a heat source: considering the AZUR SPACE 3C40C cell's peak-efficiency of 37.2% at 500× and an optical efficiency of 85%, an overall heat production of $26.7W/cm^2$ was predicted. When the worst case conditions were taken into account, the cell's efficiency was considered to fall to 0%: the heat production then rose to $42.5W/cm^2$ and a maximum cell's temperature of 150°C was accepted.

4.3.1 Governing equations and boundary conditions

The simulation was developed using the COMSOL's "Heat Transfer in Solids" module. The equations used in the simulation are reported below.

The stationary pure conductive heat transfer equation was used to model the heat exchange between solids. The heat flux depended on the conductivity of the

material (k) and on the temperature gradient between the opposite surfaces (∇T). The conduction heat flux vector (**q**) was written as [334]:

$$\boldsymbol{q} = -k \cdot \boldsymbol{\nabla}\mathrm{T} \tag{22}$$

The heat transfer in solids was expressed through the Fourier's law [334,340]:

$$\rho_D \cdot c_p \cdot \frac{\partial T}{\partial t} = Q'_v + k \cdot \boldsymbol{\nabla}^2 \mathrm{T} \tag{23}$$

where ρ_D is the density, c_p the specific heat capacity, t the time, and Q'_v the volumetric rate of heat generated. ∇^2 is the Laplace operator and k·∇^2T expresses the heat flux in the three dimensions of an isotropic medium [341]. In Cartesian coordinates it is reported in the following form:

$$\boldsymbol{\nabla}^2\mathrm{T} = \frac{\partial^2 T}{\partial x^2} + \frac{\partial^2 T}{\partial y^2} + \frac{\partial^2 T}{\partial z^2} \tag{24}$$

In this case, the steady-state temperature was not dependent on time and, then, ∂T/∂t=0. So the equation (23) reduced to the Poisson equation [334]:

$$Q'_v = -k \cdot \boldsymbol{\nabla}^2\mathrm{T} \tag{25}$$

Taking into consideration the number of cells on the plate (N_{cell}) and the volume of each cell (V_{cell}), the heat produced by all the cells of the receiver (Q) was expressed as:

$$Q = Q'_v \cdot V_{cell} \cdot N_{cell} \tag{26}$$

Some boundary conditions were set. All the media-facing surfaces were thermally insulated (27), with the exception of the backside of the prototype. A convective heat flux was introduced on the back surface of the heat sink to model the action of the cooling system or of the natural convection. The equation (28), based on the Newton's law of cooling [341], explains how this condition was modelled, taking into account the difference between in temperature between the surrounding media and the surfaces of the board (T_{amb} and T_s respectively), and requiring in input the value of the heat transfer coefficient (h). This parameter describes the thermal properties of the convective exchange between a surface and the surrounding media and is influenced by different conditions such as the geometry of the surface, and the properties and the motion of the fluid [329]. The solder paste and

the thermal interface materials were modelled as thin thermally resistive layers. The heat fluxes across these layers are described in (29) and (30), where the *u* and *d* subscripts refer respectively to the upside and the downside of the layer. For thermally resistive layers, only the thermal conductivity (k_{trl}) and the thickness (t_{trl}) were required in input.

$$q = 0 \tag{27}$$

$$q = h \cdot (T_s - T_{amb}) \tag{28}$$

$$q_u = -k_u \cdot \nabla T_u = -k_{trl} \cdot (T_u - T_d)/t_{trl} \tag{29}$$

$$q_d = -k_d \cdot \nabla T_d = -k_{trl} \cdot (T_d - T_u)/t_{trl} \tag{30}$$

The "Joule Heating" interface was used to model the heating effects of the resistive losses. This feature was based on a modified version of the heat equation at the steady state (26). In this case, the definition of Q was improved to add the contributions due to the electromagnetic losses taking place in each i-cross section of the semiconductor ($Q_{J,i}$) as boundary heat sources in the heat transfer computation:

$$Q = Q'_v \cdot V_{cell} \cdot N_{cell} + \sum_i Q_{J,i} \tag{31}$$

The expression of Q_J derives from the Ohm's law [342] and was written as:

$$Q_J = I^2 \cdot R_{el} \tag{32}$$

where R_{el} is the resistance of the conductor. Considering the length (l) and the cross-sectional area (A) of the conductor, as well as the electrical conductivity of the material (σ_{el}) it is made of, the resistance was expressed as:

$$R_{el} = \frac{l}{\sigma_{el} \cdot A} \tag{33}$$

All the surfaces facing the air and the dielectric were considered electrically insulated:

$$-n \cdot J = 0 \tag{34}$$

where J represents the magnitude of current density across the conductor, expressed as:

$$J = I/A \tag{35}$$

4.3.2 Receiver geometry and materials

In the first approach, a single cell geometry was reproduced in the software environment (Figure 73): the solar cell (CC) was placed onto the copper layer (CuL), which was accommodated onto a 21mm×21mm heat sink through a dielectric layer. The interconnectors (IC) were modelled as 0.025mm-thick silver tabs. The diode (Ds) was not considered in these thermal investigations, due to the small current flowing through it when the system was in operation. In this investigation, the copper pattern was inspired by the design of the commercial AZUR SPACE assembly, and the densely packed design was obtained by repeating the conductive patterns on the large aluminum board.
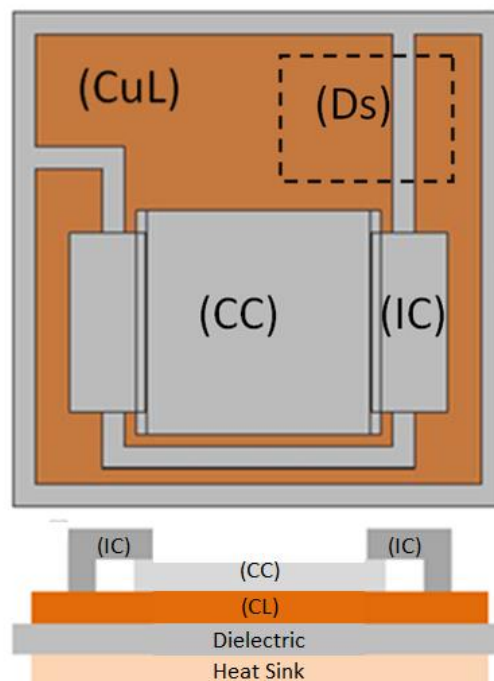
Figure 73 - Front view and cross section of the single cell receiver developed in COMSOL.

The simulations were conducted to predict the steady-state thermal behaviour of the receiver. Depending on the application, different substrates were considered: a printed circuit board (PCB), a direct bonded copper (DBC), an insulated metal substrate (IMS) or a silicon wafer. The thicknesses of the layers were established on the basis of the commercially available products or references and are reported in Table 17.

Table 17 - Thicknesses and materials for the modelled substrates

Layer	PCB	DBC	IMS	Si wafer
Interconnectors	0.025mm Ag	0.025mm Ag	0.025mm Ag	0.025mm Ag
Cell	0.190mm Ge	0.190mm Ge	0.190mm Ge	0.190mm Ge
Solder paste	0.125mm solder	0.125mm solder	0.125mm solder	0.125mm solder
Conductive layer	0.035mm Cu	0.30mm Cu	0.035mm Cu	0.001mm Cu
Dielectric	4.5µm marble resin	0.63mm AlN	4.5µm marble resin	0.001mm Si_3N_4
Heat sink	1.6mm FR-4	0.30 mm Cu	1.6mm Al	0.55 mm Si
Ref.	[337]	[116]	[337]	[84]

The COMSOL's "Heat transfer" module, used in this simulation, required three proprieties for each material: the thermal conductivity, the density, and the heat capacity at constant pressure. Wherever available, the COMSOL built-in materials were used, such as copper and aluminum. In other cases, the values were set according to external references (Table 18).

Table 18 - Proprieties of materials (Materials marked with * are COMSOL built-in materials)

Materials	Thermal conductivity [W/Km]	Density [kg/m³]	Heat Capacity [J/kgK]
Aluminum Nitride	285	3260	740
Aluminum*	160	2700	900
Copper*	400	8700	385
FR-4	1.7	1850	600
Germanium	60	5323	320
Silicon*	130	2329	700

The solder pastes used in all the substrates and the marble resin, which acted as a dielectric in the considered PCBs and IMSs, were modelled as thin thermally resistive layers: for this function, COMSOL required in input the thickness and the thermal conductivity only (Table 19).

Table 19 - Conductivity and thickness of the thermally resistive layers

Materials	Thermal conductivity [W/Km]	Thickness [mm]
Marble resin	3.0	0.0045
Solder paste	4.5	0.1250

The Joule heating calculations required in input the electrical conductivity of the materials where the current was flowing, such as the cells and the conductive layer. The resistive heating happening in the soldering layer was not considered. The parameters used in the simulation are shown in Table 20.

Table 20 - Electrical parameters employed for the investigation on the Joule losses (Materials marked with * are COMSOL built-in materials)

Materials	Electrical conductivity [S/m]
Copper*	$5.997 \cdot 10^7$
Germanium	$2.000 \cdot 10^4$

The following pictures show the temperature distribution and the isothermal contours: the scale gradually ranges from red, for high temperatures, to blue, for lower temperatures. The 3D rendering of the simulations are generally shown from either one or two views: a front view of the top surface and a lateral 3D view. All the temperatures are in °C.

4.4 Actively-cooled, densely packed cell assembly

The present investigation was conducted in COMSOL 4.3. Firstly, a single cell model was developed to compare the performance of the potential substrates. Because of its cost and fragility, the silicon wafer was not considered a suitable substrate in this large application. So, the investigation was limited to three substrates: PCB, IMS and DBC. Secondly, after an analysis of the costs and of the manufacturability, a full scaled 144-cell model was developed and the assembly was tested under different conditions: concentrator standard test, worst case, and non-uniform irradiance conditions. The effect of the Joule losses was also analysed.

In order to reproduce the action of the active water-based cooler, a uniform convective heat flux was introduced on the back of the heat sink. An initial heat transfer coefficient of $10^4 W/m^2 K$ was considered, because it had been reported as the minimum value required for densely-packed systems operating over 150 suns [65].

COMSOL measured the temperature distribution across the 144 cells modelled on the board. The temperatures were recorded at the middle of the active area of the cells. Due to the slightly asymmetrical design (described in chapter 5), out of 144 cells, the four cells on the corners and the four cells at the centre of the plate were found to have, respectively, the lowest and the highest temperatures in any simulation. For this reason, the model was implemented to automatically sort out

the maximum and the minimum temperatures of these cells: these are the values presented in the captions. In the figures, instead, the temperature distribution across both the cells and the substrates are shown: the substrate was found to work at lower temperatures than the cell and, so, the pictures depict a wider range of temperatures than that experienced by the cells alone.

4.4.1 The CPV system's geometry

The densely packed receiver was designed as part of the BioCPV project [343]. The objective of the project was to develop and to integrate highly efficient solar, biomass and hydrogen energy technologies to produce non-interrupting power supplies to the rural communities. The presented cell assembly was part of eight 500× CPV units designed for this project. The geometry of the CPV system, shown in Figure 74, was agreed with the project's partner, the Indian Institute of Technology Madras (India), whose team was in charge of the design and the development of optics, cooling system and tracker, as well as the inverter and the power electronics for current transmission.
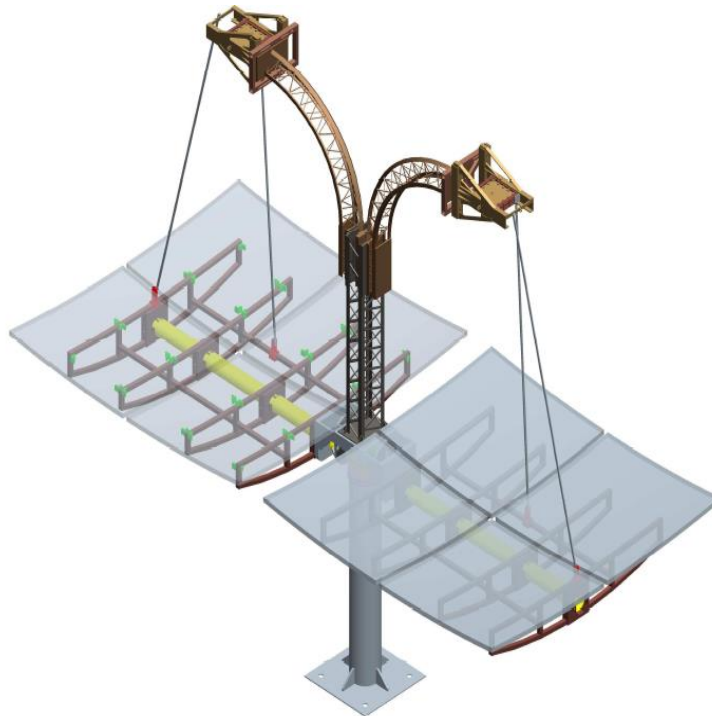
Figure 74 - The 3D rendering of the CPV system. Courtesy of the Indian Institute of Technology Madras.

Each CPV unit had two modules made of a primary concentrator and a receiver each (Figure 75). The receiver consisted of the 144-cell assembly presented in this thesis, a 4× secondary concentrator and an active cooling system. The primary 125× and the secondary 4× optics resulted in an overall geometric concentration of 500×: a summary of the concentrator specifications is reported in Table 21.
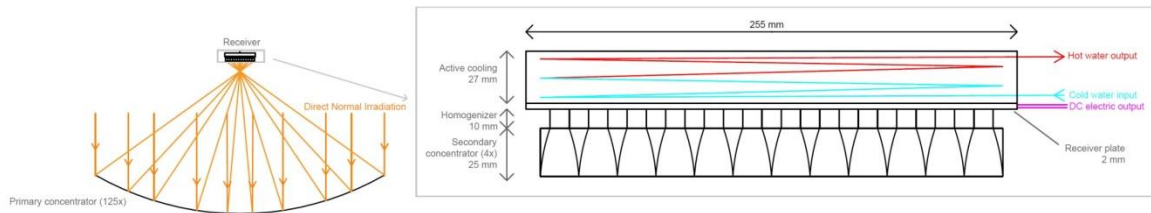
Figure 75 - Schematic of the system configuration and particular of the receiver.

Table 21 - Concentrator specifications

Primary concentrator		Secondary concentrator	
Geometric Concentration Ratio	125×	Geometric Concentration Ratio	4×
Aperture area	3m × 3m	Cell side aperture area	10mm × 10mm
Rim angle	20°	Acceptance angle	30°
Focal length (*f*)	3.37m	Length of CPC	25mm
f/d ratio	0.794	Length of homogenizer	10mm

The 125× primary concentrator was a parabolic dish with a square opening and was made up of four sections to achieve an entry aperture area of $9m^2$. The secondary concentrator was made of 144, three-dimensional, 25mm-high compound parabolic concentrators (CPCs) with a squared 2cm×2cm entrance aperture and a square 1cm×1cm exit aperture. The CPCs were arranged in a 12×12 array and each CPC reflected the light on a single solar cell. A 10mm length homogenizer was placed at the exit of each CPC to uniformly illuminate each cell. In Figure 76, the cross-sectional views of a 12-CPC array and of a single CPC are presented. Due to the geometry of the secondary concentrators, the 144 cells on the boards were allocated in 12 rows and 12 columns. The CPCs had an entry aperture of 2cm×2cm and the side walls of the concentrators were 1mm-thick: for this reason, a distance of 1.1cm was fixed between each couple of adjacent $1cm^2$-sized cells.
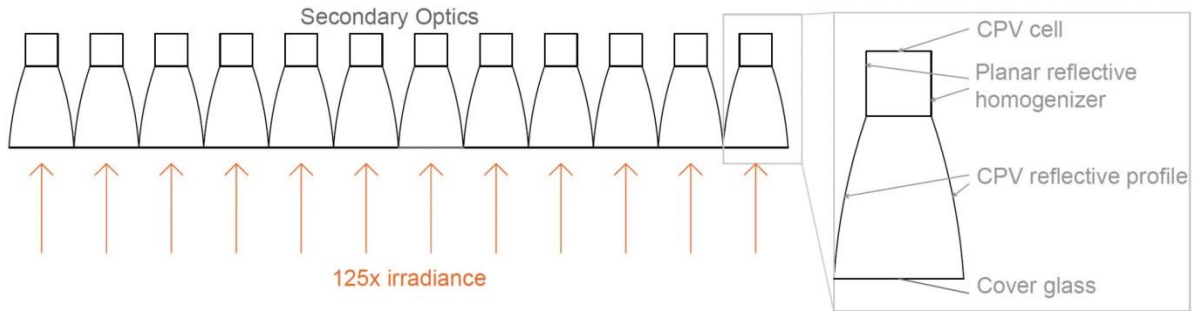
Figure 76 - Cross sectional view of the secondary optics

A continuous tracking system allowed moving the assembly in order to follow the Sun and to let the cells work at their maximum power point. An active cooling system was developed to control the temperature of each receiver of the plant.

4.4.2 Single cell model

The aim of this preliminary single cell simulation was to investigate the thermal behaviour of the potential substrates. The model was developed in stationary mode and was set to stop the simulation when converging within a relative tolerance of 10^{-3}. A heat production of 26.7W/cm^2 and a cooling flux of 10^4W/m^{2}K on the back of the cell were considered. The results are reported in the pictures below (Figure 77, Figure 78, and Figure 79).
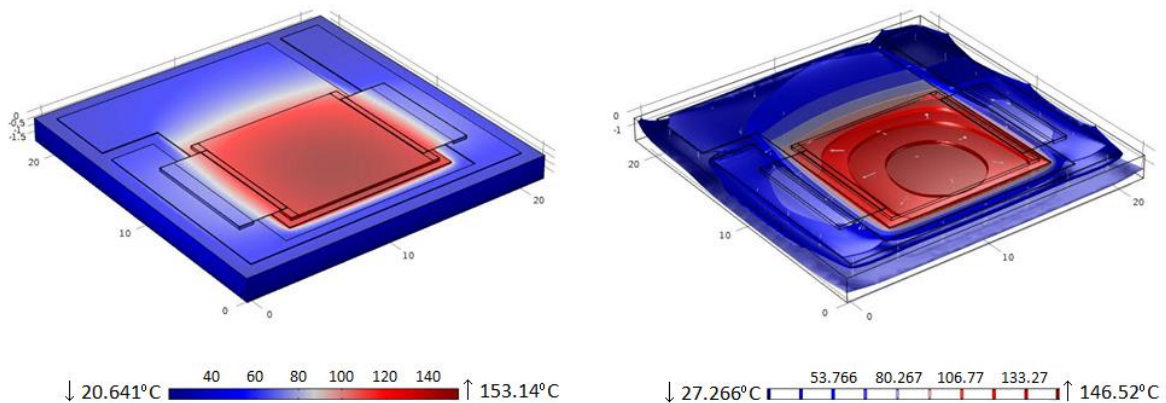
Figure 77 - Temperature distribution (a) and isothermal contours (b) in the PCB based assembly, in °C. Max cell's temperature: 153.14°C.

↓ 22.845°C 24 26 28 30 ↑ 31.573°C   ↓ 23.281°C 25.027 26.772 28.518 30.264 ↑ 31.136°C
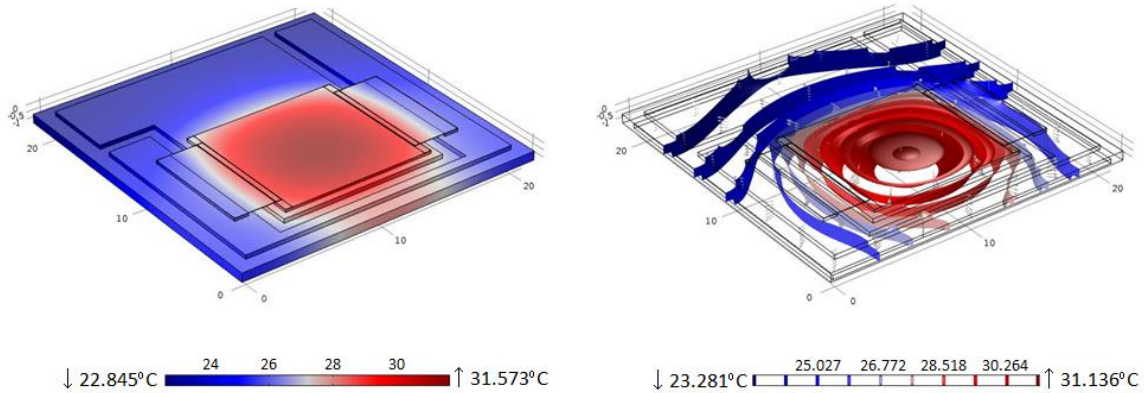
Figure 78 - Temperature distribution (a) and isothermal contours (b) in the DBC based assembly, in °C. Max cell's temperature: 31.573°C.

↓ 22.261°C 24 26 28 30 32 ↑ 33.323°C   ↓ 22.81°C 25.004 27.198 29.392 31.586 ↑ 32.684°C
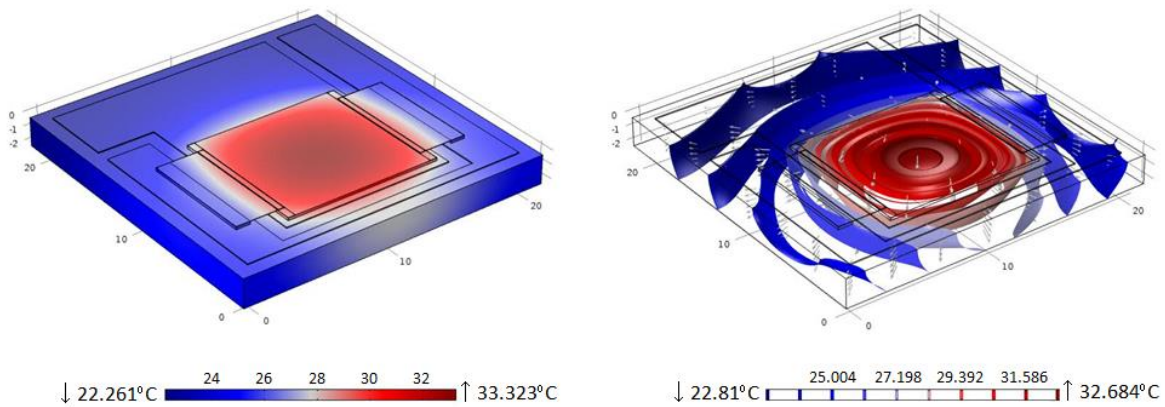
Figure 79 - Temperature distribution (a) and isothermal contours (b) in the IMS based assembly, in °C. Max cell's temperature: 33.232°C.

As expected, the PCB based assembly was the worst performing (Figure 77). In the considered conditions, it reached a maximum cell's temperature of 153.14°C, above the acceptable CPV range and more than 100 degrees higher than those recorded for the DBC and IMS assemblies (Figure 78 and Figure 79 respectively). The flat profile of the isothermal contours in Figure 77 clearly showed the difficulty for heat to move from the cells through the PCB: the heat was concentrated in the cell and was not effectively transferred to the bottom of the substrate. For this reasons, a PCB was considered as a reliable substrate for high CPV applications, even in presence of a well-performing active cooling system. The performances of the DBC and the IMS assemblies were instead similar and acceptable: both the substrates showed cell's temperatures lower than 40°C. These values were below the usual CPV operating temperature range and indicated an over-sized cooling system. In order to predict the thermal behaviour of these substrates in more

realistic conditions, the performance of the cooling system was lowered: the heat transfer coefficient was reduced to 1250W/m^{2}K.
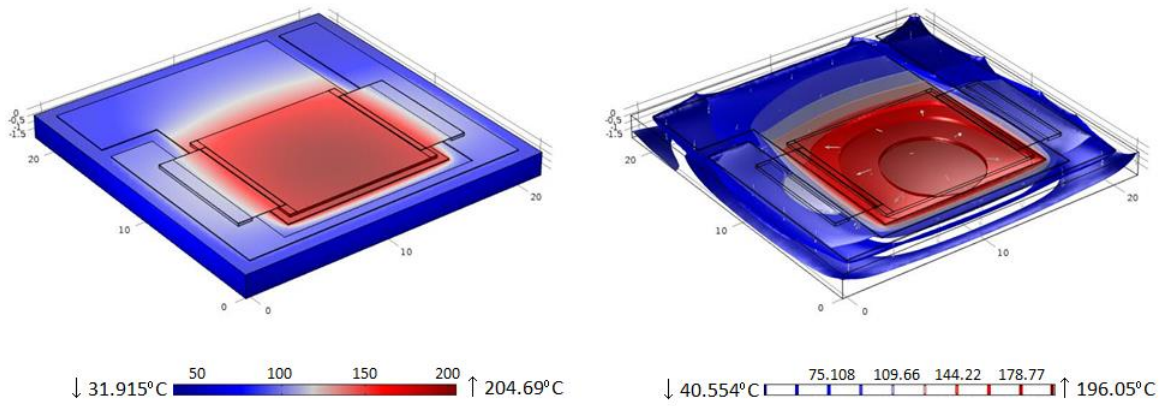
Figure 80 - Temperature distribution (a) and isothermal contours (b) in the PCB based assembly, in °C. Max cell's temperature: 204.7°C.
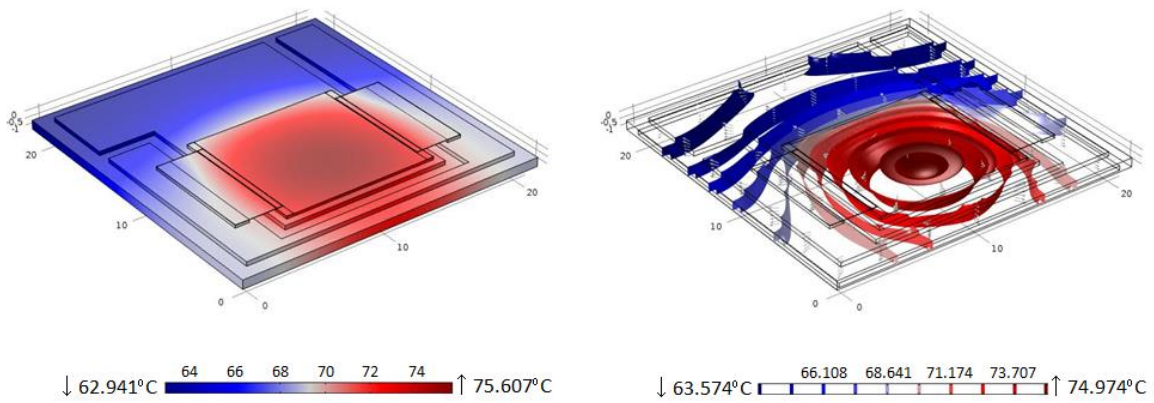
Figure 81 - Temperature distribution (a) and isothermal contours (b) in the DBC based assembly, in °C. Max cell's temperature: 75.6°C.
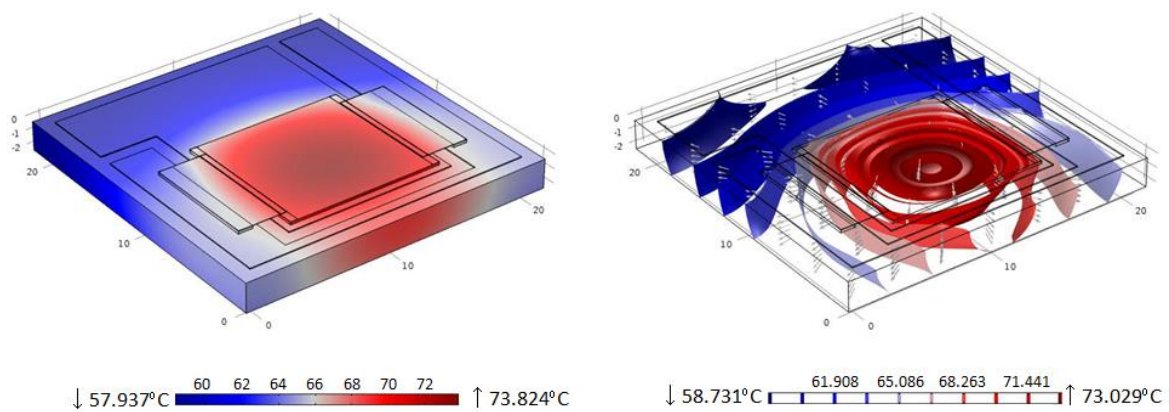
Figure 82 - Temperature distribution (a) and isothermal contours (b) in the IMS based assembly, in °C. Max cell's temperature: 73.8°C.

This second investigation confirmed that DBC and IMS behaved similarly in terms of heat removal, even in presence of a less performing cooler, with peak temperatures of 75.6°C and 73.8°C respectively. So, both the substrates had the potential to be applied to the designed CPV system.

4.4.3 Cost analysis and manufacturing restrictions

In the first design, the full scale receiver was planned to have a size of 26.2cm×25.5cm, because it would have allocated 144 multijunction cells, 1cm^2-sized and placed at a 1.1cm distance from each other. Moreover, some space had to be added for allocating the terminal tabs used for the current extraction and some tolerances on the edges needed to be considered as well. Different suppliers were contacted to fabricate the required substrates and a resume of the most competitive solutions sorted out in the survey is shown in Table 22.

Table 22 - Specifications of the DBC and the IMS

Specifications	DBC	IMS
Front dimensions	13cm×13cm	26.2cm×25.5cm
Layers	0.127mm Cu - 0.63mm AlN - 0.127mm Cu	0.070mm Cu - 0.0045mm resin - 2.003mm Al
Cost	£409	£330

It was not possible to find a supplier able to produce a 26.2cm×26.2cm DBC. The proposed solution consisted of producing four 13cm×13cm boards, at a cost of £409 each, to be later assembled in one receiver. Interconnecting four substrates to make one assembly would have increased the risk of failures and made the structure of the receiver more complex and fragile. On the other hand, the production of a large IMS was found to be easier and more cost-competitive: the cost of one 26.2cm×26.2cm IMS was £330, significantly lower than that of DBC. Moreover, the aluminum base of the IMS could be easily attached to the cooling system, typically made of aluminum too. For these reasons, the IMS substrate was preferred in this application.

4.4.4 The Joule effects: a 16-cell assembly model

A first densely packed investigation was conducted to understand the thermal response of the assembly and to study the effects of the Joule losses on the

thermal management [337]. A 16-cell IMS-based assembly was modelled on a 10cm×10cm board: the results of the simulation conducted under CSTCs are shown in Figure 83. Forcing the cell's short circuit current across the electrical circuit (Figure 84), the effect of the Joule losses on the maximum temperature was found to be negligible in terms of maximum temperature increasing. For this reasons, the Joule losses was not further considered for the following thermal simulations.
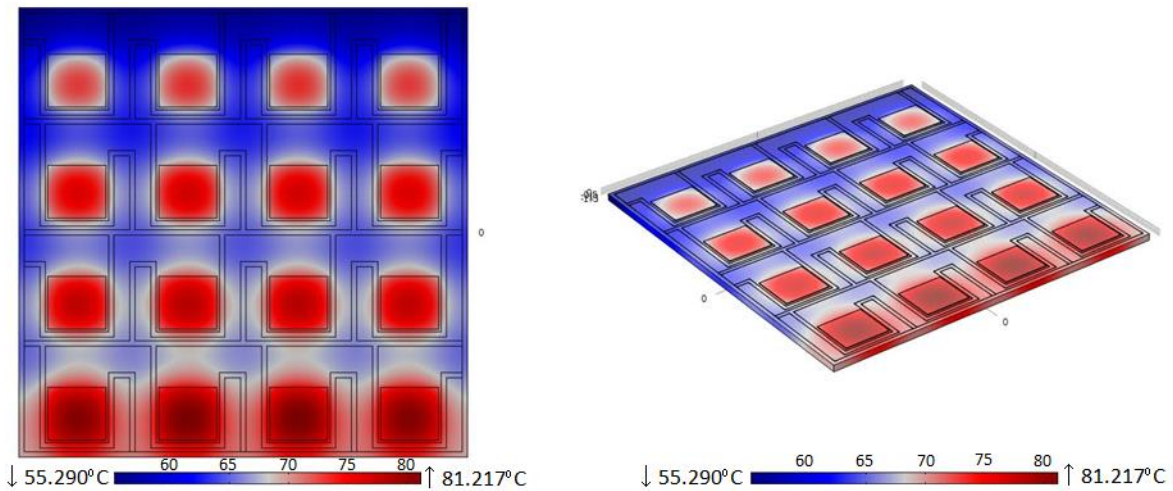
Figure 83 - Temperature distribution on a 16-cell IMS based assembly, in °C. Max cell's temperature: 81.2°C.
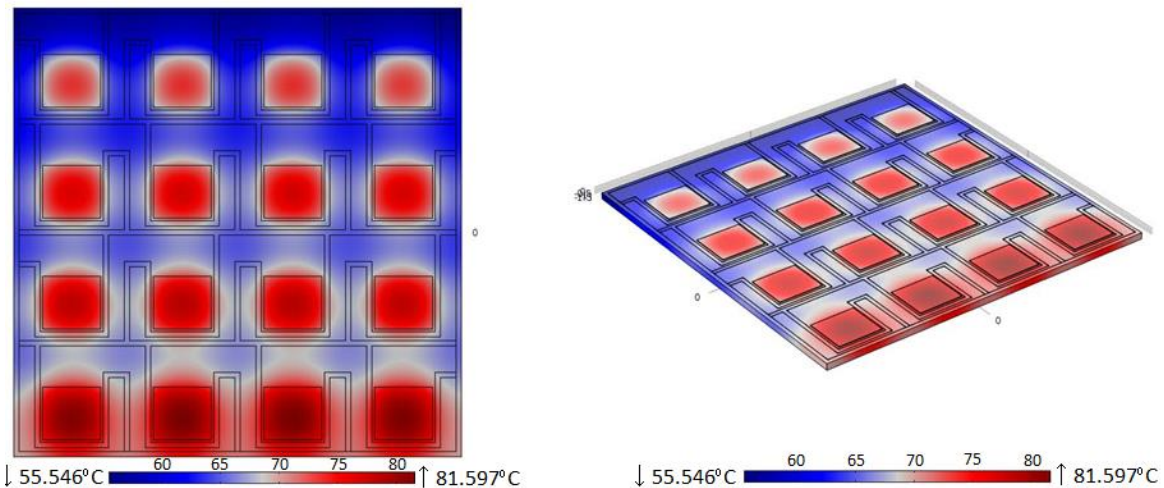
Figure 84 - Temperature distribution on a 16-cell IMS based assembly after the Joule losses have been considered, in °C. Max cell's temperature: 81.5°C.

4.4.5 Full scale model

In order to further test the thermal performance of the board, a full scale simulation was developed. The simulation demonstrated the thermal response of the assembly and its ability to remove the waste heat even in a densely packed configuration. The results are shown in Figure 85 and Figure 86: the first image reports the distribution of the temperature across the plate and the second presents the temperature contours. The final maximum temperature was similar to that reached in the single cell simulation: 76.5°C. This meant that the large IMS could perform well when coupled to an appropriate cooling system: the plate was able to remove the heat from the cells to let the system work at steady state in a suitable operating temperature range. A maximum difference of temperature of 14°C was registered among the cells installed in the assembly: the minimum temperature, achieved by the cells on the edge, was due to the 1cm room left on one side of the board to allocate the tabs for current extraction. Unfortunately, it was not possible to reduce that space and, on the other hand, adding the same room in the other edges would have increased the temperature gradient, the materials employed and therefore the costs, without any positive effect on the system's performance. As agreed with the Indian Institute of Technology Madras (IITM) team, the cooling system would have been designed to take care of this issue.
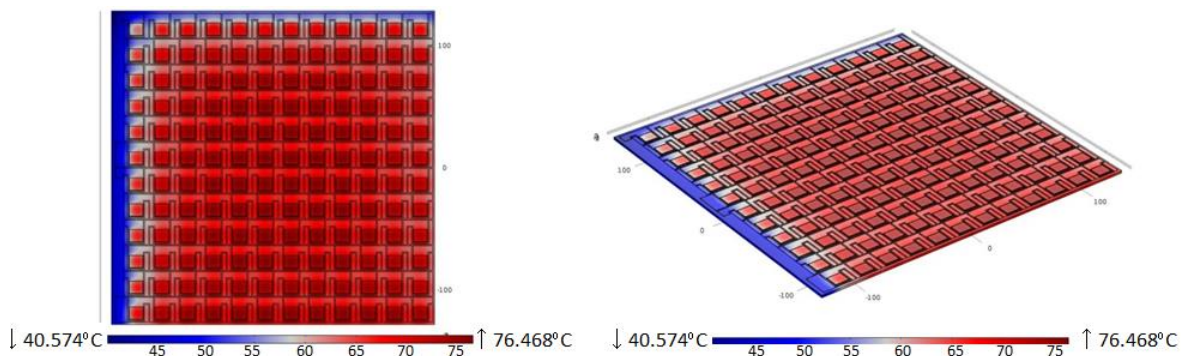
Figure 85 - Temperature distribution of the full scaled board, in °C. Max cell's temperature: 76.5°C. Min cell's temperature: 62.5°C.
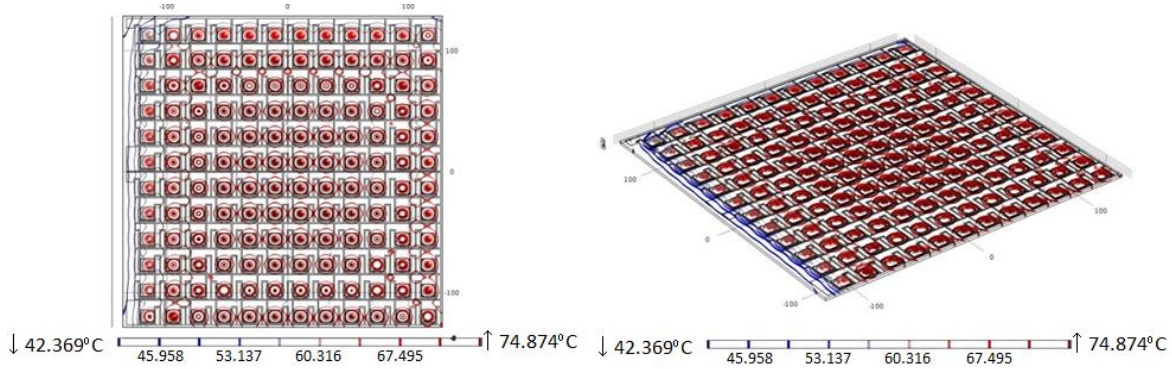
Figure 86 - Isothermal contours in the assembly of the full scaled board, in °C.

In order to predict the behaviour of the system under a wider range of conditions, the system was then tested under the worst case conditions, when all the concentrated sunlight was converted into heat. As shown in Figure 91 and Figure 92, the insulated metal substrate was able to successfully handle the large amount of heat: the cell's temperature was expected not to overtake the maximum limit of 150°C.
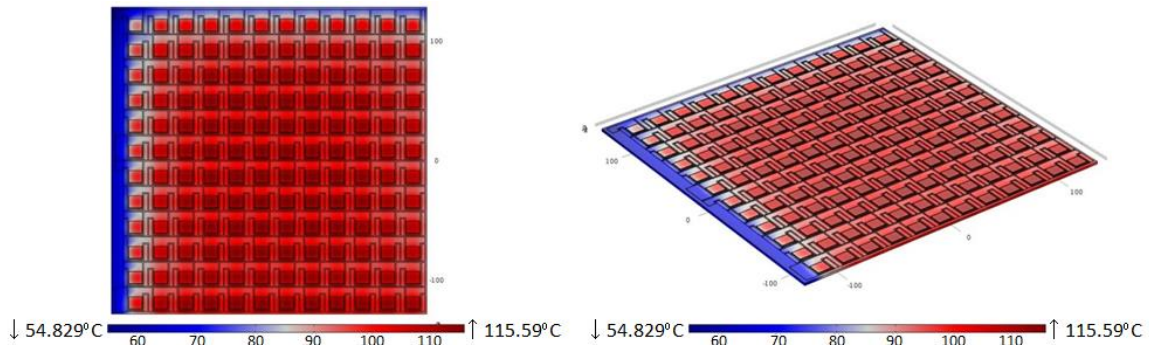
Figure 87 - **Temperature distribution of the full scaled board in the worst case conditions, in °C. Max cell's temperature: 115.6°C. Min cell's temperature: 91.9°C.**
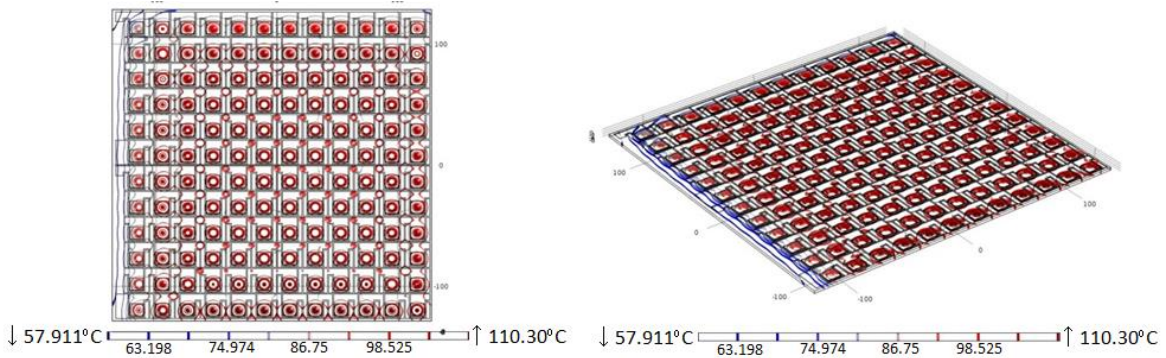
Figure 88 - Isothermal contours of the full scaled board in the worst case conditions, in °C.

4.4.6 The effects of non-uniform light distribution

The efficiency of a densely packed system strongly depended on the uniformity of irradiance. In case of non-homogenous illumination, the illumination was not homogenous, the cells would have worked at different concentrations and, thus, at different efficiencies. Moreover, because of the dissimilar efficiencies and concentrations, each cell would have been expected to generate different currents and waste heat amounts. The dissimilar heat produced by each cell would have negatively affected the efficiency itself as well. So, the most uniform irradiance profile had to be achieved in any CPV system. In the real scenarios, the irradiance profile generally followed a Gaussian distribution [344], with a peak intensity for the cells in the centre of the receiver. At the time the thesis was concluded, no predictions of the sunlight distribution were available for the CPV system in development. Despite that, it was considered essential to carry out a preliminary investigation to check the thermal behaviour of the receiver in these conditions too.

In the absence of modelled and experimental data, the non-uniform irradiance was reproduced according to a standard normal distribution (standard deviation, $\sigma_G=1$; mean, $\mu_G=0$). The average unconcentrated irradiance across the cells was kept equal to $1000W/m^2$, with a maximum and a minimum of $1366W/m^2$ and $966W/m^2$ respectively (Figure 89 and Figure 90).
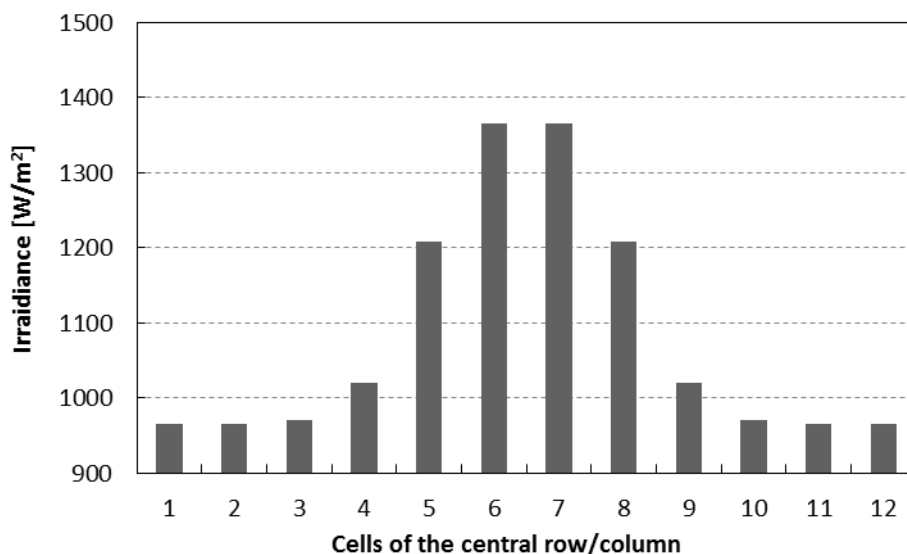
Figure 89 - Section of the irradiance distribution across one of the central rows/columns of the assembly.
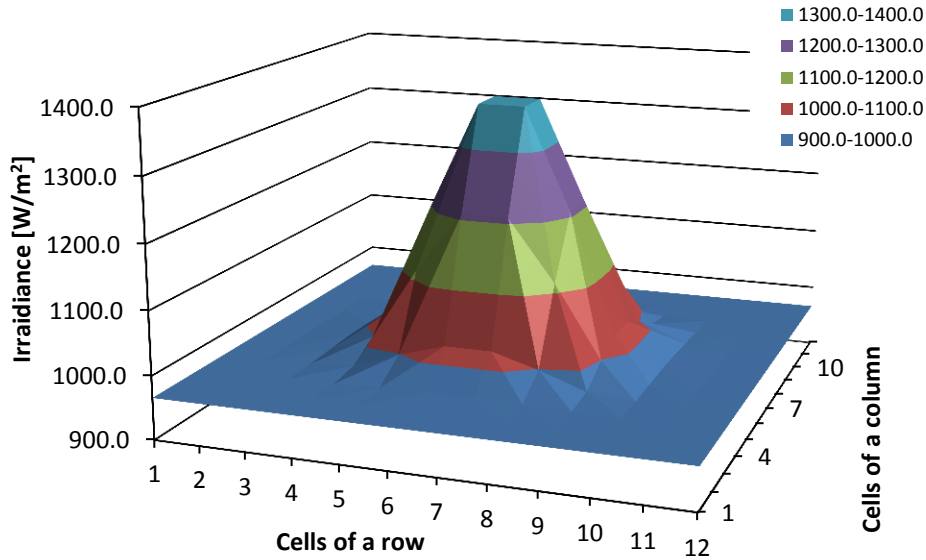
Figure 90 - 3D image of the Gaussian distribution of the irradiance on the 144 cells of the board.

In the COMSOL model, the amount of heat produced by each cell was introduced according to Figure 90. A fixed cell's efficiency of 37.2% was considered for all the cells, independently of the concentration they face. The results, shown in Figure 91 and Figure 92, predicted that the maximum temperature of the cells in conditions of non-uniform irradiance would have been below 100°C. The cells in the centre would have reached temperatures up to 91.2°C. As expected, the gradient of temperature among the cells would have become more enhanced than in the previous cases, doubling the maximum temperature difference (14°C vs. 30°C) registered for the uniform irradiance case.
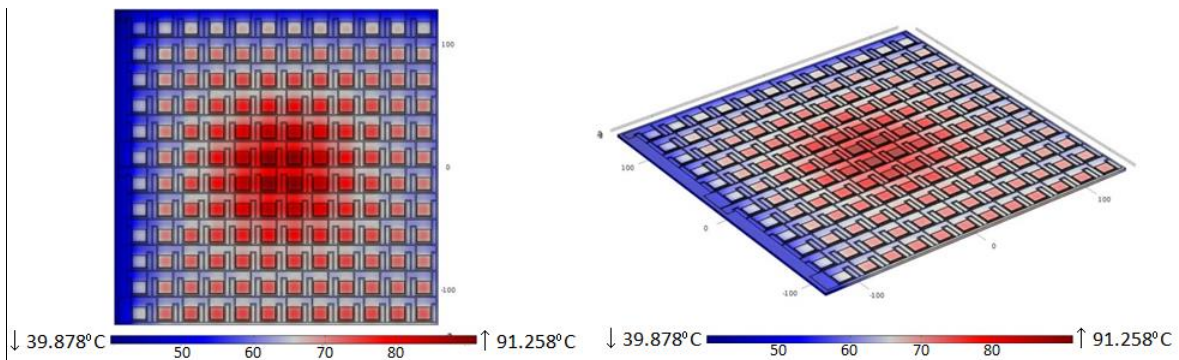
Figure 91 - **Temperature distribution of the full scaled board under non-uniform irradiance, in °C. Max cell's temperature: 91.3°C. Min cell's temperature: 61.0°C.**

135

↓ 42.369°C | 49.548 56.726 63.905 71.084 | ↑ 74.874°C   ↓ 42.369°C | 49.548 56.726 63.905 71.084 | ↑ 74.874°C
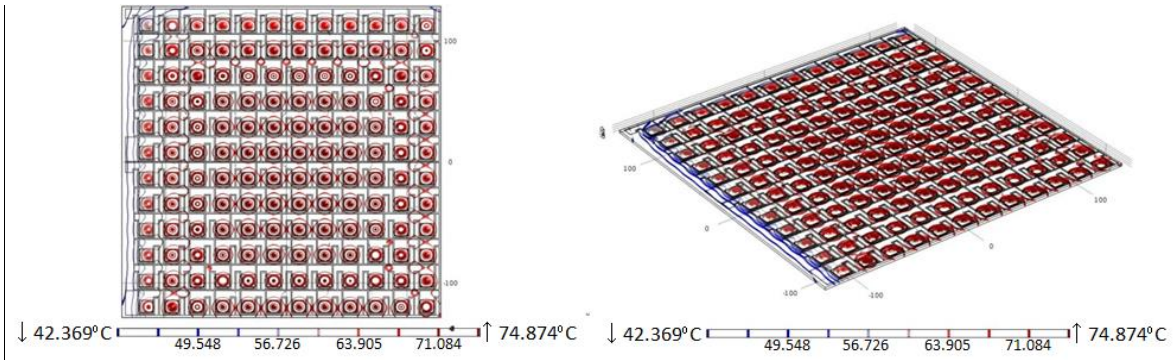
Figure 92 - **Isothermal contours of the full scaled board under non-uniform irradiance, in °C.**

As for the previous investigations, the receiver was tested under the worst case conditions too (Figure 93 and Figure 94). The temperature was expected to rise up to 133.4°C, still below the maximum 150°C allowed in these situations. The temperature gradient would have further increased up to almost 50°C under these conditions.

↓ 52.642°C | 70 90 110 130 | ↑ 133.43°C   ↓ 52.642°C | 70 90 110 130 | ↑ 133.43°C
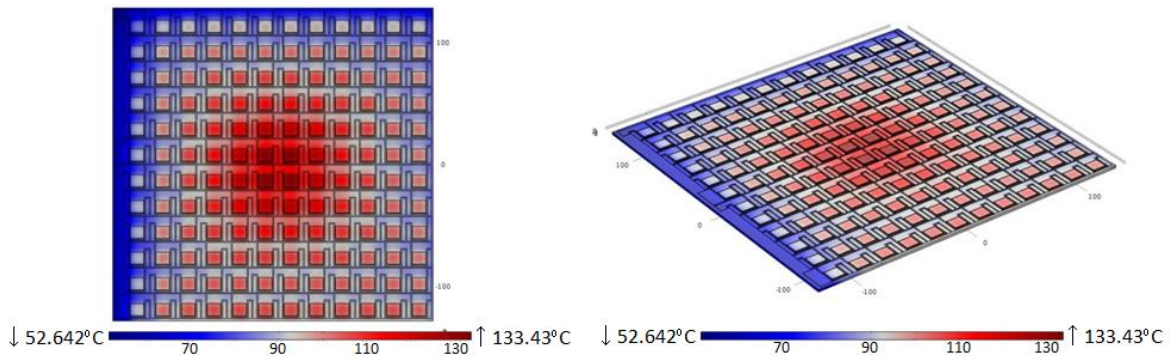
Figure 93 - **Temperature distribution of the full scaled board under non-uniform irradiance in the worst case conditions, in °C. Max cell's temperature: 133.4°C. Min cell's temperature: 85.3°C.**

. 55.730°C | 72.087 88.444 104.8 121.16 | ↑ 129.34°C   ↓ 55.730°C | 72.087 88.444 104.8 121.16 | ↑ 129.34°C
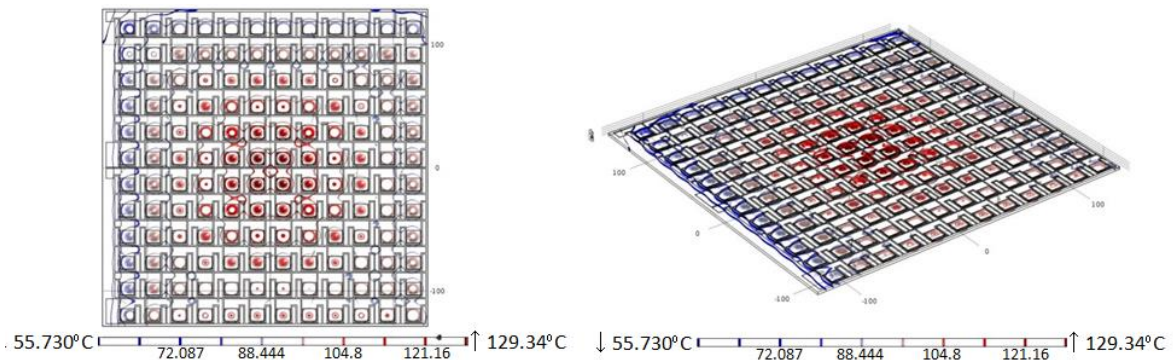
Figure 94 - **Isothermal contours of the full scaled board under non-uniform irradiance in the worst case conditions, in °C.**

4.4.7 Considerations

The large insulated metal substrate chosen for the densely packed CPV system showed a successful thermal management under all the modelled conditions (Table 23). The design of the electrical circuit and the manufacturing processes employed to fabricate the full scale assembly have then been detailed in the chapter 5.

Table 23 - Summary of the results of the full scale simulations conducted on the insulated metal substrate board.

Conditions *(DNI, cell efficiency)*	Heat waste per cell	Max cell's temperature	Min cell's temperature
Standard conditions *(1000W/m^2, η_{cell}=37.2%)*	26.7W	76.5°C	62.5°C
Worst case conditions *(1000W/m^2, η_{cell}=0%)*	42.5W	115.6°C	91.9°C
Non-uniform irradiance *(avg. 1000W/m^2, η_{cell}=37.2%)*	25.8W to 36.5W	91.3°C	61.0°C
Non-uniform irradiance and worst case conditions *(avg. 1000W/m^2, η_{cell}=0%)*	41.0W to 58.0W	133.4°C	85.3°C

4.5 Passively-cooled, single cell receiver

In the present section (4.5), the investigations on the thermal behaviour of the single cell receiver's substrate are reported. During the previous investigation (4.4.2), the PCB was found not to be a suitable solution for CPV applications, even when an over-sized cooling system had been applied. So, it had been no longer considered: the suitable substrates were limited to an IMS, a DBC and a silicon wafer.

4.5.1 Geometry, materials and components

The thermal behaviour of a CPV system depends on different factors other than the concentration and outdoor conditions only. Firstly, the generated waste heat is proportional to the size of the cell. Secondly, the geometry of the concentrators and the number and the distribution of the cells on the assembly limit the surface available for the heat exchange and influence the orientation of the heat sink. When no active cooling system is designed, all these concerns have to be taken into account, because the cooling action depends on the convection of air and on the emissivity of the receiver's materials only. Each kind of substrate has a

different thermal behaviour and this affects the temperature of the cells. For this reason, in the next subsections, an analysis of the thermal behaviour of each CPV component is reported and commented. After that, the simulations conducted to estimate the heat management abilities of the different receivers in a single cell configuration are described.

4.5.1.1   Cell's size and distribution

The range of commercially available multijunction cells has become wider in the recent years. When this investigation was conducted, AZUR SPACE offered the square cells summarized in Table 24, whose peak efficiencies at 500× maximum power point (MPP) ranged between 40.9% and 42.5%.

Table 24 - Comparison of AZUR SPACE's cells performance at 500×. An anti-reflective coating adapted to glass is considered. The waste heat is calculated taking into account 1000W/m^2 DNI, 25°C temperature, AM1.5 spectrum, and 15% optic losses.

	10mm×10mm cell	5.5mm×5.5mm cell	3mm×3mm cell
Efficiency	40.9%	41.6%	42.5%
Short circuit current	7.53A	2.31A	0.70A
Heat generated at MPP	25.12W	7.51W	2.20W
Heat generated in worst case conditions	42.50W	12.86W	3.83W

In this passive application, the performance of a 3mm×3mm multijunction cell was considered. Along with the lowest amount of heat generated because of the reduced size, this cell has the highest efficiency and, thus, the lowest rate of waste heat produced per unit of active area. Among the different geometries, the single cell configuration was the most favourable for passive cooling and, for this reason, was used in this receiver.

4.5.1.2   Concentrating optics

The optics has a high impact on the thermal management of CPV systems. In this application, an optics configuration where the receiver was not placed between the concentrators and the Sun, such as those represented in Figure 95, was selected. As previously pointed out, using these geometries, there was no risk for the cooling system to shadow the concentrators and, thus, larger surfaces were available for cooling. Despite this advantage, it was important to consider that, the heat sink, in

these configurations, was mainly downward orientated and so, it was not in the optimal conditions for natural convection [156].
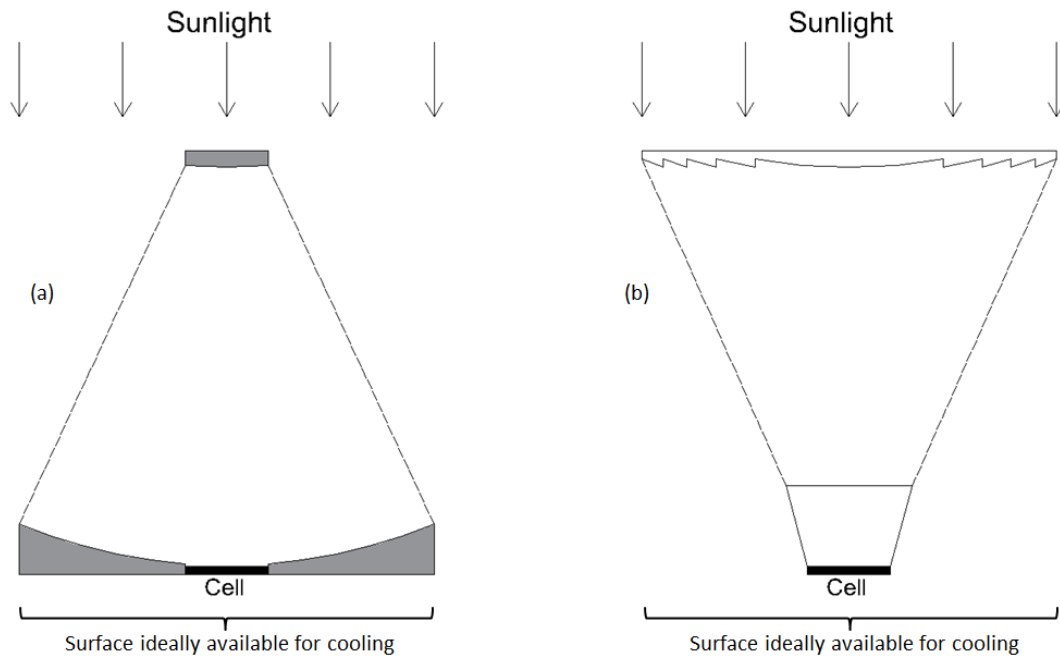
Figure 95 - The concentrators' geometries considered for the present passively cooled CPV system: (a) primary and secondary reflective concentrators, (b) Fresnel lens.

4.5.2 Dimensions of the substrate

The waste heat produced by a cell is moved by conduction to the heat sink, where it is then transferred to the ambient. Any object placed in contact with a fluid exchanges heat with it through natural convection and radiation and this happens for a solar receiver mounted in an outdoor CPV system too. The heat transferred by natural convection (q_c) is approximately proportional to the temperature difference between the cooling surface and the free stand fluid, respectively reported as T_{HS} and T_{amb}:

$$q_c = A_{HS} \cdot h_c \cdot (T_{HS} - T_{amb})$$

(36)

where A_{HS} stands for the area of the heat sink and h_c represents the convective heat transfer coefficient. This coefficient depends on the fluid, the state of the flow and the geometry of the system. The heat transfer coefficient for air in free convection usually ranges between 3 and 25W/m^{2}K [334]. On the other hand, the

heat transferred by radiation (q_r) is a function of the difference between the temperatures' fourth powers:

$$q_r = \sigma \cdot A_{HS} \cdot F_{i-k} \cdot \varepsilon \cdot (T_{HS}^4 - T_{amb}^4) \tag{37}$$

where σ is the Stefan-Boltzmann constant, F_{i-k} the view factor between the surface and the ambient, and ε the emissivity of the surface's material.

The simplest solution to dissipate the waste heat generated by the cell was to use a large, flat heat sink, placed at the bottom of the heat spreader. Aluminium is the material generally chosen to fabricate the heat sinks due to its good balance among thermal performances, weight and costs. Combining the two equations (36) and (37), and considering the bottom surface only, it was then possible to calculate the minimum area (A_{HS}) the CPV heat sink required to work properly.

$$A_{HS} = \frac{q_{cell}}{h_c \cdot (T_{HS} - T_{amb}) + \sigma \cdot F_{i-k} \cdot \varepsilon \cdot (T_{HS}^4 - T_{amb}^4)} \tag{38}$$

Assuming that [325]:

- all the heat generated by the cell reached the heat sink,
- only the flat bottom surface of the receiver exchanged heat with the ambient,

and considering:

- an upper bound for emissivity of 0.09,
- a view factor of 1,
- an optimistic value of 25W/m^{2}K for the air heat transfer coefficient,
- a heat sink surface temperature of 60°C,
- and an ambient temperature of 25°C,

a dissipating area of 0.0025m^2 for the aluminium heat sink was found to be necessary for passively cooling a 3mm×3mm sized cell. It corresponded to a 5cm×5cm aluminium plate. Assuming the same surface's temperature, a silicon wafer would have needed a smaller surface because of the higher emissivity than aluminium, but, because of 5cm×5cm were standard sizes for the three considered

substrates and similar to those of standard commercial receivers, the same dimensions were taken into account to compare the behaviour of the three substrates.

4.5.3 Choice of the substrate

The three 5cm×5cm substrates were reproduced in COMSOL and the results are shown in the figures below. The geometries were the same shown in Table 17: the DBC was 1.23mm-thick, the IMS 1.64mm-thick and the silicon wafer 0.55mm-thick. In order to make the comparison easier, the results are shown using the same scale: the temperature scale starts from 35°C (dark blue) to 75°C (dark red). In this passively-cooled system, air was naturally acting as cooling fluid: this action is modelled considering a convective heat flux of 10W/m^{2}K at an ambient temperature of 25°C.

(a) Direct bonded copper
Max temperature: 75.0⁰C

(b) Insulated metal substrate
Max temperature: 72.8⁰C

(c) Silicon wafer
Max temperature: 53.3⁰C
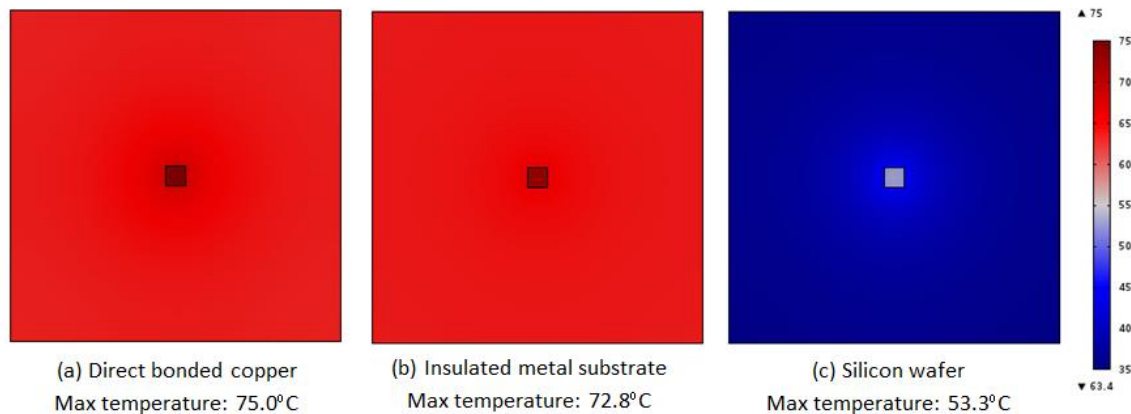
Figure 96 - The temperature distribution on the three substrates: a) direct bonded copper, b) insulated metal substrate, c) silicon wafer direct bonded copper.

All the receivers achieved cell temperatures between 50°C and 80°C, within the operating range of CPV systems [142,143]. The direct bonded copper (Figure 96a) and the insulated metal substrate (Figure 96b) showed similar maximum temperatures of 75.0°C and 72.8°C respectively. The silicon wafer (Figure 96c) instead achieved the lowest temperature (53.3°C) and, for this reason, appeared to be the most suitable substrate for a passive cooled CPV application.

As further proof of reliability, the performance of the three substrates under the worst case conditions was investigated as well. The results are shown in Figure 97, and similarly to the previous investigation, the scale has not been varied among the studies: from 40°C (dark blue) to 120°C (dark red). The simulation confirmed the better thermal behaviour of the silicon wafer, expected to reach a maximum cell's temperature of 78°C, about 30 to 40°C degrees below the other two substrates' temperatures.
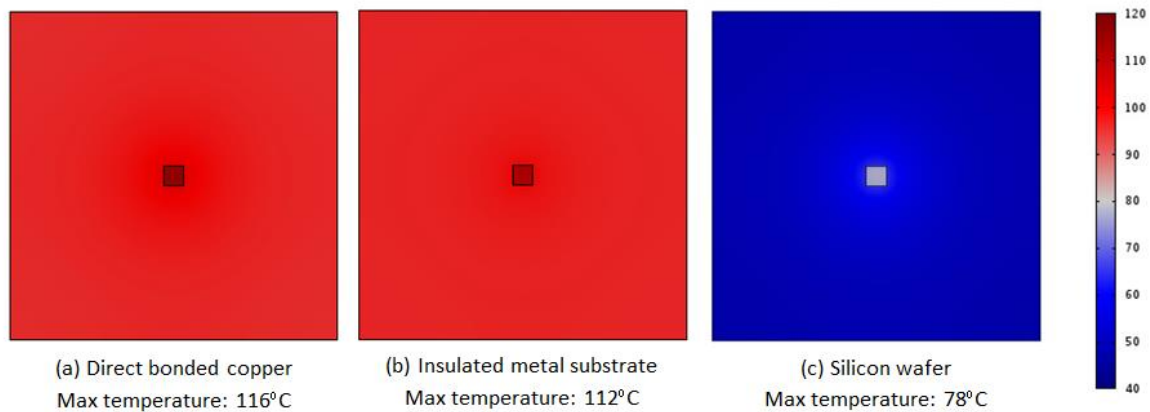
Figure 97 - The temperature distribution on the three substrates under the worst case conditions: a) direct bonded copper, b) insulated metal substrate, c) silicon wafer direct bonded copper.

4.5.4 Considerations

The silicon wafer was found to show the best performance in terms of heat removal for a single cell configuration in natural convective conditions. According to a survey made among different suppliers, the average cost of a 5cm×5cm silicon wafer was about £55 each, for an order larger than 10 wafers. The 5cm×5cm DBC and IMS instead costed respectively £15 and £10 each for more than 50 units. Despite the highest cost, the silicon wafer was preferred even because of the highest emissivity of the material, compared to aluminum and copper, and because silicon micro-machining had already been widely deployed [168]. As already pointed out, the receiver's layers could be directly sputtered onto the wafer [83,84]. So, the silicon wafer was chosen as substrate for the single cell receiver to be designed and has been furthered investigated in chapter 7.

4.6 Conclusions

CPV substrates are designed to give the mechanical support to the whole receiver, to remove the waste heat from the cell and to allocate the electrical circuitry. In the present chapter, a thermal investigation on the substrates to be employed for the development of CPV cell assemblies has been presented. The choice of the most appropriate cooling system depends on the features of the systems. Active cooling systems usually grant excellent thermal performance and are easy to control. So, an active cooler was employed for the large high concentration receiver designed in this work, where a high number of packed cells were accommodated. On the other hand, passive cooling systems are generally more simple and reliable. Therefore, a passive cooler was preferred for the single cell CPV systems, where an extended surface was available for heat exchanging.

In the densely packed receiver designed in this work, where an active cooling system was mounted, an insulated metal substrate was found to be the most convenient board. The IMS proved to have a thermal behaviour analogous to that of the DBC, since the maximum cell's temperatures shown by the two boards under the same conditions were similar. Overall, the IMS was found to be more advantageous in terms of costs and fabricability. First of all, producing the IMS for the present application was less expensive than producing a DBC with the same characteristics. Secondly, no supplier was found to be able to deliver a DBC with the required dimensions: it would have been needed to fabricate four different boards and to interconnect them in a later stage. The large IMS could, instead, be produced in one piece, improving the quality and the reliability of the final receiver.

On the other hand, a silicon wafer was preferred for the single cell application. Despite the high costs, this substrate had lowest cell's temperature as compared to DBC and IMS. Moreover, the high emissivity of the silicon wafer further enhanced the benefit in terms of passive cooling. Silicon was a well-known material and the cooling system, such as the micro-fins, could be easily machined in it. This way, integrating the cooling system in the substrate, would have reduced the receiver's thermal resistance that was particularly affected by the thermal interface materials used to attach the substrate and the heat sink.

In the following chapters, the design and development of the large receiver for active cooled, densely packed systems and the studies about an integrated passive cooling system for high CPV applications are reported.

Chapter 5: **Densely packed cell assembly: design and fabrication**

After the selection of the most appropriate substrate, this chapter describes the design of the electrical circuitry and the fabrication of the densely packed 144-cell assembly. The original outline of the conductive copper layer is developed to minimize Joule losses by reducing the number of interconnections among the cells in series. The whole pattern fits the standards requirements and restrictions, and matches the optics' design. Schottky diodes are employed for by-passing purposes: they are oversized to increase the safety factor. The plate is manufactured using standard electronic processes presented here.

5.1 Introduction

The cost-effectiveness of HCPV depends on the annual energy yield: each material, component and fabrication process has to be designed to maximize the energetic and economic performance. The cells are mounted on a cell assembly, which collects and conveys the current output to the inverter, facilitates the transport of the heat towards the heat sink, and gives mechanical strength to the structure. The present chapter describes the design of a densely packed cell assembly for high concentrating photovoltaic systems. The assembly allocated 144 cells and was rated at a peak power output of $2.6kW_e$ at 500✗ under CSTCs. It was conceived to be coupled with the concentrators developed by the Indian Institute of Technology Madras (India) and represented in Figure 98: a primary 125✗ parabolic mirror and a set of 144 secondary 4✗ concentrating parabolic compounds. An active cooling systems and a continuous tracker were being fabricated by the same Institute.
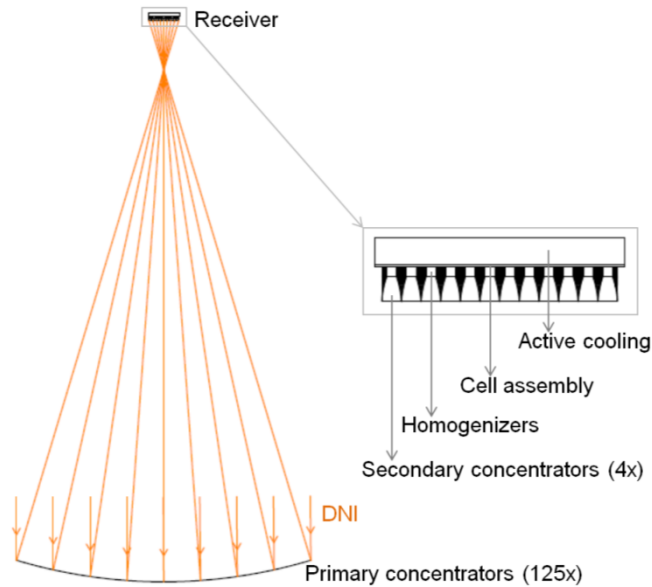
Figure 98 - Schematic of the system: a parabolic 3m×3m mirror reflects the light onto the receiver, composed by the secondary concentrators, the homogenizers, the cell assembly and the active cooling. Dimensions are not to scale.

The design was developed to limit to the risk of experiencing failures or performance issues [345]. In the first case, one or more components of the CPV stop performing the original designed function, such as a cell that is no generating power. In the second case, instead, the power output of the system drops by at least a 5% for reasons other than irradiance variation, spectral variation, cell temperature variation, tracker alignment, module alignment, or external soiling. For these reasons, the instructions of the standards were followed and adequate safety factors and tolerances were considered. Moreover, limitations related to the fabrication processes, the safety and the transportability had to be considered, and, therefore, are here accounted.

The high electrical currents and power densities taking place in HCPV systems were concerns that had to be taken into account at any stage between the design and the production of a reliable and durable cell assembly [346]. All these concerns increase the complexity of a cell assembly, restricting the opportunity of employing procedures commonly used for fabrication of flat-PV or silicon cells. Although in the last decade the development of new CPV assemblies had been presented in many researches [347–349] and patents [350–352], and new CPV power plants had been deployed worldwide [353–355], only limited information and experiences on

the cell assemblies fabrication were available at the time [21]. In this light, the main aim of this chapter is to illustrate the design procedures and the fabrication processes realized to develop the novel densely packed solar cell assembly for 500✕ CPV applications.

5.2 The by-pass diodes

Along with the cells, the diodes were allocated on the assembly. Taking into account the investigation presented by Vorster and van Dyk [111], one by-pass diode per cell was installed in the presented assembly to maximize the performance even in conditions of shading. The diodes applied in the systems were surface-mount technologies, because of the reduced cost compared to the discrete ones [356]. The Vishay V10P45S Schottky diode was chosen because of granting the best compromise between dimensions and performance among the commercially available ones. Analysing the commercial CPV assemblies (Table 25), a safety factor of at least 1.5 was found out to be needed to reduce the reverse voltage drop and the risk of breakage. In some application, safety factors to 10 could be considered to achieve a more conservative approach [113].

Table 25 - Comparison of the safety factors used by CPV industries and in the developed system

Company	Assembly code	Cell dimensions [mm✕mm]	Max CR [✕]	Max cell current [A]	No of diodes per cell	Maximum forward current per diode [A]	Safety factor
AZUR SPACE [78]	3C40A	10✕10	1000	13.088	2	10	1.5
Emcore [80]	CTJ Receiver Assembly	5✕5	1000	4.4	1	10	2.2
Spectrolab [79]	CCA 100 C3MJ 1A	10✕10	500	6.95	1	12	1.7
Ergonsolair [357]	CPV submounts and modules	5.5✕5.5	500	2	1	10	5.0
		7✕7	500	4.5	1	10	2.2
		10✕10	500	7	1	12	1.7
University of Exeter	144-cell receiver	10✕10	500	6.587	1	10	1.5

Taking into account the cell's short circuit current in the presented scheme (6.587A), a 10A Schottky diode granted an acceptable safety factor of 1.5. The peak repetitive reverse voltage was always higher than the cell voltage, even when a conservative safety factor was applied: the cell voltage was less than 75% of the

peak repetitive reverse voltage. Using two diodes would have enhanced the safety factor, but there was no available space to allocate them.

5.3 The conductive pattern

The design of the electrical circuit was developed to incorporate all the components, to have a high efficiency and to be easy to realize. In order to enhance the performance, the same copper plate was used to directly connect the negative pad of the cell with the positive pad of the following cell. This way, the number of connections was reduced, limiting the contact resistances. To facilitate the manufacturing, the whole copper pattern was designed to be made of only few shapes, periodically repeated in the space to obtain the final drawing.

The pattern was realized taking into account the requirements and the restrictions of the optical geometries and the recommendations of the standards, which are listed in the paragraph 5.3.1. In the design stage, AutoCAD was used to check the matching between the receiver's geometry and the optics systems restrictions. Different conductive patterns were proposed before the final design: the geometries and the features of each version are described in the following paragraph, along with the improvements introduced at each step. A symbolic representation of the CPV key components is shown in Figure 99: the same symbols are used in all the drawings reported in this chapter.
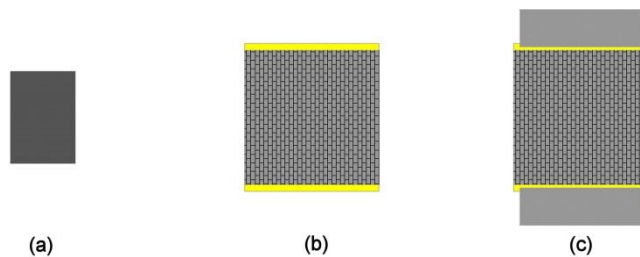
Figure 99 - Key of the components schematics: (a) diode, (b) bare cell and (c) cell with front interconnectors.

The electrical circuit was composed of two series of 72 cells each: each series was expected to produce 6.440A at about 208V at the maximum power point. The main challenge was to fit all the components in the available space. A 4✕ secondary system was placed above each $1cm^2$-sized cell: this meant that the available surface to allocate the cell, the diode, the interconnectors and the conductive

layers, inclusive clearances and tolerances, was four times larger than the cell's active area (10mm×10 mm).

A 4.5µm-thick layer of marble resin was used to bond the aluminum substrate and the conductors. It worked as a dielectric as well and had to be able to withstand a maximum open circuit voltage of 230V per series. It had a DC dielectric strength of $60 \cdot 10^3$V/mm, which means that it would have been able to support maximum voltages of 270V.

5.3.1 The IPC standards restrictions

The design was drawn up according to the IPC-2221 Generic Standards on Printed Board Design [358], produced by the Association Connecting Electronics Industries. The width of the conductor (w) was set according to the following equation [358]:

$$w = \frac{\left(\frac{I}{c_1 \cdot \Delta T^{c_2}}\right)^{1/c_3}}{t} \cdot c_4 \tag{39}$$

where I is the current, ΔT is temperature rise due to the current flowing in the conductor, and z is the thickness of the conductor. The constants have values of: c_1=0.048, c_2=0.44, c_3=0.725 and c_4=6.541·10^{-7}. A 70µm-thick copper was considered for this application: the most common 35µm thickness was not enough to safely carry the nominal currents in the restricted volumes available in CPV. In order to be able to limit the temperature raise to 5°C, the minimum 70µm-thick copper widths had to be equal to or larger than 1.17mm (Figure 100a) where a maximum short-circuit current of 3.293A was expected to flow and than 3.05mm (Figure 100b) where the short circuit current could raise up to 6.587A. Table 26 shows the minimum width required for a 70µm-thick copper plate depending on the conductor's temperature and on the maximum current flowing into it.

By limiting the effects of the Joule losses, the temperature of the system was decreased: so, the cell would have been able to work at lower temperatures and higher efficiencies. At the same time, a lower temperature reduced the thermal stresses and the risks of fatigue failures. In the proposed designs, a 10%-tolerance

and the effects of the thermal expansion were considered as well and the minimum widths were increased accordingly.
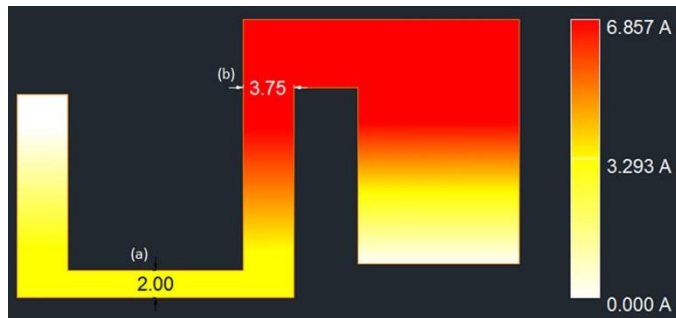
Figure 100 - Current distribution across the C2 copper shape. The dimensions are in mm.

Table 26 - Minimum width (in mm) of the 70µm-thick copper, for ambient temperature of 25°C, depending on current and copper's temperature (according to the IPC-2221 Standards).

Current vs Temperature rise	3°C	4°C	5°C	15°C	25°C	35°C	45°C	55°C	65°C
6.5870A	4.26	3.58	3.12	1.60	1.18	0.96	0.82	0.73	0.66
3.2935A	1.64	1.37	1.20	0.62	0.45	0.37	0.32	0.28	0.25

Across the plate, adjacent copper shapes faced various voltages while in operation. In conditions of open circuit at 500**x**, the negative pads of two consecutive cells faced a difference up to 3.17V. The ends of two consecutive rows met a maximum difference of 76.08V. The largest voltage difference was registered between the last pad of one series and the first one of the other series: there, the shapes faced a maximum difference of 228.24V. The standards struck clearly out the required electrical clearance between DC external coated conductors: 0.13mm for any for voltages lower than 100V and 0.40mm for voltages up to 300V.

5.3.2 Version 1.0

A particular of the first version (V1.0) of the conductive pattern is shown in Figure 101. All the dimensions are in millimeters and shown in Figure 102. All the cells were aligned and placed at a distance of 10mm from the adjacent ones. A tolerance of 0.5mm was introduced in the two cell's sides. A gap of 1.0mm was considered between the negative and the positive pads of each cell to reduce the risk of shorticircuiting when the interconnectors were mounted, and a gap between

of 0.5mm between each row was considered as well. The pattern was based on the three shapes shown in Figure 102, and the subsequent rows of cells were designed to be connected by a ribbon.
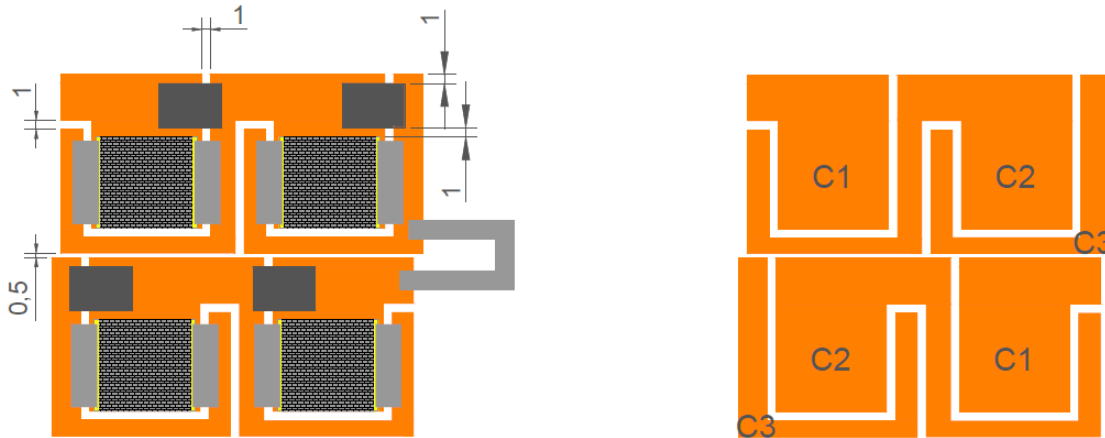
Figure 101 - A four-cell V1.0 pattern. In (a) the cells and diodes are reported with dimensions in mm. In (b) the copper shapes employed for the pattern are highlighted.
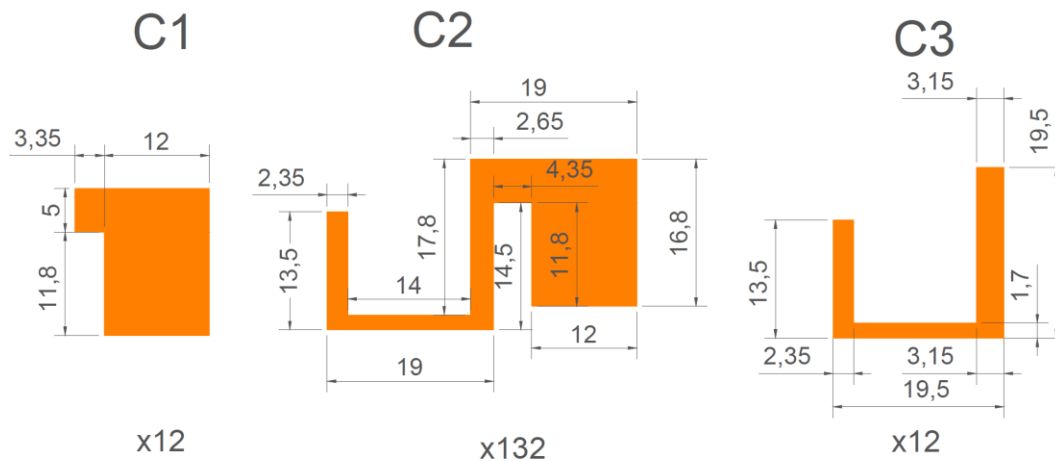
Figure 102 - The three shapes of the V1.0: C1 recurs 12 times, C2 recurs 132 times, and C3 recurs 12 times in the 144-cell design. Dimensions are in mm.

5.3.3 Version 2.0

The distance between adjacent cells was increased from 10mm to 11mm to take into account the secondary optical concentrator wall's thickness. The distance between the cell and the diode was then increased from 1.0 to 2.0mm to avoid contacts between the walls of the optics and the diodes. A 0.5mm tolerance was considered on the third side of the cell too, and the diode's distance from the edge was reduced from 1.0mm to 0.5mm instead. The room gained on each side of the

copper made it possible to increase the gap between the rows to 1.0mm. A symmetry was introduced by equalizing the width of the conductors where the interconnectors were allocated: each of them sized 3mm.
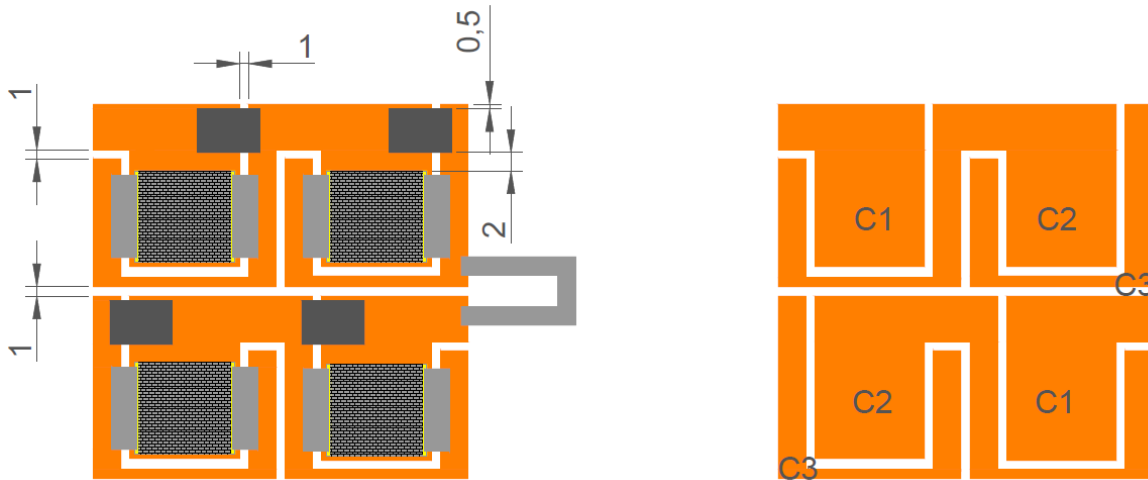
Figure 103 - A four-cell V2.0 pattern. In (a) the cells and diodes are reported with dimensions in mm. In (b) the copper shapes employed for the pattern are highlighted.
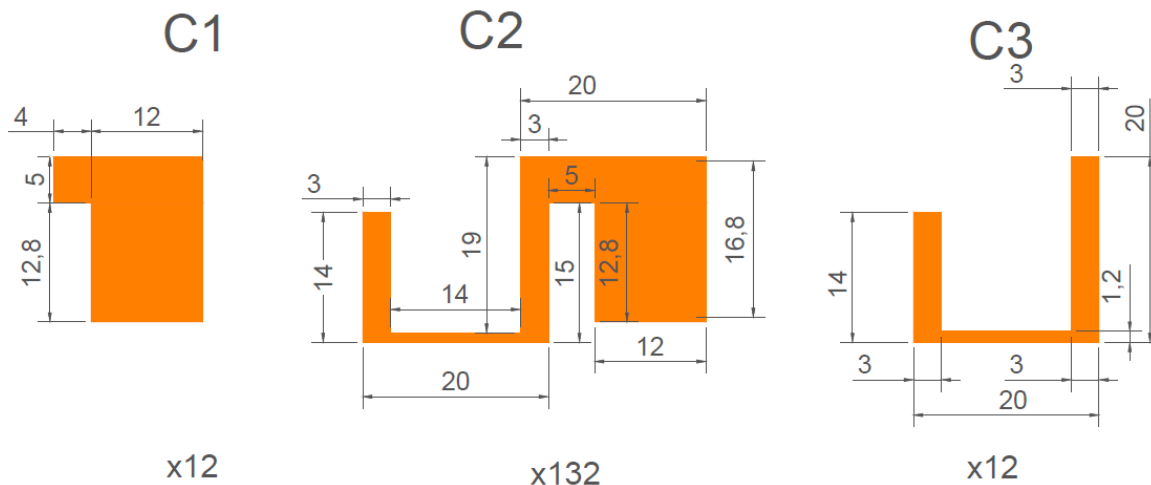
Figure 104 - The three shapes of the V2.0: C1 recurs 12 times, C2 recurs 132 times, and C3 recurs 12 times in the 144-cell design. Dimensions are in mm.

5.3.4 Version 3.0

The version 3.0 was made of four shapes (Figure 105 and Figure 106), instead of the three used for the previous designs. The ends of two adjacent rows of cells no longer needed to be externally interconnected: the connection was made with a novel copper shape, C4, which was placed at the end of each row, recurring 10

times in the 144-cell design. The gaps were reduced to 0.5mm, in order to increase the volume of the board occupied by copper and, thus, to reduce the Ohmic losses.
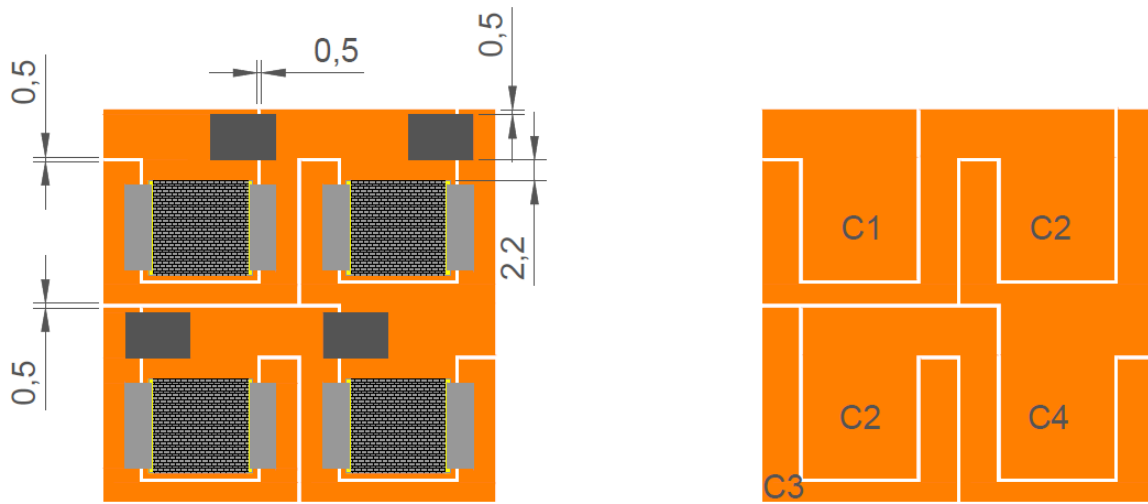
Figure 105 - A four-cell V3.0 pattern. In (a) the cells and diodes are reported with dimensions in mm. In (b) the copper shapes employed for the pattern are highlighted.
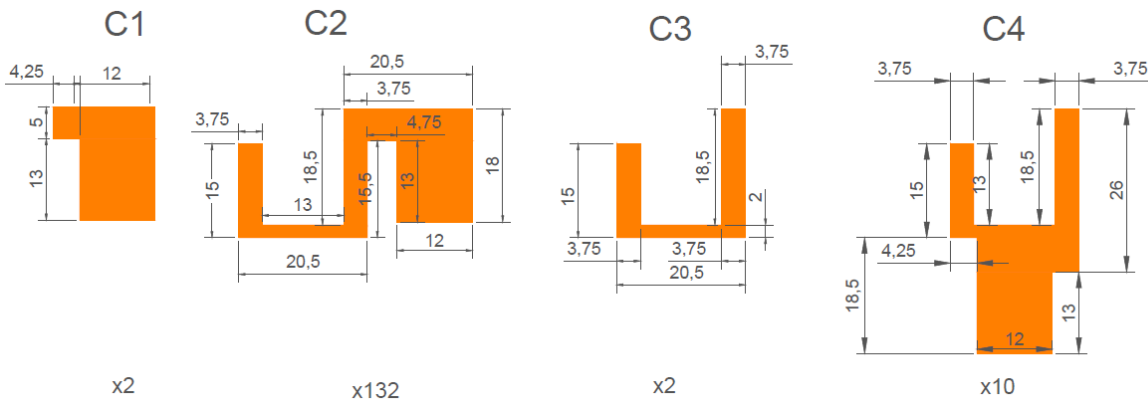
Figure 106 - The four shapes of the V3.0: C1 recurs twice, C2 recurs 132 times, C3 recurs twice, and C4 recurs 10 times in the 144-cell design. Dimensions are in mm.

5.3.5 Version 3.1

After a meeting with the board supplier, a small modification was made to the pattern: some room was added to C1 and C3 to make it possible to allocate the terminal tabs for current extraction at the end of each series. The terminal tabs required a minimum landing pad of 6.5mm×8.0mm.
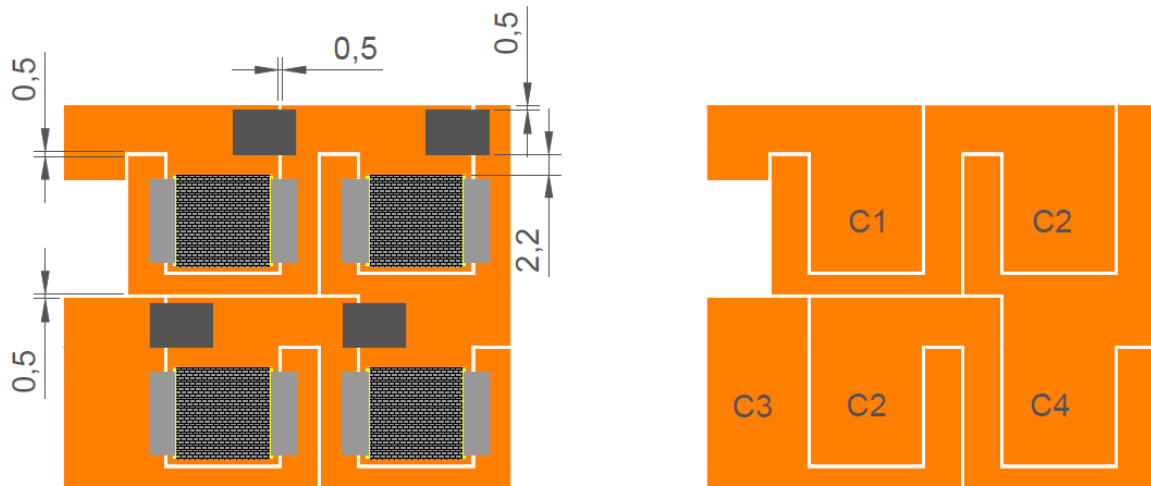
Figure 107 - A four-cell V3.1 pattern. In (a) the cells and diodes are reported with dimensions in mm. In (b) the copper shapes employed for the pattern are highlighted.
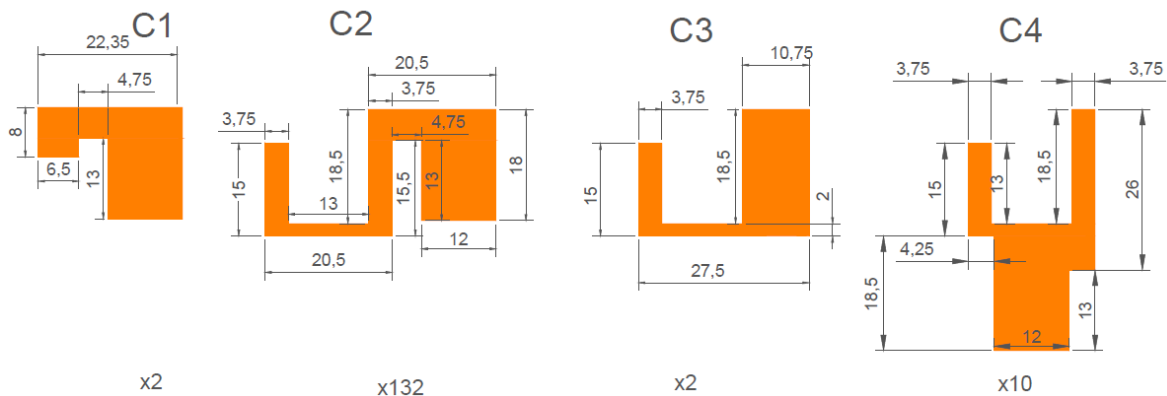
Figure 108 - The four shapes of the V3.0: C1 recurs twice, C2 recurs 132 times, C3 recurs twice, and C4 recurs 10 times in the 144-cell design. Dimensions are in mm.

The main differences between the 2.0 and final 3.1 pattern versions are highlighted in Figure 109: each change is marked with the same letter in both the designs. Firstly, C1 and C3, respectively placed at the positive (a) and the negative (b) pole of each series, were modified to accommodate the terminal tabs. Secondly, C4 was introduced to replace the interconnections between the ends of two rows and, thus, to reduce the Ohmic losses of the copper pattern (c). Furthermore, the gaps the conductive materials were reduced (d) to gain space to extend the conductive area. Thanks to this change, the minimum copper width (e) could be enlarged.
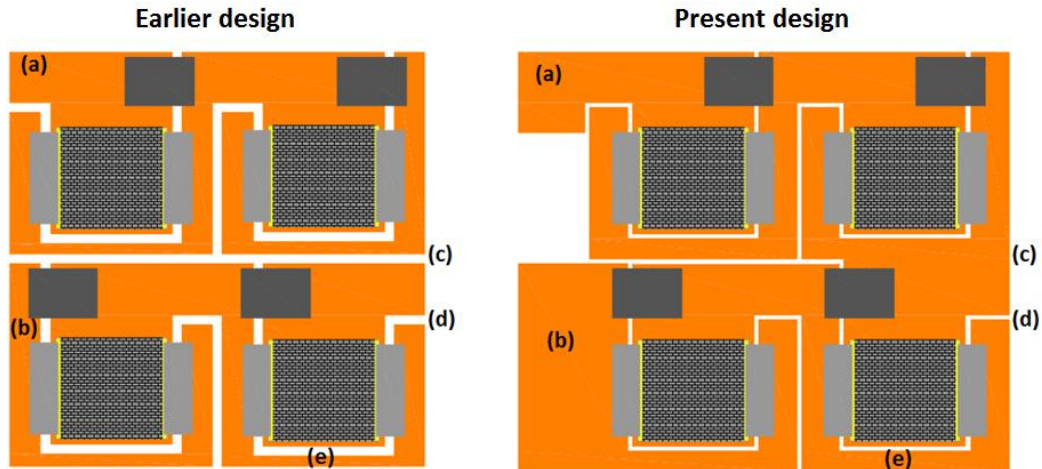
Figure 109 - Particulars of the old and the new designs, respectively on the left and the right hand side. The differences are marked with letters from a to e.

The version 3.1 was the final version of the pattern, and was used to print the CPV receiver's substrate. A full scale image is shown in Figure 110: the copper pattern sized 251.0mm×258.5mm. An aluminum board sized 255.0mm×262.5mm was used as baseplate because a minimum of 2mm distance between the copper and the aluminum edges were required to realize the chemical etching.

The large, 144-cell conductive layer was composed by 146 copper elements, opportunely etched on the substrate. C2 was repeated 132 times. C3 recurred 10 times: it was used at the end of each row, excepted for the start and the end of each series, where C1 and C4 were respectively placed. C1 and C4 were then present twice each on the 144-cell plate, respectively at the positive and the negative ends of each series.
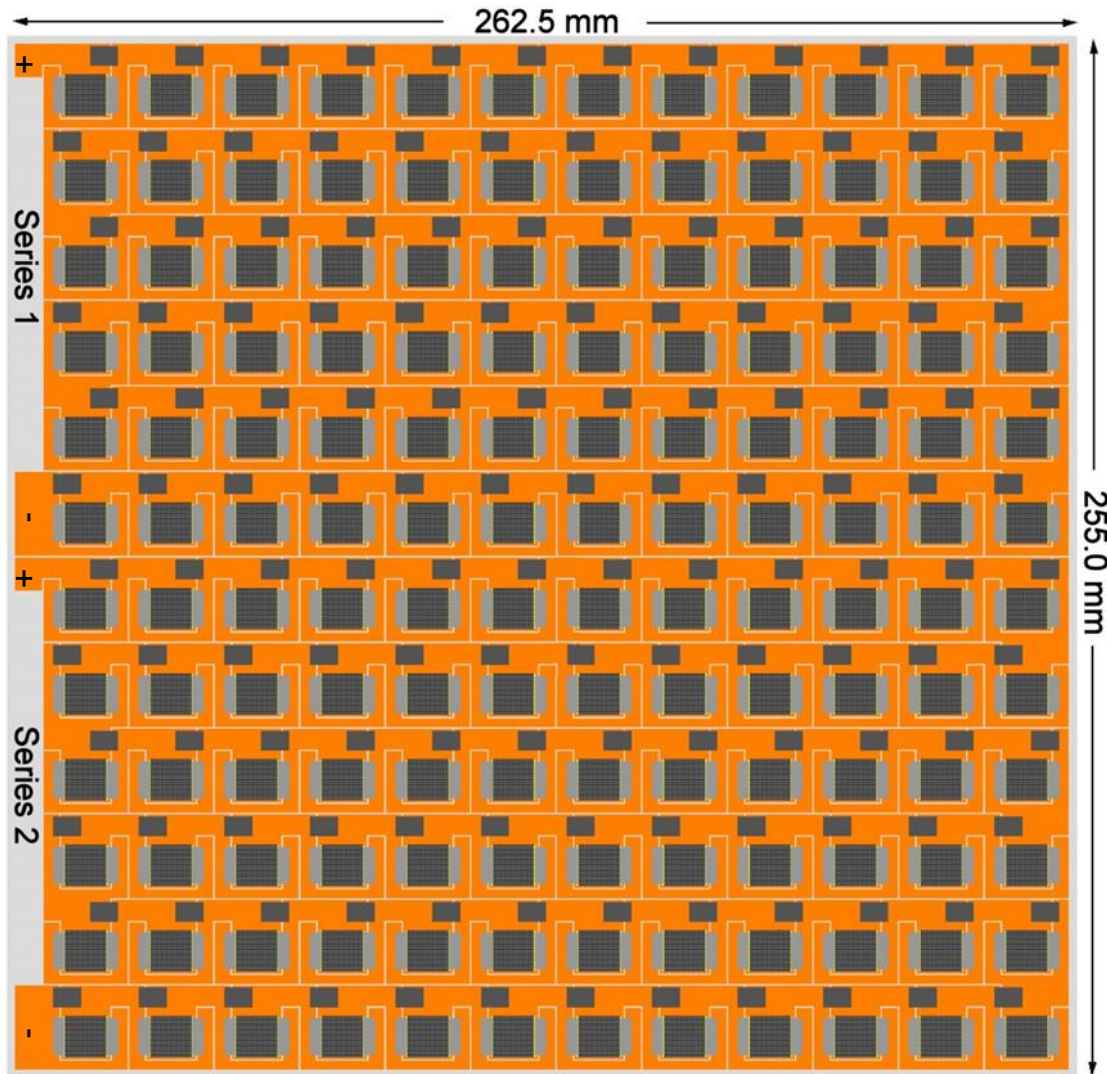
Figure 110 - Complete assembly: the dimensions of the aluminum board are shown.

5.3.6 Features of the novel design

In any electronic application, interconnectors represent one of the weakest points, because of the high electrical contact resistance and the fragility of the bonding. The original design of the copper pattern designed in this work had only one set of interconnections between adjacent cells: one shape of copper was used both as landing surface for the interconnectors coming from the negative pole of the cell and as mounting pad for the positive pole of the adjacent cell. This approach allowed lowering the electrical resistance of the circuit and, thus, the electrical losses.

A second feature of the design was the scalability: it could be easily adapted to allocate a different number of cells. Opportunely combining the copper shapes, it was possible to create less or more populated arrays of aligned cells. In the present work, the design was used to produce several single cell receivers, a 16-cell receiver (Figure 111) and the presented 144-cell receiver [337].
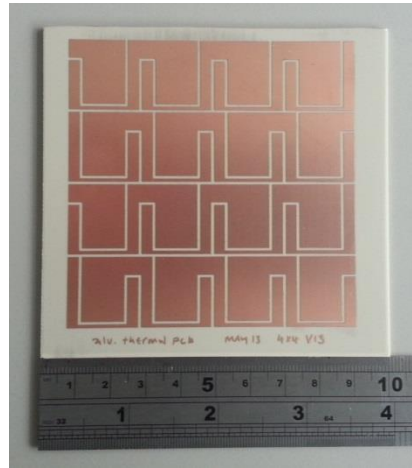
Figure 111 - Densely packed 16-cell assembly

5.3.7 Thermal expansion analysis

An investigation about the effects of the thermal expansion on the electrical circuitry was then undertaken, in order to prevent problems due to the high temperatures involved. The plate was designed and manufactured at a room temperature of 25°C. The maximum working temperature was 100°C, but for a tracking or a mechanical failure the system could face a higher stagnation temperature of 150°C. A maximum difference of temperature of 125°C (ΔT_{cu}=150°C-25°C) was then considered between the operating and the designing temperatures.

Copper has a coefficient of thermal expansion (α_{cu}) of 17ppm/°C and the maximum dimension (L_{max}) in the presented design was 20.5mm. According to the standard equation for the linear thermal expansion (40), the maximum expected deformation (ΔL_{max}) due to the temperature was the 0.00435mm for the considered geometries. The linear thermal expansion equation is expressed as:

$$\frac{\Delta L_{max}}{L_{max}} = \alpha_{cu} \cdot \Delta T_{cu}$$

(40)

Considering the expansion of both the copper shapes that were facing the gap, a maximum decrease in distance of about 0.01mm was expected and this would have still maintained the width of the gap above the minimum value recommended by the standards (0.4mm).

5.3.8 A different cell's configuration

As noted in 4.4.6, the CPV concentrators generally showed a non-uniform sunlight distribution on the receiver, which could be described by a Gaussian function, with a higher irradiance in the centre of the assembly. The same standard normal distribution shown in Figure 89 and Figure 90 was considered: a mean, maximum and a minimum DNI of 1000W/m^2, 1366W/m^2 and 966W/m^2 respectively were accounted. In the present application, this distribution resulted in differently-irradiated cells and, so a cells' series configuration different than the proposed one would have offered the opportunity to enhance the electrical performance of the system.

When considering the configuration of cells in a densely packed geometry, it was important to design the same voltage output across each cells' series. Cell's voltage can be assumed as constant while slightly varying the irradiance [11], so the same number of cells needed to be planned on each series. In the considered standard normal distribution, the sunlight intensity was quite uniform across the cells on the edge of the boards: a maximum difference in intensity of 0.6% was expected among the cells placed in the three rows closer to each edge. Among the remaining cells, instead, the difference grew up to 40%. So, in this approach, it was decided to divide the cells in the centre, in order to maximize the performance of the rest of the cells which were similarly irradiated. Three 48-cell series were designed, as shown in Figure 112: two symmetric series connected the cells on the edges and one series connected instead the cells in the centre. The equivalent electrical circuits of the old and new configurations are compared in Figure 113.
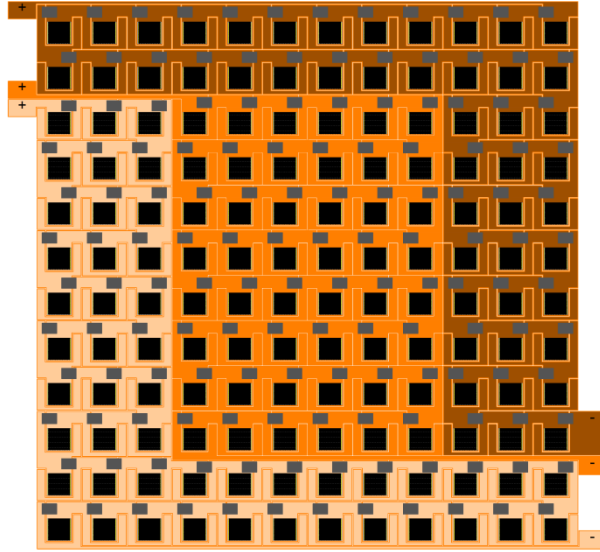
Figure 112 - Densely packed assembly in a three series configuration. The three series are represented by different colours.
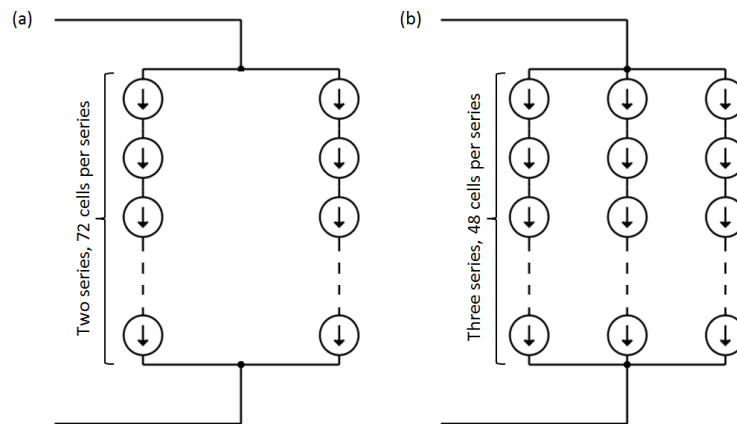
Figure 113 - Equivalent electrical circuits of the two series (a) and the three series (v) configurations. The cells are represented as current sources.

The assembly proposed was conceived to be installed on the same 282.0mm×275.2mm aluminum-based IMS considered earlier. Due to the presence of the central series, some copper shapes were modified to allocate all the same-polarity terminal tabs on the same side of the substrate. The requirements of the standards (Table 27) were considered as well: the new maximum short-circuit current (I_{sc_x}) of 9.0A was calculated, taking into account the maximum irradiance of 1366W/m^2, as follow [359]:

$$I_{sc_{1366}} = I_{sc_{1000}} \cdot \frac{1366W/m^2}{1000W/m^2}$$

(41)

where $I_{sc_{1000}}$ is the reference short circuit current under CSTCs. The minimum copper width in this new design was 1.85mm where a maximum short-circuit current of 9.0A was expected, meaning that the current flow would lead to an increase in temperature of 25°C.

Table 27 - Minimum width (in mm) according to the IPC-2221 Standards, for ambient temperature of 25°C and non-uniform irradiance.

Current vs Temperature rise	5°C	15°C	25°C	35°C	45°C	55°C	65°C
9.0 A	4.80	2.47	1.81	1.47	1.27	1.12	1.01
4.5 A	1.85	0.95	0.70	0.57	0.49	0.43	0.39

A preliminary analytical investigation was conducted to understand the benefit of this three-series approach under a non-uniform illumination. Combining the irradiance predictions and the data reported on the cell's datasheet, the new configuration had the potential to enhance the overall maximum power output up to the 25% (Table 28). The overall voltage output was expected to decrease according to the reduction in number of cells per series, whereas the sum of the short circuit currents of the three series was expected to increase because of the larger number of series. The higher currents would have increased the Ohmic losses, which had not been taken into account in these preliminary calculations. Despite the promising results, in lack of data about the real performance of the concentrators and because of the simpler design and the wider operating temperature range, the original two-series configuration was adopted for the fabrication of the receivers.

Table 28 - Comparison of performance between the different configurations under a standard Gaussian concentrated sunlight distribution.

	2-series under uniform illumination	2-series under non uniform illumination	3-series under non uniform illumination	Difference between the two configurations under non uniform illumination
Overall power output [W]	2678.40	1568.09	1973.80	25.87%
Sum of short-circuit currents [A]	13.17	14.50	16.53	13.97%
Open circuit voltage [V]	228.24	204.21	152.16	-25.49%

5.4 Interconnections

As anticipated, the wire bonding technology was selected to interconnect the front tabs of the cell with the conductive layer. In this application, aluminium wires were bonded because of the higher mechanical strength, the lower temperature required for the bonding process and the lower cost of aluminium compared to gold.

5.4.1 System sizing

In view of lack of recognized standards the approach suggested by Shah [360] was used to dimension the wires bonded on the receiver. This method was based on the principle that at steady state all the heat produced by the Joule losses (Q_g) on the wires needed to be removed (42). This procedure was centred on the conservative assumption that the heat was dissipated only through thermal conductivity and did not take into account radiative nor convective exchange: the amount of heat dissipated through the wire (Q_d) needs to equalize Q_g. In the present case, the amount of heat generated on the wire (43) was directly proportional to the square of the current flowing through the wire itself (I_w), with the proportion given by the electrical resistance of aluminum (R_{el_Al}).

$$Q_g = Q_d \tag{42}$$

$$Q_g = I_w^2 \cdot R_{el\_Al} \tag{43}$$

The amount of heat removed by the wire was estimated through the equation of the heat transfer by conduction, given as:

$$Q_d = \frac{k_{Al} \cdot A_w \cdot \Delta T_w}{l_w} \tag{44}$$

where k_{Al} represents the thermal conductivity of aluminum, A_w and l_w are respectively the sectional area and the length of the wire, and ΔT_w indicates the difference of temperature between the two ends of the wire.

The electrical resistance depends on the electrical resistivity of the material (ρ_{Al}), the length and the cross-sectional area of the conductor. Applying the definition of electrical resistance (45), and considering the circular section of the wire, Shah

[360] obtained (46), which was used to determine the maximum (I_w) current allowed to flow through one wire, with a diameter D_w.

$$R_{el\_Al} = \frac{\rho_{Al} \cdot l_w}{A_w} \tag{45}$$

$$I_w = \frac{\pi}{4} \cdot \frac{D_w^2}{l_w} \cdot \sqrt{\frac{k_{Al} \cdot \Delta T_w}{\rho_{Al}}} \tag{46}$$

The current generated by the cell (I_{cell}) was distributed on different wires. The minimum number of wires needed to carry it safely (N_w) was established through the ratio between the total amount of current and the maximum current per wire (47).

$$N_w \geq \frac{I_{cell}}{I_w} \tag{47}$$

Aluminum had a thermal conductivity of 205W/mK and an electrical resistivity of $2.82*10^{-8}\Omega$m. Standard aluminium wires were being used in this application: their diameter was 32µm. The distance between the front contacts on the cell and the landing pads on the copper was 2mm and this corresponded to the length of the wire. Considering a difference of temperature of about 15°C between the two terminals of a wire, 50 wires were needed to safely carry the expected maximum short circuit current.

5.4.2 Safety factor

In addition to the employment of a conservative sizing method, a surplus of 20 wires per cell was bonded. Installing 70 wires per cell led to a safety factory of 1.4 and was considered necessary to overcome two issues that could have occurred during manufacturing and operation: wire bond non-sticks and non-uniform current generation. Some wires were found not to stick on the tabs, as shown in Figure 114, because of some solder paste contamination left on the surface even after the cleaning process. In the present system, 3.75% of the connections were found to be faulty or unstuck after the fabrication: this meant that an average of 3 connections was missing on each cell, out of 70 bonded. A peak of 14 missing connections per cell was counted, with a maximum of 10 per cell's side. The

surplus of bonded wires prevented the system from dangerous overcurrents that would damage the remaining operating wires: in the case of a wire failure, the most of its current would flow in the nearest wires. So, the safety factor reduced the load for each wire in case of missing connections too. Furthermore, the excess of wires allowed the system to accommodate any potential non-uniformity in current generation due to partial shading or non-homogeneous light distribution onto the cell's surface. Under a non-uniform illumination, each cell locally operates at higher irradiance [35]: a larger number of interconnections than designed helped to fairly distribute any surplus of current, in order not to overload some of the wires.
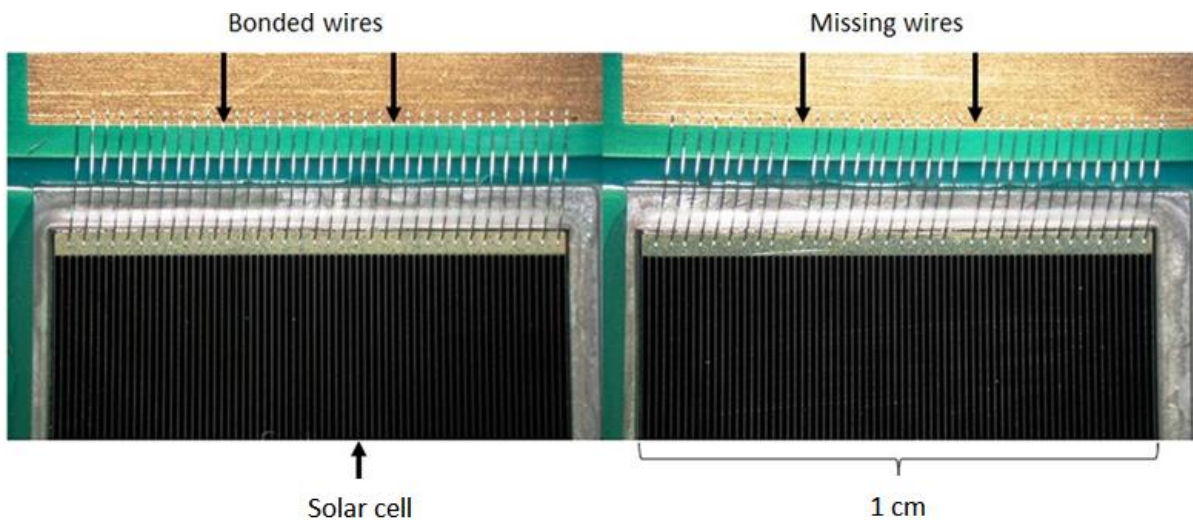
Figure 114 - A completely bonded cell's tab (left) and a cell's tab with two missing wires (right).

5.4.3 Bonding

Wire bonding machines were usually able to handle systems up to $400cm^2$. The board used in this application went over this limit, sizing about $670cm^2$. This meant that the machine had to be stopped time by time, to let the operator move the panel. After that, the machine could be re-threaded, and then started again. During the fabrication of the presented 144-cell receiver, the operator needed to take action approximately every 120 wires. Considering 70 wires per cell and 144 cells on the plate, it meant about 85 human interventions per plate and higher manufacturing costs.

5.5 Ohmic losses

The plate was designed to work at a peak power of $2.678kW_p$: this was the expected output from 144 cells working at the maximum power point under 500× at 25°C. In any circuit, part of the electrical energy is wasted in the copper circuit and in the interconnectors. Therefore, an analytical investigation was conducted to determine the Ohmic losses taking place in those conditions. These two cases were separately studied, in order to understand the effect of the interconnections on the performances of the system.

The 144-cell copper pattern was made of 146 copper components, with a common thickness of 70µm. The overall power losses (Q_Ω) was calculated as the sum of the losses on each i-copper shape, as reported in Table 29, taking into account the current flowing (I), the width (w) of each section and the electrical resistivity of copper (ρ), the length (L) and the thickness (z) of the shape:

$$Q_\Omega = \sum_i^{146} \frac{\rho}{z} \int_x^L I^2(x) \cdot \frac{dx}{w(x)} \tag{48}$$

A representation of the current flow is reported in Figure 115. Considering an electrical resistivity of $1.62 \cdot 10^{-8} \Omega m$ for copper, a loss of $10.50W_e$ was estimated while in operation. This value represented about the 0.4% of the whole power output.

Table 29 - Power losses breakdown in the conductive pattern.

Component Code	Geometry	Power losses per piece [W]	Number of repetition in 144-cell design	Total power losses [W]
C1		0.013	2	0.026
C2		0.077	132	10.202
C3		0.067	2	0.134
C4		0.014	10	0.140
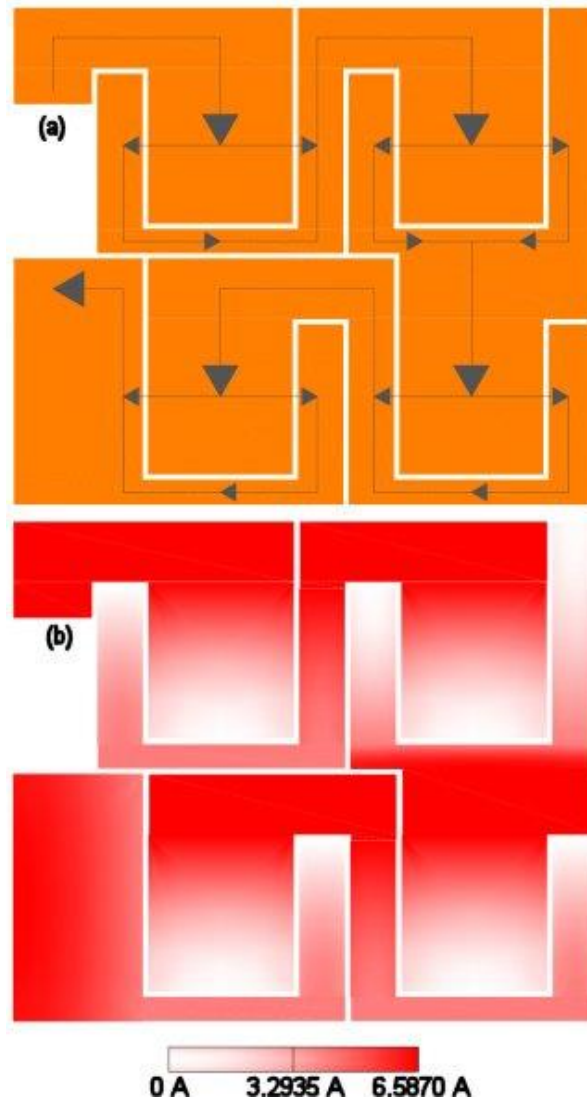
Figure 115 - Current flow (a) and current density (b) across a 4-cell design.

The power losses taking place in the wires were calculated using the equations and procedures reported in the paragraph 5.4.1. On each cell, 70 aluminum wires were installed, to transfer a current of 6.440A at the maximum power point. Taking into account an electrical resistivity of $2.82 \cdot 10^{-8} \Omega m$, about $0.063 W_e$ were expected to be wasted on each cell and, then, about $9.00 W_e$ to be lost on each plate (0.34% of the power output). In the presented plate, an average number of 3 wires were missing on each cell: this issue raised the power losses to $9.40 W_e$, with an increase of 4.5% compared to the ideal case. It is interesting to highlight that the interconnectors caused almost half of the Joule losses on the plate. The wires were designed to operate safely when up to 20 of them fail on each cell. With only 50 wires working on each cell, the power loss would have raised to $12.60 W_e$ (+40%

compared to the 70-wire case). The losses would have decreased by using materials with higher electrical conductivity: 70 gold wires per cell and 70 copper wires per cell would have dropped the losses per plate respectively to $7.80W_e$ (-12%) and $2.68W_e$ (-70%).

The effect of the solder joint on the overall electrical resistance had not been considered. Taking into account the current flowing perpendicularly to the cross-section of the solder and the copper for a length l, the global electrical resistance can be calculated as [328]:

$$R_{el} = \cfrac{1}{\cfrac{1}{R_{solder}} + \cfrac{1}{R_{copper}}} = \cfrac{1}{\cfrac{A_{solder}}{\rho_{solder} \cdot l} + \cfrac{A_{copper}}{\rho_{copper} \cdot l}} \qquad (49)$$

The electrical resistance is inversely proportional to the thickness and to the electrical conductivity of the material. Therefore, despite the lower electrical conductivity, the solder, which had a thickness much higher than the copper layer (Table 17), increased the area of the cross-section normal to the current flow and, so, was expected to reduce the electrical losses. A simplified electrical circuit is reproduced in Figure 116.
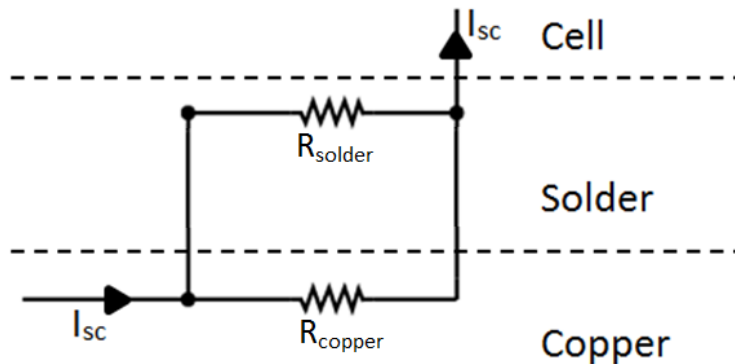
Figure 116 - Equivalent electrical circuits of the solder joint.

5.6 Encapsulation

During the wire bonding, no encapsulation of the interconnectors was attempted, in order not to risk the dark encapsulant to cover part of the cell's active area: an example of encapsulated interconnectors, realized on a previously-developed single cell sample, is shown in Figure 117. Moreover the size of the board would

have made the interconnectors globing more challenging, expensive and time-consuming to realize.
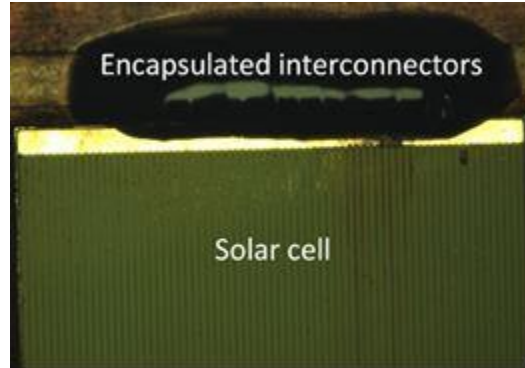
Figure 117 - Example of encapsulated interconnectors

Nonetheless, a transparent encapsulation of the plate was considered essential to reduce the risk of damages to the components, protecting them from external agents and accidental collisions. The clear Sylgard 184 was used in this application and its effects on the cell performance were preliminary tested using a spectrometer. An average transmittance of 85.77% was registered for the whole absorption band of the MJ solar cell. The optical transmittance (t_{Syl}) for each subcell's bandgap is shown in Table 30. The drops in short-circuit current within each i-subcell (ΔI_{sci}) and the whole MJ cell, caused by the encapsulant, was estimated using (50) and (51) respectively, adapted from the correlations reported in [361,362].

$$\Delta I_{sci} = \frac{\int E_{ref}(\lambda) \cdot t_{syl}(\lambda) \cdot SR_i(\lambda)\, d\lambda}{\int E_{ref}(\lambda) \cdot SR_i(\lambda)\, d\lambda} \tag{50}$$

$$\Delta I_{sc} = \frac{\min\left(\int E_{ref}(\lambda) \cdot t_{syl}(\lambda) \cdot SR_i(\lambda)\, d\lambda\right)}{\min\left(\int E_{ref}(\lambda) \cdot SR_i(\lambda)\, d\lambda\right)} \tag{51}$$

where $E_{ref}(\lambda)$ is the reference spectrum AM1.5d ASTM G-173-03, $t_{Syl}(\lambda)$ is the optical transmittance of Sylgard and $SR_i(\lambda)$ is the spectral response of the i-subcell. As reported in Table 30, Sylgard did not affect the current-matching among the subcells: the current drops in the GaInP and the GaAs subcells were comparable, whereas the it was higher for the Ge subcell. This discrepancy was balanced by the excess current produced by the Ge subcell compared to the other two subcells,

which usually settled at about 30% [363,364]. Overall, a reduction of 7.30% in the cell's short circuit current was expected due to the transmittance of Sylgard.

Table 30 - Transmissivity of Sylgard (tSyl) and drop in Short-circuit current (ΔIsci) per subcell at 500×, 1000W/m2, AM1.5d, 25°C

	GaInP	GaAs	Ge
t_{Syl}	89.95%	92.33%	84.69%
ΔI_{sci}	92.72%	92.79%	89.61%

Sylgard was poured as uniformly as possible across the surface, thick enough to cover all the components and the interconnections. The board was then placed in a vacuum oven for 35 minutes at 100°C to cure the Sylgard solution. The whole encapsulation process was completed in less than 90 minutes, as per Sylgard datasheet's requirement.

5.7 Improving safety and transportability

After the production of the first prototype, it was decided to increase the size of the aluminum base of the IMS in order to improve the handleability: one centimetre was added to each side (Figure 118), leading the dimensions to 282.5mm×275.0mm. This modification increased the safety in handling the board, by reducing the risk of damaging the components and the wires when touching the edges (Figure 119).
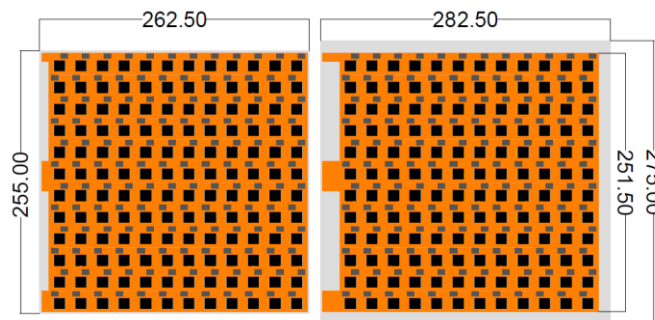
Figure 118 - Comparison between the geometries of the prototype and the final board. Dimensions are in mm.
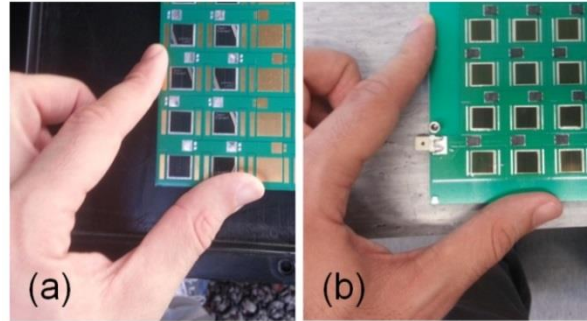
Figure 119 - Particulars of the edges of the boards: the prototype design (a) and the improved one (b).

Moreover, four holes were drilled on the edges of the aluminum for transportation purposes. One female-female standoff was placed between two boards and fixed to them through M3.5 screws inserted in the holes (Figure 120a). This way, two boards were safely packed together and the components were protected from hurts (Figure 120b). Once the plates were delivered, screws and standoff were removed and the holes were used for assembling the receiver.
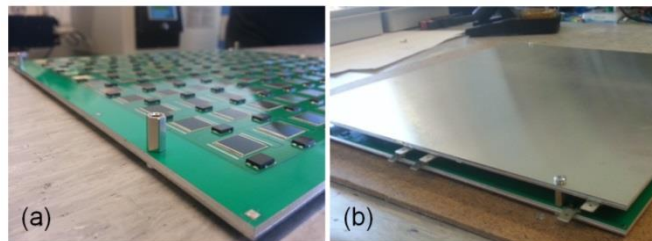
Figure 120 - The standoff placed on a cell assembly (a) and two packed assemblies (b).

The assembly was initially conceived to be mounted on a thick aluminum layer, which would have been in contact with the channels of the water-based cooling system. In the final design instead, in accordance with the requirement of the Indian Institute of Technology Madras, the thickness of the aluminum baseplate was increased to 3mm. This way, the substrate had enough strength to resist to the water pressure without any additional aluminium layer. Removing one additional structure layer and one thermal interface material decreased the thermal resistance of the receiver, and was then expected to improve the thermal performance of the whole system.

5.8 Conclusions

This chapter described the design and the fabrication of a new, densely packed assembly for 500× CPV applications, developed on an insulated metal substrate.

This assembly was a novelty for the unique low-resistance design of the conductive layers and the application of IMS represented a step ahead towards the awaited cost-cutting for CPV. The receiver was designed to accommodate 144 cells and to work at a peak power output of $2.6kW_e$. Although a number of publications emphasized on the design of new, high efficiency CPV receivers, a lack of information on CPV fabrication was recorded. Manufacturing strongly influenced the performance, the durability and the cost of a system, especially in CPV, where requirements for small volumes, high electrical power densities and high heat fluxes had to be satisfied. Due to the large number of cells and the high concentration, the leading issues were to design a receiver able to handle the large waste heat generation, to keep high electrical performance and to assure long term reliability of the system. The geometry of all the components was designed to fit the requirements of the standards and to grant acceptable thermal management and electrical performance to the assembly. The shape of the electrically conductive layer was conceived to minimize the electrical resistance, by reducing the number of interconnections. The simple design could be used in different applications with few changes: it could be easily scaled to be used in a more or less populated configuration. All the assumptions and the analytical investigations made during the design stage have been reported in the text. Schottky diodes were employed in the receiver to avoid damages to shaded cells and to reduce the power losses in case of current mismatch among different series-connected cells. The diodes were slightly oversized, consistently with the safety factors applied in commercial applications, in order to ensure better performance and a longer life to the device. Aluminum wires were bonded to interconnect the cells and the conductive layers: they were sized to safely work even in presence of overcurrents. In the following chapter, the results of experimental tests on the reliability of the components and the interconnections, and the electrical characterization of the produced assembly are described.

Chapter 6: **Densely packed cell assembly: analysis and characterization**

This chapter describes the tests conducted on the materials and on the components of the large receivers. The interconnectors and the cell's die attach are studied applying standard electronic tests, a microscope image allowed to visually inspect the solder paste distribution below the solar cell, and some experiments are conducted on the encapsulant to prove its reliability. Both indoor and outdoor characterizations of the assembly are presented to complete the survey about the reliability of the designed product. In conclusion, an analysis of the costs is introduced, along with some considerations on how the economy of scale affected the fabrication.

6.1 Introduction

The design and the choice of the materials and the components of the cell assembly were carried out to optimize the performance of the system and, at the same time, to limit the expense. Similarly, the manufacturing processes were selected to achieve the highest quality. CPV systems were expected to survive 20+ years in outdoor conditions [345], and, thus, engineering testing of components was generally recommended. The die attaches were reported to be one of the major causes of failure [25]: for this reason, firstly, the strength of the cell's soldering was appropriately tested following the guidance of international standards. Similarly, the bonding strength of the interconnecting wires was proven. The thermal stresses due to different coefficients of thermal expansions were also investigated. The high resistance of IMS to thermal cycles had been already proven in literature [73], whereas the high thermal expansion coefficient of Sylgard could have led to failures: for this reason, it was experimentally studied and the results are commented upon in the chapter. In addition to the mechanical concerns, the electrical performance of the assembly was tested: an indoor, one-sun characterization was conducted to firstly check the quality of the electrical circuitry. After success in these tests, the assembly was mounted outdoors to carry out a full scale investigation. The preliminary results of this test are presented in the chapter. The main goal of the CPV community is to delivery reliable, high-

efficiency and cost-competitive systems for power generation. In this light, the chapter ends with an analysis of the costs of the CPV: a breakdown of the expenses is reported and compared with the data available in literature. Systems such as the CPV are strongly affected by the economy of scale: it was found that a production of a larger number of assemblies would have lowered the prices of the systems.

6.2 Quality tests

In order to prove the quality of the fabrication processes, some tests were carried out on the components of the assembly. The die attaches and the interconnectors were analysed through both visual inspection and standard destructive tests. A thermal test was then conducted on the encapsulant, to study the effects of the thermal expansion.

6.2.1 Solder paste inspection

The design of the paste mask was optimized to improve the adhesion between the cell and the copper and to prevent the presence of voids in the solder joint. The die attach was monitored through a visual analysis and a die shear strength test [365,366]. The full visual analysis was conducted taking a cross-sectional Scanning Electron Microscope (SEM) scan. The low vacuum SEM (JEOL JSM-5400LV) used an electron beam to examine the sample and produce digital photomicrographs with a resolution of 1µm, displayed in Figure 121. The cross-sectional scan showed a uniform solder paste distribution between the cell and the mounting pad.
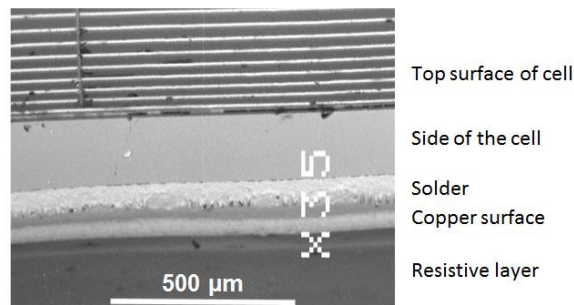
Figure 121 - SEM cross sectional photomicrograph of the cell assembly.

After the visual investigation, a mechanical test was conducted: the die shear strength test. In this test, a force was applied using a linear motion tool, moving along the plane of the substrate and perpendicularly to the cell (Figure 122). The force needed to break the joint was registered, and, according to the latest microelectronic standard MIL-STD-883 [367], any die area larger than $0.04cm^2$ shall have withstood a minimum force of $4.9kg_F$ without any separation.
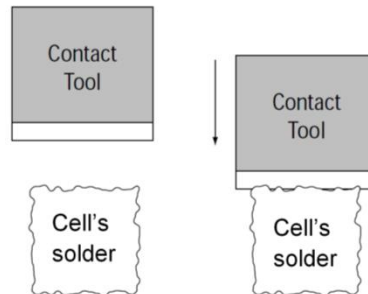
Figure 122 - Schematic of the die shear strength test, adapted from [365]**.**

Five single cell assemblies were used to carry out the tests. The cells were found to break before the solder joints, under an average force of $10.337kg_F$, and a minimum force of $5.998kg_F$ was experienced. All the samples successfully passed the test, as for the standard's requirements.

6.2.2 Wire bonding strength

A wire bond pull strength test was then carried out to check the quality of the interconnections. In this test, a hook pulled the wire in a direction normal to the substrate (Figure 123), while the cell assembly was clamped. According to the standards [368,369], 32μm aluminum wires should have not failed under forces smaller than $3g_F$.
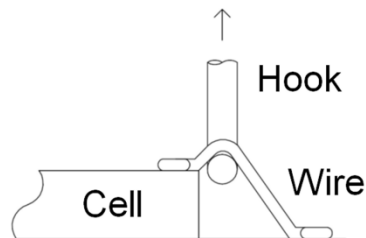
Figure 123 - Schematic of the wire bond pull strength test.

Out of fifty wires tested, only one wire was found to break below the minimum requirement, at $2.954g_F$. All the remaining wires successfully passed the test, with

an average load of 10.169g_F and a standard deviation of 2.244g_F. As shown in Figure 124, the wires predominantly broke in connection with the substrate bond. In almost 30% of the cases, however, the wires were found to lift from the cell's tab, under an average force of 7.861g_F. The registered failure happened because of lifting and was probably due to solder paste contamination left on the cells. Overall, the average force needed to break the wire on the substrate bond was 11.102g_F, more than twice the minimum force required by the standards. The number of failures was lower than the surplus of wires installed on the cell, and proved the reliability of the interconnections.
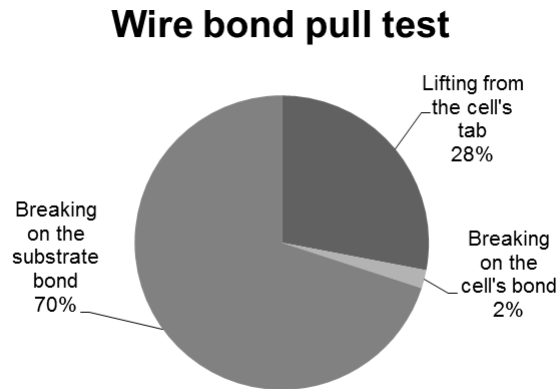
Wire bond pull test

Figure 124 - Causes of the wire breaking during the wire bond pull test results.

6.2.3 Thermal expansion of the encapsulant

Despite the operating temperatures usually ranging between 50 and 80°C [143,148], CPV cells can face temperatures up to 150°C while in operation. Among the board's components, Sylgard presented the highest coefficient of linear thermal expansion (CTE, $\alpha_{Syl}=3.1\cdot10^{-4}K^{-1}$): its CTE was about one order of magnitude higher than that of aluminum ($\alpha_{Al}=2.3\cdot10^{-5}K^{-1}$). Considering a pouring temperature of 25°C and the maximum board length of 26.5cm, linear thermal expansions of 2.8mm and 10.2mm were expected at 60°C and 150°C respectively. In the same temperature range, the linear thermal expansion of aluminum spanned between 0.21mm and 0.75mm. A simple visual experiment was then conducted to quantify the effect of the thermal expansion on the board, using the FLIR T425 infrared thermal imaging camera and pouring Sylgard on the surface of a non-populated assembly. The setup is shown in Figure 125: the test board was placed in the
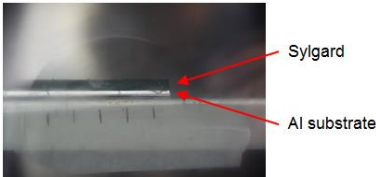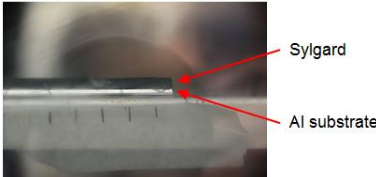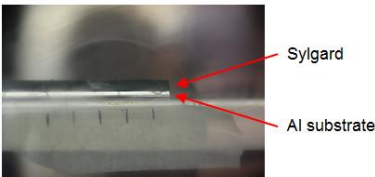
vacuum oven, a digital camera was used to record the expansion of Sylgard and the thermo-camera was employed to check the temperature of the board.

Figure 125 - Setup of the thermal expansion experiment

The test was carried out raising the oven's temperature from the ambient temperature of 30°C to the maximum temperature of 150°C. The temperatures were set using the oven's controls, but the real temperature of Sylgard was measured through the thermal imaging camera. The emissivity was set to 0.86 for Sylgard [370]. The digital camera was used to record the images of the sections of Sylgard at different temperatures. The investigation, whose results are summarized in Table 31, did not show any effect of the expansion due to the rise in temperature, because of the high bonding strength between the Sylgard and the surface of the cell assembly.

Table 31 - Images of the visual inspection conducted to check the thermal expansion of Sylgard.

Oven temperature: 30°C Sylgard temperature: 28.5°C	Oven temperature: 100°C Sylgard temperature: 98.5°C	Oven temperature: 150°C Sylgard temperature: 144°C

6.3 Indoor characterization

In order to quickly verify the reliability and the quality of the assembly before installing it in outdoor conditions, an indoor characterization was conducted using the WACOM solar simulator. Due to the dimensions of the assembly, the characterization was carried out only at one sun under the following conditions: 1000W/m^2 DNI, AM1.5, and 28°C temperature. The measured I-V curves are shown in Figure 126: the two series of the boards were separately characterized

and therefore named A and B, because the I-V tracer could not work with voltages higher than 300V. In this study, it was not possible to vary the irradiance, because of the impossibility for the I-V tracer to measure at the same time currents lower than 10mA and voltages higher than 30V, as previously shown in Figure 40.
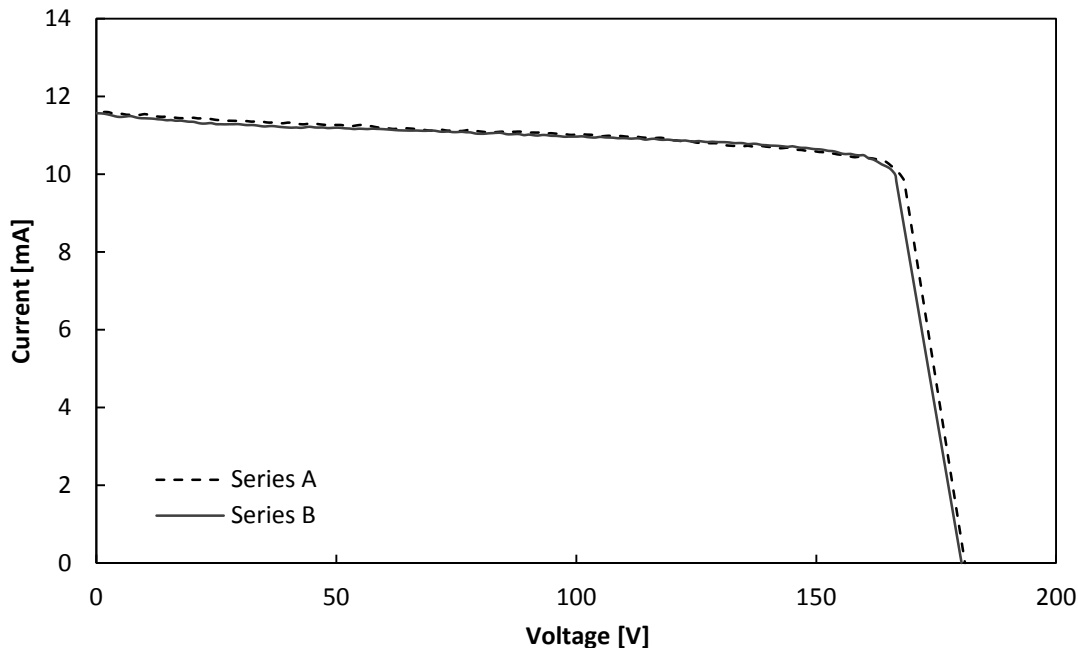
Figure 126 - I-V curves of the series of the fabricated assembly at 1× under 1000W/m² DNI, AM1.5, and 28°C temperature.

A short-circuit current of 11.6mA was measured and open circuit voltages of 181V and 180V were recorded for the two cell series on the assembly. The discrepancy in the voltage outputs was probably due to the hand-placement of the components and to the solder paste contamination found during the wire bonding. The fill factor ranged between 80.3% and 80.9%. The high values of fill factor proved a low series resistance in the board, whereas the shape of the I-V curve meant that the fabrication was properly realized: the lack of steps in the curve was due to the good connections and to the absence of mismatches between the cells.

The measured outputs, shown in Table 32, were compared with those of the AZUR SPACE's 3C40A single-cell assembly tested in the same conditions. The average outputs of each cell of the large cell assembly were calculated and the I-V curves are compared in Figure 127.

Table 32 - Electrical outputs per cell of the two series of the produced cell assembly, compared with those of the commercial 3C40A assembly, under AM1.5, 1000W/m², at 28°C.

Assembly	No of cells	I_{sc} [mA]	V_{oc} per cell [V]	P_{MPP} per cell [mW]	I_{MPP} [mA]	V_{MPP} per cell [V]	F.F.
Series A	72	11.57	2.50	23.58	10.31	2.29	0.814
Series B	72	11.59	2.51	23.38	10.32	2.26	0.801
3C40A	1	12.11	2.58	25.64	11.00	2.33	0.820
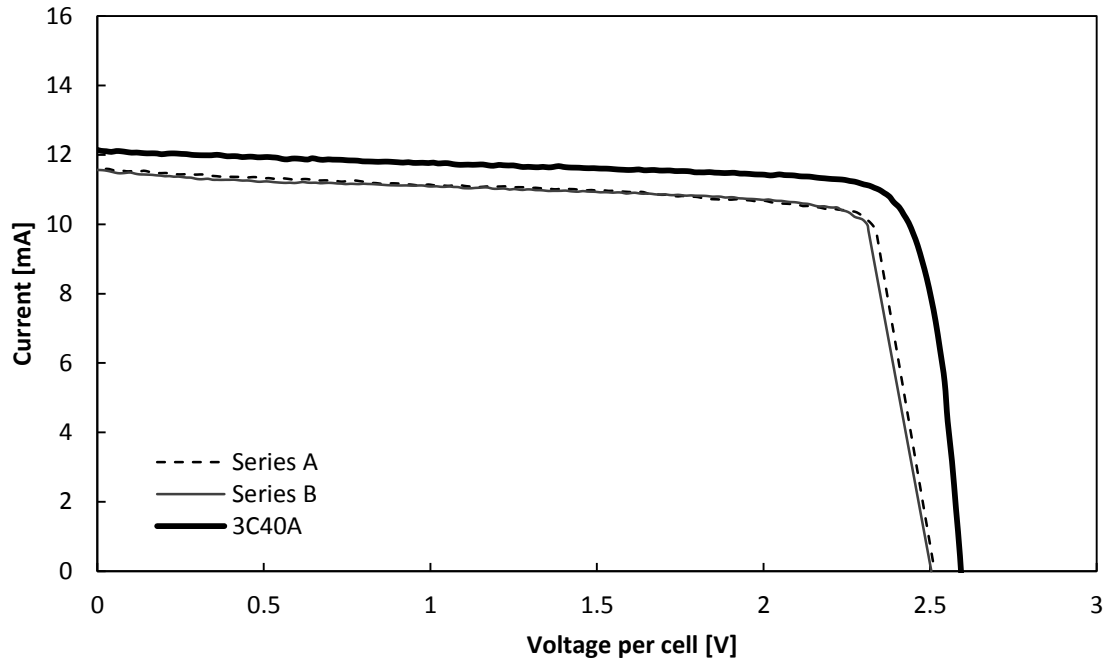
Figure 127 - Comparison of the I-V curves of one of the cells mounted on the large cell assembly and that of the 3C40A single cell receiver produced by AZUR SPACE. The curves are measured in the same conditions: 1× under 1000W/m² DNI, AM1.5, and 28°C temperature.

For a better prediction, the measured values were refined to simulate a full scale characterization. In the following numerical investigation, the values of the series A only were considered: an average open circuit voltage of 2.50V per cell was generated. The equations reported in [359] were used to estimate the performance of the cell assembly at the designed 500× concentrations. The intensity of the current (I) at any concentration (X) was estimated as:

$$I(X) = X \cdot I(X = 1) \tag{52}$$

The voltage (V) was instead obtained according to

$$V(X) = V(X=1) + \frac{n \cdot k_B \cdot T}{q_{el}} \ln(X) - I(X) \cdot R_s \qquad \textbf{(53)}$$

where n is the ideality factor, k_B is the Boltzmann's constant ($1.38 \cdot 10^{-23}$J/K), T is the cell's temperature, q_{el} is the elementary charge ($1.60 \cdot 10^{-19}$C) and R_s the series resistance of the circuit. Cell's ideality factors are influenced by recombination and concentration ratio [371]. For multijunction cells, which consisted of a stack of series-connected cells, the ideality factor usually ranged between 3 and 4 [359]: an average factor of 3.5 was considered for this application. The measurements were conducted at a temperature of 28°C, 3 degrees higher than the standard one. For this reason, the values obtained by (52) and (53) were corrected according to the temperature coefficients reported in the cell's datasheet [117]. R_s was calculated as described in Section 5.5.

A minimum short-circuit current of 5.77A and an average open circuit voltage per cell of 3.08V were predicted at 500×, under CSTCs. The current and the voltage measured for the large receiver were respectively 4.80% and 2.06% lower than those obtained for the commercial single-cell assembly under the same conditions [372]. This discrepancy was justified by the difference in the cell's number between the 144-cell plate and the single cell receiver and by a potential non-uniformity in the solar simulator irradiance, which affected the largest assembly only.

Table 33 - Refined electrical outputs of the two series of the produced cell assembly, compared with those of the commercial 3C40A assembly for a concentration of 500× under AM1.5, 1000W/m^2, at 25°C.

	I_{sc}(500×) [A]	$V_{oc\text{-}cell}$(500×) [V]
Series A	5.77	3.08
Series B	5.78	3.09
3C40A	6.04	3.16

In a similar way, the maximum power point values were predicted. At 500×, each cell was expected to work at a maximum power point power of 14.7W, achieving, under 1000W/m^2 DNI, an efficiency of 29.4%. The commercial assembly instead reached an efficiency of 31.9%. The difference between the two efficiencies was due to the dimensions of the tested boards: the larger assemblies were expected to be more affected than the single cell receiver by any non-uniform light flux

generated by the simulator. Moreover, the larger number of components increased the risks of manufacturing imperfections and, thus, the related losses.

The cell's datasheet reported a peak efficiency of 37.2% at 500×, under standard test conditions. The discrepancy between the cell's and both the assemblies' efficiencies was probably partly due to the spectrum of the simulator, which was optimized for silicon cells, whereas was less performing when triple-junction cells were tested. Moreover, the characterization was conducted at one sun, instead of at full 500× scale: the cells were designed to work at high concentrations, so they were expected to behave differently at one sun.

6.3.1 Improving the performance: higher-efficiency cells

In 2013, AZUR SPACE introduced a new $1cm^2$-sized MJ cell [144], named *3C42*, with a peak-efficiency of 40.3% at 500× under standard conditions (Table 34).

Table 34 - AZUR SPACE's 3C42 cell's performance. Data are reported for AM1.5, 1000 W/m² DNI, T= 25°C conditions at 500× [144]**.**

Cell (year)	Efficiency (%)	Short circuit current (A)	Open circuit Voltage (V)	Power at MPP (W)	Fill factor
3C40 (2011)	37.2	6.587	3.17	18.6	89.1
3C42 (2013)	40.3	7.39	3.11	20.25	88.1

One prototype of the large assembly was produced using these higher-performance cells. The new board was fabricated with the same procedures presented before. The cell short-circuit current increased from 6.587A to 7.39A: the width of the conductive layer was still sufficient to let the system safely work. In this case, the characterization was carried out at one sun under the following conditions: 900-1150W/m² DNI, AM1.5, and 28°C temperature. The I-V curves of the two series are shown in Figure 128. As expected, the open circuit current and the power at maximum power point were found to increase according to the irradiance, whereas the variation in open circuit voltage was found to be negligible.
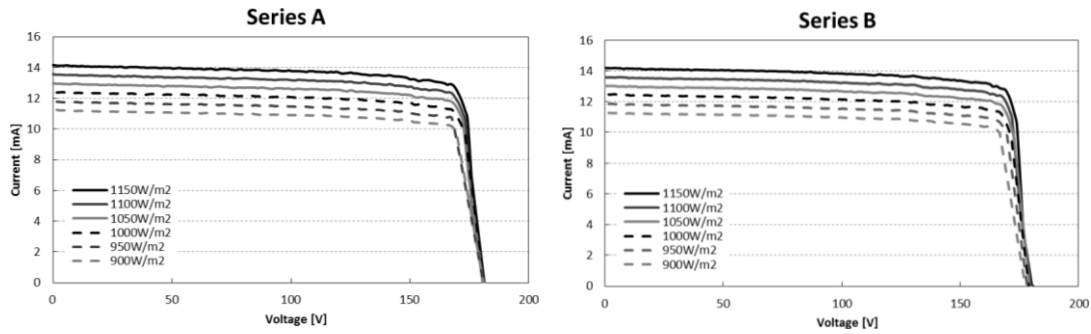
Figure 128 - I-V curves of the two series composing the produced board. Testing conditions: DNI 900-1150W/m^2, AM1.5, and 28°C temperature.

A comparison of the performance of the old and the new boards is shown in Figure 129: in line with the values reported in the datasheet [144], the new cells enhanced the short-circuit current and the maximum power output, while no significant variations in voltage was found. The fill factor instead increased up to the 84%, achieving an absolute improvement of more than 3% compared to the previous boards. Using the same procedure employed before, the efficiency was found to increase up to the 32.4%.
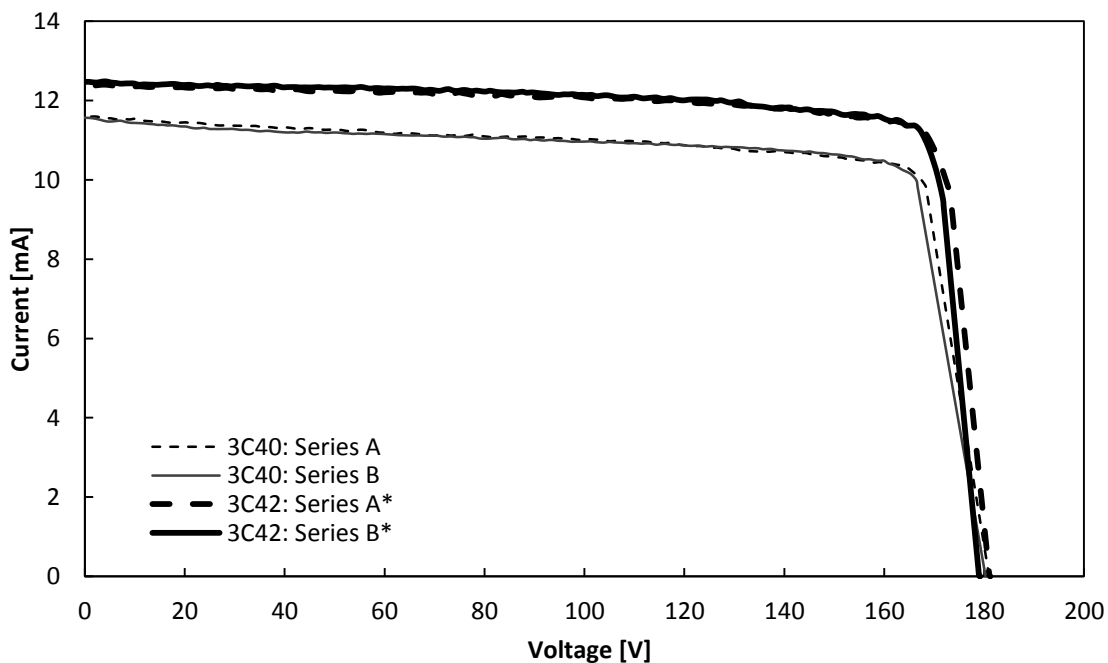
Figure 129 - Comparison of I-V curves for the fabricated assemblies at 1× under 1000W/m^2 DNI, AM1.5, and 28°C temperature.

6.4 Outdoor characterization

6.4.1 Limits of the indoor characterization

In a real full-scale scenario, a combination of optical, mismatch and Ohmic losses, along with the impacts of the temperature and the spectra, can occur and negatively affect the performances of the system [363]. The indoor characterization was a fast and cost-effective testing procedure, but a lack of appropriate characterization instruments for CPV systems had been already pointed out by previous researchers [373]. Solar simulators were widely used for flat plane photovoltaics, but presented some issues when used for concentrating photovoltaics: these difficulties were mainly related to the spectrum, the beam collimation, and the size. Firstly, due to the multi-junction cell's geometry, which consisted of three series-connected subcells, replicating the spectrum in the most realistic way became particularly important to limit any current mismatch. Solar simulators were classified on the basis of the spectral match: the spectral match was determined by measuring the deviation of irradiance share for different portions of the spectrum in the range between 400nm to 1100nm [374]. The best performing solar simulators had spectral matches ranging between 0.75 and 1.25 as compared to the AM1.5G standard spectrum. The gap between the real spectrum and the simulated one was one of the causes of discrepancies between experimental and real data. Secondly, the reproduced solar beam should have had an angular size similar to that of the Sun ($\pm0.275^0$) [375]. Flat PV was not affected by this phenomenon and, thus, conventional simulators did not reproduce this behaviour, whereas the beam collimation had already been pointed out as possible cause of optical losses and mismatches between the results of CPV indoor and outdoor tests [376]. In 2008, the first solar simulator for triple-junction cells in a CPV system was presented by Domínguez *et al.* [377]: it replicated the light collimation, but could not accept CPV modules larger than 2 meters in diameter. Thirdly, CPV systems could reach concentrations of thousands of suns, meaning that out-sized reflective or refractive areas could be needed when densely packed systems were considered. In this application, the primary concentrators sized

3m×3m and an outdoor characterization was the only way to conduct a full scale investigation on the performance of the assembly.

6.4.2 Preliminary tests

The first prototype of the board was delivered in November 2013 and then firstly outdoor tested in April 2014, in the facilities of the Indian Institute of Technology Madras, India. The overall system is shown in Figure 130: each pillar supported two modules, each one equipped with a primary and a secondary optics and the receiver plate. Two 4m×4m mirrors were installed, instead of the designed 3m×3m concentrators. A ceramic plate replaced one of the receivers and was used to identify the focal point of the reflectors.

Figure 130 - Experimental setup: the ceramic plate on the left hand side mirror and the receiver on the right hand side one.

A set of thermocouples were installed on the plate and connected to the control room. The electrical outputs of one 72-cell series were measured using a Mastech

MS8217 digital multimeter (for the voltage) and an Escort ECT-689 clamp-on meter (for the current), both shown in Figure 131.
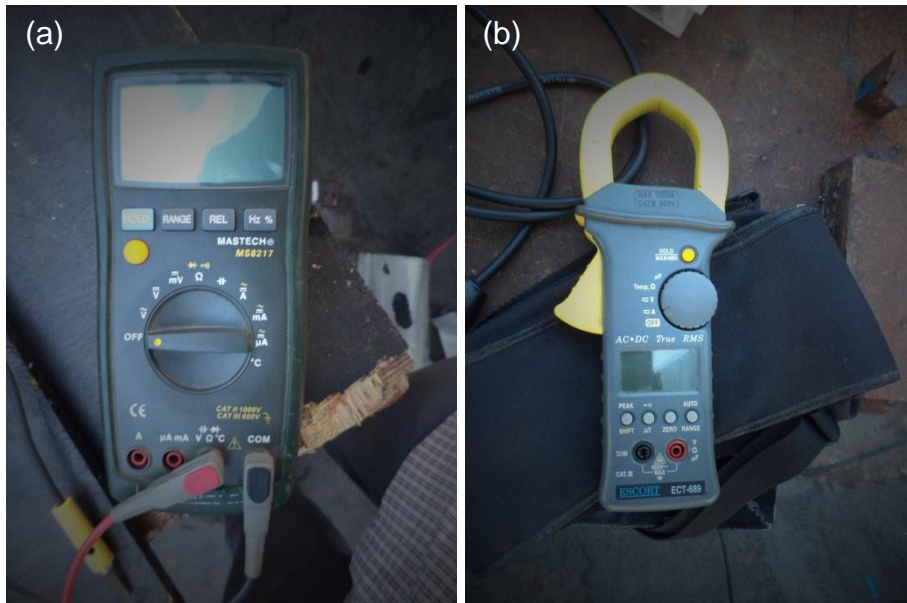
Figure 131 - Multimeter (a) and the clamp-on meter (b).

Since the I-V tracer had not been delivered, five 10W light bulbs were initially used to check the flow of current. The bulbs were connected in parallel to the CPV, along with a voltmeter. Each bulb had its own switch, to be independently connected or disconnected (Figure 132).
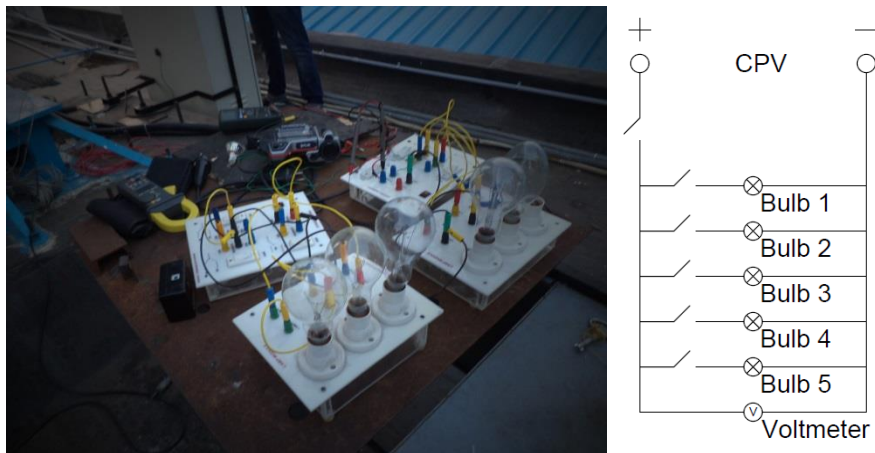
Figure 132 - A picture and a schematic of the five bulbs system.
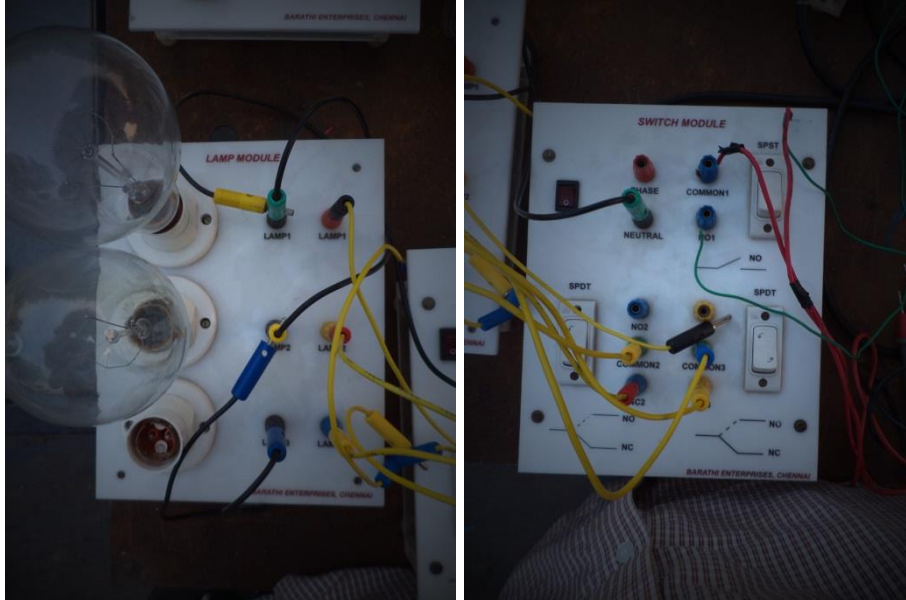
Figure 133 - Two bulbs on the left side and the control panel on the right side.

A first test was conducted at 500× using both the concentrators. No current was shown, whereas a voltage of about an open circuit voltage of 180V was registered when the board was on focus. When the bulbs were connected, the voltage was found to drop, no bulbs were illuminated and the instruments did not show any current. A non-uniform illumination appeared on the secondary (Figure 134), raising doubts about the matching between the 4m×4m primary and the secondary, designed for a 3m×3m primary optics.
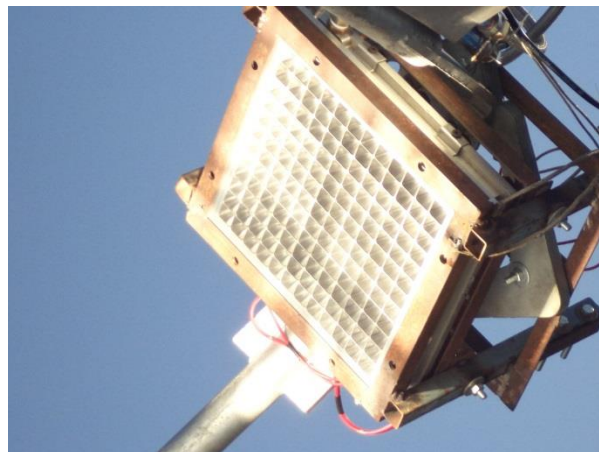
Figure 134 - Non uniform illumination on the secondary.

Since no current was flowing and in order to overtake any potential problems due to the optic mismatch, the secondary concentrator (Figure 135) was removed to visually check the illumination over the cells.

Figure 135 - The plate mounted without the secondary.

Without the secondary, the heat sink could be fixed only if the pipes and the pumps were removed. So, no active cooling was applied in this primary-optics only configuration. A thermocamera was then used to instantaneously measure the temperature of the plate, in order to be able to stop the test when the board reached a temperature of 150°C.

A new test was conducted under natural sunlight at 440W/m^2 DNI, 28°C ambient temperature. An off-track voltage of 150.8V was measured. Once on-track, four complete rows of cells (two per series) were still shaded both in vertical and in horizontal directions, as clearly shown in Figure 136.
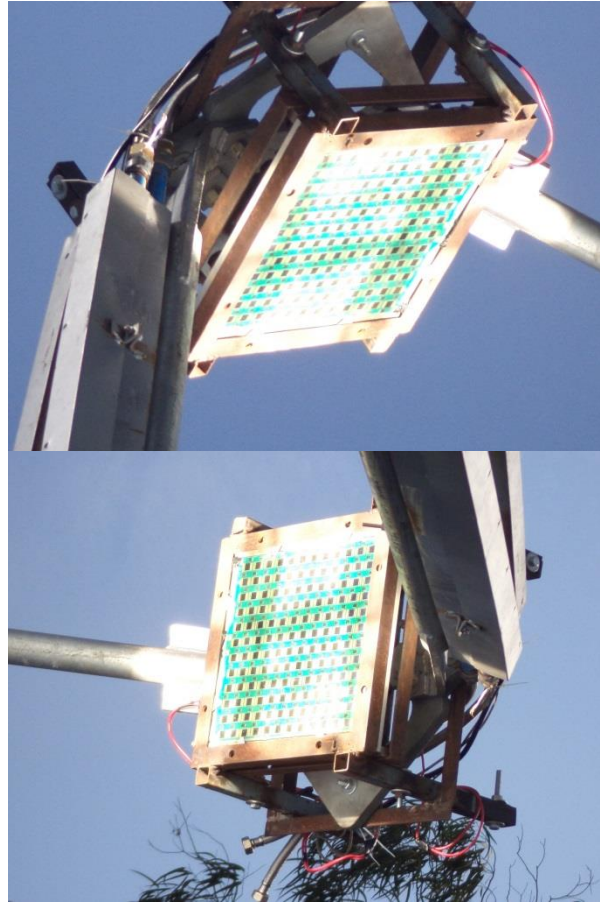
Figure 136 - The non-uniform illumination on the board.

When the tracker moved the plate in the focal point, no current was measured by the instruments, but some current was flowing in a 10W bulb used as load, as shown by red filament in Figure 137. The voltage dropped down to few units (4-5V).

Figure 137 - The current flowing in the central bulbs.

The presence of open circuit current and of a low current in the bulbs was considered a first positive sign, since the electronic circuit did not seem to be damaged by the current flow. The cause of the low performance was addressed to the strong shading, but more information could be obtained with a more accurate electrical performance reading. For this reason, for the following test, four resistors (Figure 138), one analog amp meter and one analog volt meter (Figure 139) were mounted. During the tests, the resistors had to be manually set to change the resistance and no digital output was coming out from the instruments: this system was fine for a qualitative test, not for a quantitative one.

Figure 138 - The four rheostats.

Figure 139 - The Amp and Volt meters.

A few-second test was conducted at 125✕ (without the secondary), getting a maximum current of about 1A and a voltage of 50V per series. During the tests, at least three rows were found to be not illuminated: 18 cells out of 72 per series were by-passed, as shown in Figure 140. Considering a DNI of 750W/m^2 (measured

global irradiance: 840W/m^2), and a geometric concentration of 125 suns, the illumination on the board was about 18.8% of that reported in datasheet for 1000W/m^2 and 500**×**. Considering a linear relation between irradiance and current [11], a short circuit current of about 1.24A was expected. The efficiency of the concentrators might be one of the causes of the lower registered value. Apart from the shaded cells, the low voltage (0.93V per non-shaded cell) might be due to some resistances in the contacts between the board and the instruments, as well as to the high cell temperatures.

Figure 140 - The non-uniformly illuminated board

A uniform illumination and an adequate temperature controlling systems are required when the CPV modules are rated. In this case, the use of a primary concentrator larger than designed and the combination of non-uniform irradiance and lack of active cooling compromised the tests and led to the damaging of the board. The cell temperature could not be checked properly and, due to the hot spots, four cells were found to be broken (red square in Figure 141). So, it was decided not to conduct any further test before the concentrators and the active cooler had been fixed. At the time the thesis was submitted, no outdoor characterization had been completed yet.
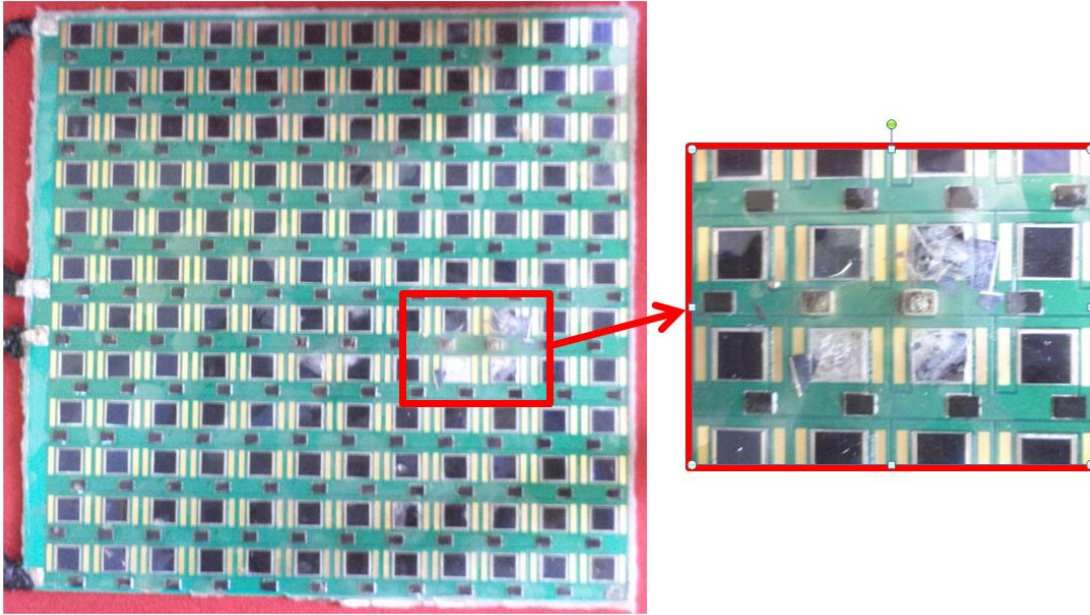
Figure 141 - The damaged board and a zoom on the four damaged cells.

6.5 Cost analysis

The price of a CPV system was expected to be as low as $1.20/$W_p$ by 2020 [378]. In 2013, an average price of $2.62/$W_p$ was reported [379] whereas, at the time the thesis was submitted, the cost was ranging between $1.55/$W_p$ and $2.42/$W_p$ [31]. In 2011, the module still represented 41.5% of the whole CPV cost [378]. This quote included the optics, the cell assembly and the cooling system. In the present work, the cell assembly only was considered and was fabricated with an expense of £0.57/W_p, which, at the time of the fabrication, corresponded to about $0.91/$W_p$, the 34.7% of the full module's average price in 2013[i]. It is interesting to report a cost breakdown of the presented cell assembly (Figure 142). The largest part of the expenses was due to the multijunction cells, whose price was strongly influenced by the volume ordered. The other components (diodes and interconnectors) represented about a fourth of the overall price. The remaining part was due to the aluminum board and to the workload required for assembling.

---

[i] Conversion rate for November 2013: £1=$1.610311 (Source: X-rates[TM])
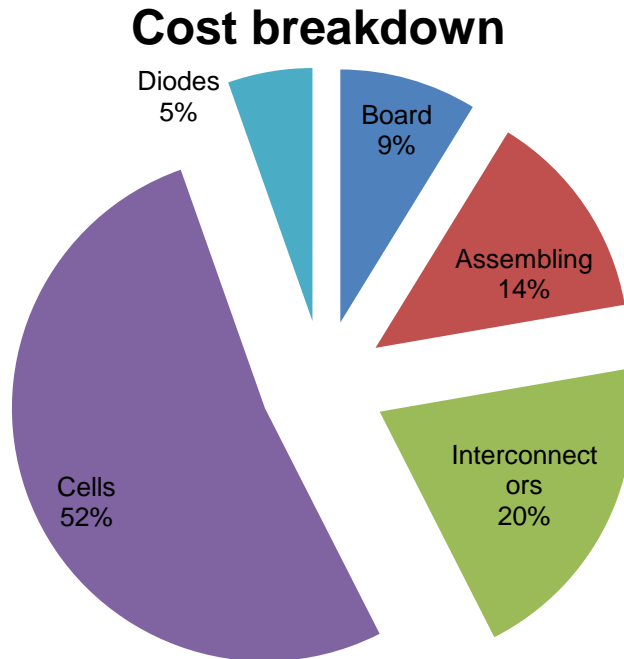
Cost breakdown

Figure 142 - Cost breakdown of the produced cell assembly

The development of prototypes and the low volume fabrication usually present higher costs than the high-quantity production. This is due to the inverse proportionality between the cost and the quantities of materials and components. All the components used in this work were influenced by the economy of scale: according to the prices of components used in this application, a drop of 17% in the total cost of a single cell assembly could have been achieved by increasing the number of units, only because of the reduction in the component's cost per unit. Moreover, a small scale fabrication usually limits the possibility of exploiting automatic processes that generally require longer setting times, but eventually enable lower cost for large volumes productions.

6.6 Conclusions

After the description of the fabrication, the results of the tests conducted on the receiver's prototypes to prove the reliability of the design and the components were reported in the chapter and commented. Along with a visual inspection, both the die attaches and the bonded wires were tested using the destructive tests described by international standards. The cell's soldering showed a bonding strength almost twice higher than the minimum requirement of the standards.

Similarly, the results of the wire bonding strength test proved the reliability of the interconnections, with a rate of failures fully balanced by the safety factor considered during the installation. An experimental investigation was conducted to understand the effects of the thermal expansion on the encapsulant. The receiver were then indoor tested and showed a short circuit current of 0.011A at one sun and an open circuit voltage of 2.5V per cell, similar to the one exhibited by a commercial receiver under the same conditions. A peak efficiency of 29.4% was predicted at 500× and the fill factor ranged between 80.1% and 81.4%. The efficiency and the fill factor were improved up to 32.4% and 84% respectively by using more efficient cells. A full scale outdoor characterization was being undertaken at the time this work was conducted, to test the durability of the materials and their resistance to cycles. A preliminary outdoor characterization was attempted and was described in the chapter, but no further results were yet available: the cooling and the concentrating optics had to be firstly fixed and tested before conducting an appropriate electrical characterization at full scale. For a more complete analysis of the fabrication process, a summary of the costs have been reported and commented. The scale economy strongly affected the production of CPV cell assemblies: in this case, the price of the cell assembly would have been decreased by the 17%, if the number of produced units was increased.

Chapter 7:   **Natural convective micro-fins for high CPV receivers cooling**

This chapter investigates the opportunity of integrating a micro-passive cooling system in a HCPV receiver. The results of an original experimental investigation and the data available in literature are merged and analysed to first better understand natural convection at the micro-scale. After an initial investigation on the correlations among geometry, orientation and heat transfer coefficient at micro-scale, different heat sink metrics is considered, such as the fin effectiveness and the mass specific heat transfer coefficient. The introduction of micro-fins is found not to be always beneficial in terms of heat transfer, although always positive in terms of material usage. Moreover, the results of the investigation are used to identify the most effective micro-fin geometries for HCPV passive cooling: a thermal model is developed to prove their efficacy compared to conventional macro-scaled heat sinks. Overall, micro-fins are found to be particularly advantageous in those applications requiring a minimized weight of the heat sinks, such as concentrating photovoltaics.

7.1 Introduction

The temperature of any CPV cell needs to be minimized in order to enhance the electrical efficiency, to limit the thermal stresses, and to avoid mechanical damages. The low operating temperature is not the only goal that a CPV cooling system needs to achieve. The uniformity of the temperature has to be considered as well, both for single cells and for series of connected cells. Temperature gradients across the cell are generally due to non-uniform illumination on the active area, cause power losses and may lead to damage [35]. Series-connected cells working at different temperatures generate different currents and the overall series current is limited by the least performing cell. An optimal CPV cooling system should prevent the occurrence of current-mismatch due to non-uniform temperature. Moreover, the cooler is generally required to be simple, in order to assure high reliability and not to strongly affect the CPV plant cost. A reliable system is essential: any failure can cause damage to the cells and long interruptions to power generation.

After having investigated the electrical properties of a densely packed receiver, this chapter focuses on the opportunity of employing a micro-passive system for cooling a single cell high-CPV receiver. In the literature review, the micro-fins were found to be one of the most promising solutions to improve the CPV cooling. The effects of the CPV system's geometry and cell's size on the thermal behaviour were previously described, and a silicon wafer was found to be the most appropriate substrate to develop a single cell CPV receiver with an integrated passive cooling system. Due to the limited number of publications available on the performance of micro-fins in natural convection, an experimental investigation was initially conducted to examine the correlations between the fin geometry and the thermal performance. Electrically heated micro-fin arrays were tested in a controlled, natural convective environment: the results of the experimental investigation are reported and commented upon and were then used to determine the best solution for passive CPV cooling purposes. To conclude, a thermal model was developed to predict the performance of the designed micro-finned array in HCPV.

7.2 Methodology and scope

7.2.1 Previous investigations

Fins are widely used to enhance the heat transfer from a surface to the surrounding fluid. Despite that, as already reported in the literature review, the studies conducted on naturally convective micro-scaled fins were still limited at the time this work was conducted. Kim *et al.* [251] investigated vertically orientated micro-fins and demonstrated the impossibility of using the macro-fin heat transfer correlations for micro-scaled systems. Mahmoud *et al.* [252] firstly showed the correlation between the fin height, the fin spacing and the heat transfer coefficients. Shokouhmand and Ahmadpour [253] numerically demonstrated that the contribution of the radiative exchange could not be neglected in a micro-fin array. In the light of further contributing to understand the heat transfer phenomena at micro-scale, a preliminary experimental investigation was considered essential.

7.2.2 Experimental setup

The configuration and the validation of the experimental setup was already described in Section 3.6 and shown in Figure 57. In the current study, 1.4mm-thick, 5cm×5cm-sized squared undoped silicon wafers were employed. Eleven different fin geometries were diced and tested, and their thermal behaviours were compared with that of a flat silicon wafer. The micro-fins arrays were firstly designed using AutoCAD and then fabricated through a mechanical dicing machine. The fin dimensions were measured using a microscope and are reported in Table 35, according with the nomenclature shown in Figure 61.

Table 35 - Fin dimensions

Type	Width, W [mm]	Length, L [mm]	Fin thickness, t [μm]	Fin spacing, s [μm]	Fin height, H [μm]	Base thickness, t_b [μm]	Number of fins, N_{fin}
Flat	49.9	49.9	-	-	-	-	-
Plate fin	50.0	49.7	200	200	600	800	121
Plate fin	49.8	49.8	200	200	800	600	124
Plate fin	50.0	49.9	200	400	1000	400	83
Plate fin	50.0	49.9	200	800	600	800	50
Plate fin	49.9	49.9	400	200	1000	400	83
Plate fin	49.9	49.9	400	400	600	800	61
Plate fin	50.0	49.9	400	800	600	800	41
Plate fin	50.1	49.9	800	400	800	600	42
Plate fin	49.8	49.9	800	800	600	800	31
Pin fin	49.8	49.8	200	200	600	800	15376
Pin fin	50.2	50.0	400	400	600	800	3844
Uncertainty	0.05%	0.05%	4%	4%	6%	6%	-

The fin temperature was recorded using the FLIR infrared camera: it was considered constant across the whole volume of the fin array. An overall experimental uncertainty on the calculation of the heat transfer coefficient (Uh_{fins}/h_{fins}) of 8.25% was evaluated: it fell within the range of uncertainties considered by previous researchers, resumed in Table 36. In the present investigation, power inputs of 1.0kW/m^2, 2.0kW/m^2, 2.5kW/m^2, 3.0kW/m^2, 3.5kW/m^2 and 4.0kW/m^2 were supplied to the heater: these values were higher than those previously considered (Table 36) and were closer to the waste heat

generation rates of MJ cells working at 500×. In this experimental setup, it was found that, despite the employment of insulating materials, an average of 26% of the heat in input was dissipated by surfaces other than the fins. This value was higher than those reported for the previous researches on micro-fins [252]: the difference was due to the configuration of the setup. In the present work, similarly to the study on tilted macro-fins in [155], the setup was moved in different orientations, and, so, a limited volume was available for the insulating case surrounding the sample. Moreover, a percentage ranging between 44% and 56% of the heat in input was found to be exchanged by radiation through the fins. This was due to the high emissivity of silicon and to the temperature achieved during the tests, higher than those experienced by previous micro-fins investigations [251,252].

Table 36 - Summary of the radiative thermal transfer and of the losses.

Ref.	Scale	Orientation	Uh_{fins}/h_{fins}	Power density in input	Radiative (Q_r)	Losses (Q_{loss})
Current work	Micro-fins	Tilted	8.25%	1.0-4.0kW	44-56%	26%
[251]	Micro-fins	Horizontal	5.1-6.5%	N.A.	24%	N.A.
[252]	Micro-fins	Vertical	9.4%	0.2-1.0kW	9-13%	6%
[155]	Macro-fins	Tilted	≤5%	0.1-0.3kW	N.A.	24-26%

7.2.3 Motivation of the research

Firstly, the effects of the fin geometry was investigated for power loads not previously considered, in order to give a contribution towards the optimization of geometries for micro-finned heat sinks in natural convection. In particular, the correlation between thickness and heat transfer, which had not been analysed before, was investigated for the first time and commented. The previous micro-fins research used to consider the same conditions, horizontal upward facing or vertical micro-finned heat sinks. In real applications, instead, the designer might be forced to orientate the heat sinks in different, less-effective directions, such as in downward facing position [380]. For this reason, the second scope of this research was to report the differences in thermal performance between an upward facing and a downward facing micro-fins array. The effects of orientations other than horizontal or vertical were considered as well, in order to achieve a wider

understanding towards the application of passive cooling micro-technologies in CPV systems.

7.3 Correlations among geometry and heat transfer coefficient for upward facing oriented fins

7.3.1 Effects of fin thickness, spacing and height

The correlation between fin geometry and thermal performance for upward facing fins array was investigated in order to improve the temperature range considered in [252], which was limited to power loads up to 1W and maximum temperatures in the order of 100°C. The experimental data collected in this study were found to be consistent with the outcomes of the previous research: the values of convective heat transfer coefficient increased when the fin spacing as increased (Figure 143) and the fins height was decreased (Figure 144). As stated by the authors [252], this behaviour was due to the complex relations between the upward and the downwards currents. Increasing the fin height could cause a reduction in the convective motion between the fins, decreasing therefore the heat transfer coefficient. On the other hand, larger fin spacings facilitated the convective exchanges between the fins and the ambient.
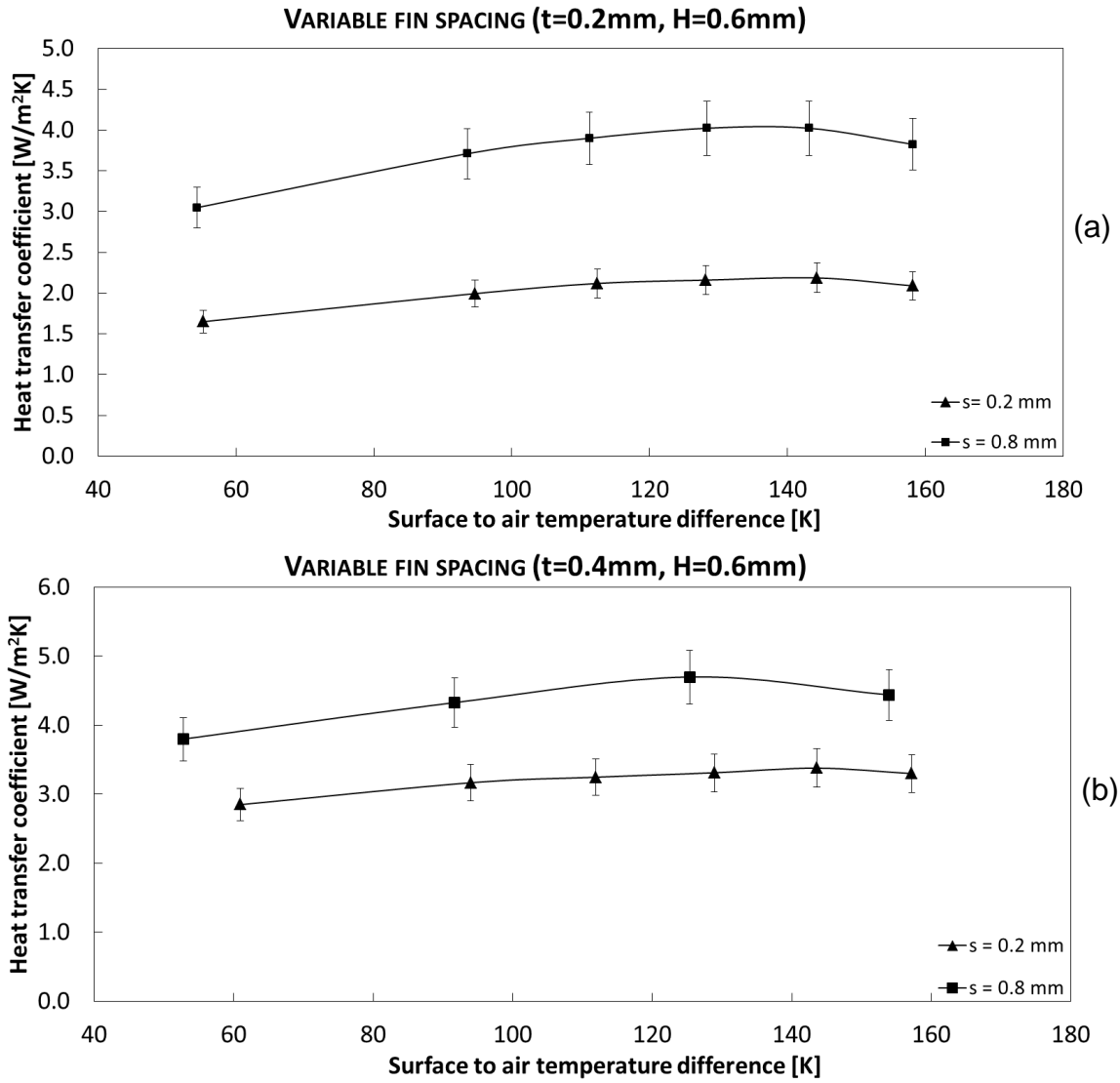
Figure 143 - Effects of fin spacing on the heat transfer coefficient: (a) for t=0.2mm and (b) for t=0.4mm.
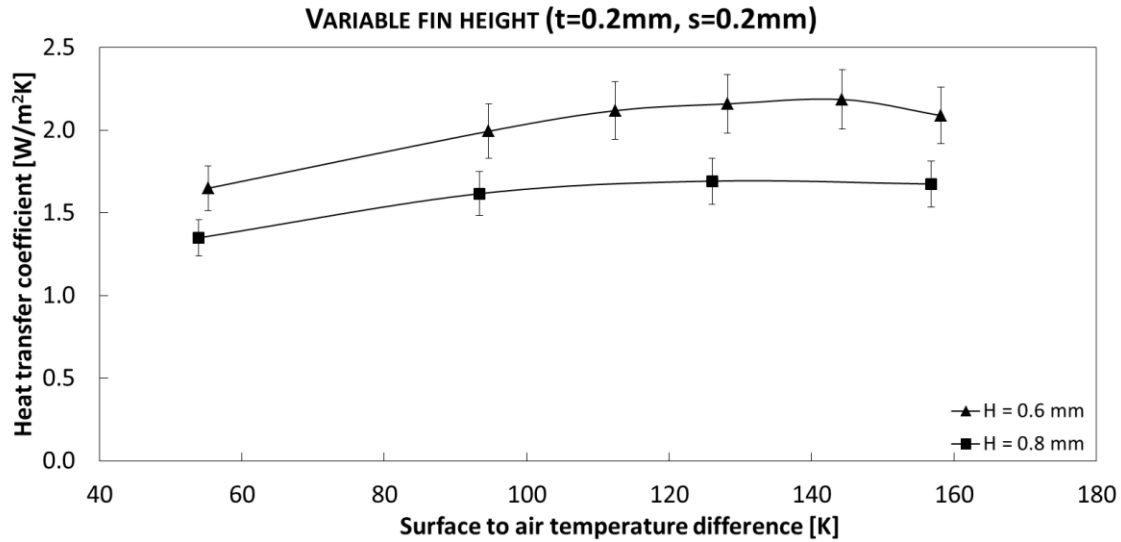
Figure 144 - Effects of the fin height on the heat transfer coefficient.

For the first time, the effects of the fin thickness on the heat transfer were investigated. As shown in Figure 145, the heat transfer coefficient was found to increase when the fin thickness increased. This behaviour can be explained because, at micro-scale, within the narrow air volumes between two adjacent fins, the conduction is dominant over the natural convection [251], and, thus, the air trapped within two micro-fins transfers heat by conduction mainly. The silicon fins and the air volumes are acting as parallel thermally conductive layers along the heat path. Increasing the fin thicknesses while keeping the spacing constant raises the high-conductive volume of silicon compared to the low-conductive volume of air, and, so the overall thermal conductance is enhanced. For this reason, the micro-fin thickness has to be taken into account when dimensioning an optimal micro-finned heat sink and should not be neglected.
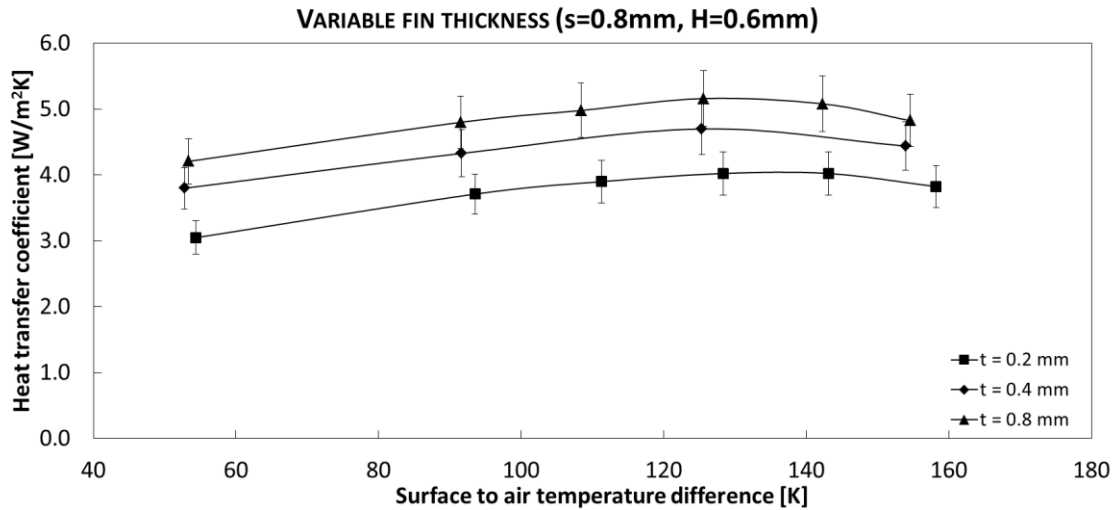
Figure 145 - Effects of the fin thickness on the heat transfer coefficient and the thermal resistance.

As noted by [252], the heat transfer coefficient tends to increase when the temperature increases. Although, at the higher temperature differences experienced in the present study, the enhancement of the heat transfer coefficient was lower and, in each test, the coefficient was found to reach a maximum value before starting decreasing. This was probably due to the viscosity of air that increases with the temperature [329]: the higher the temperature, the more difficult are the convective movements of air and this negatively affect the convective heat transfer. Moreover, the high temperatures benefitted the radiative heat transfer, whose contribution was proportional to the fourth power of the temperature different and, so, grew at higher rate than the convective one when the temperature difference rises. So, at the high temperatures achieved in this work, the radiation became the dominant player for heat transfer. For these reasons, at high temperature differences, the heat transfer coefficients were found to decrease.

7.3.2 Nusselt number correlations

Natural convection conditions are usually described by dimensionless numbers, which make it possible to reduce the number of total variables. Among these parameters, the Nusselt number compares the heat transfer due to natural convection and that due to conduction in a fluid layer [328]. It is generally used to estimate the heat transfer coefficient in natural convective conditions. For upwards

micro-finned array, the following empirical equation was proposed by Kim *et al.* [251]:

$$Nu = 1.18 \cdot \left[Ra_r \cdot \left(\frac{r}{H} \right)^4 \cdot \left(\frac{r}{L} \right)^4 \right]^{0.147} \tag{54}$$

where *r* is the hydraulic radius and the Rayleigh number for micro-finned surfaces is expressed as:

$$Ra_r = \frac{g \cdot \beta \cdot \left(T_{fins} - T_{amb} \right) \cdot r^3}{v \cdot \alpha_D} \tag{55}$$

where α_D and v are the thermal diffusivity (m^2/s) and the kinematic viscosity (m^2/s) of air respectively, as reported by [329]. The hydraulic radius (r) is a function of the geometry of the fins and, for horizontal finned surfaces, is expressed as [252]:

$$r = \frac{2 \cdot H \cdot s}{2 \cdot H + s} \tag{56}$$

The experimental Nusselt numbers obtained in the present investigation and those predicted by equation (54) showed an average deviation of 10.59%. This was an acceptable value, taking into account the uncertainty reported by the authors of the correlation (6.3%) and that predicted in this work (8.25%). For this reason, the correlation in (54) could be considered as verified for upward facing silicon micro-finned array and the range of validity of the Nusselt correlation could be extended, as reported in Table 37.

Table 37 - Extended range of validity of the Nusselt correlation for micro-finned arrays.

Parameters	Original range	Present range	Extended range
H	0.1 mm to 1 mm	0.6 mm to 1 mm	0.1 mm to 1 mm
L	10 mm to 20 mm	50 mm	10 mm to 50 mm
s/H	0.15 to 7.7	0.19 to 1.45	0.15 to 7.7

As already pointed out, at micro-scale the fin thickness had a non-negligible effect on the heat transfer coefficient, which was not accounted in (54). In the previous investigations [251,252], fins with a fixed thickness had only been considered: in the present study instead, the average discrepancy between the real and the predicted Nusselt numbers was found to get wider when the thickness increases (Figure 146).
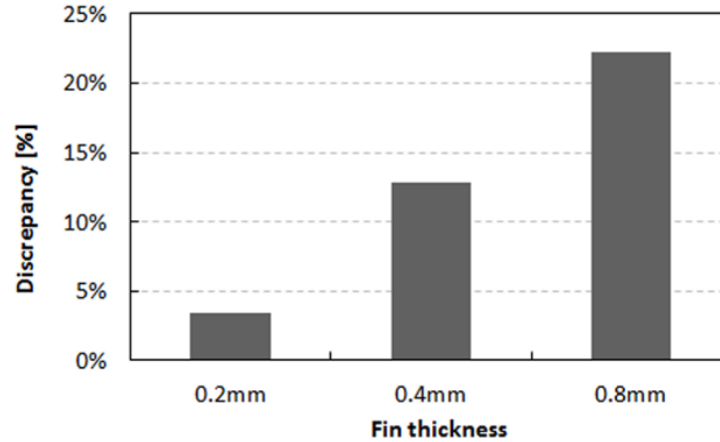
Figure 146 - The average percentage discrepancies between real and predicted Nusselt numbers, depending on the fin thickness.

In order to introduce the thickness in the Nusselt correlation, equation (54) was adapted as follow:

$$Nu^* = 1.18 \cdot \left[Ra_r \cdot \left(\frac{r}{H}\right)^4 \cdot \left(\frac{r}{L}\right)^4 \right]^{0.147} \cdot \left[1 + \left(\frac{t}{r}\right)^2 \right]^{0.147} = 1.18 \cdot \left[Ra_r \cdot \left(\frac{r}{H}\right)^4 \cdot \left(\frac{r}{L}\right)^4 \cdot \left(1 + \left(\frac{t}{r}\right)^2\right) \right]^{0.147} \qquad \textbf{(57)}$$

In equation (57), the Nusselt number increased when thickness was increased. Equation (54) was proposed for t<<r: in those same conditions, Nu* equalized Nu. Using the new correlation, the average discrepancy was found to drop to 6.05% and ranged between 5% and 8% at different thicknesses.

Despite the samples' dimensions (H=0.25-1.00mm, L=31.75mm, S/H=0.5-4) fell within the range of validity of equation (54), Mahmoud and his colleagues [252] reported a discrepancy of 29% between the experimental and the predicted Nusselt numbers. Digitalizing their data, it was found that equation (54) consistently underestimated the Nusselt number of copper micro-fins with an average deviation of 26%, still too high to be considered as due to the experimental and data-digitalization process' uncertainties only. In [252], the thickness was higher than that tested in [251]. Moreover, the conductivity of copper, much higher than that of silicon, could have enhanced the discrepancy. As depicted in Figure 147, using the modified Nusselt number correlation in equation (57) reduced the average discrepancy from 26% to 7.41%. The validity range of the modified correlation (57) could then be extended to those arrays where H ranges from 0.25mm to 1.0mm, L from 31.75 to 50mm, and S/H from 0.2 to 2. For

a more accurate Nusselt number estimation, further investigations on a wider range of micro-fin dimensions are needed to understand the influence of thickness.
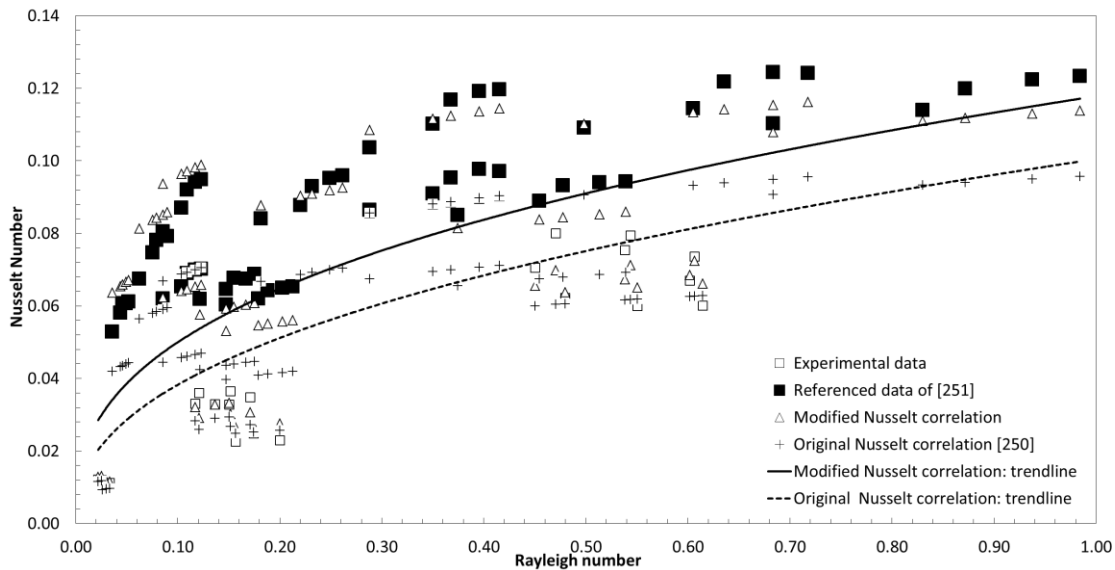
Figure 147 - Comparison of the present experimental results (□), the experimental results reported in [252] **(■), the predictions of the Nusselt correlation for micro-finned heat sinks proposed by** [251] **(Δ), and the modified correlation presented in this work (+).**

7.3.3 Plate fins vs pin fins

In this section, the performance of plate fin and pin fin arrays were compared. The two geometries were based on the same dimensions: spacing (s), fin thickness (t), fin height (H) and base thickness (t_b) were the same for each couple of plate/pin finned geometries. The dimensions are reported in Table 38.

Table 38 - The dimensions of the plate/pin fins arrays

Plate/Pin Fins Sample No.	T [μm]	s [μm]	H [μm]	tb [μm]	Number of fins (Plate fins - Pin fins)
#1	200	200	600	800	121 - 15376
#2	400	400	600	800	61 - 3844

The use of pin fins instead of plate fins reduced the volume of the heat sink: the overall pin-finned wafer volume was found to decrease by 13% compared to the plate-finned one. On the other hand, since in both the considered geometries the fin spacing was equal to the fin thickness, no change in surface was registered between the pin-finned and the plate-finned configurations. Despite that, the thermal exchange was expected to change: in a pin-finned geometry, an

enhancement in the extension of the fin base surface and a reduction of the top fin surface were registered.

In the present study, the contribution of radiation was estimated by using the model in [324] to determine the view factors. Since two different fin structures were now compared, a different model should have been used for estimating the view factors. Unfortunately, at the time the work was conducted, no model to estimate the view factor in a pin fin array was found. In lack of that, it was preferred to consider the overall heat exchanged by the fins, intended as the sum of the radiative and convective heat transfers happening through the fins (Q_{tot}):

$$Q_{tot} = Q_{fins} + Q_r \qquad (58)$$

A combined heat transfer coefficient, named *average heat transfer coefficient* by [381], was then calculated:

$$h_{tot} = \frac{Q_{tot}}{A_{fins} \cdot (T_{fins} - T_{amb})} \qquad (59)$$

As shown in Figure 148, the pin fins had better average heat transfer coefficients than plate fins and consistently showed lower fin temperatures for the same power inputs. It means that more heat was transferred from the heat sink by radiation and convection in pin fins than in plate fins. This was probably due to the increased surface of the pin fin configuration, which balanced any loss due to the reduction of the fin tip extension, which was the surface where the heat transfer was usually maximized.
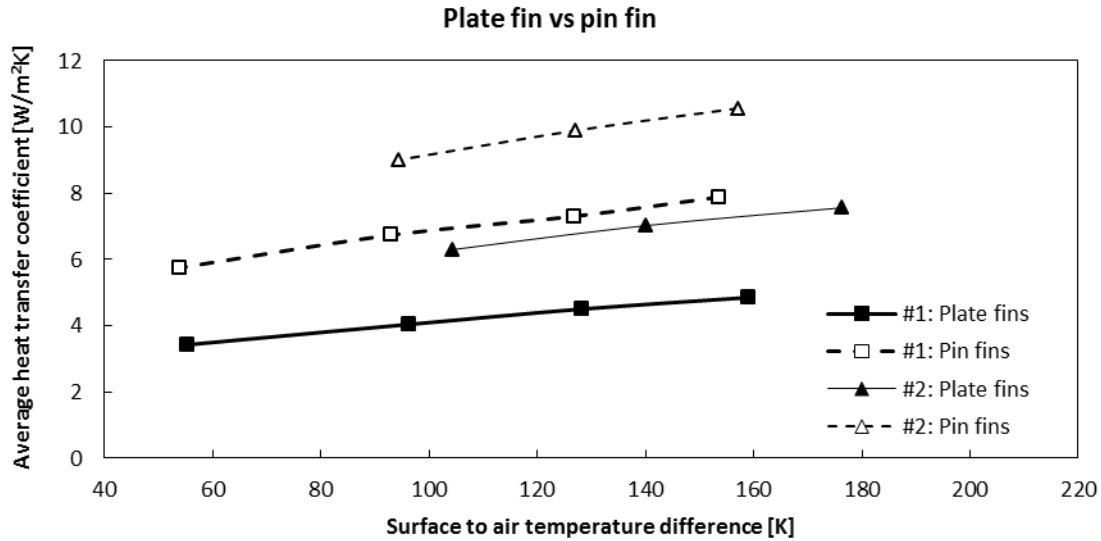
Figure 148 - Comparison between heat transfer coefficients in flat and pin fin configurations

7.3.4 The contribution of the radiative exchange

As pointed out by Khor *et al.* [382], among the studies on thermal performance of finned heat sinks, only in few cases the effect of radiation had been considered. Despite that, neglecting the effects of the radiative heat transfer can lead to errors higher than 30% in estimating the heat transfer coefficients. This error could rise up to more than 60% if radiation was considered discarding the view factors. The test presented in this chapter confirmed the importance of the radiative exchange in a micro-heat sink in natural convection conditions, in accordance with the numerical investigation in [253], which was conducted for a 10mm-width and 40µm-thick heat sink with an emissivity of 0.70. In that work, the authors predicted a maximum radiative contribution of 22% for power inputs between 1.7 and 1.8mW and temperatures of 100°C. In the conditions considered in the present work, instead, the radiative exchange was found to dissipate up to the 56% of the heat exchanged by the fins, so it should be neglected when designing a micro-passive cooling system under natural convection. Figure 149 shows the combined convective and radiative heat transferred by the fins (Q_{tot}), as calculated in (59). The overall heat was compared with the contributions given by the radiative and the convective components. As expected, at high temperatures the radiative component contributed more than the convective one to the heat transfer, because of the dependence on the difference of the fourth power of the temperatures. The

intersection point between the two trends varied at different geometries: when dimensioning a micro-finned heat sink, the contribution of the radiative exchange has to be taken into account using one of the models available in literature. The high contribution showed made these micro-scaled systems interesting for spatial applications too, where radiation was the dominant heat transfer mode.

Usually, when finned heat sinks were selected, the convective heat transfer only was taken into account. The results shown in this chapter proved, instead, that, when a heat sink is dimensioned, the radiation should not be neglected. In this light, further studies are needed to develop models able to predict the combined contributions of radiation and convection.
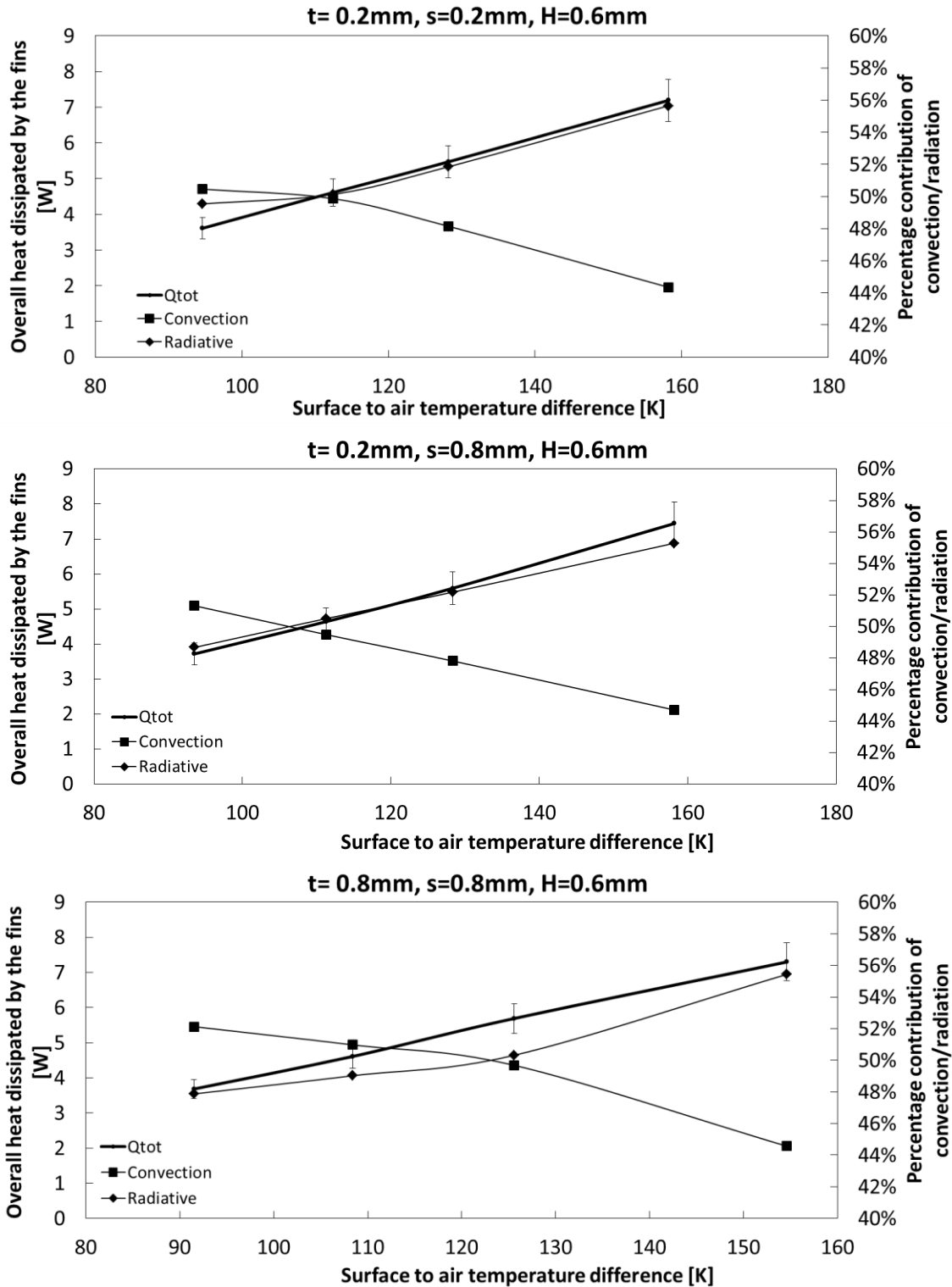
Figure 149 - Global heat exchange at different fins geometries.

7.4 Alternative heat sink metrics

7.4.1 Definitions

So far, the behaviour of the fins was evaluated using the heat transfer coefficient only. In the real world applications, instead, engineers and system designers look for thermal resistance, compactness, weight and cost of the heat sinks and, therefore, they are required to understand the effective heat transfer enhancement introduced by the fins compared to the original flat surface. The heat transfer coefficient measures the thermal property per unit of surface and it is not an indicator of the thermal performance of the whole heat sink, because it does not take into account the extension in thermal exchanging surface due to the fins. For this reason, a different metric, called *fin effectiveness*, is usually employed to evaluate the performance of fins. It compares the heat transfer of the finned surface and that of the unfinned surface [329,383]:

$$\varepsilon_{fins} = \frac{Q_{fins}}{Q_{flat}}$$ (60)

where Q_{fins} and Q_{flat} are the heat transferred by the fins and by the flat plate respectively. The fin effectiveness measures the improvement in thermal exchange due to the fins: if $\varepsilon_{fins} > 1$, the fins have enhanced the thermal behaviour of the unfinned surface.

Micro-fins are usually obtained through material subtractions, such as dicing, etching or electrical discharge machining. Along with the effects on the heat transfer, a benefit in terms of mass reduction is expected. This feature becomes particularly important in portable or tracked systems, such as the concentrating photovoltaics, where reduced weights mean reduced loads for the tracker. The *mass specific heat transfer coefficient* measures the effectiveness with which fin material is utilized in the promotion of heat transfer [157] and is expressed as:

$$h_m = \frac{Q_{fins}}{\rho_D \cdot V_{fins} \cdot (T_{fins} - T_{amb})}$$ (61)

where ρ_D is the density of the fin material and V_{fins} is the volume of the whole micro-finned heat sink.

7.4.2 Fin effectiveness

Kim *et al.* [251] measured a heat transfer enhancement up to 10% due to the installation of fins, in agreement with the findings of previous researches on micro-fins under forced flow conditions [384]. In particular, the fin effectiveness was found to increase when the fin spacing decreased. This was explained because of the limited fin spacing decreased the volume of air compared to that of the higher-conductive fin material, increasing the overall thermal conductance. The reduced enhancement was confirmed in the present experimental investigation, where the fin effectiveness was found to range between 0.98 and 1.02. This meant that the introduction of micro-fins for natural convection was not necessarily positive for the overall heat transfer. The same results were obtained by analysing the data reported by [252], where the fin effectiveness was found to range between a minimum of 0.86 and a maximum of 1.14. In Figure 150, a summary of the effectivenesses presented in this work and in [252] is reported. The data from the two investigations showed an average effectiveness of 0.985.
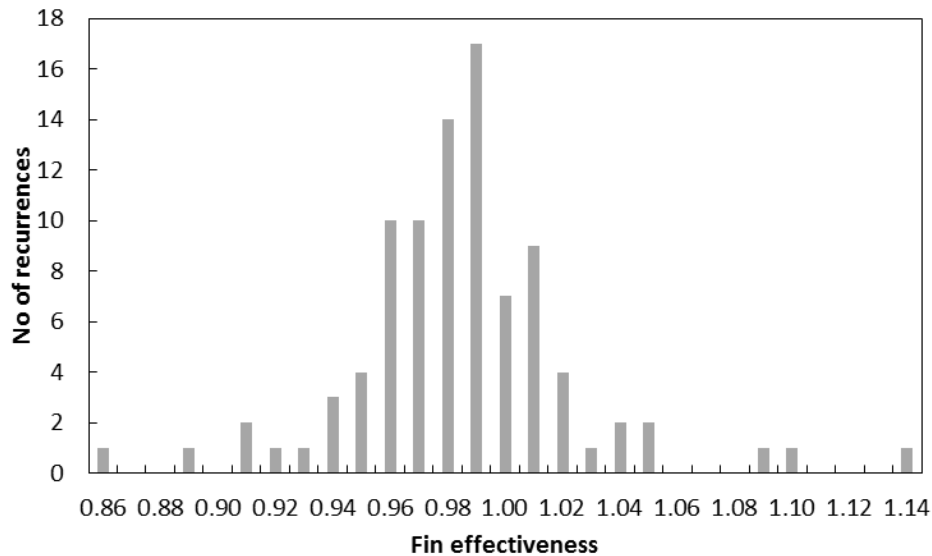
Figure 150 - Number of recurrence per fin effectiveness, merging data from the present research and [252].

No clear correlations between geometry and fin effectiveness was found. Further studies needed to be conducted to understand how to optimize the design of a micro-fins array for natural conductive applications.

7.4.3 Mass specific heat transfer

The mass specific heat transfer coefficient measures the thermal performances per unit of mass of the heat sink. Even when the traditional heat transfer coefficient was negatively affected, the mass specific heat transfer coefficient was found to be always enhanced by the introduction of fins. It means that that the benefit in weight reduction due to the material subtraction was more effective than the change in the thermal performance.

The correlations between the mass specific heat transfer and the fin geometries are not consistent with those reported for the heat transfer coefficients. It was found that the specific mass heat transfer increased when increasing the spacing of the fins (Figure 151), and/or increasing the height (Figure 152). The increase in fin height means a drop in the heat sink weight, because the base thickness is decreased. Similarly, the mass heat transfer increased when the fin thickness decreased (Figure 153). These results confirmed that the drop in weight, instead of an enhancement in heat transfer, was the most important benefit obtained by dicing micro-fins on a flat cooling surface. This made micro-finned heat sinks particularly preferable for moved systems, where the weight had to be limited.
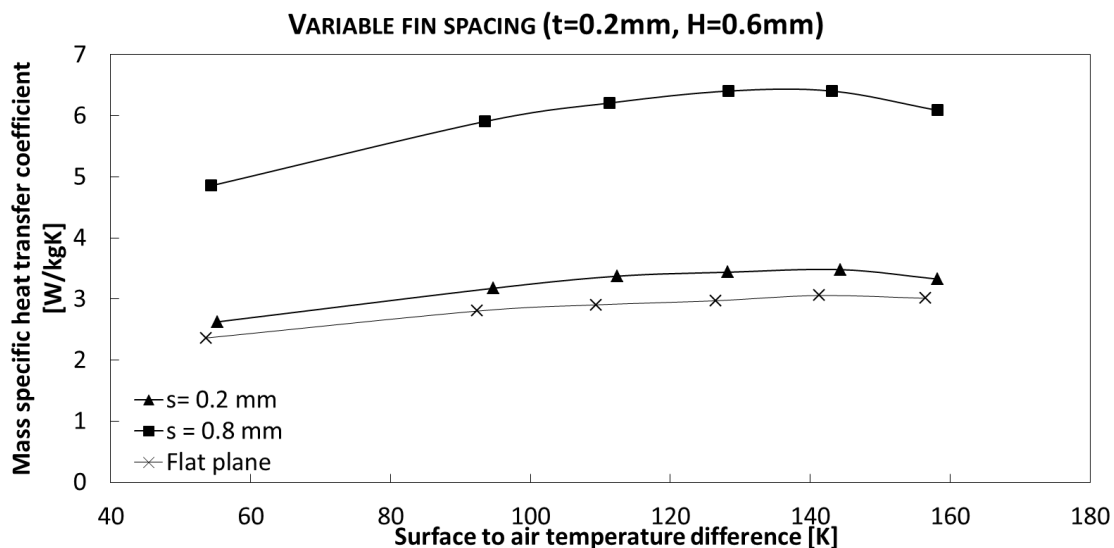
Figure 151 - The effects of the fin spacing for horizontal fin arrays on the mass specific heat transfer coefficient.
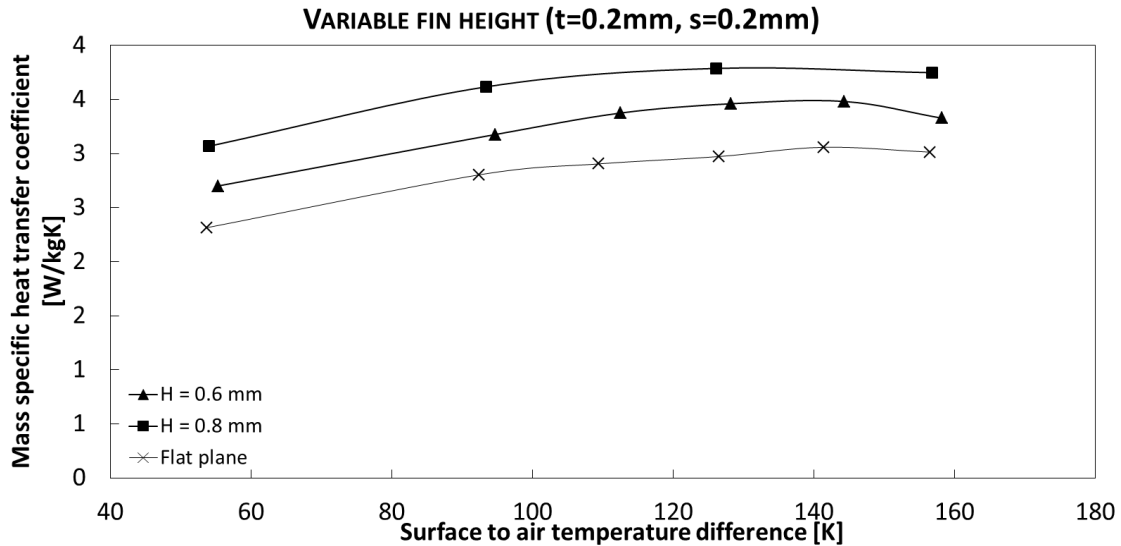
Figure 152 - The effects of the fin height for horizontal fin arrays on the mass specific heat transfer coefficient.
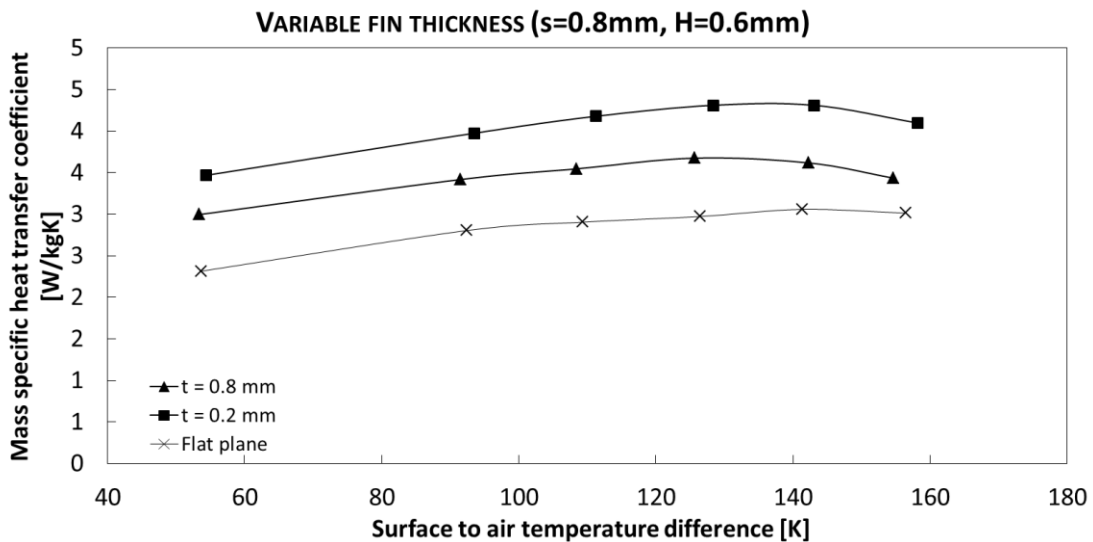
Figure 153 - The effects of the fin thickness for horizontal fin arrays on the mass specific heat transfer coefficient.

7.4.4 Considerations

Heat transfer from extended surface is more complex at micro-scale than in macro-scale conditions. This is due to the fact that, in the small air volumes, the conduction is dominant over the natural convection. When confined in the narrow space between two fins, the air tends to behave as an insulating layer, because of the low thermal conduction and the higher viscous forces than the buoyancy. For this reason, a reduction in heat transfer coefficient was registered when micro-fins were added to a flat plane surface. The drop in thermal convection could be

balanced by the increase in thermal exchanging surface: the effectiveness of micro-fins in natural convection was found to be as high as 1.14, but the correlation between it and the fin geometry had yet to be formalized. The introduction of micro-fins gives always a benefit related to the material usage when it was referred to the unit of mass. The present investigation showed that introducing micro-fins in CPV system could, at the same time, improve the thermal performance and reduce the weight of the system. The current investigation considered only fins in upward facing orientation, whereas, in the following sections, the effects of the orientation on the thermal performance of CPV are presented.

7.5 Performance of tilted fins

HCPV are usually tracked systems: the cell and the whole receiver are continuously moved, to be normal to the sunlight. This means that the heat sink is not static, but changes its orientation during the day. Moreover, in the configuration selected for this application, the fins are likely to be facing downwards during the hours when the Sun is higher and the irradiance is more intense. All the previous research on passive micro-fins arrays used to consider fixed heat sink, vertically or upward orientated [251,252]. Previous studies showed the effects of the orientation on a macro-finned heat sink [156] and some correlations between the inclination angle and the thermal exchange had been proposed [155]: a similar behaviour could be expected at micro-scale. No researches were found for micro-scaled systems, and, for this reason, the behaviour of tilted fins was analysed in the present work.

7.5.1 Horizontal fins: upwards vs downwards orientation

It was already known that downward facing was not the best orientation for natural convective heat sinks [380] and this was confirmed also in the present experimental investigation on micro-fins. In this case, the thermal resistance of the fin array (R_{fins}) was taken into account:

$$R_{fins} = \frac{T_{fins} - T_{amb}}{Q_{fins}}$$

(62)

Figure 154 shows the behaviour of the thermal resistance when varying the power input for different fin arrays. An average discrepancy of 12% in thermal resistance was found between the heat sinks' performance in upward and downward orientation.
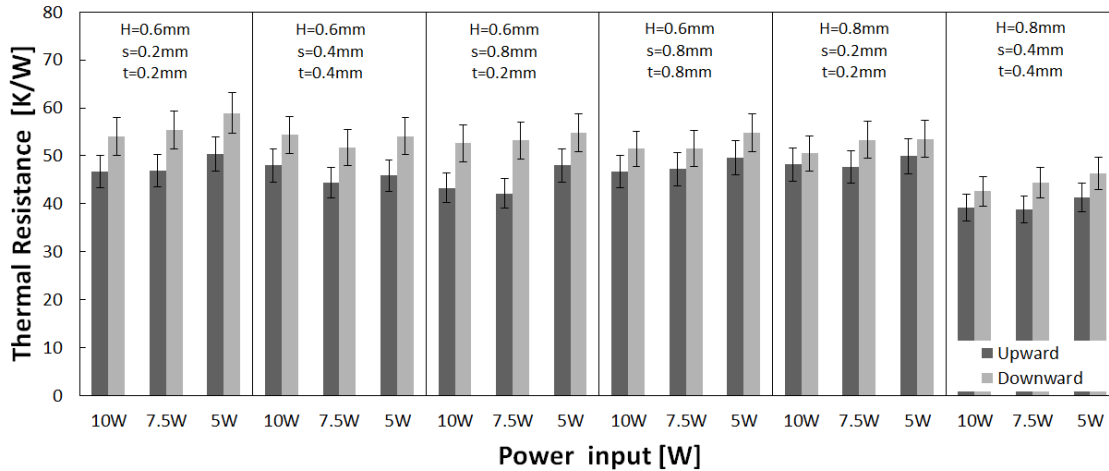
Figure 154 - Thermal resistance of the different fin geometries: upward vs. downward

As shown in Figure 155, the behaviour of the downward facing heat sinks was found to be similar to that of the upward facing ones: the heat transfer coefficients increased when increasing the fin thickness and the fin spacing, and when decreasing the fin height. Each trend of heat transfer coefficient reached a maximum at high temperature, before decreasing. As expected, compared to the upward conditions, the downward trend was shifted down, similarly to the case of an horizontal downward facing plate [341]. This could be physically explained because, when the heated surface faced downwards, the plate itself represented an obstacle to the tendency of the warm air to ascend, lowering the heat transfer. In upwards configuration, instead, the heat transfer was due to descending and ascending columns of cold and warm fluids respectively: because of the space vacated by the heated fluid was occupied by the cooler and heavier fluid, the heat transfer was more effective in this case.
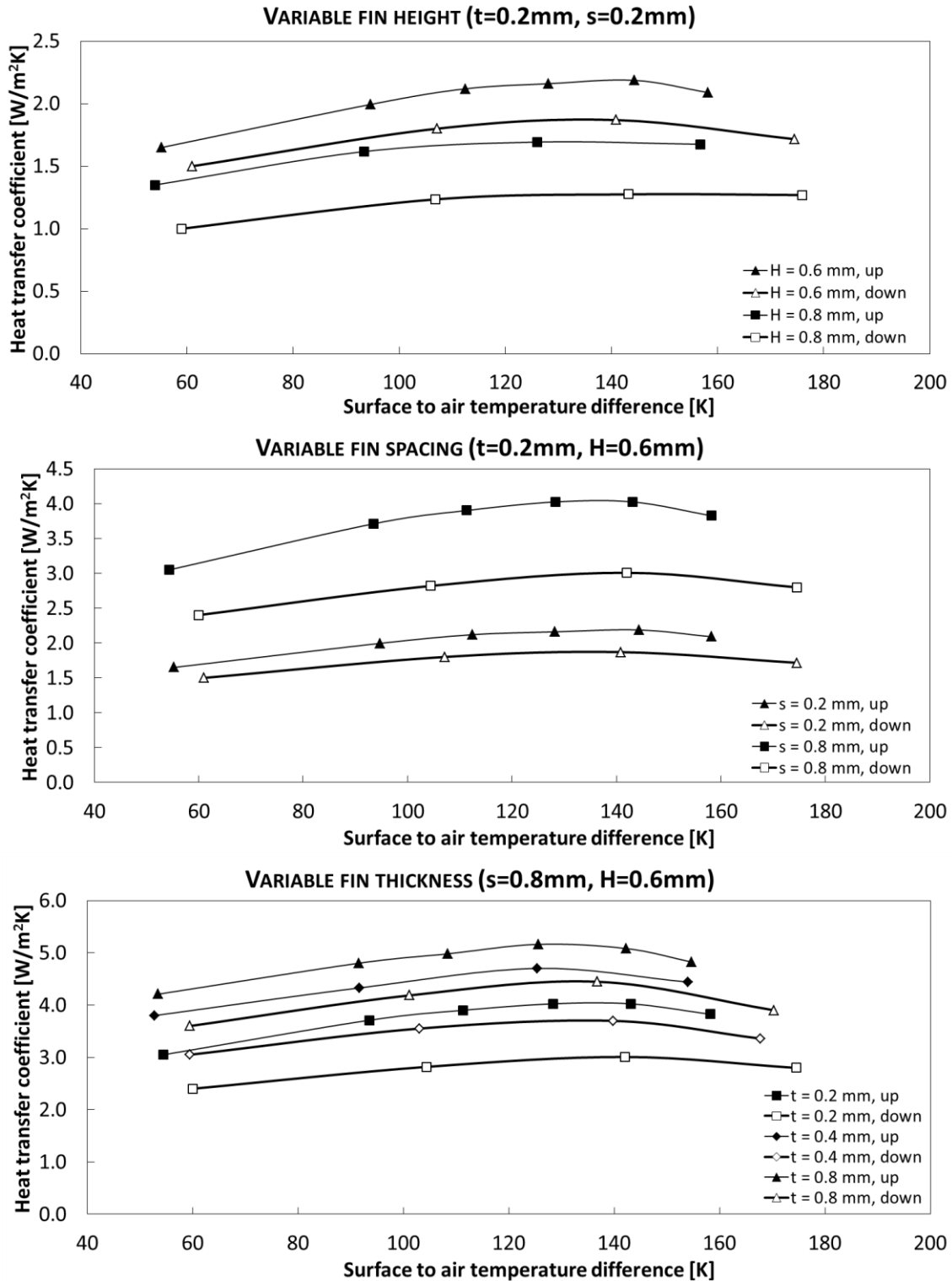
Figure 155 - Effect of geometry on the thermal behaviour of downward facing heat sink.

7.5.2 Vertical vs horizontal oriented fins

The vertically orientated fins consistently showed higher values of heat transfer coefficients than those horizontally oriented: the vertical convective movements of

the air facilitated the convection within the narrow spacing between the fins. As already pointed out, instead, when in horizontal position, the small air volumes kept in the fin spacing exchange heat by conduction mainly, lowering the thermal performance. This behaviour was confirmed when the fin effectiveness was studied: it was usually higher at a tilt angle of 0°. Due to the increased movement of the air, the enhancement in surface obtained by dicing vertical fins became more significant. The increase in fin effectiveness between the horizontal and the vertical positions varied between 2% and 11%. In particular, the highest enhancement was achieved for the arrays with the largest spacing (Figure 157): this proved that convective movements were facilitated and the heat transfer was then enhanced in larger air volumes.
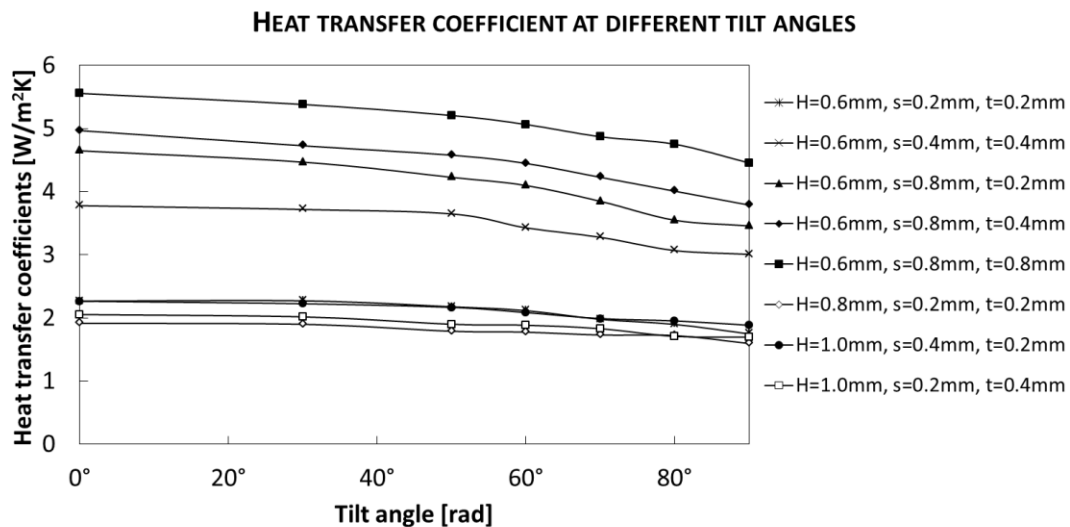
Figure 156 - Behaviours of the heat transfer coefficient depending on the tilt angle, under a constant heat input of 10W. The tilt angles are reported in radians: 0 rad (0°) stands for vertical heat sinks, 1.57 rad (90°) for horizontal downward facing heat sinks.
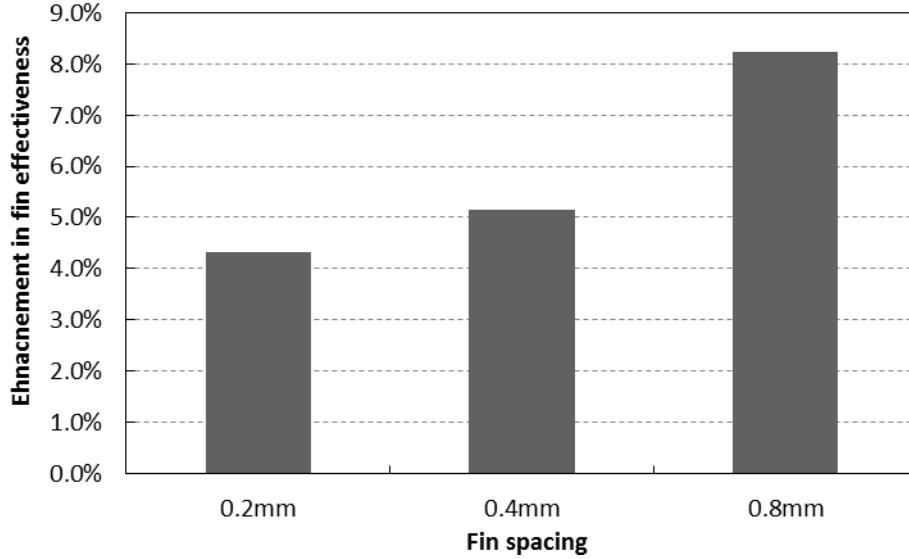
Figure 157 - Average fin effectiveness enhancement between tilt angles of 90° and 0°.

7.5.3 Tilted fins

The correlation between micro-fin geometry and heat transfer coefficient was found to be consistent at different tilt angles: the heat transfer coefficient increased when the fin spacing increased (Figure 158), the fin height decreased (Figure 159) and/or the fin thickness increased (Figure 160).
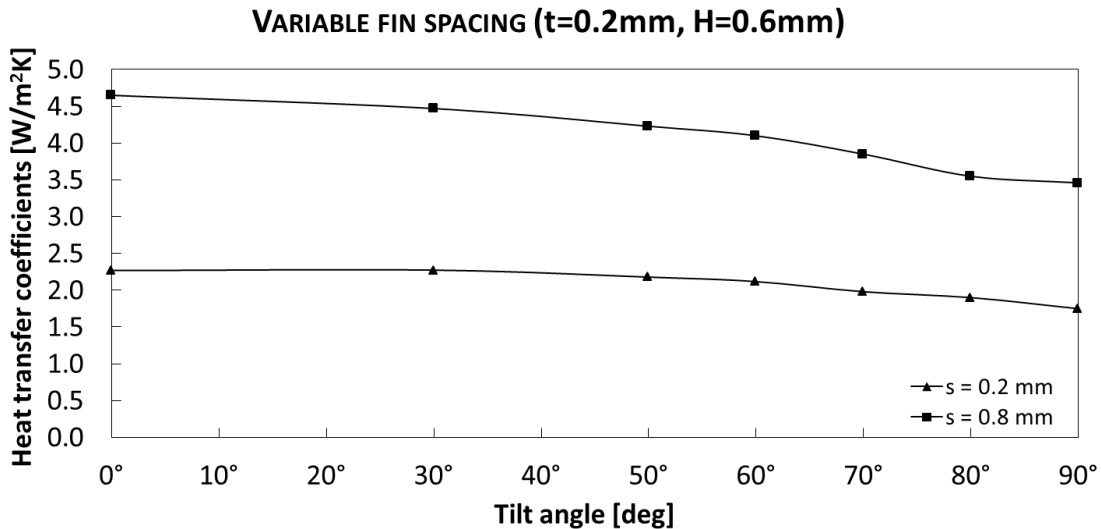
Figure 158 - Heat transfer coefficient vs fin spacing for 10W of power input at different tilt angles

VARIABLE FIN HEIGHT (t=0.2mm, s=0.2mm)
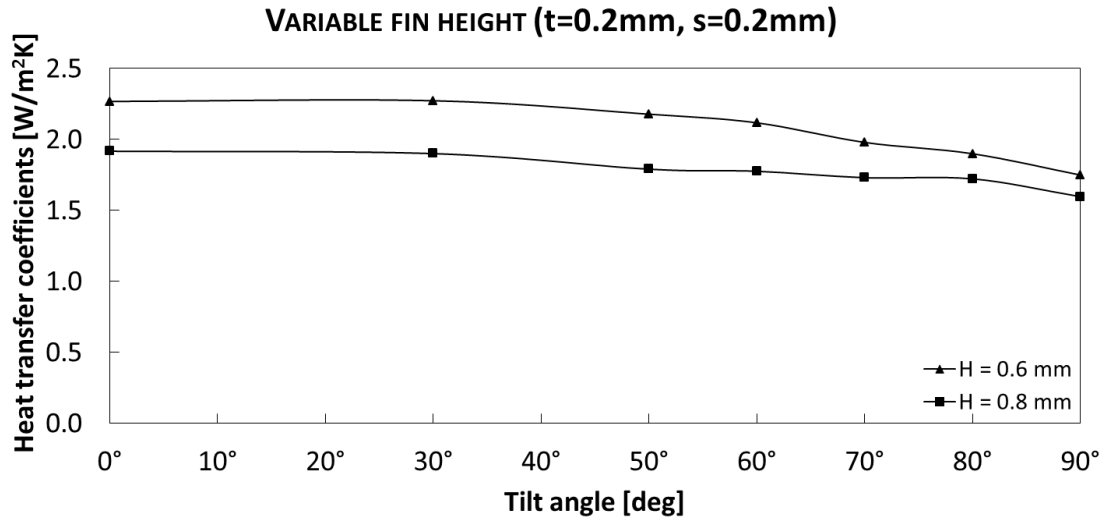
Figure 159 - Heat transfer coefficient vs fin height for 10W of power input at different tilt angles

VARIABLE FIN THICKNESS (s=0.8mm, H=0.6mm)
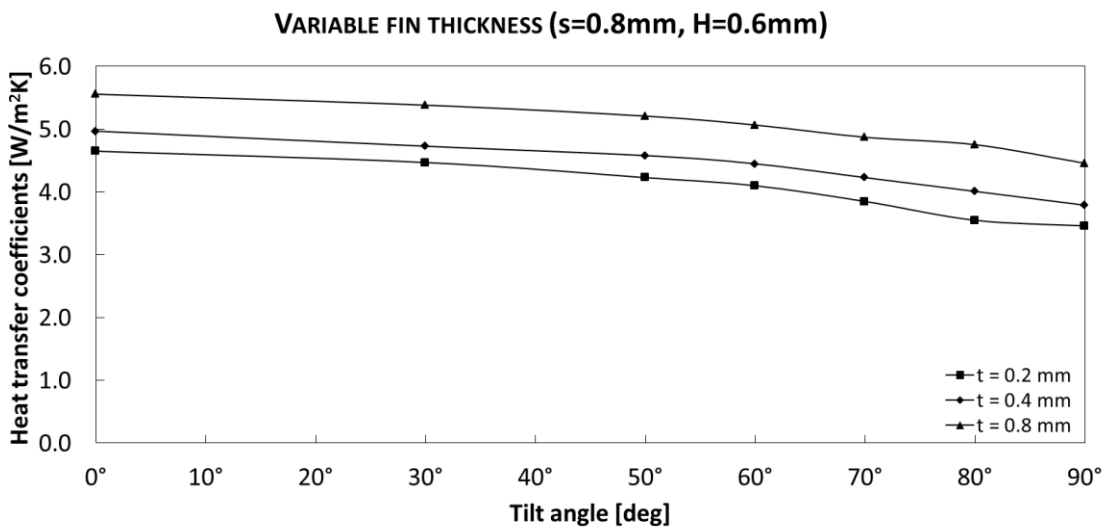
Figure 160 - Heat transfer coefficient vs fin thickness for 10W of power input at different tilt angles

As shown in the graphs above, the heat transfer coefficient decreased while increasing the tilt angles. In agreements with the outcomes reported by Do *et al.* [155], a limited reduction in the heat transfer coefficient was registered between 0° and 50°, whereas major performance drops took place for higher tilt angles.

Do *et al.* [155] first presented an experimental correlation between the tilt angle and the heat transfer coefficients of macro-finned heat sinks. In their study, the authors took into account the fin spacing, and the fin height of the array. A similar correlation between the tilt angle and the thermal performance of micro-fins would

be a useful tool to design of passive micro-finned heat sinks and it was being investigated when this thesis was submitted.

7.6 Micro-finned heat sink for CPV

The experiments described in the previous paragraphs was conducted in conditions of low thermal exchanges from all the surfaces other than the fins and using a heater sized as the heat sink (5cm×5cm). In the real scenario, all the surfaces of the system exchange heat with the ambient and the heat source coincide with the cell, so it has a limited extension compared to the heat sink. In order to predict the realistic behaviour of micro-fins in a CPV system, a COMSOL simulation was conducted, using the heat transfer coefficients determined by the experimental investigation and a heat source sized as the solar cell (3mm×3mm). The unfinned and finned geometries reproduced in COMSOL are shown in Figure 161.
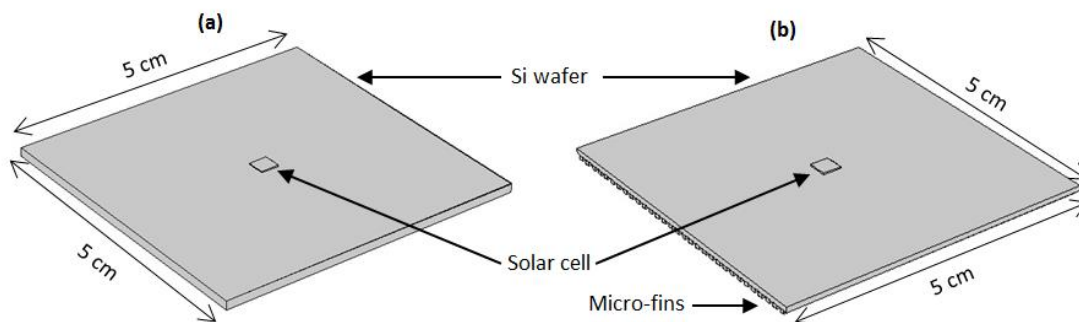
Figure 161 - Geometries of: (a) unfinned flat silicon wafer, (b) micro-finned silicon wafer.

7.6.1 Best performing fin geometries

The research presented in this chapter led to several outcomes. Firstly, it was found that the heat transfer coefficient increased when the fin spacing and the fin thickness increased and when the fin height decreased. Secondly, the mass specific heat transfer was found to increase when the fin spacing and the fin height increases and when the fin thickness decreased.

In this section the best performing micro-plate fin arrays among the ones available for the experimentation were considered and modelled. The thermal management of the fins was compared with that of the flat plane silicon wafer. The first plate fin

geometry was chosen in order to enhance the mass specific heat transfer coefficient: the maximum fin spacing, the maximum fin height and the minimum fin thickness were considered. This array was expected to be able to handle the heat generated by the cell, limiting the weight of the heat sink.

In a second approach, the fin array with the best effectiveness was selected: it corresponded to the one with the highest values of fin thickness and spacing. In this case, the array was expected to improve the thermal performance of the silicon wafer, but the heat sink weight would not be as low as for the previous micro-finned array. All the fin dimensions are reported in Table 39.

Table 39 - Dimensions of the modelled heat sinks.

Type	Width, W [mm]	Length, L [mm]	Fin thickness, t [μm]	Fin spacing, s [μm]	Fin height, H [μm]	Base thickness, t_b [μm]	Number of fins, N_{fin}
Best mass specific heat transfer	50.0	49.9	200	800	600	800	50
Best effectiveness	50.0	49.9	800	800	600	800	31

In the previous investigation, it was found that pin-finned arrays had a better thermal behaviour than plate-finned ones. Unfortunately, it was not possible to quantify the contributions of radiation and convection. For this reason, the performance of a micro-pin finned array could not be modelled at this stage and will be presented in future works.

7.6.2 Heat transfer coefficients

The fins were modelled at 500✕ under CSTCs (1000W/m^2 DNI, 25°C ambient temperature, 42.5% cell efficiency) and worst case conditions (1000W/m^2 DNI, 25°C ambient temperature, 0% cell efficiency). The cell was modelled as a heat source: in the first case the power input was 2.20W, whereas in the second case the power input was increased to 3.83W. An optical efficiency of 0.85 was considered. In all the simulations, the fins were modelled facing downwards: this is

the most challenging condition a CPV cooling system has to face while in operation.

The same assumptions made in section 4.5 were considered in the present model: the fins were reproduced in COMSOL and their heat transfer coefficients were set according to the results of the experimental investigation. Because of the experimental losses accounting for the 26% of the heat in input, DC power inputs of 2.6W and 4.1W were supplied to the experimental setup to measure the heat transfer under CSTCs (2.20W) and worst case conditions (3.25W) respectively. Natural convection from the upper surface was considered as well: it was set according to the experimental heat transfer of the horizontally facing upward flat plane. All the heat transfer coefficients are summarized in Table 40.

Table 40 - Values of the heat transfer coefficients experimentally obtained and used in the thermal model

Surface\Q_{cell}	2.20W	3.25W
Upper flat surface (upwards)	3.72W/m^{2}K	4.73W/m^{2}K
Unfinned surface (downwards)	3.44W/m^{2}K	3.80W/m^{2}K
Best mass specific heat transfer (downwards)	2.44W/m^{2}K	2.85W/m^{2}K
Best effectiveness (downwards)	3.33 W/m^{2}K	3.65W/m^{2}K

The emissivity was taken into account as well: a silicon emissivity of 0.78 was introduced. The view factors of the fins were calculated according to the methodology reported in the section 3.6.2.

7.6.3 Results of the thermal model

7.6.3.1 *Flat plane*

The results of the simulation are shown in Figure 162 and Figure 163. A maximum cell temperature of 78.7°C was registered for the flat silicon wafer under CSTCs. Also the performances under the worst case scenario conditions were modelled, and the cell temperature should not exceed 150°C: in this case, the temperature rose up to 111°C. In both cases, the temperatures were acceptable, falling within the CPV operating range and confirming the quality of the assumptions made in 4.5.2, when the substrate was initially dimensioned. As expected, the maximum temperatures were higher than those shown during the experimental investigation:

in this case, the heat was generated by the cell which had a smaller surface than the electrical heater. For this reason, the real heat distribution was not uniform as in the experiment, but a higher density of heat was concentrated close to the cell and this led to higher local temperatures.
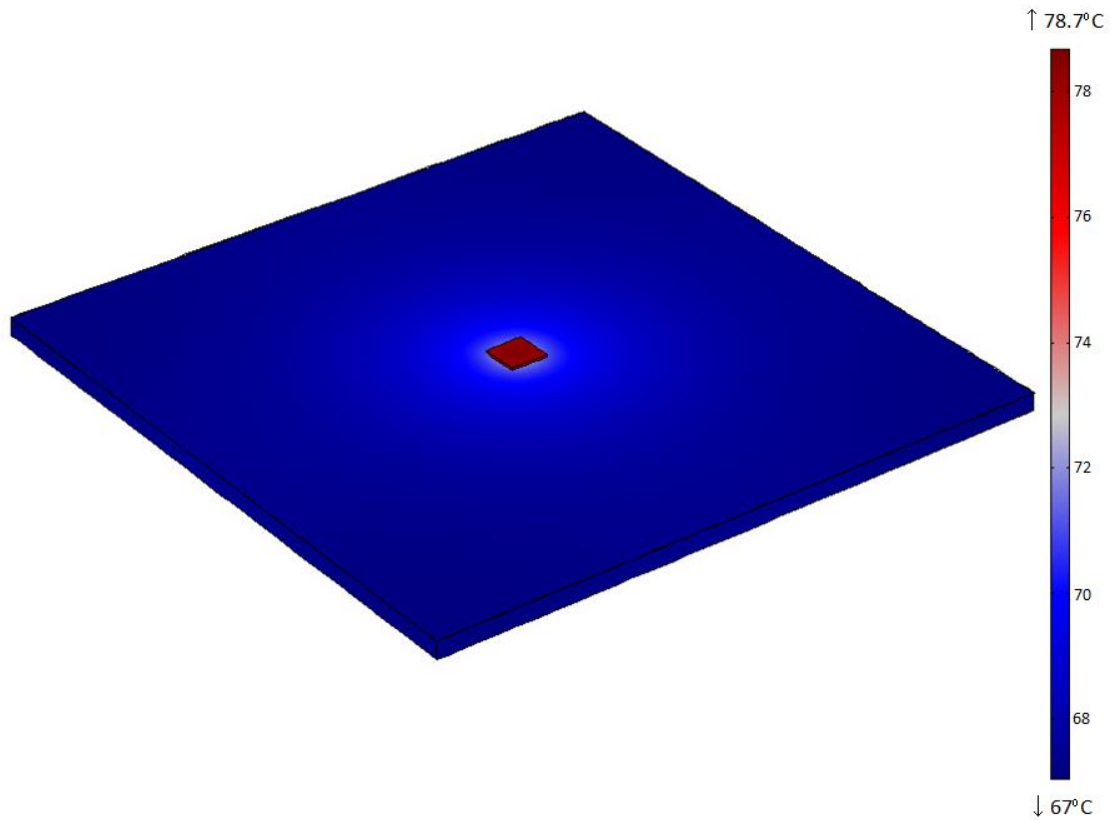
Figure 162 - Temperature distribution in the unfinned flat wafer under CSTCs (maximum cell's temperature: 78.7°C).
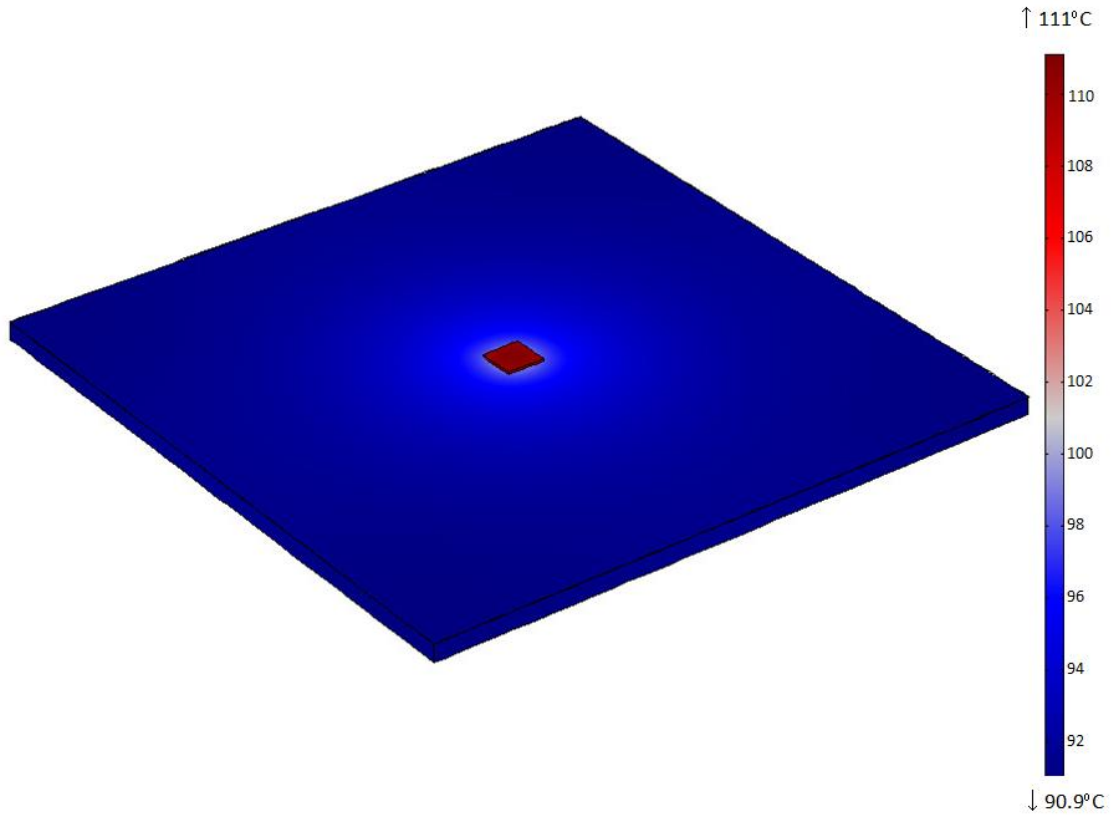
Figure 163 - Temperature distribution in the unfinned flat wafer under CPV worst case conditions (maximum cell's temperature: 111°C).

7.6.3.2 *Best mass specific heat transfer array*

The cell temperatures achieved by the best mass specific heat transfer array were shown in Figure 164 and Figure 165. A maximum cell temperature of 73.0°C was predicted under CSTCs and fell within the range usually accepted for CPV. The temperature was lower than that registered for the flat plane silicon.
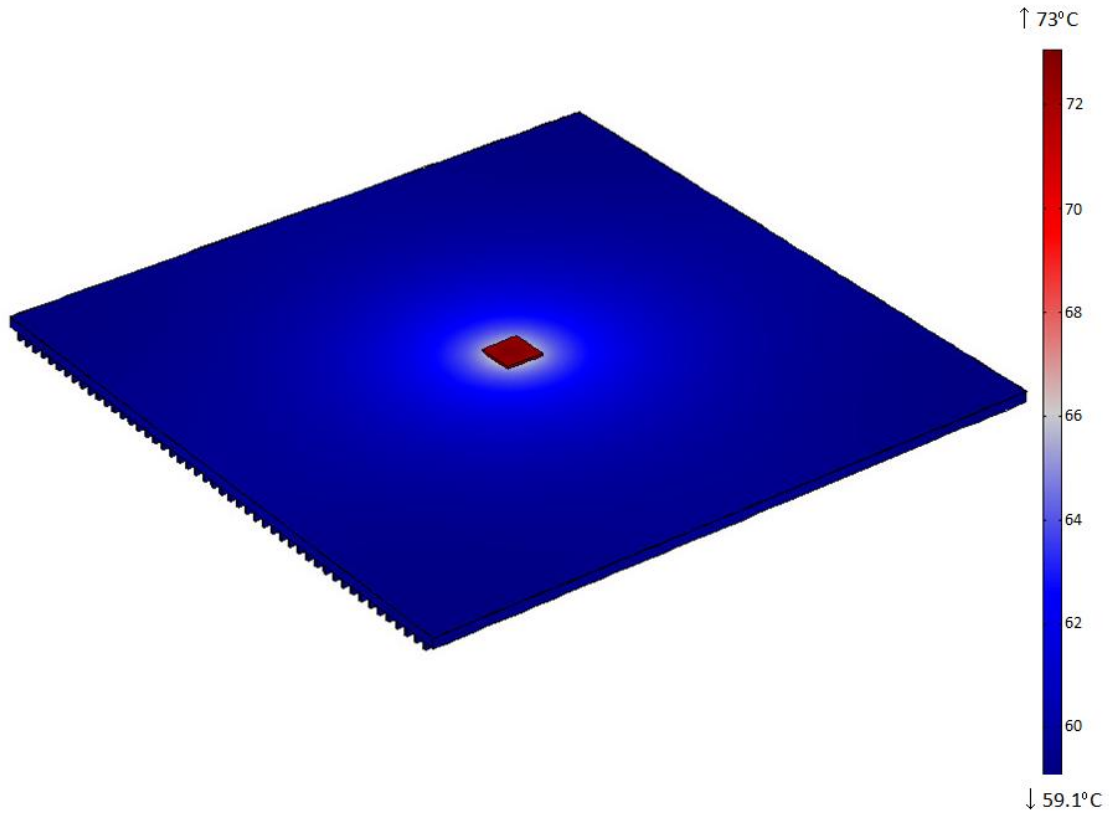
Figure 164 - Temperature distribution in the best mass specific heat transfer micro-finned array under CSTCs (maximum cell's temperature: 73.0°C).

A maximum cell's temperature of 103°C was predicted instead under the worst case conditions, almost ten degree lower than the unfinned case. Both the temperatures recorded for this array were below the temperature limits imposed for CPV applications and the temperatures of the unfinned silicon wafer
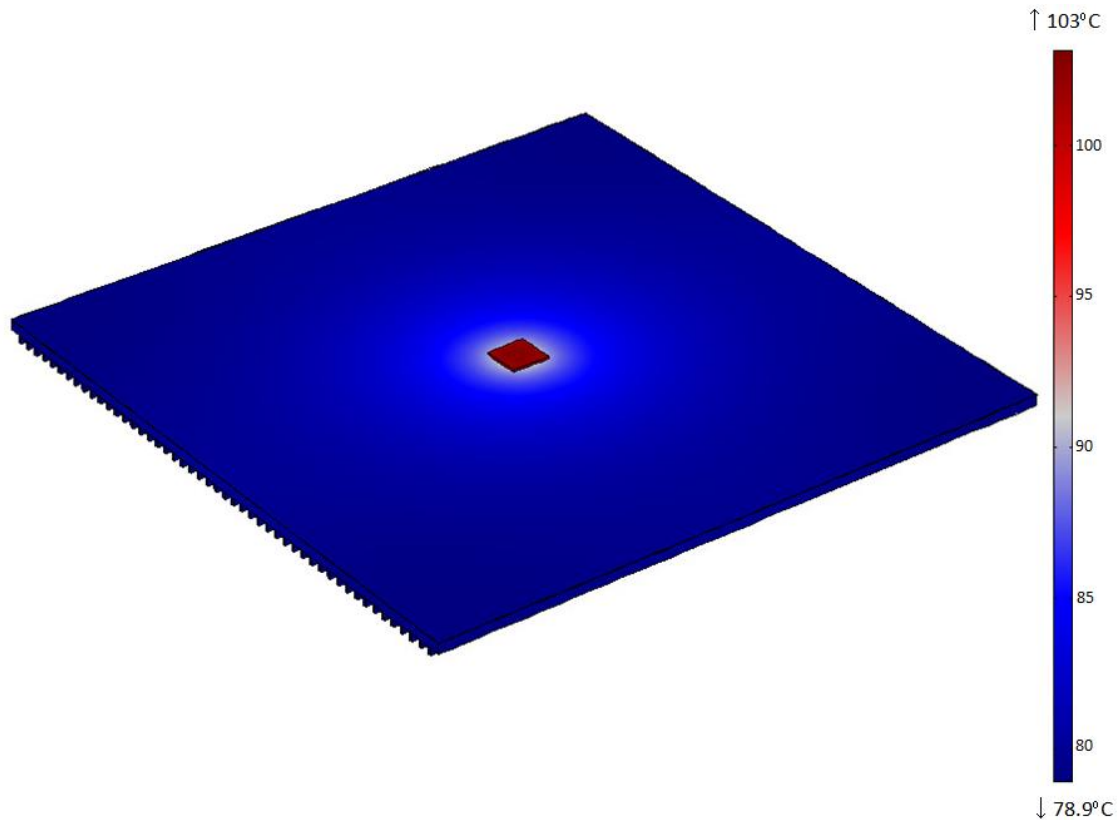
Figure 165 - Temperature distribution in the best mass specific heat transfer micro-finned array under CPV worst case conditions (maximum cell's temperature: 103°C).

7.6.3.3   Best effectiveness array

The maximum cell temperatures of the best effectiveness array are shown in Figure 167 and Figure 169. A maximum cell's temperature of 70.4°C was predicted under CSTCs. As expected by the geometry with the best fin effectiveness, the temperature was the lowest among the ones obtained by the simulation for the three modelled heat sinks. Similarly, a maximum cell's temperature of 99.9°C was predicted in the worst case conditions, below the maximum CPV requirements.
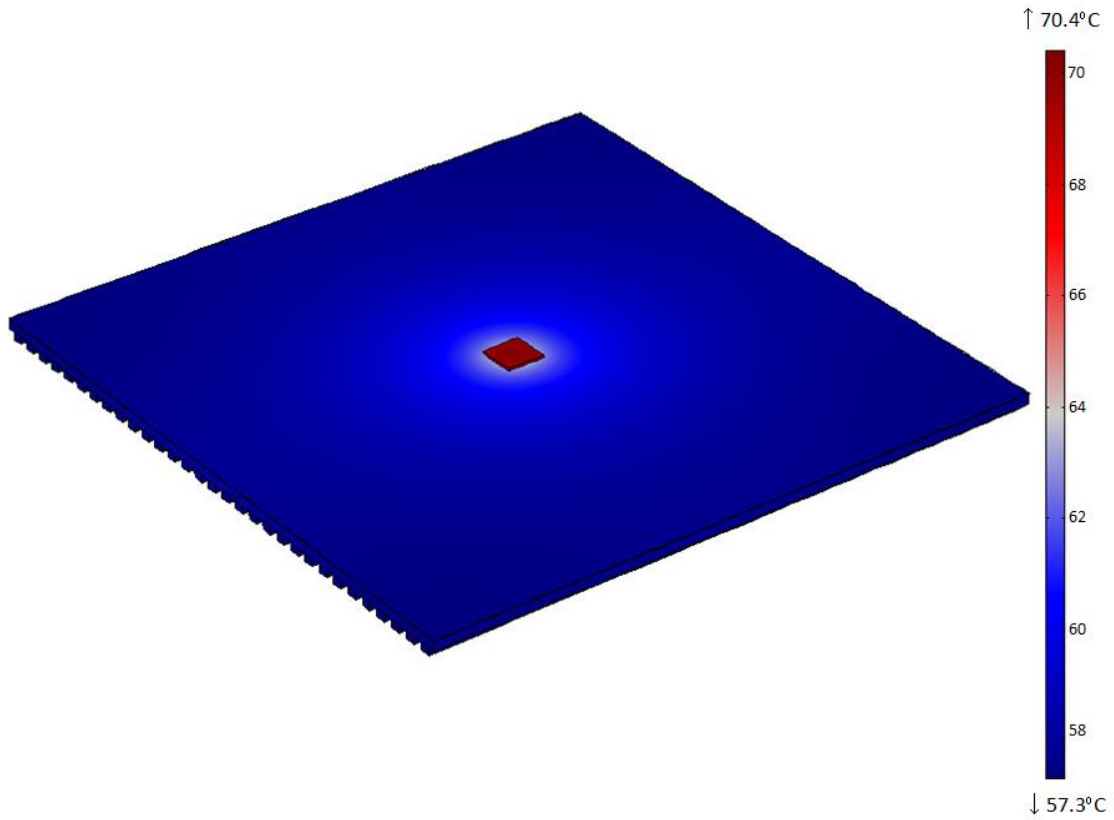
Figure 166 - Temperature distribution in the best effectiveness micro-finned array under CSTCs (maximum cell's temperature: 70.4°C).
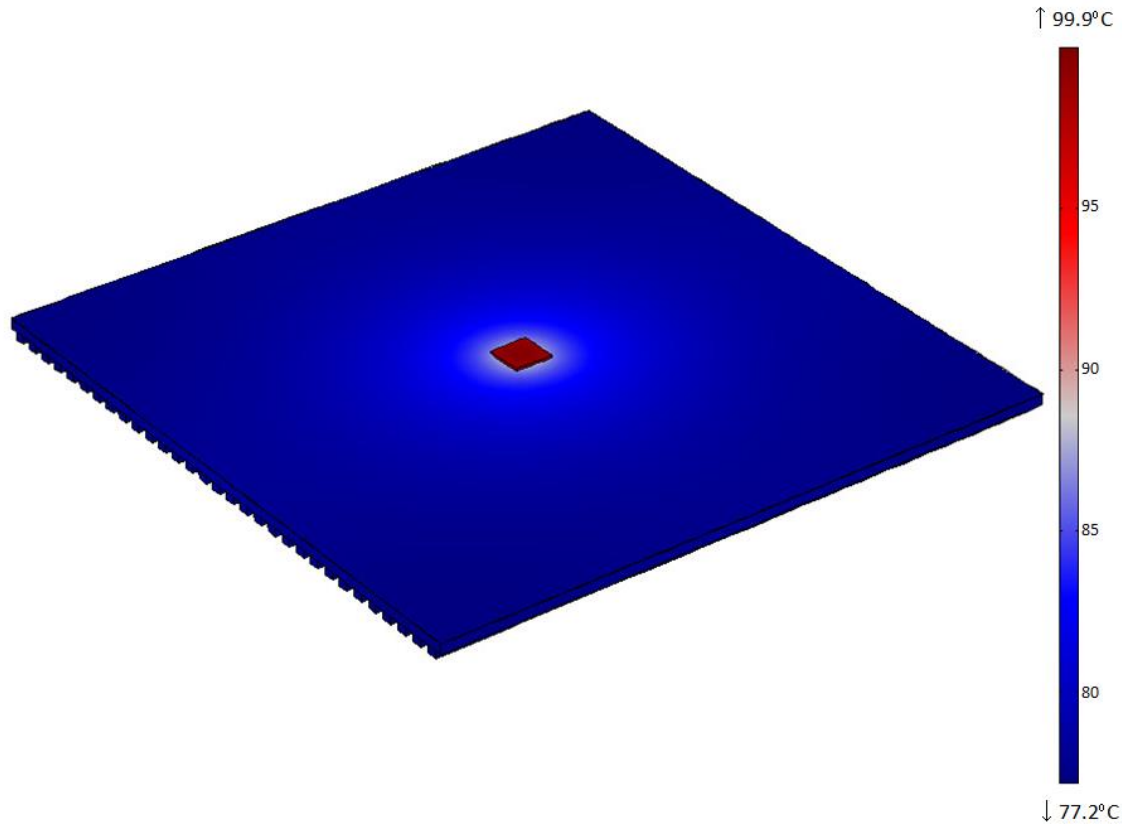
Figure 167 - Temperature distribution in the best effectiveness micro-finned array under CPV worst case conditions (maximum cell's temperature: 99.9°C).

In order to predict the performance of a micro-finned array in a wider range of environments, the Concentrator Standard Operating Conditions [385] were taken into account as well: the DNI was reduced to 900W/m^2 and a wind speed of 2m/s was introduced. The drop in DNI leads to a reduction in heat generation: considering the same 42.5% efficiency at 500×, the 3mm×3mm produced 1.98W of heat at maximum power point. Taking into account the thermal losses experienced in the experimental investigation, a power input of 2.5W was supplied to the heater. The wind was reproduced using a 10cm-diameter fan and its intensity was measured through a digital anemometer (Vktech GM8908 Digital Anemometer). The fan was placed 5cm away from the setup and was blowing the wind horizontally. Under these conditions, the heat transfer coefficient was found to increase up to 17.80W/m^{2}K. According to the COMSOL investigation, the cell temperature of the CPV cell decreased to 48.2°C under the Concentrator Standard Operating Conditions (Figure 168).
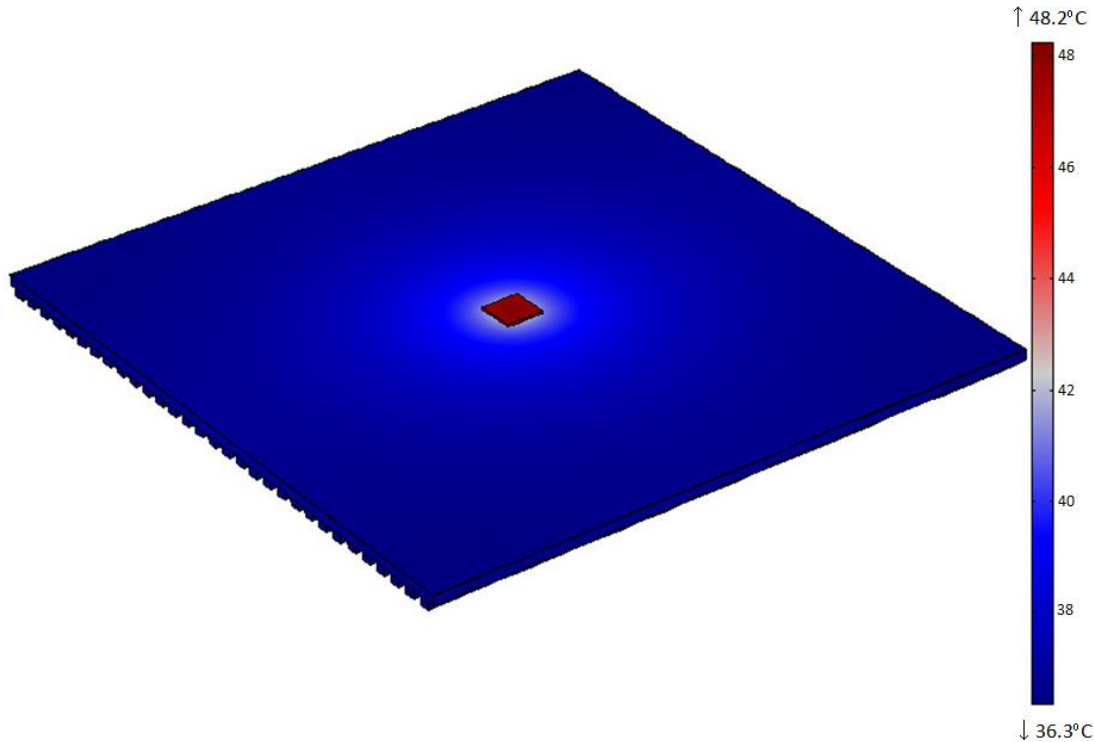
Figure 168 - Temperature distribution in the best effectiveness micro-finned array under Concentrator Standard Operating Conditions (maximum cell's temperature: 48.2°C).

7.6.3.4   Summary

In this chapter, the thermal behaviour of three different heat sinks was compared: a flat 5cm×5cm squared silicon wafer, the best-mass specific heat transfer fin array and the best effectiveness fin array. The selected micro-fins were found to introduce a benefit in terms of heat management, lowering the temperatures both under the operating and the worst case conditions compared to the flat silicon case (Table 41). A maximum drop in temperature of 8.4°C was predicted between the flat silicon wafer and the best performing fin geometry. Taking into account the temperature coefficients of the cell (-0.106%$_{(rel)}$/°C), reducing the cell's temperature of 8.4°C was expected to lead to a relative improvement in cell's efficiency of 0.89% under standard test conditions.

Table 41 - Resume of the maximum cell' temperatures predicted by the thermal investigation.

Heat sink	CSTCs	Worst case conditions
Unfinned silicon wafer	78.8°C	111°C
Best mass specific heat transfer	73.0°C	103°C
Best effectiveness	70.4°C	99.9°C

In order to demonstrate the important contribution of the radiative exchange, a new simulation was conducted not taking into account the emissivity of the materials. As shown in Figure 169 and Figure 170, the temperature of the finned silicon wafer dramatically raised to 131°C and to 125°C for the best mass specific heat transfer and the best effectiveness cases respectively under CSTCs. These results confirmed that the radiative exchange should not be neglected when designing a micro-finned array.
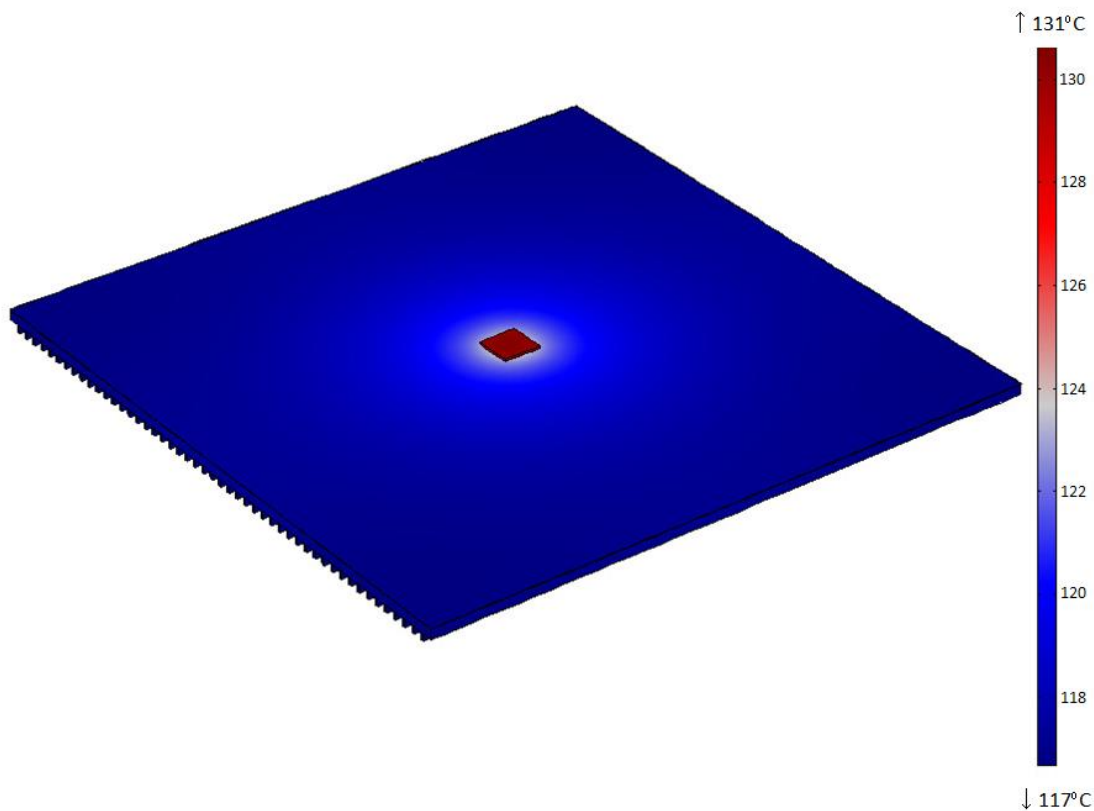
Figure 169 - Temperature distribution in the best mass specific heat transfer micro-finned array under CSTCs (maximum cell's temperature: 131°C) without the emissivity.
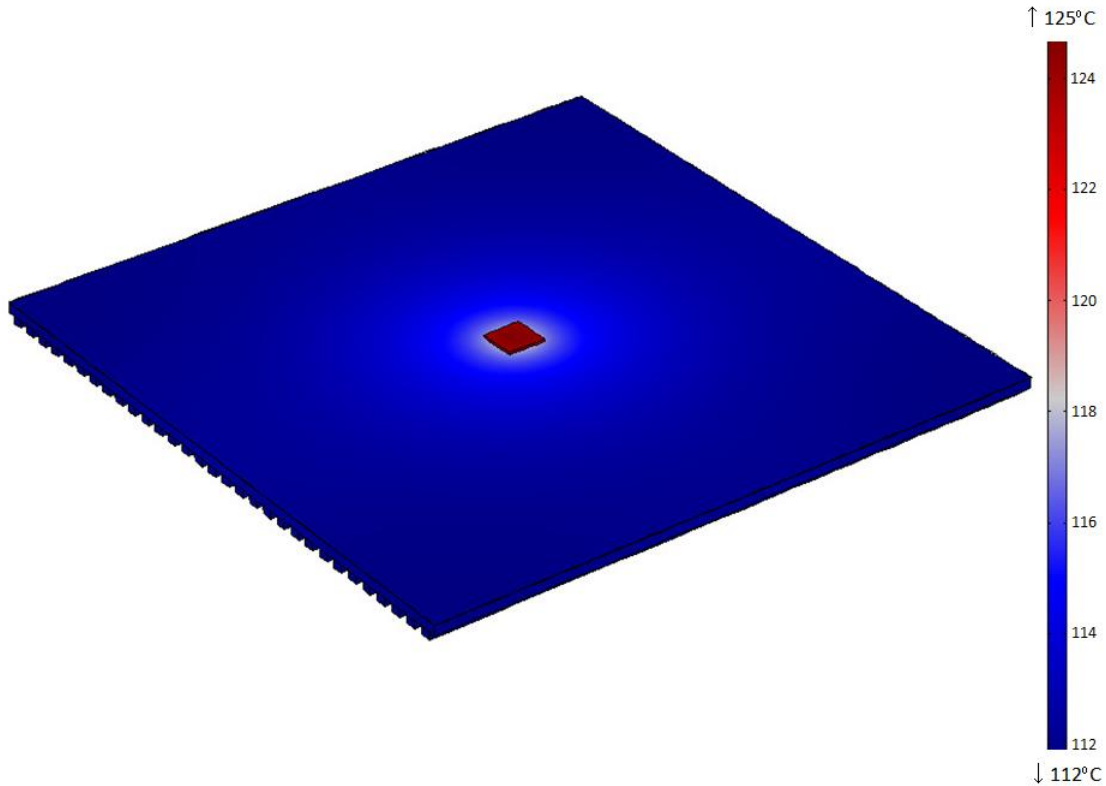
Figure 170 - Temperature distribution in the best effectiveness micro-finned array under CPV operating conditions (maximum cell's temperature: 125°C) without the emissivity.

7.6.4 Mass specific power

In tracked systems, the weight of the heat sink is a factor that can sensibly affect the overall performances. The heat sink was one of the heaviest components of a CPV receiver and, for this reason, reducing the weight would have lowered the tracker's load and, thus, increased the system's efficiency. The mass specific power expresses the ratio between the electrical power output and the heat sink weight. The higher the mass specific power, the lower is the weight of the heat sink per unit of power output. Considering the same electrical output conditions, systems with a high mass specific power are lighter than those with a low mass specific power. Unfortunately, only a limited number of studies reported the dimensions of the heat sinks used in CPV applications, as listed in Table 42.

Table 42 - Properties and mass specific power of passive cooled systems presented in literature. Whereas not reported, a density of 2700 kg/m^3 for aluminum and a 1cm^2 sized cell, with a power output of 20.71W at 500× maximum power point, have been considered.

Ref.	Type of heat sink	Weight of the heat sink/receiver	Cell's size	Max electrical power output (concentration)	Mass specific power
[176]	Heat spreader	0.405 kg	1cm×1cm	20.71W$_e$ (500×)	51.13 W$_e$/kg
[386]	Radial finned	0.600 kg	1cm×1cm	34.99W$_e$ (1000×)	58.32 W$_e$/kg

By using a smaller cell, it was possible to increase the mass specific power: the flat silicon wafer used for a 3mm×3mm cell had a mass specific power about 5 times higher than the one of the heat sinks used for the 1cm×1cm cells. The introduction of the micro-fins was found to further enhance the mass specific power of 50% compared to the unfinned case (Table 43).

Table 43 - Properties and mass specific power of passive cooled systems studied in the present work.

Type of heat sink	Weight of the heat sink	Cell's size	Max electrical power output at 500×	Mass specific power
Flat	0.007798kg	0.3cm×0.3cm	1.96W$_e$	251.34W$_e$/kg
Best mass specific heat transfer	0.005135kg	0.3cm×0.3cm	1.96W$_e$	381.71W$_e$/kg
Best effectiveness	0.006126kg	0.3cm×0.3cm	1.96W$_e$	319.95W$_e$/kg

The best mass specific heat transfer array was found to have a better mass specific power than the best effectiveness array. Taking into account the maximum temperatures of the cells, it was possible to refine the previous predictions, revising the expected maximum electrical power outputs according to the temperature's coefficient reported in the cell's datasheet (-1.8mW/°C). As shown in Table 44, the drops in mass specific power due to the effect of the temperature on the cell's efficiency were in the order of magnitude approximately of 5%.

Table 44 - Refined mass specific powers of passive cooled systems studied in the present work.

Type of heat sink	Max predicted temperature	Refined max electrical power output at 500×	Weight of the heat sink	Mass specific power
Flat	78.8°C	1.86W$_e$	0.007798 kg	238.52W$_e$/kg
Best mass specific heat transfer	73.0°C	1.87W$_e$	0.005135kg	364.18W$_e$/kg
Best effectiveness	70.4°C	1.88W$_e$	0.006126kg	306.88W$_e$/kg

Despite the low number of heat sinks that could be compared, these results confirmed that the micro-fins were able to introduce two benefits to an unfinned

surface: a reduction in maximum temperature and a stronger improvement in terms of mass specific power. This outcome strengthens the thesis that the reduction in weight is the main achievement of micro-fins. Therefore, micro-finned heat sinks can find application in many fields, where the reduction of volumes, weight and costs is a priority, such as the mobile phones, the tablets or laptop markets.

The research of novel heat transfer solutions for electronics packages had been constantly increasing, following the miniaturization of the electronic components. In particular, much effort has been spent on the thermal management of LEDs [387,388]. Table 45 lists different solutions proposed in the last years and compares the masses and the thermal resistances with those of a referenced heat sink presented in [389]. The thermal resistance and the mass of each heat sink varied with the application, so no exhaustive analysis could be conducted in this case. Despite that, the comparison confirmed that the reduction in weight is the main benefit of micro-fins: compared to the reference heat sinks, the micro-fins showed a reduction in mass much important than the increase in thermal resistance.

Table 45 - Comparison of various referenced fin arrays developed for LED applications.

Ref.	Type of heat sink	Power [W]	Mass [kg]	Thermal Resistance [°C/W]	Mass/ Ref. Mass	Thermal resistance/ Ref. thermal resistance
[389]	Radial	5.30	0.230	2.97	Ref.	Ref.
[389]	Radial	5.30	0.179	3.44	0.778	1.160
[389]	Radial	5.30	0.251	2.90	1.091	0.978
[390]	Triangular fins	1	N.A.	97.57	N.A.	32.852
[391]	Plate fins	112	3.930	0.16	17.08	0.054
-	Best mass specific heat transfer	2.2	0.005	21.82	0.022	7.346
-	Plate micro-fins	2.2	0.006	20.64	0.027	6.948

The deployment of different fin geometries can further enhance the thermal and weight benefit of micro-fins. In particular, pin fins were already found to perform better, in terms of heat transfer, than plate fins with the same dimensions. Moreover, pin fins would introduce a significant reduction in weight, leading to an important increase in mass specific power.

7.7 Conclusions

The present chapter reported the investigation on a passively-cooled solar receiver for high concentrating applications. Micro-finned surfaces were found to be one of the most promising solutions for passive CPV cooling and can find use in many applications, such as electronics or communications. In lack of literature on the thermal behaviour of natural convective micro-fins, different fin geometries were diced on the back surface of a silicon wafer and tested in a controlled environment. The correlations between the geometry and the thermal performance were presented: the heat transfer coefficient was found to increase when the fin spacing and the fin thickness were increased and to decrease when the fin height was increased. These correspondences were found to be consistent if the arrays were tilted. A refined Nusselt number correlation for horizontal fin arrays was presented: for the first time, the effects on the thermal behaviour of the micro-fin thickness were considered. The new equation was able to predict the Nusselt number with the highest accuracy so far reported: the average discrepancies dropped from 10.59% and 26% to 6.05% and 7.41% for the data obtained in the present experimental work and in literature respectively. The contribution of the radiative exchange should not be neglected in the study of a micro-fin array in natural convection, since up to the 56% of the heat transferred in the conducted experiment was exchanged by the fins through radiation.

Different heat sinks metrics were considered, since the heat transfer coefficient was not sufficient to predict the thermal performance of a heat sink in natural convection. The micro-fins were found not to be always effective: a ±14% variation in heat transfer was calculated for different geometries compared to a flat surface. It meant that in some applications, due to the small dimensions and the small air volumes involved at micro-scale, the introduction of micro-fins could lead to the deterioration of the thermal exchange. Although no clear correlation was found between the fin effectiveness and the geometry, the results indicated that the fin effectiveness tended to be higher for vertically orientated arrays. On the other hand, the micro-fins were proven to benefit in terms of mass and weight reduction compared to flat heat sinks: in particular, the specific mass heat transfer was found

to increase when increasing the fin spacing or the fin height and decreasing the fin thickness.

A thermal investigation of the micro-finned heat sink was reported to prove the reliability of this solution in CPV. The geometry that maximized the specific mass heat transfer and that one that maximized the fin effectiveness were taken into account. The fins were tested using the input data from an experimental investigation to predict the thermal management of CPV under standard operation and worst case conditions. Under both these conditions, the fins performed well, keeping the solar cell at a lower temperature than the maximum acceptable one and below that predicted for a flat silicon wafer. Along with good thermal performance, the fins showed an increased mass specific power compared to similar solutions currently applied in CPV and LEDs. In particular, the highest value of mass specific power was registered for the array that optimized the mass specific heat transfer: it was about 20% higher than that of the best effectiveness array. This parameter is expected to be further enhanced by different fin geometries, such as the pin fins: along with the proven benefit in heat transfer, pin fins would furtherly decrease the weight of the heat sink and, then, improve the mass specific heat transfer. Reducing the heat sink's weight would reduce the load for the solar tracker and, then, improve the system's efficiency.

Despite the high potential, natural convective micro-fins are still a widely unexplored subject. Only a limited number of papers have been published, and the wide knowledge available for macro-scale heat transfer cannot be applied at micro-scale. Further investigations need to be carried out, in order to reveal the full potentials of this technology. In particular, a correspondence between fin effectiveness and geometry would be useful to design optimized micro-finned systems. In this light, more geometries and materials need to be tested for a wider understanding. Moreover, defining the correlation between the thermal behaviour and the tilt angles of the fin array would be a practical tool for designing naturally convective micro-finned heat sinks for tracked or mobile applications.

Chapter 8:   **Conclusions and future work**

8.1 Summary

Theoretical and experimental investigations on innovative solutions to improve the performance of high concentrating photovoltaic receivers have been presented in this thesis. The research followed two directions: the development of a densely packed cell assembly for a 500× CPV system and a study on the applicability of micro-fins for the passive cooling of single cell HCPV receivers. Both these studies were conducted with the aim to contribute to the development of a low-cost and reliable HCPV, able to increase its share in the competitive power generation market. The most important outcomes of the work are resumed in the following paragraphs.

8.1.1 Selection of materials and components for CPV receivers

The solar receiver is the part of the CPV where the concentrated sunlight is focused and where the current is extracted. It consists of several components: one or more solar cells, by-pass diodes, interconnections, an encapsulant layer, a substrate, and a heat sink. A summary of the most common materials for CPV and the most suitable ones has been first presented. The surface mounted components, such as cells and diodes, are allocated on a substrate, which mechanically supports the whole receiver, transferring the waste heat from the cell to the cooling system and allocating the electrical circuitry. Among the different available substrates, the most appropriate materials were selected through a thermal investigation. A 3D model of the substrates was developed and both the operating and the worst case conditions were reproduced to check the maximum temperatures achieved by the CPV cells.

- Multijunction (MJ) cells were selected because widely recognized as the most convenient device for HCPV applications. Indeed, the commercial triple-junction cells have achieved now efficiencies ranging from 37% to 42%.

- MJ cells are particularly susceptible to the effects of shading, thus, one by-pass diode per cell was installed to reduce electrical losses and risks of

damages. In particular, Schottky diodes were the most suitable ones for HCPV because of the reduced forward voltage drop that led to lower losses and a lower operating temperature.

- The interconnectors were realized by employing the wire bonding technology, considered a reliable solution able to extract the current generated by the cells with limited losses and low costs.

- The encapsulation was made of PDMS, a clear silicone resin solution already employed in CPV systems because of its high transmittance and the long degradation time.

- Despite a thermal behaviour similar to that of the direct bonded boards, the most common substrate used in HCPV applications, insulated metal substrates were preferred for the development of the 144-cell receiver because of the lower costs and the easier manufacturability. The cheap and common printed circuit boards, instead, showed an inappropriate thermal management for the high thermal fluxes of HCPV.

- Despite the higher costs, a 5cm×5cm silicon wafer was selected for the single cell, passively-cooled application, because of the lower temperatures attained. Moreover, the opportunity of integrating a cooling system in the receiver with no need of an intermediate bonding layer was expected to enhance the thermal performance of the system.

8.1.2 Design and fabrication of a densely packed cell assembly

The development of a novel, 144-cell densely packed cell assembly, rated for a peak power of $2.6kW_e$ under standard test conditions, has been presented. The extreme conditions in which CPV systems operate, as well as the high electrical currents and power densities faced, make the design of CPV more complex than that of flat-PV. In the present thesis, the design of the densely packed cell assembly has been explained: the pattern of the electrical circuit, the choice and the size of the components, and the expected electrical and optical losses have been reported in detail and are summarized below. The receivers were manufactured by using standard micro-electronic processes and the whole fabrication process has been detailed in the thesis also.

- The innovative design of the conductive pattern was realized to limit the electrical losses and to minimize the risks of failures, according to the specifications reported by the international standards. Overall, Joule losses were expected to affect the total power output for less than the 1%.

- The cell assembly was conceived to limit the raise in temperature due to the current flow to 5°C. Conservative approaches were followed to size the diodes and the aluminum bonded wires: safety factors of 1.5 and 1.4 were respectively introduced. These initiatives, along with the consideration of adequate mechanical tolerances, enhanced the reliability of the receiver.

- The conductive pattern consisted of four simple copper shapes that, repeated in space, formed the whole electrical circuit and could be easy scaled and adapted to different applications.

- The losses due to the non-ideal optical transmittance of the encapsulation were estimated: out of an average 85.77% optical transmittance, the drop in current output was limited to 7.30% due to the current mismatch between the bottom and the two top-junctions of the cells.

- The insulated metal substrate was produced by chemical etching and the components were manually picked-and-placed. A tin based solder paste with a 3%-content of silver was used to enhance the mechanical strength of the joint. The solder paste was displaced through a specially made thin metallic paste mask.

- Before bonding the wires, the board was cleaned to remove any solder paste left on the surfaces. Despite this process, the 3.75% of the bonded wires were found to unstick, a number that was anyway balanced by the safety factor introduced while dimensioning the wires.

- The methods to enhance the safety of the board when handled or moved have been described in the thesis: some room was left between the cells and the edges of the boards to protect the components from hurts, and four holes were drilled on the boards to allow a safer packaging.

- The design of the substrate was conceived to be directly mounted on the active-cooling system, without any intermediate epoxy or bonding layers.

8.1.3 Analysis and characterization of a densely packed cell assembly

The quality and the reliability of the produced cell assembly were verified through standardized tests and electrical characterizations. Particular effort was spent to demonstrate the strength of the electrical joints, generally the most fragile components in any electric device. Both indoor and outdoor characterizations were conducted to predict the electrical performance of the system while in operation. The first prototype was tested using an AAA solar simulator: due to the size of the board, only a one sun characterization could be conducted in indoor conditions. The experimental data were refined by using a referenced methodology to predict the performance at 500×. The electrical outputs were compared to those of a commercial receiver equipped with the same solar cell. A breakdown of the costs has been reported as well, along with the predictions on the potential cost cutting.

- A cross-sectional visual inspection of the solder joint conducted through a Scanning Electron Microscope showed an uniform distribution of the solder paste below the cell, which was expected to enhance the electrical and thermal performance of the system. A die shear strength test was carried out as well. All the tested samples succeeded, showing higher mechanical strength than the minimum requirement of the international standards: out of a minimum limit of $5.998kg_F$, the joints were found to break under an average force of $10.337kg_F$.

- Similarly, a wire bonding strength test was conducted on the interconnectors. Only one out of the 50 tested wires was found to fail below the minimum force imposed by the standards, probably due to some solder paste contamination left despite the cleaning. The number of faulty connections was well balanced by the adopted safety factor. Overall, the average registered force of $10.169g_F$ was more than three times higher than the minimum load of $2.954g_F$ recommended by the standards.

- An experimental investigation proved the negligible effect of the encapsulant's thermal expansion, due to the high bonding strength of the silicone.

- It was found that the short circuit current generated by the board was 4.80% lower than the one of the commercial receiver under the same testing conditions. Similarly, the open circuit voltage of 3.08V per cell was about 2.06% lower than that of the commercial receiver.

- A peak electrical efficiency of 29.4% was predicted: it was raised up to 32.4% by using more efficient cells. In the same way, the fill factor was enhanced from 81% up to 84%.

- A preliminary outdoor characterization was conducted: the first results demonstrated the reliability of electrical components under the high current expected for HCPV applications.

- The first cell assembly prototypes were produced with a cost of $0.91/$W_p$, which represents about one third of the actual cost of modules reported in literature.

- A drop of 17% in costs was expected by increasing the number of produced units, merely because of components' price reduction if the number of ordered units was increased. Moreover, the exploitation of automatic manufacturing processes would further lower the costs.

8.1.4 Thermal performance of micro-fins in natural convection

A detailed review of cooling technologies for HCPV has been presented. The research focused on suitable passive micro/nano solutions. Among all the reported technologies, micro-fins in natural convections were found to be one of the most attractive because of the simplicity, reliability and potential ability to handle the high fluxed of a 500× CPV system. Despite the wide range of applications of macro-fins and the considerable number of papers published on micro-fins in forced flow conditions, only a restricted number of studies on naturally conductive micro-fins were found. For this reason, a preliminary experimental investigation was conducted to broaden the knowledge on this solution and to contribute to the identification of optimal micro-fin geometries.

- An experimental apparatus was prepared following the methodologies presented in literature: an uncertainty of 8.25% was predicted, which was in line with those reported by the previous investigations.

- In agreement with previous studies, the experimental results indicated that the micro-fin heat transfer coefficient increased with the fin spacing and decreased with the fin height.

- For the first time, the fin heat transfer coefficient was found to increase with the thickness of the fins. At micro-scale, the fins and the air volumes acted as parallel conductive layers, thus increasing the fin thicknesses while keeping the spacing constant enlarged the high-conductive volume of silicon compared to the low-conductive volume of air. So, the overall thermal conductance of the array was enhanced by a larger micro-fin thickness.

- The heat transfer coefficients were shown to increase with the difference between the fin and the air temperatures till a maximum value. For the first time, the heat transfer coefficient was found to decrease after a peak at high temperatures. This was due to the heat transferred by radiation that grows at higher rates than that transferred by convection.

- A refined Nusselt number correlation was proposed. For the first time, the fin thickness was taken into account and the new equation was able to minimize the difference between predicted and experimental data, with an average discrepancy as low as 6.05%.

- Pin fins were found to perform better than plate fins, in terms of heat transfer coefficients.

- Radiation contributed up to the 56% of the heat transfer and was shown to significantly enhance it when increasing the difference between the fin and the air temperatures.

- Micro-fins were found not to always enhance the heat transfer of a flat surface: the fin effectiveness of the considered experimental data ranged between 0.86 and 1.14.

- The mass specific heat transfer was found to increase when fin spacing or height increased, and/or the fin thickness decreased. These results supported the thesis that the drop in weight was the main goal achieved by dicing a micro-fins array on a flat surface.

- The correlations between the heat transfer coefficients and the fin geometry were found to be qualitative consistent when the orientation of the fins was varied.

- The average thermal resistance of micro-fins was found to increase by 12% when the fins had a downward orientation, as compared to the upward facing ones.

- The fin effectiveness was found to achieve higher values for vertically oriented fins: the observed enhancement between horizontal and vertical fins ranged between 2% and 11%.

8.1.5 Applicability of micro-finned heat sinks for passive cooling of HCPV

The experimental investigation conducted on micro-fins under natural convection led to the identification of two optimal fin geometries to be applied for the passive cooling of HCPV. The first geometry enhanced mass specific heat transfer and, was, thus, expected to minimize the weight of the receiver, whereas the second one maximized the fin effectiveness and was expected to optimize the thermal exchange. A 3D thermal model was developed, taking into account the heat transfer coefficients measured in the experiment. The thermal behaviours of the two considered fin geometries were compared with that of an unfinned silicon wafer. Both the operating and the worst case conditions for a 500× CPV system were considered. The numerical investigations showed the outcomes listed below.

- Both fin geometries were found to keep the cell temperature below the maximum allowed limits for CPV and showed enhanced thermal performance than the unfinned surface.

- The best mass specific heat transfer array showed temperatures of 73.0°C in operating conditions and 103°C in the worst case conditions.

- The best effectiveness array showed the lowest cell's temperatures: 70.4°C in operating conditions and 99.9°C in the worst case conditions.

- The cell temperature of the best effectiveness array was found to drop to 48.2°C by reducing the DNI to 900W/m^2 and considering a wind speed of 2m/s.

- The contribution of radiation was demonstrated to be not negligible, since ignoring the emissivity of the material would have increased the cell temperature of the two micro-finned receivers to over 125°C under operating conditions.

- Overall, the employment of micro-fins was found to lead to an improvement of 0.89% in terms of electrical efficiency, as compared to an unfinned surface. Along with that, a significant reduction in the heat sink's weight was achieved.

- The mass specific power of commercial HCPV heat sinks was found to range between 50 and 60W$_e$/kg. The micro-fins studied in this work showed the potential to increase it up to more than 350W$_e$/kg, strongly reducing the load for the tracker.

- Micro-fins enhanced the mass specific power by almost 75% as compared to an unfinned surface. Further enhancements were expected by employing micro-pin fins instead of micro-plate ones.

8.2 Achievements

In 2011, among the research priorities to be addressed by the CPV community, the European Union [46] identified the development of larger modules and the design of effective cooling systems as key targets. The present study was conceived as an effective contribution towards those goals. This thesis reported novel proposals for the optimization of high concentrating photovoltaic receivers. A new densely packed cell assembly was developed, introducing an original low-resistance design of the conductive layers. The exploitation of standard micro-electronics manufacturing processes can lead to a cost reduction, without any negative effect on the quality of the module. Moreover, the use of an insulated metal substrate represented an improvement towards the awaited cost-cutting for CPV. For the first time, all the stages of the design and fabrication of a CPV cell assembly were described. The specific knowledge accumulated on the issues and the challenges

connected with the fabrication of receivers were made available in literature, contributing to the development of more reliable and competitive CPV devices.

The deployment of passively-cooled single cell receivers represents an attractive alternative to large, actively-cooled receivers. Passive cooling systems were proven to be more reliable than active ones and to reduce the risks of damages to the CPV components. Moreover, they are generally cheaper and the employment of micro-technologies can decrease the mass usage required for the heat sink, thus reducing both the costs and the load for the tracker. The investigation on micro-fins in natural convection conditions led to novel fundamental outcomes on the basics of the micro-scaled heat transfer. For the first time, the effect of the fin thickness on the thermal performance was identified and explained. A refined equation to determine the Nusselt number was proposed to predict the heat transfer of different micro-fin geometries. The investigation took into account heat power and temperature ranges that had not been considered before. More importantly, micro-fins were found not to be necessarily beneficial in terms of heat transfer. Despite being unusual and unexpected for extended surfaces, this behaviour was explained because of the conduction is dominant over natural convection when air is constrained within the narrow volumes between micro-fins.

The experimental investigation carried out in this study allowed identifying the most favourable micro-fin geometry to be applied to CPV. As for the employment of micro-fins for the passive cooling of HCPV, no previous attempts were reported in literature. Micro-fins machined on a silicon wafer showed the potential to introduce a double benefit: decreasing the CPV cell temperature and, at the same time, reducing the heat sink weight. Along with that, the use of micro-fins can likely enhance the mass specific power of the receiver as compared to the currently available heat sinks and micro-scaled flat silicon wafers. These results suggest that the employment of cooling micro-fins can be beneficial in several mobile or tracked applications where the reduction of weight and costs are primary requirements.

8.3 Recommendations for future works

The major objectives of the project were achieved and have been reported in detail in the present thesis. However, some of the BioCPV project's tasks have yet to be concluded. The full scale prototype was being installed in the Indian Institute of Technology Madras, India: a full scale outdoor characterization would allow refining the design of the presented receivers, in order to enhance the electrical and the thermal performance of the system. A long term outdoor testing would also prove the durability of the developed receivers and highlight which modifications need to be introduced. Moreover, the fabrication of the single cell receiver would allow a full scale characterization, in terms of electrical and thermal performance. Finally, new ideas to be investigated emerged during the current study. Hence, a list of recommendations for future works is reported here:

- Minimize the non-uniform optical losses from the CPV module to improve the electrical performance.

- Evaluate different configurations of the cells' series on the densely-packed cell assembly in order to maximize the electrical performance according to the distribution of light. As pointed out, a significant enhancement in power output (up to the 25%) can be achieved by increasing the number of series and dividing the central cells from those on the sides. In this light, further experimental data about the light distribution are needed.

- Improve the quality of the manufactured receivers, through the employment of automatic processes.

- Perform accelerated weather tests to enhance the stability of the cell assembly.

- On-field installation and continuous monitoring of the produced receiver to get more information on the long term performance and on the durability of the components.

- Evaluate the effect of dust on the performance of the densely packed receiver.

- Investigate the behaviour of MJ cells under IR reflecting coverglasses.

- Analyse the levelized cost of energy (LCOE) of the whole CPV system.

- Investigate the correspondence between the fin effectiveness and the fin geometry to optimize the design of micro-finned heat sinks. In particular, the benefits for CPV cooling due to the introduction of micro-pin fins instead of plate ones should be studied.

- Perform a detailed energy analysis of the benefits of a light, micro-passive cooling heat sink as compared to an active cooling system.

- Develop and test the single cell receiver with an integrated micro-finned array.

These recommendations are expected to improve the performance and reduce the costs of CPV systems. These investigations could not be conducted earlier because of time constraints, and because they were out of the primary scope of the PhD project, but would definitely contribute to CPV cost-cutting and to its diffusion in the future power generation market. Moreover, the installation of the full BioCPV project power system will allow broadening the investigation: researches on the integration of different energy sources and on the opportunity of providing reliable and continuous renewable power to rural areas will be presented.

The study on micro-technologies for passive CPV cooling led to the discovery of a high potential solution which has been yet limitedly investigated. More research on the fundamentals of micro-fin heat transfer should be conducted. Moreover, further experimental investigations on the application of micro-fins for cooling purposes are recommended because they can be beneficial for both the scientific and the industrial communities. Possible approaches in this respect are:

- Research on fin geometries different than plate or pin fins, on a wider range of fins dimensions, including the nano-scale, and on a broader variety of materials.

- Investigate the behaviour of micro-finned arrays made of different materials.

- Experimental investigation on the cooling performance of micro-fins for a concentrated heat source. So far, the heat transfer in micro-fins has been experimentally studied only for uniform heat sources, with a heating surface as large as the heat sink.

- Correlation between the thermal behaviour and the orientation of the fins. This research would be useful for the prediction of the thermal performance of tracked systems, such as CPV.

Micro- and nano-technologies can address the requirements for smaller volumes and lower costs that are currently sought after by industries and customers. When the dimensions of the components are scaled to the micro- or nano-range, important changes in the materials properties take place. These changes need to be investigated to maximize the benefits that micro- and nano-technologies can provide to our everyday life.

Bibliography

[1]   British Petroleum, BP Statistical Review of World Energy June 2014, 2014.

[2]   International Energy Agency, Key World Energy Statistics 2014, Paris, 2014.

[3]   World Energy Council, World Energy Resources, London, 2013.

[4]   International Energy Agency, World Energy Investment Outlook, Paris, 2014.

[5]   Renewable Energy Policy Network for the 21st Century, Renewables 2014: Global status report, 2014.

[6]   World Commission on Environment and Development, Report of the World Commission on Environment and Development, 1987.

[7]   M. Hosenuzzaman, N.A. Rahim, J. Selvaraj, M. Hasanuzzaman, A.B.M.A. Malek, A. Nahar, Global prospects, progress, policies, and environmental impact of solar photovoltaic power generation, Renew. Sustain. Energy Rev. 41 (2015) 284–297. doi:10.1016/j.rser.2014.08.046.

[8]   N.S. Lewis, Toward cost-effective solar energy use., Science. 315 (2007) 798–801. doi:10.1126/science.1137014.

[9]   K.S. Reddy, T.K. Mallick, D. Chemisana, Solar Power Generation, Int. J. Photoenergy. 2013 (2013) 1–2. doi:http://dx.doi.org/10.1155/2013/950564.

[10]   L. Micheli, Model and analysis of Compound Parabolic Collectors and Organic Rankine Cycles applied to Concentrating Solar Power plants, 2011.

[11]   A. Luque, S. Hegedus, Handbook of Photovoltaic Science and Engineering, John Wiley & Sons, Ltd, Chichester, UK, 2003. doi:10.1002/0470014008.

[12]   A. Goetzberger, V. Hoffmann, Photovoltaic solar energy generation, Springer, 2005.

[13]   P.D. Lund, How fast can businesses in the new energy sector grow? An analysis of critical factors, Renew. Energy. 66 (2014) 33–40. doi:http://dx.doi.org/10.1016/j.renene.2013.11.061.

[14]   A. Orioli, A. Di Gangi, Review of the energy and economic parameters involved in the effectiveness of grid-connected PV systems installed in multi-storey buildings, Appl. Energy. 113 (2014) 955–969. doi:10.1016/j.apenergy.2013.08.014.

[15]   J. Ondraczek, N. Komendantova, A. Patt, WACC the dog: The effect of financing the levelized cost of solar PV power, Renew. Energy. 75 (2013) 1–32. doi:http://dx.doi.org/10.2139/ssrn.2321130.

[16]   US Energy Information Administration, Levelized Cost and Levelized Avoided Cost of New Generation Resources in the Annual Energy Outlook 2014, 2014.

[17]   Parsons Brinckerhoff, Solar PV cost update, 2012.

[18]   S. Kurtz, Opportunities and challenges for development of a mature concentrating photovoltaic power industry, Golden, CO, 2011.

[19]   P. Verlinden, A. Lewandowski, C. Bingham, G. Kinsey, R. Sherif, J. Lasich, Performance and Reliability of Multijunction III-V Modules for Concentrator Dish and Central Receiver Applications, in: 2006 IEEE 4th World Conf. Photovolt. Energy Conf., IEEE, 2006: pp. 592–597. doi:10.1109/WCPEC.2006.279526.

[20]   E.R. Messmer, CPV Market Evolution and the Potential in Cost Reduction of CPV Modules, in: 9th Conf. Conc. Photovolt. Syst., 2013: pp. 1–4.

[21]   G. Timò, Results of the APOLLON Project and Concentrating Photovoltaic Perspective, Milan (IT), 2014.

[22]   GlobalData, Concentrated Photovoltaics (CPV), Update 2014 – Global Market Size, Competitive Landscape and Key Country Analysis to 2020, 2014.

[23]   M. Mendelsohn, T. Lowder, B. Canavan, Utility-Scale Concentrating Solar Power and Photovoltaics Projects : A Technology and Market Overview, 2012.

[24]   J. Foresi, A. Babej, R. Han, C. Wang, D. King, Suncore's CPV power plant deployment in western China, 2014 IEEE 40th Photovolt. Spec. Conf. (2014) 3282–3286. doi:10.1109/PVSC.2014.6925636.

[25]   A. Luque, V.M. Andreev, Concentrator Photovoltaics, Springer Berlin Heidelberg, Berlin, Heidelberg, 2007. doi:10.1007/978-3-540-68798-6.

[26]   C. Algora, I. Rey-Stolle, I. Garcia, B. Galiana, M. Baudrit, P. Espinet, et al., III–V multijunction solar cells for ultra-high concentration photovoltaics, in: 2009 34th IEEE Photovolt. Spec. Conf., IEEE, 2009: pp. 001571–001575. doi:10.1109/PVSC.2009.5411372.

[27]   P. Antonini, Concentrated PhotoVoltaics (CPV): Is it a real opportunity?, EPJ Web Conf. 54 (2013) 01015. doi:10.1051/epjconf/20135401015.

[28]   A.W. Bett, S.P. Philipps, S.S. Essig, S. Heckelmann, R. Kellenbenz, V. Klinger, et al., Overview about Technology Perspectives for High Efficiency Solar Cells for Space and Terrestrial Applications, in: 28th Eur. Photovolt. Sol. Energy Conf. Exhib., Paris, 2013: pp. 1–6. doi:10.4229/28thEUPVSEC2013-1AP.1.1.

[29]   P. Pérez-Higueras, E. Muñoz, G. Almonacid, P.G. Vidal, High Concentrator PhotoVoltaics efficiencies: Present status and forecast, Renew. Sustain. Energy Rev. 15 (2011) 1810–1815. doi:10.1016/j.rser.2010.11.046.

[30]   N. Sarmah, Design and Performance Evaluation of a Low Concentrating Line-axis Dielectric Photovoltaic System, Heriot-Watt University Edinburgh, 2012.

[31]   S.P. Philipps, A.W. Bett, K. Horowitz, S. Kurtz, Current status of concentrator photovoltaic (CPV) technology, 2015.

[32]   M. Yamaguchi, T. Takamoto, K. Araki, M. Imaizumi, N. Kojima, Y. Ohshita, Present and Future of High Efficiency Multi-Junction Solar Cells, in: CLEO2011 - Laser Appl. to Photonic Appl., OSA, Washington, D.C., 2011: p. CMT5. doi:10.1364/CLEO_SI.2011.CMT5.

[33]   H. Cotal, C. Fetzer, J. Boisvert, G. Kinsey, R. King, P. Hebert, et al., III–V multijunction solar cells for concentrating photovoltaics, Energy Environ. Sci. 2 (2009) 174. doi:10.1039/b809257e.

[34]   R.D. Schultz, F.. Vorster, E.. van Dyk, Performance of multi-junction cells due to illumination distribution across the cell surface, Phys. B Condens. Matter. 407 (2012) 1649–1652. doi:10.1016/j.physb.2011.09.108.

[35]   H. Baig, K.C. Heasman, T.K. Mallick, Non-uniform illumination in concentrating solar cells, Renew. Sustain. Energy Rev. 16 (2012) 5890–5909. doi:10.1016/j.rser.2012.06.020.

[36]   M. Khamooshi, H. Salati, F. Egelioglu, A. Hooshyar Faghiri, J. Tarabishi, S. Babadi, A Review of Solar Photovoltaic Concentrators, Int. J. Photoenergy. 2014 (2014) 1–17. doi:10.1155/2014/958521.

[37]   N. Sellami, Design and characterisation of a novel translucent solar concentrator, Heriot-Watt University, 2013.

[38]   W.T. Xie, Y.J. Dai, R.Z. Wang, K. Sumathy, Concentrated solar energy applications using Fresnel lenses: A review, Renew. Sustain. Energy Rev. 15 (2011) 2588–2606. doi:10.1016/j.rser.2011.03.031.

[39]   J. Fraden, Handbook of Modern Sensors: Physics, Designs, and Applications, Springer, 2010.

[40]   V.D. Rumyantsev, 8 Terrestrial Concentrator PV Systems, in: Springer Ser. Opt. Sci., Springer, 2007.

[41]   P.J. Sonneveld, G.L.A.M. Swinkels, B.A.J. Van Tuijl, H.J.J. Janssen, J. Campen, G.P.A. Bot, Performance of a concentrated photovoltaic energy system with static linear Fresnel lenses, Sol. Energy. 85 (2011) 432–442. doi:10.1016/j.solener.2010.12.001.

[42]   D.C. Miller, S.R. Kurtz, Durability of Fresnel lenses: A review specific to the concentrating photovoltaic application, Sol. Energy Mater. Sol. Cells. 95 (2011) 2037–2068. doi:10.1016/j.solmat.2011.01.031.

[43]   M.A. Green, K. Emery, Y. Hishikawa, W. Warta, E.D. Dunlop, Solar cell efficiency tables (Version 45), Prog. Photovoltaics Res. Appl. 23 (2015) 1–9. doi:10.1002/pip.2573.

[44]   T.N.D. Tibbits, P. Beutel, M. Grave, C. Karcher, E. Oliva, G. Siefer, et al., New efficiency frontiers with wafer-bonded multi-junction solar cells, in: 29th Eur. Photovolt. Sol. Energy Conf. Exhib., Amsterdam, The Netherlands, 2014: pp. 1–4.

[45]   C.H. Henry, Limiting efficiencies of ideal single and multiple energy gap terrestrial solar cells, J. Appl. Phys. 51 (1980) 4494. doi:10.1063/1.328272.

[46]   European Commission, A Strategic Research Agenda for Photovoltaic Solar Energy Technology, 2011. doi:10.2788/15824.

[47]   M.J. Keevers, C. Fai, J. Lau, M.A. Green, I. Thomas, J.B. Lasich, et al., High Efficiency Spectrum Splitting Prototype Submodule Using Commercial CPV Cells, in: 6th World Conf. Photovolt. Energy Convers., Kyoto, Japan, 2014.

[48]   M. Steiner, A. Bösch, A. Dilger, F. Dimroth, T. Dörsam, M. Muller, et al., FLATCON CPV

module with 36.7% efficiency equipped with four-junction solar cells, Prog. Photovoltaics Res. Appl. (2014). doi:10.1002/pip.2568.

[49]   K. Ghosal, D. Lilly, J. Gabriel, S. Seel, B. Fisher, S. Burroughs, et al., Semprius Module and System Results, in: Photovolt. Spec. Conf. (PVSC), 2014 IEEE 40th, 2014: pp. 3287–3292.

[50]   K. Araki, T. Yano, Y. Kuroda, 30 kW concentrator photovoltaic system using dome-shaped Fresnel lenses., Opt. Express. 18 (2010) A53–63.

[51]   ZenithSolar, Revolutionary Concentrated PV reaches world record of 72 % solar efficiency in the field, now connected to the grid, (2010) 1–4.

[52]   E. Wesoff, Rest in Peace: The List of Deceased Solar Companies, 2009 to 2013, Greentech Media. (2013).

[53]   J. Gifford, SolFocus no more, Pv Mag. (2013).

[54]   E. Wesoff, Big 50MW CPV Project in the Works for SolFocus in Mexico, Greentech Media. (2012).

[55]   Soitec, Soitec CPV Installations, n.d.

[56]   J. Runyon, Soitec To Give Up on Solar CPV, RenewableEnergyWorld.com. (2015).

[57]   K.S. Dicks, Soitec 1.29 MWp Portugal CPV plant "opens the way" for similar projects in Southern Europe, PV Insid. (2014).

[58]   K.S. Dicks, Hami to be home to one of Asia's largest CPV plants, PV Insid. (2014).

[59]   H. Hashem, Saudi PV ambitions take a new turn, PV Insid. (2014).

[60]   N. Choudhury, Soitec installs 25kW CPV demonstration plant in Namibia, PV-Tech.org. (2013).

[61]   B. Gonzalez, CPV Intelligence Brief 15 – 28 May 2013, PV Insid. (2013).

[62]   IEC, IEC 62670-1 Concentrator photovoltaic (CPV) module and assembly performance testing and energy rating - Part 1: Performance measurements and power rating - Irradiance and temperature, (2012).

[63]   E.F. Fernández, G. Siefer, M. Schachtner, a. J. García Loureiro, P. Pérez-Higueras, Temperature coefficients of monolithic III-V triple-junction solar cells under different spectra and irradiance levels, in: AIP Conf. Proc., Toledo, Spain, 2012: pp. 189–193. doi:http://dx.doi.org/10.1063/1.4753865.

[64]   G. Siefer, A.W. Bett, Analysis of temperature coefficients for III-V multi-junction concentrator cells, Prog. Photovoltaics Res. Appl. 22 (2014) 515–524. doi:10.1002/pip.2285.

[65]   A. Royne, C.J. Dey, D.R. Mills, Cooling of photovoltaic cells under concentrated illumination: a critical review, Sol. Energy Mater. Sol. Cells. 86 (2005) 451–483. doi:http://dx.doi.org/10.1016/j.solmat.2004.09.003.

[66]   A. Al-Alili, Y. Hwang, R. Radermacher, I. Kubo, A high efficiency solar air conditioner using concentrating photovoltaic/thermal collectors, Appl. Energy. 93 (2012) 138–147. doi:10.1016/j.apenergy.2011.05.010.

[67]   R. Kumar, M. a. Rosen, A critical review of photovoltaic–thermal solar collectors for air heating, Appl. Energy. 88 (2011) 3603–3614. doi:10.1016/j.apenergy.2011.04.044.

[68]   IEEE-SA Standards Board, IEEE Recommended Practice for Qualification of Concentrator Photovoltaic (PV) Receiver Sections and Modules, 2001.

[69]   International Electrotechnical Commission, Concentrator photovoltaic (CPV) modules and assemblies - Design qualification and type approval (IEC 62108 ed1.0), (2007).

[70]   P. Rodrigo, E.F. Fernández, F. Almonacid, P.J. Pérez-Higueras, Review of methods for the calculation of cell temperature in high concentration photovoltaic modules for electrical characterization, Renew. Sustain. Energy Rev. 38 (2014) 478–488. doi:10.1016/j.rser.2014.06.008.

[71]   Spirit Circuits Limited, Requirements of PCB's in solar & LED applications, in: EIPC Winter Conf. 2013, 2013.

[72]   M. Correvon, J. Nagashima, R. Apter, Power modules with IMS substrates for automotive applications, in: Veh. Technol. Conf. IEEE 55th Veh. Technol. Conf. VTC Spring 2002 (Cat. No.02CH37367), IEEE, 2002: pp. 2056–2062. doi:10.1109/VTC.2002.1002986.

[73]   L. Mabille, C. Mangeant, M. Baudrit, Development of CPV solar receiver based on insulated metal substrate (IMS): Comparison with receiver based on the direct bonded copper substrate (DBC) - A reliability study, in: AIP Conf. Proc., 2012: pp. 289–293.

doi:10.1063/1.4753888.

[74]   A. Antonini, Photovoltaic Concentrators - Fundamentals, Applications , Market & Prospective, in: R. Manyala (Ed.), Sol. Collect. Panels, Theory Appl., Sciyo, 2010: pp. 31–54. doi:10.5772/10330.

[75]   M. Cozzini, Solar Cell Cooling and Heat Recovery in a Concentrated Photovoltaic System, in: 2012 COMSOL Conf. Milan, Milan, 2012.

[76]   I. Fishbein, N.M. Abramowitz, Insulated metal substrates improve in performance and product implementation, in: [Proceedings] APEC '92 Seventh Annu. Appl. Power Electron. Conf. Expo., IEEE, Boston, MA, 1992: pp. 633–638. doi:10.1109/APEC.1992.228352.

[77]   P. Mottier, LED for Lighting Applications, 1 edition, Wiley-ISTE, 2009. doi:10.1002/9780470612019.fmatter.

[78]   AZURSPACE Solar Power GmbH, Enhanced Fresnel Assembly - EFA, 2010.

[79]   Spectrolab Inc., CCA 100 C3MJ 1A Concentrator Cell Assembly, 91342 (2011).

[80]   Emcore Corporation, CTJ Receiver Assembly – 5.5 mm x 5.5 mm, Assembly. (2011) 617360.

[81]   J.S. Foresi, L. Yang, P. Blumenfeld, J. Nagyvary, G. Flynn, D. Aiken, EMCORE receivers for CPV system development, in: 2010 35th IEEE Photovolt. Spec. Conf., IEEE, Honolulu, HI, 2010: pp. 209–212. doi:10.1109/PVSC.2010.5614511.

[82]   O. Arenas, S. Chow, L.-M. Collin, J.F. Wheeldon, C.E. Valdivia, A. Turala, et al., Advances in Cell Carriers for CPV Applications, Physics (College. Park. Md). 66 (2010) 66–69. doi:10.1063/1.3509234.

[83]   W. Escher, S. Paredes, S. Zimmermann, C.L. Ong, P. Ruch, B. Michel, Thermal management and overall performance of a high concentration PV, in: 8th Int. Conf. Conc. Photovolt. Syst., 2012: pp. 239–243. doi:10.1063/1.4753877.

[84]   W. Escher, R. Ghannam, A. Khalll, S. Paredes, B. Michel, Advanced liquid cooling for concentrated photovoltaic electro-thermal co-generation, in: Therm. Issues Emerg. Technol., IEEE, Cairo, 2010: pp. 9–17.

[85]   R.A. Messenger, J. Ventre, Photovoltaic Systems Engineering, 2005.

[86]   M. a. Green, A. Ho-Baillie, Forty three per cent composite split-spectrum concentrator solar cell efficiency, Prog. Photovoltaics Res. Appl. 18 (2010) 42–47. doi:10.1002/pip.924.

[87]   B. Mitchell, G. Peharz, G. Siefer, M. Peters, T. Gandy, J.C. Goldschmidt, et al., Four-junction spectral beam-splitting photovoltaic receiver with high optical efficiency, Prog. Photovoltaics Res. Appl. 19 (2011) 61–72. doi:10.1002/pip.988.

[88]   J.D. McCambridge, M.A. Steiner, B.L. Unger, K.A. Emery, E.L. Christensen, M.W. Wanlass, et al., Compact spectrum splitting photovoltaic module with high efficiency, Prog. Photovoltaics Res. Appl. 19 (2011) 352–360. doi:10.1002/pip.1030.

[89]   A. Barnett, D. Kirkpatrick, C. Honsberg, D. Moore, M. Wanlass, K. Emery, et al., Very high efficiency solar cell modules, Prog. Photovoltaics Res. Appl. 17 (2009) 75–83. doi:10.1002/pip.852.

[90]   M. Stefancich, A. Zayan, M. Chiesa, S. Rampino, D. Roncati, L. Kimerling, et al., Single element spectral splitting solar concentrator for multiple cells CPV system., Opt. Express. 20 (2012) 9004–18.

[91]   B. Burnett, The basic physics and design of III-V multijunction solar cells, 2002.

[92]   M. Yamaguchi, III–V compound multi-junction solar cells: present and future, Sol. Energy Mater. Sol. Cells. 75 (2003) 261–269. doi:10.1016/S0927-0248(02)00168-X.

[93]   G. Zubi, J.L. Bernal-Agustín, G.V. Fracastoro, High concentration photovoltaic systems applying III–V cells, Renew. Sustain. Energy Rev. 13 (2009) 2645–2652. doi:10.1016/j.rser.2009.07.002.

[94]   S.P. Philipps, F. Dimroth, A.W. Bett, High Efficiency III-V Multijunction Solar Cells, in: Pract. Handb. Photovoltaics, Elsevier Ltd, 2012: pp. 417–448. doi:10.1016/B978-0-12-385934-1.00013-1.

[95]   A. De Vos, Detailed balance limit of the efficiency of tandem solar cells, J. Phys. D. Appl. Phys. 13 (1980) 839–846. doi:10.1088/0022-3727/13/5/018.

[96]   R.R. King, D. Bhusari, A. Boca, D. Larrabee, X.-Q. Liu, W. Hong, et al., Band gap-voltage offset and energy production in next-generation multijunction solar cells, Prog. Photovoltaics Res. Appl. 19 (2011) 797–812. doi:10.1002/pip.1044.

[97]   D.C. Law, R.R. King, H. Yoon, M.J. Archer, a. Boca, C.M. Fetzer, et al., Future technology pathways of terrestrial III–V multijunction solar cells for concentrator photovoltaic systems,

Sol. Energy Mater. Sol. Cells. 94 (2010) 1314–1318. doi:10.1016/j.solmat.2008.07.014.

[98]   R.R. King, D. Bhusari, D. Larrabee, X.-Q. Liu, E. Rehder, K. Edmondson, et al., Solar cell generations over 40% efficiency, Prog. Photovoltaics Res. Appl. 20 (2012) 801–815. doi:10.1002/pip.1255.

[99]   C. Chukwuka, K.A. Folly, Overview of Concentrated Photovoltaic (CPV) Cells, J. Power Energy Eng. 02 (2014) 1–8. doi:10.4236/jpee.2014.211001.

[100]   a. W. Bett, F. Dimroth, G. Stollwerck, O.V. Sulima, III-V compounds for solar cell applications, Appl. Phys. A Mater. Sci. Process. 69 (1999) 119–129. doi:10.1007/s003390050983.

[101]   A.W. Bett, C. Baur, R. Beckert, F. Diimroth, Development of high-efficiency mechanically stacked GaInP/GaInAs-GaSb triple-junction concentrator solar cells, in: 17th EU-PVSEC, Munich, 2001: pp. 3–6.

[102]   A. Woyte, J. Nijs, R. Belmans, Partial shadowing of photovoltaic arrays with different system configurations: literature review and field test results, Sol. Energy. 74 (2003) 217–233.

[103]   R.M. Sullivan, Shadow effects on a series-parallel array of solar cells, Greenbelt, Maryl. NASA, Goddard Sp. Flight Cent. (1965) 1–18.

[104]   P. Rodrigo, E.F. Fernández, F. Almonacid, P.J. Pérez-Higueras, A simple accurate model for the calculation of shading power losses in photovoltaic generators, Sol. Energy. 93 (2013) 322–333. doi:10.1016/j.solener.2013.04.009.

[105]   K. Brecl, M. Topič, Self-shading losses of fixed free-standing PV arrays, Renew. Energy. 36 (2011) 3211–3216. doi:10.1016/j.renene.2011.03.011.

[106]   M.C. Alonso-Garcia, J.M. Ruiz, F. Chenlo, Experimental study of mismatch and shading effects in the – characteristic of a photovoltaic module, Sol. Energy Mater. Sol. Cells. 90 (2006) 329–340. doi:10.1016/j.solmat.2005.04.022.

[107]   S. Silvestre, A. Boronat, A. Chouder, Study of bypass diodes configuration on PV modules, Appl. Energy. 86 (2009) 1632–1640. doi:10.1016/j.apenergy.2009.01.020.

[108]   J. Leloux, E. Lorenzo, B. García-Domingo, J. Aguilera, C. a. Gueymard, A bankable method of assessing the performance of a CPV plant, Appl. Energy. 118 (2014) 1–11. doi:10.1016/j.apenergy.2013.12.014.

[109]   P. Rodrigo, E.F. Fernández, F. Almonacid, P.J. Pérez-Higueras, Outdoor measurement of high concentration photovoltaic receivers operating with partial shading on the primary optics, Energy. 61 (2013) 583–588. doi:10.1016/j.energy.2013.09.024.

[110]   Vishay, Solar Cell Bypass Diodes in Silicon Crystalline Photovoltaic Panels, 2011.

[111]   F.J. Vorster, E.E. van Dyk, Current-voltage characteristics of high-concentration, photovoltaic arrays, Prog. Photovoltaics Res. Appl. 13 (2005) 55–66. doi:10.1002/pip.563.

[112]   H.J.J. Janssen, P.J. Sonneveld, G.L.A.. . Swinkels, B.A.J. van Tuijl, H.F. de Zwart, F. Dimroth, et al., The Effect of Shadow Lines on a Low Concentrating Photovoltaic System, in: 7th Int. Conf. Conc. Photovolt. Syst. CPV-7, Las Vegas, NE, 2011: pp. 150–153. doi:10.1063/1.3658315.

[113]   A.P. Malvino, D.J. Bates, Electronic Principles, McGraw-Hill, 2007.

[114]   R.T. Paynter's, Introductory Electronic Devices and Circuits, Seventh Ed, Pearson, 2001.

[115]   G. Acciari, D. Graci, A. La Scala, Higher PV Module Efficiency by a Novel CBS Bypass, IEEE Trans. Power Electron. 26 (2011) 1333–1336. doi:10.1109/TPEL.2010.2095469.

[116]   G. Martinelli, M. Stefancich, 7 Solar Cell Cooling, in: Conc. Photovoltaics, Springer, 2007: pp. 133–149.

[117]   AZURSPACE Solar Power GmbH, 3C40 Concentrator Triple Junction Solar Cell datasheet, (2010).

[118]   N. Bosco, C. Sweet, S. Kurtz, Reliability testing the die-attach of CPV cell assemblies, in: Conf. Rec. IEEE Photovolt. Spec. Conf., 2009: pp. 917–922. doi:10.1109/PVSC.2009.5411139.

[119]   G. Calabrese, F. Gualdi, S. Baricordi, P. Bernardoni, V. Guidi, L. Pozzetti, et al., Numerical simulation of the temperature distortions in InGaP/GaAs/Ge solar cells working under high concentrating conditions due to voids presence in the solder joint, Sol. Energy. 103 (2014) 1–11. doi:http://dx.doi.org/10.1016/j.solener.2014.02.007.

[120]   DOW Corning, Thermally Conductive Adhesives, (2009).

[121]   A. Duckham, Z. He, Method for solder bonding CPV receiver to heat sink, in: Photovolt.

Spec. Conf. (PVSC), 2009 34th IEEE, IEEE, Philadelphia, PA, 2009: pp. 001975–001977.

[122]   J. Ross, G. Caswell, C. Hillman, Ensuring and Predicting the Reliability of Concentrated Photovoltaics (CPV): Interconnect Structures Reliability Challenges in CPV Interconnects, DfR Solut. (2010).

[123]   M. Cao, S. Butler, J.T. Benoit, Y. Jiang, R. Radhakrishnan, Y. Chen, et al., Thermal Stress Analysis/Life Prediction of Concentrating Photovoltaic Module, J. Sol. Energy Eng. 130 (2008) 021011. doi:10.1115/1.2840572.

[124]   AUREL s.p.a., Concentration PhotoVoltaic (CPV): the next generation, (n.d.).

[125]   M.L. Minges, Electronic Materials Handbook: Vol 1, Packaging, CRC Press, 1989.

[126]   Heraeus, Bonding Wires for Semiconductor Technology, (n.d.) 2009.

[127]   M. Kempe, Overview of Scientific Issues Involved in Selection of Polymers for PV Applications Preprint, in: 37th IEEE Photovolt. Spec. Conf. (PVSC 37), IEEE, Seattle, 2011.

[128]   D.C. Miller, M.D. Kempe, C.E. Kennedy, S.R. Kurtz, Analysis of Transmitted Optical Spectrum Enabling Accelerated Testing of CPV Designs Preprint, Renew. Energy. (2009).

[129]   M.D. Kempe, M. Kilkenny, T. Moricone, J. Zhang, Accelerated stress testing of hydrocarbon-based encapsulants for medium-concentration CPV applications, in: Photovolt. Spec. Conf. (PVSC), 2009 34th IEEE, IEEE, 2009: pp. 001826–001831.

[130]   D.C.D.C. Miller, M.D.M.D. Kempe, K. Araki, C.E. Kennedy, S.R. Kurtz, The durability of polymeric encapsulation materials for Concentrating Photovoltaic Systems, in: PV Modul. Reliab. Work., 2011: p. 80401.

[131]   K. McIntosh, J. Cotsell, J. Cumpston, The effect of accelerated aging tests on the optical properties of silicone and EVA encapsulants, 24th EU PVSEC. (2009).

[132]   A. Norris, N. Powell, B. Ketola, J.N.J. Cotsell, K.R. Mcintosh, Advanced Silicone Photovoltaic Encapsulants, Futur. Photovoltaics. (2010) 1–8.

[133]   M. Velderrain, Choosing a Silicone Encapsulant for Photovoltaic Applications, in: 7. Int. Conf. Conc. Photovolt. Syst., 2011: pp. 79–83. doi:10.1063/1.3658299.

[134]   H. Yoon, D.E.D.E. Joslin, D.C.D.C. Law, D. Krut, R.R.R. King, P. Vijayakumar, et al.,

Application of infrared reflecting (IRR) coverglass on multijunction III-V solar cells, in: Photovolt. Energy Conversion, Conf. Rec. 2006 IEEE 4th World Conf., IEEE, 2006: pp. 1861–1864.

[135]   L. Micheli, N. Sarmah, X. Luo, K. Reddy, T. Mallick, Infrared reflecting coverglass for multijunction cells in a terrestial high-concentrating photovoltaic system, in: 27th Eur. Photovolt. Sol. Energy Conf. Exhib., Frankfurt, 2012: pp. 266–270.

[136]   J.F. Geisz, J. Scott Ward, A. Duda, W. Olavarria, L. Gedvilas, M. Young, et al., Infrared Reflective and Transparent Inverted Metamorphic Triple Junction Solar Cells, Physics (College. Park. Md). 11 (2010) 11–15. doi:10.1063/1.3509169.

[137]   H. Yoon, M. Haddad, S. Mesropian, J. Yen, K. Edmondson, D. Law, et al., Progress of inverted metamorphic III–V solar cell development at Spectrolab, in: Photovolt. Spec. Conf. 2008. PVSC'08. 33rd IEEE, IEEE, 2008: pp. 1–6.

[138]   K. Mullaney, G. Jones, C. Kitchen, D. Jones, Infra-red reflective coverglasses: the next generation, in: Photovolt. Spec. Conf. 1993., Conf. Rec. Twenty Third IEEE, IEEE, 1993: pp. 1363–1368.

[139]   J. Russell, G. Jones, J. Hall, A new UVR/IRR coverglass for triple junction cells, in: Photovolt. Energy Conversion, Conf. Rec. 2006 IEEE 4th World Conf., IEEE, 2006: pp. 1911–1914.

[140]   K. Araki, M. Kondo, H. Uozumi, M. Yamaguchi, Development of a robust and high efficiency concentrator receiver, in: Photovolt. Energy Conversion, 2003. Proc. 3rd World Conf., IEEE, 2003: pp. 630–633.

[141]   A.W. Bett, B. Burger, F. Dimroth, G. Siefer, H. Lerchenmuller, High-Concentration PV using III-V Solar Cells, 2006 IEEE 4th World Conf. Photovolt. Energy Conf. (2006) 615–620. doi:10.1109/WCPEC.2006.279530.

[142]   G.S. Kinsey, K.M. Edmondson, Spectral response and energy output of concentrator multijunction solar cells, Prog. Photovoltaics Res. Appl. 17 (2009) 279–288. doi:10.1002/pip.875.

[143]   E.F. Fernández, F. Almonacid, P. Rodrigo, P. Pérez-Higueras, Calculation of the cell temperature of a high concentrator photovoltaic (HCPV) module: A study and comparison of different methods, Sol. Energy Mater. Sol. Cells. 121 (2014) 144–151. doi:10.1016/j.solmat.2013.11.009.

[144]   A.S.P. GmbH, 3C42 Concentrator Triple Junction Solar Cell datasheet, (2014) 1–4.

[145]   M.Y. Feteha, G.M. Eldallal, The effects of temperature and light concentration on the GaInP/GaAs multijunction solar cell's performance, Renew. Energy. 28 (2003) 1097–1104. doi:10.1016/S0960-1481(02)00211-2.

[146]   D. Aiken, M. Stan, C. Murray, P. Sharps, J. Hills, B. Clevenger, Temperature dependent spectral response measurements for III-V multi-junction solar cells, in: Conf. Rec. Twenty-Ninth IEEE Photovolt. Spec. Conf. 2002., Ieee, 2002: pp. 828–831. doi:10.1109/PVSC.2002.1190704.

[147]   M. Muller, C. Deline, B. Marion, S. Kurtz, Determining outdoor CPV cell temperature, in: 7th Int. Conf. Conc. Photovolt. Syst., 2011.

[148]   F. Almonacid, P.J. Pérez-Higueras, E.F. Fernández, P. Rodrigo, Relation between the cell temperature of a HCPV module and atmospheric parameters, Sol. Energy Mater. Sol. Cells. 105 (2012) 322–327. doi:10.1016/j.solmat.2012.06.043.

[149]   G. Peharz, J.P. Ferrer Rodríguez, G. Siefer, A.W. Bett, A method for using CPV modules as temperature sensors and its application to rating procedures, Sol. Energy Mater. Sol. Cells. 95 (2011) 2734–2744. doi:10.1016/j.solmat.2011.03.030.

[150]   M. Muller, T.J. Silverman, M. Deceglie, S. Kurtz, E. Menard, S. Burroughs, Optical cell temperature measurements of multiple CPV technologies in outdoor conditions, 2013 IEEE 39th Photovolt. Spec. Conf. (2013) 3426–3430. doi:10.1109/PVSC.2013.6745184.

[151]   E. Menard, M. Meitl, S. Burroughs, Indirect temperature measurement of CPV solar cells using wavelength shift of the sub-cells luminescence emission peaks, in: 27th Eur. Photovolt. Sol. Energy Conf. Exhib., 2012: pp. 189–193.

[152]   J. Yeom, M.A. Shannon, 3.16 Micro-Coolers, in: Y. Gianchandani, O. Tabata, H. Zappe (Eds.), Compr. Microsystems, Elsevier, New York, 2007: pp. 499–550.

[153]   Y.-S. Tseng, H.-H. Fu, T.-C. Hung, B.-S. Pei, An optimal parametric design to improve chip cooling, Appl. Therm. Eng. 27 (2007) 1823–1831. doi:10.1016/j.applthermaleng.2007.01.012.

[154]   Y. Zhangbo, L. Qifen, Z. Qunzhi, P. Weiguo, The cooling technology of solar cells under concentrated system, 2009 IEEE 6th Int. Power Electron. Motion Control Conf. 3 (2009) 2193–2197. doi:10.1109/IPEMC.2009.5157766.

[155]   K.H. Do, T.H. Kim, Y.-S. Han, B.-I. Choi, M.-B. Kim, General correlation of a natural convective heat sink with plate-fins for high concentrating photovoltaic module cooling, Sol. Energy. 86 (2012) 2725–2734. doi:10.1016/j.solener.2012.06.010.

[156]   G. Mittelman,   a. Dayan, K. Dado-Turjeman,   a. Ullmann, Laminar free convection underneath a downward facing inclined hot fin array, Int. J. Heat Mass Transf. 50 (2007) 2582–2589. doi:10.1016/j.ijheatmasstransfer.2006.11.033.

[157]   A. Bar-Cohen, M. Iyengar, A.D. Kraus, Design of Optimum Plate-Fin Natural Convective Heat Sinks, J. Electron. Packag. 125 (2003) 208. doi:10.1115/1.1568361.

[158]   S.K. Natarajan, T.K. Mallick, M. Katz, S. Weingaertner, Numerical investigations of solar cell temperature for photovoltaic concentrator system with and without passive cooling arrangements, Int. J. Therm. Sci. 50 (2011) 2514–2521. doi:10.1016/j.ijthermalsci.2011.06.014.

[159]   A. Royne, C.J. Dey, Design of a jet impingement cooling device for densely packed PV cells under high concentration, Sol. Energy. 81 (2007) 1014–1024. doi:10.1016/j.solener.2006.11.015.

[160]   L. Zhu, R.F. Boehm, Y. Wang, C. Halford, Y. Sun, Water immersion cooling of PV cells in a high concentration system, Sol. Energy Mater. Sol. Cells. 95 (2011) 538–545. doi:10.1016/j.solmat.2010.08.037.

[161]   W. Anderson, S. Tamanna, D. Sarraf, P. Dussinger, R. Hoffman, Heat Pipe Cooling of Concentrating Photovoltaic (CPV) Systems, in: 6th Int. Energy Convers. Eng. Conf., Ieee, 2008: pp. 1–6. doi:10.1109/PVSC.2008.4922577.

[162]   W.G.J.H.M. Van Sark, Feasibility of photovoltaic – Thermoelectric hybrid modules, Appl. Energy. 88 (2011) 2785–2790. doi:10.1016/j.apenergy.2011.02.008.

[163]   P. Valeh-e-Sheyda, M. Rahimi, E. Karimi, M. Asadi, Application of two-phase flow for cooling of hybrid microchannel PV cells: A comparative study, Energy Convers. Manag. 69 (2013) 122–130. doi:10.1016/j.enconman.2013.01.029.

[164]   I.K. Karathanassis, E. Papanicolaou, V. Belessiotis, G.C. Bergeles, Multi-objective design optimization of a micro heat sink for Concentrating Photovoltaic/Thermal (CPVT) systems using a genetic algorithm, Appl. Therm. Eng. 59 (2013) 733–744. doi:10.1016/j.applthermaleng.2012.06.034.

[165]   K. V. Wong, O. De Leon, Applications of Nanofluids: Current and Future, Adv. Mech. Eng. 2010 (2010) 1–11. doi:10.1155/2010/519659.

[166]   A.N. Al-Shamani, M.H. Yazdi, M. a. Alghoul, A.M. Abed, M.H. Ruslan, S. Mat, et al.,

Nanofluids for improved efficiency in cooling solar collectors – A review, Renew. Sustain. Energy Rev. 38 (2014) 348–367. doi:10.1016/j.rser.2014.05.041.

[167]   R. Taylor, S. Coulombe, T. Otanicar, P. Phelan, A. Gunawan, W. Lv, et al., Small particles, big impacts: A review of the diverse applications of nanofluids, J. Appl. Phys. 113 (2013) 011301. doi:10.1063/1.4754271.

[168]   L. Micheli, N. Sarmah, X. Luo, K.S. Reddy, T.K. Mallick, Opportunities and challenges in micro- and nano-technologies for concentrating photovoltaic cooling: A review, Renew. Sustain. Energy Rev. 20 (2013) 595–610. doi:10.1016/j.rser.2012.11.051.

[169]   J. Barrau, a. Perona, a. Dollet, J. Rosell, Outdoor test of a hybrid jet impingement/micro-channel cooling device for densely packed concentrated photovoltaic cells, Sol. Energy. 107 (2014) 113–121. doi:10.1016/j.solener.2014.05.040.

[170]   J. Barrau, J. Rosell, D. Chemisana, L. Tadrist, M. Ibañez, Effect of a hybrid jet impingement/micro-channel cooling device on the performance of densely packed PV cells under high concentration, Sol. Energy. 85 (2011) 2655–2665. doi:10.1016/j.solener.2011.08.004.

[171]   M.K. Sung, I. Mudawar, Single-phase and two-phase cooling using hybrid micro-channel/slot-jet module, Int. J. Heat Mass Transf. 51 (2008) 3825–3839. doi:10.1016/j.ijheatmasstransfer.2007.12.015.

[172]   A. Kribus, D. Kaftori, G. Mittelman, A. Hirshfeld, Y. Flitsanov, A. Dayan, A miniature concentrating photovoltaic and thermal system, Energy Convers. Manag. 47 (2006) 3582–3590. doi:10.1016/j.enconman.2006.01.013.

[173]   G. Mittelman, a Kribus, a Dayan, Solar cooling with concentrating photovoltaic/thermal (CPVT) systems, Energy Convers. Manag. 48 (2007) 2481–2490. doi:10.1016/j.enconman.2007.04.004.

[174]   J. Barrau, D. Chemisana, J. Rosell, L. Tadrist, M. Ibañez, An experimental study of a new hybrid jet impingement/micro-channel cooling scheme, Appl. Therm. Eng. 30 (2010) 2058–2066. doi:10.1016/j.applthermaleng.2010.05.013.

[175]   Y. Sun, Y. Wang, L. Zhu, B. Yin, H. Xiang, Q. Huang, Direct liquid-immersion cooling of concentrator silicon solar cells in a linear concentrating photovoltaic receiver, Energy. 65 (2014) 264–271. doi:10.1016/j.energy.2013.11.063.

[176]   K. Araki, H. Uozumi, M. Yamaguchi, A simple passive cooling structure and its heat analysis for 500× concentrator PV module, Conf. Rec. Twenty-Ninth IEEE Photovolt. Spec. Conf.

2002. (n.d.) 1568–1571. doi:10.1109/PVSC.2002.1190913.

[177]   R. Chein, J. Chuang, Experimental microchannel heat sink performance studies using nanofluids, Int. J. Therm. Sci. 46 (2007) 57–66. doi:10.1016/j.ijthermalsci.2006.03.009.

[178]   Z.-Y. Guo, Z.-X. Li, Size effect on single-phase channel flow and heat transfer at microscale, Int. J. Heat Fluid Flow. 24 (2003) 284–298. doi:10.1016/S0142-727X(03)00019-5.

[179]   M. Müller, W. Escher, R. Ghannam, J. Goicochea, B. Michel, C.L. Ong, et al., Ultra-High-Concentration Photovoltaic-Thermal Systems Based on Microfluidic Chip-Coolers, in: AIP Conf. Proc., 2011: pp. 231–234. doi:10.1063/1.3658333.

[180]   D.-Y. Lee, K. Vafai, Comparative analysis of jet impingement and microchannel cooling for high heat flux applications, Int. J. Heat Mass Transf. 42 (1999) 1555–1568. doi:10.1016/S0017-9310(98)00265-8.

[181]   H.A. Mohammed, G. Bhaskaran, N.H. Shuaib, R. Saidur, Heat transfer and fluid flow characteristics in microchannels heat exchanger using nanofluids: A review, Renew. Sustain. Energy Rev. 15 (2011) 1502–1512. doi:10.1016/j.rser.2010.11.031.

[182]   D. Bogojevic, K. Sefiane, A.J. Walton, H. Lin, G. Cummins, Two-phase flow instabilities in a silicon microchannels heat sink, Int. J. Heat Fluid Flow. 30 (2009) 854–867. doi:10.1016/j.ijheatfluidflow.2009.03.013.

[183]   L. Zhu, Z. Fang, Y. Wang, Q. Huang, L. Han, Higher Performance of Silicon Solar Cells Immersed in Dielectric Liquid, in: D.Y. Goswami, Y. Zhao (Eds.), Proc. ISES World Congr. 2007 (Vol. I – Vol. V) SE - 202, Springer Berlin Heidelberg, 2009: pp. 1043–1047. doi:10.1007/978-3-540-75997-3_202.

[184]   X. Han, V. Everett, Y. Wang, L. Zhu, A new efficient receiver design using direct liquid immersion cooling for linear concentrating photovoltaic systems, 25th EU PVSEC. Val. Spain. (2010) 6–10.

[185]   M. Victoria, S. Askins, C. Domínguez, I. Antón, G. Sala, Durability of dielectric fluids for concentrating photovoltaic systems, Sol. Energy Mater. Sol. Cells. 113 (2013) 31–36. doi:10.1016/j.solmat.2013.01.039.

[186]   W.G. Anderson, P.M. Dussinger, D.B. Sarraf, S. Tamanna, Heat pipe cooling of concentrating photovoltaic cells, in: 2008 33rd IEEE Photovolatic Spec. Conf., Ieee, 2008: pp. 1–6. doi:10.1109/PVSC.2008.4922577.

[187]   B. Bhushan, 01 Introduction to Nanotechnology, Semin. Cell Dev. Biol. 714 (2010) 1–6. doi:10.1016/j.semcdb.2010.02.009.

[188]   B.A. Shakouri, Nanoscale Thermal Transport and Microrefrigerators on a Chip, Nanotechnology. 94 (2006) 1613–1638.

[189]   B. Gromoll, Micro cooling systems for high density packaging, Rev. Générale Therm. 37 (1998) 781–787.

[190]   D.G. Cahill, W.K. Ford, K.E. Goodson, G.D. Mahan, A. Majumdar, H.J. Maris, et al., Nanoscale thermal transport, J. Appl. Phys. 93 (2003) 793. doi:10.1063/1.1524305.

[191]   B.D. Gates, Q. Xu, J.C. Love, D.B. Wolfe, G.M. Whitesides, Unconventional Nanofabrication, Annu. Rev. Mater. Res. 34 (2004) 339–372. doi:10.1146/annurev.matsci.34.052803.091100.

[192]   D. Qin, B.A. Riggs, Nanotechnology: A Top-Down Approach, in: Encycl. Supramol. Chem., Taylor & Francis, 2012: pp. 1–9. doi:doi:10.1081/E-ESMC-120047104.

[193]   K. Jagannadham, T. Watkins, R. Dinwiddie, Novel heat spreader coatings for high power electronic devices, J. Mater. Sci. 37 (2002) 1363–1376.

[194]   A.M. Abyzov, S. V. Kidalov, F.M. Shakhov, High thermal conductivity composite of diamond particles with tungsten coating in a copper matrix for heat sink application, Appl. Therm. Eng. 48 (2012) 72–80. doi:10.1016/j.applthermaleng.2012.04.063.

[195]   A. Bar-cohen, P. Wang, On-Chip Thermal Management and Hot-Spot Remediation, in: C.P. Wong, K.-S. Moon, Y. (Grace) Li (Eds.), Nano-Bio- Electron. Photonic MEMS Packag., Springer US, Boston, MA, 2010: pp. 349–429. doi:10.1007/978-1-4419-0040-1.

[196]   K.J. Gray, Effective thermal conductivity of a diamond coated heat spreader, Diam. Relat. Mater. 9 (2000) 201–204. doi:10.1016/S0925-9635(00)00230-2.

[197]   Z. Zhang, H. Schneider, P. Tounsi, A promising solution using CVD diamond for efficient cooling of power devices, Mater. Sci. Eng. B. 177 (2012) 1358–1361. doi:10.1016/j.mseb.2012.03.005.

[198]   D.J. Twitchen, C.S.J. Pickles, S.E. Coe, R.S. Sussmann, C.E. Hall, Thermal conductivity measurements on CVD diamond, Diam. Relat. Mater. 10 (2001) 731–735. doi:10.1016/S0925-9635(00)00515-X.

[199]   J.C. Sung, M.-C. Kan, S.-C. Hu, M.M. Sung, B.G. Monteith, B.G. Montheith, Diamond Composite Heat Spreader, (2006).

[200]   K. Nishiyabu, Y. Kanoko, D. Tanabe, S. Tanaka, Diamond additionsdon't guaranteebetter heat sinks, Met. Powder Rep. 66 (2011) 27–32. doi:10.1016/S0026-0657(11)70060-1.

[201]   A. Geim, K. Novoselov, The rise of graphene, Nat. Mater. (2007) 183–191.

[202]   K.S. Novoselov, V.I. Fal'ko, L. Colombo, P.R. Gellert, M.G. Schwab, K. Kim, A roadmap for graphene., Nature. 490 (2012) 192–200. doi:10.1038/nature11458.

[203]   D.L. Nika, S. Ghosh, E.P. Pokatilov, a. a. Balandin, Lattice thermal conductivity of graphene flakes: Comparison with bulk graphite, Appl. Phys. Lett. 94 (2009) 203103. doi:10.1063/1.3136860.

[204]   B. Buonomo, O. Manca, Transient natural convection in a vertical microchannel heated at uniform heat flux, Int. J. Therm. Sci. 56 (2012) 1–13. doi:10.1016/j.ijthermalsci.2012.01.013.

[205]   C.-K. Chen, H.C. Weng, Natural Convection in a Vertical Microchannel, J. Heat Transfer. 127 (2005) 1053. doi:10.1115/1.1999651.

[206]   B. Buonomo, O. Manca, Natural convection slip flow in a vertical microchannel heated at uniform heat flux, Int. J. Therm. Sci. 49 (2010) 1333–1344. doi:10.1016/j.ijthermalsci.2010.03.005.

[207]   O.M. Haddad, M.M. Abuzaid, M. a. Al-Nimr, Developing Free-Convection Gas Flow in a Vertical Open-Ended Microchannel Filled with Porous Media, Numer. Heat Transf. Part A Appl. 48 (2005) 693–710. doi:10.1080/10407780590968006.

[208]   R.W. Tjerkstra, M. De Boer, E. Berenschot, J.G.E. Gardeniers, A. van den Berg, M.T. Elwenspoek, Etching technology for microchannels, Proc. IEEE Tenth Annu. Int. Work. Micro Electro Mech. Syst. An Investig. Micro Struct. Sensors, Actuators, Mach. Robot. (1997) 147–152. doi:10.1109/MEMSYS.1997.581790.

[209]   V.K. Dwivedi, R. Gopal, S. Ahmad, Fabrication of very smooth walls and bottoms of silicon microchannels for heat dissipation of semiconductor devices, Microelectronics J. 31 (2000) 405–410.

[210]   M. Alavi, S. Büttgenbach, A. Schumacher, H.-J. Wagner, Fabrication of microchannels by laser machining and anisotropic etching of silicon, Sensors Actuators A Phys. 32 (1992) 299–302. doi:10.1016/0924-4247(92)80002-K.

[211]   D.H. Kam, L. Shah, J. Mazumder, Femtosecond laser machining of multi-depth microchannel networks onto silicon, J. Micromechanics Microengineering. 21 (2011) 045027. doi:10.1088/0960-1317/21/4/045027.

[212]   T. Chen, J. Si, X. Hou, S. Kanehira, K. Miura, K. Hirao, Photoinduced microchannels inside silicon by femtosecond pulses, Appl. Phys. Lett. 93 (2008) 051112. doi:10.1063/1.2969401.

[213]   S. Iijima, Helical microtubules of graphitic carbon, Nature. 354 (1991) 56–58.

[214]   A. Aqel, K.M.M.A. El-Nour, R. a. a. Ammar, A. Al-Warthan, Carbon nanotubes, science and technology part (I) structure, synthesis and characterisation, Arab. J. Chem. 5 (2010) 1–23. doi:10.1016/j.arabjc.2010.08.022.

[215]   L.S. Ying, M.A. bin Mohd Salleh, H. b. Mohamed Yusoff, S.B. Abdul Rashid, J. b. Abd. Razak, Continuous production of carbon nanotubes – A review, J. Ind. Eng. Chem. 17 (2011) 367–376. doi:10.1016/j.jiec.2011.05.007.

[216]   L. El Chaar, L.A. lamont, N. El Zein, Review of photovoltaic technologies, Renew. Sustain. Energy Rev. 15 (2011) 2165–2175. doi:10.1016/j.rser.2011.01.004.

[217]   R.M. Reilly, Carbon nanotubes: potential benefits and risks of nanotechnology in nuclear medicine., J. Nucl. Med. 48 (2007) 1039–42. doi:10.2967/jnumed.107.041723.

[218]   M. Endo, M.S. Strano, P.M. Ajayan, Potential Applications of Carbon Nanotubes, Carbon Nanotub. 62 (2008) 13–62.

[219]   Z. Han, A. Fina, Thermal conductivity of carbon nanotubes and their polymer nanocomposites: A review, Prog. Polym. Sci. 36 (2011) 914–944. doi:10.1016/j.progpolymsci.2010.11.004.

[220]   E. Chiavazzo, P. Asinari, Enhancing surface heat transfer by carbon nanofins: towards an alternative to nanofluids?, Nanoscale Res. Lett. 6 (2011) 249. doi:10.1186/1556-276X-6-249.

[221]   P. Kim, L. Shi, a. Majumdar, P. McEuen, Thermal Transport Measurements of Individual Multiwalled Nanotubes, Phys. Rev. Lett. 87 (2001) 19–22. doi:10.1103/PhysRevLett.87.215502.

[222]   M.B. Jakubinek, M.A. White, G. Li, C. Jayasinghe, W. Cho, M.J. Schulz, et al., Thermal and

electrical conductivity of tall, vertically aligned carbon nanotube arrays, Carbon N. Y. 48 (2010) 3947–3952. doi:10.1016/j.carbon.2010.06.063.

[223]   T. Tong, Y. Zhao, L. Delzeit, A. Kashani, M. Meyyappan, A. Majumdar, Dense Vertically Aligned Multiwalled Carbon Nanotube Arrays as Thermal Interface Materials, IEEE Trans. Components Packag. Technol. 30 (2007) 92–100. doi:10.1109/TCAPT.2007.892079.

[224]   S. Berber, Y. Kwon, D. Tomanek, Unusually high thermal conductivity of carbon nanotubes, Phys. Rev. Lett. 84 (2000) 4613–6.

[225]   K. Kordás, G. Tóth, P. Moilanen, M. Kumpumäki, J. Vähäkangas, a. Uusimäki, et al., Chip cooling with integrated carbon nanotube microfin architectures, Appl. Phys. Lett. 90 (2007) 123105. doi:10.1063/1.2714281.

[226]   M. Keidar, Factors affecting synthesis of single wall carbon nanotubes in arc discharge, J. Phys. D. Appl. Phys. 40 (2007) 2388–2393. doi:10.1088/0022-3727/40/8/S18.

[227]   R. Engel-Herbert, H. Pforte, T. Hesjedal, CVD synthesis and purification of single-walled carbon nanotubes using silica-supported metal catalyst, Mater. Lett. 61 (2007) 2589–2593. doi:10.1016/j.matlet.2006.10.004.

[228]   D. Takagi, Y. Homma, Y. Kobayashi, Selective growth of individual single-walled carbon nanotubes suspended between pillar structures, Phys. E Low-Dimensional Syst. Nanostructures. 24 (2004) 1–5. doi:10.1016/j.physe.2004.04.013.

[229]   J.P. Gore, A. Sane, Flame synthesis of carbon nanotubes, in: S. Yellampalli (Ed.), Carbon Nanotub. - Synth. Charact. Appl., InTech, 2011. doi:10.5772/21012.

[230]   W.K. Maser, A.M. Benito, M.T. Martınez, Production of carbon nanotubes : the light approach, Source. 40 (2002) 1685–1695.

[231]   P. Nikolaev, M. Bronikowski, R.K. Bradley, F. Rohmund, D.T. Colbert, K.A. Smith, et al., Gas-phase catalytic growth of single-walled carbon nanotubes from carbon monoxide, Chem. Phys. Lett. (1999) 91–97.

[232]   C.H. See, A.T. Harris, A review of carbon nanotube synthesis via fluidized-bed chemical vapor deposition, Ind. Eng. Chem. Res. 46 (2007) 997–1012.

[233]   J.A. Isaacs, A. Tanwani, M.L. Healy, L.J. Dahlben, Economic assessment of single-walled carbon nanotube processes, J. Nanoparticle Res. 12 (2009) 551–562. doi:10.1007/s11051-009-9673-3.

[234]   O. Jašek, M. Eliáš, L. Zajíčková, V. Kudrle, M. Bublan, J. Matějková, et al., Carbon nanotubes synthesis in microwave plasma torch at atmospheric pressure, Mater. Sci. Eng. C. 26 (2006) 1189–1193. doi:10.1016/j.msec.2005.09.024.

[235]   O. Jašek, M. Eliáš, L. Zajíčková, Z. Kučerová, J. Matějková, A. Rek, et al., Discussion of important factors in deposition of carbon nanotubes by atmospheric pressure microwave plasma torch, J. Phys. Chem. Solids. 68 (2007) 738–743. doi:10.1016/j.jpcs.2007.01.039.

[236]   L. Zajíčková, P. Synek, O. Jašek, M. Eliáš, B. David, J. Buršík, et al., Synthesis of carbon nanotubes and iron oxide nanoparticles in MW plasma torch with Fe(CO)5 in gas feed, Appl. Surf. Sci. 255 (2009) 5421–5424. doi:10.1016/j.apsusc.2008.09.003.

[237]   C. Schwandt, A.T. Dimitrov, D.J. Fray, High-yield synthesis of multi-walled carbon nanotubes from graphite by molten salt electrolysis, Carbon N. Y. 50 (2012) 1311–1315. doi:10.1016/j.carbon.2011.10.054.

[238]   M.D. Diener, N. Nichelson, J.M. Alford, Synthesis of Single-Walled Carbon Nanotubes in Flames, Society. (2000) 9615–9620.

[239]   M.J. Height, J.B. Howard, J.W. Tester, Flame synthesis of single-walled carbon nanotubes, Proc. Combust. Inst. 30 (2005) 2537–2543. doi:10.1016/j.proci.2004.07.015.

[240]   S. Naha, S. Sen, A.K. De, I.K. Puri, A detailed model for the flame synthesis of carbon nanotubes and nanofibers, Proc. Combust. Inst. 31 (2007) 1821–1829. doi:10.1016/j.proci.2006.07.224.

[241]   M.R. Smith, S.W. Hedges, R. Lacount, D. Kern, N. Shah, G.P. Huffman, et al., S elective oxidation of single-walled carbon nanotubes using carbon dioxide, Carbon N. Y. 41 (2003) 1221–1230.

[242]   I. Rosca, F. Watari, M. Uo, T. Akasaka, Oxidation of multiwalled carbon nanotubes by nitric acid, Carbon N. Y. 43 (2005) 3124–3131. doi:10.1016/j.carbon.2005.06.019.

[243]   A. Suri, K.S. Coleman, The superiority of air oxidation over liquid-phase oxidative treatment in the purification of carbon nanotubes, Carbon N. Y. 49 (2011) 3031–3038. doi:10.1016/j.carbon.2011.03.023.

[244]   K. MacKenzie, O. Dunens, A.T. Harris, A review of carbon nanotube purification by microwave assisted acid digestion, Sep. Purif. Technol. 66 (2009) 209–222. doi:10.1016/j.seppur.2009.01.017.

[245]   K.B. Shelimov, R.O. Esenaliev, A.G. Rinzler, C.B. Huffman, R.E. Smalley, Purification of single-wall carbon nanotubes by ultrasonically assisted filtration, Scanning. (1998) 429–434.

[246]   L. Vaccarini, C. Goze, R. Aznar, V. Micholet, C. Journet, P. Bernier, et al., Purification des nanotubes de carbone monofeuillets, Comptes Rendus l'Académie Des Sci. IIB-Mechanics-Physics-Astronomy. 327 (1999) 925–931.

[247]   K.B. Hong, A.A.B. Ismail, M.E.B.M. Mahayuddin, A.R. Mohamed, S.H.S. Zein, Production of high purity multi-walled carbon nanotubes from catalytic decomposition of methane, J. Nat. Gas Chem. 15 (2006) 266–270.

[248]   K. Dasgupta, R. Venugopalan, D. Sathiyamoorthy, The production of high purity carbon nanotubes with high yield using cobalt formate catalyst on carbon black, Mater. Lett. 61 (2007) 4496–4499. doi:10.1016/j.matlet.2007.02.042.

[249]   D. Fleury, J. a. S. Bomfim, A. Vignes, C. Girard, S. Metz, F. Muñoz, et al., Identification of the main exposure scenarios in the production of CNT-polymer nanocomposites by melt-moulding process, J. Clean. Prod. 53 (2013) 22–36. doi:10.1016/j.jclepro.2011.11.009.

[250]   Z.D. Ok, J.C. Benneyan, J. a. Isaacs, Modeling Production Costs for SWNT Manufacturing Given Uncertain Health and Safety Standards, Proc. 2007 IEEE Int. Symp. Electron. Environ. (2007) 85–90. doi:10.1109/ISEE.2007.369372.

[251]   J.S. Kim, B.K. Park, J.S. Lee, Natural Convection Heat Transfer Around Microfin Arrays, Exp. Heat Transf. 21 (2008) 55–72. doi:10.1080/08916150701647835.

[252]   S. Mahmoud, R. Al-Dadah, D.K. Aspinwall, S.L. Soo, H. Hemida, Effect of micro fin geometry on natural convection heat transfer of horizontal microstructures, Appl. Therm. Eng. 31 (2011) 627–633. doi:10.1016/j.applthermaleng.2010.09.017.

[253]   H. Shokouhmand, A. Ahmadpour, Heat Transfer from a Micro Fin Array Heat Sink by Natural Convection and Radiation under Slip Flow Regime, in: Proc. World Congr. Eng., 2010.

[254]   F. Laermer, A. Schilp, Method for anisotropic etching of silicon, US Pat. 6,284,148. (2001).

[255]   Y. Peles, A. Koşar, C. Mishra, C.-J. Kuo, B. Schneider, Forced convective heat transfer across a pin fin micro heat sink, Int. J. Heat Mass Transf. 48 (2005) 3615–3627. doi:10.1016/j.ijheatmasstransfer.2005.03.017.

[256] M. Bopp, P. Coronel, C. Hibert, a. M. Ionescu, 3D stacked arrays of fins and nanowires on bulk silicon, Microelectron. Eng. 87 (2010) 1348–1351. doi:10.1016/j.mee.2009.12.036.

[257] F. Laermer, S. Franssila, L. Sainiemi, K. Kolari, Deep Reactive Ion Etching, in: L. Veikko, T. Markku, L. Ari, M. Teruaki (Eds.), Handb. Silicon Based MEMS Mater. Technol., Elsevier, 2009: p. 349.

[258] K. Murakami, Y. Wakabayashi, K. Minami, M. Esashi, Cryogenic dry etching for high aspect ratio microstructures, in: Micro Electro Mech. Syst. 1993, MEMS'93, Proc. An Investig. Micro Struct. Sensors, Actuators, Mach. Syst. IEEE., IEEE, 1993: pp. 65–70.

[259] A. Koşar, C. Mishra, Y. Peles, Laminar Flow Across a Bank of Low Aspect Ratio Micro Pin Fins, J. Fluids Eng. 127 (2005) 419. doi:10.1115/1.1900139.

[260] R. Abdolvand, F. Ayazi, An advanced reactive ion etching process for very high aspect-ratio sub-micron wide trenches in silicon, Sensors Actuators A Phys. 144 (2008) 109–116. doi:10.1016/j.sna.2007.12.026.

[261] G. Zhang, Nanowire Applications: Thermoelectric Cooling and Energy Harvesting, in: A. Hashim (Ed.), Nanowires - Fundam. Res., InTech, 2008.

[262] J. Li, H. Yu, S.M. Wong, X. Li, G. Zhang, P.G.-Q. Lo, et al., Design guidelines of periodic Si nanowire arrays for solar cell application, Appl. Phys. Lett. 95 (2009) 243113. doi:10.1063/1.3275798.

[263] Jet Propulsion Laboratory, Amplified Thermionic Cooling Using Arrays of Nanowires. Cooling devices could be highly miniaturized., NASA Tech Briefs. (2007) 42–43.

[264] S.G. Volz, G. Chen, Molecular dynamics simulation of thermal conductivity of silicon nanowires, Appl. Phys. Lett. 75 (1999) 2056. doi:10.1063/1.124914.

[265] Y. Li, K. Buddharaju, N. Singh, G.Q. Lo, S.J. Lee, Silicon Nanowires Thermoelectric Devices, Power. (2010) 1181–1185.

[266] H. Masuda, A. Ebata, K. Teramae, N. Hishinuma, Alteration of thermal conductivity and viscosity of liquid by dispersing ultra-fine particles (dispersion of AL2O3, Si02, and TiO2 ultra-fine particles), Netsu Bussei. 7 (1993) 227–233. doi:http://dx.doi.org/10.2963/jjtp.7.227.

[267] S.U.S. Choi, J.A. Eastman, Enhancing thermal conductivity of fluids with nanoparticles, in: ASME Int. Mech. Eng. Congr. Expo., ASME, San Francisco, CA (US), 1995: pp. 99–106.

[268]   M. Rafati, A. a. Hamidi, M. Shariati Niaser, Application of nanofluids in computer cooling systems (heat transfer performance of nanofluids), Appl. Therm. Eng. 45-46 (2012) 9–14. doi:10.1016/j.applthermaleng.2012.03.028.

[269]   L. Godson, B. Raja, D. Mohan Lal, S. Wongwises, Enhancement of heat transfer using nanofluids—An overview, Renew. Sustain. Energy Rev. 14 (2010) 629–641. doi:10.1016/j.rser.2009.10.004.

[270]   Y. Li, J. Zhou, S. Tung, E. Schneider, S. Xi, A review on development of nanofluid preparation and characterization, Powder Technol. 196 (2009) 89–101. doi:10.1016/j.powtec.2009.07.025.

[271]   F.S. Oueslati, R. Bennacer, Heterogeneous nanofluids: natural convection heat transfer enhancement., Nanoscale Res. Lett. 6 (2011) 222. doi:10.1186/1556-276X-6-222.

[272]   K. Hwang, J. Lee, S. Jang, Buoyancy-driven heat transfer of water-based Al2O3 nanofluids in a rectangular cavity, Int. J. Heat Mass Transf. 50 (2007) 4003–4010. doi:10.1016/j.ijheatmasstransfer.2007.01.037.

[273]   N. Putra, W. Roetzel, S.K. Das, Natural convection of nano-fluids, Heat Mass Transf. 39 (2003) 775–784. doi:10.1007/s00231-002-0382-z.

[274]   P. Selvakumar, S. Suresh, Convective performance of CuO/water nanofluid in an electronic heat sink, Exp. Therm. Fluid Sci. 40 (2012) 57–63. doi:10.1016/j.expthermflusci.2012.01.033.

[275]   C. a. Nieto de Castro, S.M.S. Murshed, M.J.V. Lourenço, F.J.V. Santos, M.L.M. Lopes, J.M.P. França, Enhanced thermal conductivity and specific heat capacity of carbon nanotubes ionanofluids, Int. J. Therm. Sci. 62 (2012) 34–39. doi:10.1016/j.ijthermalsci.2012.03.010.

[276]   C. a. Nieto de Castro, M.J.V. Lourenço, A.P.C. Ribeiro, E. Langa, S.I.C. Vieira, Thermal Properties of Ionic Liquids and IoNanofluids of Imidazolium and.pdf, J. Chem. Eng. Data. 55 (2010) 653–661. doi:10.1021/je900648p CCC.

[277]   W. Yu, H. Xie, A Review on Nanofluids: Preparation, Stability Mechanisms, and Applications, J. Nanomater. 2012 (2012) 1–17. doi:10.1155/2012/435873.

[278]   X. Wei, L. Wang, Synthesis and thermal conductivity of microfluidic copper nanofluids, Particuology. 8 (2010) 262–271. doi:10.1016/j.partic.2010.03.001.

[279]   A. Amrollahi, A.A. Hamidi, A.M. Rashidi, The effects of temperature, volume fraction and vibration time on the thermo-physical properties of a carbon nanotube suspension (carbon nanofluid)., Nanotechnology. 19 (2008) 315701. doi:10.1088/0957-4484/19/31/315701.

[280]   N.N. Venkata Sastry, A. Bhunia, T. Sundararajan, S.K. Das, Predicting the effective thermal conductivity of carbon nanotube based nanofluids., Nanotechnology. 19 (2008) 055704. doi:10.1088/0957-4484/19/05/055704.

[281]   S.U.S. Choi, Z.G. Zhang, W. Yu, F.E. Lockwood, E. a. Grulke, Anomalous thermal conductivity enhancement in nanotube suspensions, Appl. Phys. Lett. 79 (2001) 2252. doi:10.1063/1.1408272.

[282]   M.J. Assael, C.-F. Chen, I. Metaxa, W. a. Wakeham, Thermal Conductivity of Suspensions of Carbon Nanotubes in Water, Int. J. Thermophys. 25 (2004) 971–985. doi:10.1023/B:IJOT.0000038494.22494.04.

[283]   Y. Hwang, Y. Ahn, H. Shin, C. Lee, G. Kim, H. Park, et al., Investigation on characteristics of thermal conductivity enhancement of nanofluids, Curr. Appl. Phys. 6 (2006) 1068–1071. doi:10.1016/j.cap.2005.07.021.

[284]   V. Kumaresan, R. Velraj, S.K. Das, Convective heat transfer characteristics of secondary refrigerant based CNT nanofluids in a tubular heat exchanger, Int. J. Refrig. 35 (2012) 2287–2296. doi:10.1016/j.ijrefrig.2012.08.009.

[285]   V. Kumaresan, R. Velraj, Experimental investigation of the thermo-physical properties of water–ethylene glycol mixture based CNT nanofluids, Thermochim. Acta. 545 (2012) 180–186. doi:10.1016/j.tca.2012.07.017.

[286]   A. Nasiri, M. Shariaty-Niasar, A.M. Rashidi, R. Khodafarin, Effect of CNT structures on thermal conductivity and stability of nanofluid, Int. J. Heat Mass Transf. 55 (2012) 1529–1535. doi:10.1016/j.ijheatmasstransfer.2011.11.004.

[287]   M.E. Meibodi, M. Vafaie-Sefti, A.M. Rashidi, A. Amrollahi, M. Tabasi, H.S. Kalal, The role of different parameters on the stability and thermal conductivity of carbon nanotube/water nanofluids, Int. Commun. Heat Mass Transf. 37 (2010) 319–323. doi:10.1016/j.icheatmasstransfer.2009.10.004.

[288]   C. Kleinstreuer, Y. Feng, Experimental and theoretical studies of nanofluid thermal conductivity enhancement: a review., Nanoscale Res. Lett. 6 (2011) 229. doi:10.1186/1556-276X-6-229.

[289]   A. Ghadimi, R. Saidur, H.S.C. Metselaar, A review of nanofluid stability properties and

characterization in stationary conditions, Int. J. Heat Mass Transf. 54 (2011) 4051–4068. doi:10.1016/j.ijheatmasstransfer.2011.04.014.

[290]   T. Cotter, Principles and prospects for micro heat pipes, 1984.

[291]   C.B. Sobhan, R.L. Rag, G.P. Peterson, A review and comparative study of the investigations on micro heat pipes, Int. J. Energy Res. (2007) 664–688. doi:10.1002/er.

[292]   Y.M. Hung, Q. Seng, Effects of geometric design on thermal performance of star-groove micro-heat pipes, Int. J. Heat Mass Transf. 54 (2011) 1198–1209. doi:10.1016/j.ijheatmasstransfer.2010.09.070.

[293]   G.F. Peterson, A.B. Duncan, M.H. Weichold, Experimental investigation of micro heat pipes fabricated in silicon wafers, J. Heat Transfer. 115 (1993) 751–756.

[294]   S.H. Moon, G. Hwang, S.C. Ko, Y.T. Kim, Experimental study on the thermal performance of micro-heat pipe with cross-section of polygon, 44 (2004) 315–321. doi:10.1016/S0026-2714(03)00160-4.

[295]   B. Suman, P. Kumar, An analytical model for fluid flow and heat transfer in a micro-heat pipe of polygonal shape, Int. J. Heat Mass Transf. 48 (2005) 4498–4509. doi:10.1016/j.ijheatmasstransfer.2005.05.001.

[296]   S. Kang, D. Huang, Fabrication of star grooves and rhombus grooves micro heat pipe, J. Micromechanics Microengineering. 12 (2002) 525–531.

[297]   Y.X. Wang, G.P. Peterson, Analysis of Wire-Bonded Micro Heat Pipe Arrays, J. Thermophys. Heat Transf. 16 (2002) 346–355. doi:10.2514/2.6711.

[298]   Y. Wang, G.P. Peterson, Optimization of micro heat pipe radiators in a radiation environment, J. Thermophys. Heat Transf. 16 (2002) 537–546.

[299]   W. Liu, J. Kang, X. Fu, C. Stefanini, P. Dario, Analysis on heat resistance of the micro heat pipe with arteries, Microelectron. Eng. 88 (2011) 2255–2258. doi:10.1016/j.mee.2011.02.082.

[300]   H. Chien, C. Tsai, P. Chen, P. Chen, Improvement On Thermal Performance Of, Micro. (2003) 389–391.

[301]   Z.-H. Liu, Y.-Y. Li, A new frontier of nanofluid research – Application of nanofluids in heat

271

pipes, Int. J. Heat Mass Transf. 55 (2012) 6786–6797. doi:10.1016/j.ijheatmasstransfer.2012.06.086.

[302]   S.-W. Kang, W.-C. Wei, S.-H. Tsai, S.-Y. Yang, Experimental investigation of silver nano-fluid on heat pipe thermal performance, Appl. Therm. Eng. 26 (2006) 2377–2382. doi:10.1016/j.applthermaleng.2006.02.020.

[303]   W. Wei, S. Tsai, S. Yang, S. Kang, Effect of Nanofluid Concentration on Heat Pipe Thermal Performance, (2005).

[304]   X.F. Yang, Z.-H. Liu, J. Zhao, Heat transfer performance of a horizontal micro-grooved heat pipe using CuO nanofluid, J. Micromechanics Microengineering. 18 (2008) 035038. doi:10.1088/0960-1317/18/3/035038.

[305]   K.H. Do, S.P. Jang, Effect of nanofluids on the thermal performance of a flat micro heat pipe with a rectangular grooved wick, Int. J. Heat Mass Transf. 53 (2010) 2183–2192. doi:10.1016/j.ijheatmasstransfer.2009.12.020.

[306]   M. Shafahi, V. Bianco, K. Vafai, O. Manca, Thermal performance of flat-shaped heat pipes using nanofluids, Int. J. Heat Mass Transf. 53 (2010) 1438–1445. doi:10.1016/j.ijheatmasstransfer.2009.12.007.

[307]   M. Shafahi, V. Bianco, K. Vafai, O. Manca, An investigation of the thermal performance of cylindrical heat pipes using nanofluids, Int. J. Heat Mass Transf. 53 (2010) 376–383. doi:10.1016/j.ijheatmasstransfer.2009.09.019.

[308]   Z.-H. Liu, Y.-Y. Li, R. Bao, Thermal performance of inclined grooved heat pipes using nanofluids, Int. J. Therm. Sci. 49 (2010) 1680–1687. doi:10.1016/j.ijthermalsci.2010.03.006.

[309]   G.-S. Wang, B. Song, Z.-H. Liu, Operation characteristics of cylindrical miniature grooved heat pipe using aqueous CuO nanofluids, Exp. Therm. Fluid Sci. 34 (2010) 1415–1421. doi:10.1016/j.expthermflusci.2010.07.004.

[310]   M. Ivanova, A. Lai, C. Gillot, N. Sillon, C. Schaeffer, F. Lefèvre, et al., Design, fabrication and test of silicon heat pipes with radial microcapillary grooves, in: Therm. Thermomechanical Phenom. Electron. Syst. 2006 ITHERM06 Tenth Intersoc. Conf., 2006: pp. 545–551.

[311]   M. Le Berre, S. Launay, V. Sartre, M. Lallemand, Fabrication and experimental investigation of silicon micro heat pipes for cooling electronics, J. Micromechanics Microengineering. 13 (2003) 436–441. doi:0960-1317/13/3/313.

[312]   Y.-S. Lee, Y.-P. Lee, Y. Lee, The effects of surface tension and wire diameter on the rise velocity of a bubble in a miniature two-phase closed thermosyphon, Appl. Therm. Eng. 16 (1996) 655–668. doi:10.1016/1359-4311(95)00081-X.

[313]   A. Pal, Y.K. Joshi, M.H. Beitelmal, C.D. Patel, T.M. Wenger, Design and performance evaluation of a compact thermosyphon, Components Packag. Technol. IEEE Trans. 25 (2002) 601–607. doi:10.1109/TCAPT.2002.807997.

[314]   Z.H. Liu, X.F. Yang, G.L. Guo, Effect of nanoparticles in nanofluid on thermal performance in a miniature thermosyphon, J. Appl. Phys. 102 (2007) 013526. doi:10.1063/1.2748348.

[315]   Z. Liu, X. Yang, G. Wang, G. Guo, Influence of carbon nanotube suspension on the thermal performance of a miniature thermosyphon, Int. J. Heat Mass Transf. 53 (2010) 1914–1920. doi:10.1016/j.ijheatmasstransfer.2009.12.065.

[316]   C. Ramaswamy, Y. Joshi, W. Nakayama, W. Johnson, Compact thermosyphons employing microfabricated components, Microscale Thermophys. Eng. 3 (1999) 273–282.

[317]   N. Sarmah, Progress in BioCPV Project: Internal assessment, Heriot-Watt University, Edinburgh (UK), 2012.

[318]   EKO Instruments Co., MP-160 I-V Curve Tracer Instruction Manual, (2009).

[319]   J.-W. Yoon, B.-I. Noh, S.-B. Jung, Comparative Study of ENIG and ENEPIG as Surface Finishes for a Sn-Ag-Cu Solder Joint, J. Electron. Mater. 40 (2011) 1950–1955. doi:10.1007/s11664-011-1686-x.

[320]   M. Ratzker, A. Pearl, M. Osterman, M. Pecht, G. Milad, Review of Capabilities of the ENEPIG Surface Finish, J. Electron. Mater. 43 (2014) 3885–3897. doi:10.1007/s11664-014-3322-z.

[321]   K.J. Puttlitz, K.A. Stalter, Handbook of Lead-Free Solder Technology for Microelectronic Assemblies, CRC Press, 2004.

[322]   K. Dusek, Study of the components self-alignment in surface mount technology, in: 35th Int. Spring Semin. Electron. Technol., IEEE, Vienna, 2012: pp. 197–200.

[323]   P. Hebert, J. Frost, R. Cravens, R. Woo, What Not to Do, (2011).

[324]   N.V. Suryanarayana, Engineering Heat Transfer, West Publishing Company, 1995.

[325]   D.P. Kulkarni, D.K. Das, Analytical and numerical studies on microscale heat sinks for electronic applications, Appl. Therm. Eng. 25 (2005) 2432–2449. doi:10.1016/j.applthermaleng.2004.12.010.

[326]   T. Fujii, H. Imura, Natural-convection heat transfer from a plate with arbitrary inclination, Int. J. Heat Mass Transf. 15 (1972) 755–767.

[327]   T.A. Reddy, Applied Data Analysis and Modeling for Energy Engineers and Scientists, Springer Science & Business Media, 2011.

[328]   J.P. Holman, Heat Transfer, Tenth Edit, McGraw-Hill, 2010.

[329]   Y.A. Çengel, Introduction to thermodynamics and heat transfer, Second Edi, McGraw-Hill, 2008.

[330]   S.W. Churchill, H.H.S. Chu, Correlating equations for laminar and turbulent free convection from a vertical plate, Int. J. Heat Mass Transf. 18 (1975) 1323–1329.

[331]   S. Paredes, W. Escher, R. Ghannam, C.L. Ong, B. Michel, Low Thermal Resistance HCPV Multi Chip Receiver for Thermal Energy Reuse, in: 28th Eur. Photovolt. Sol. Energy Conf. Exhib., 2012.

[332]   G. Duggan, Concentrated photovoltaic (cpv) cell module with secondary optical element and method of fabrication, WO2014037722 A1, 2014.

[333]   H. Cotal, J. Frost, Heat transfer modeling of concentrator multijunction solar cell assemblies using finite difference techniques, in: Photovolt. Spec. Conf. (PVSC), 2010 35th IEEE, IEEE, 2010: pp. 000213–000218.

[334]   A.F.A. Mills, Basic Heat and Mass Transfer, 2nd ed., Prentice Hall, London, UK, 1999.

[335]   S. Chow, C.E. Valdivia, J.F. Wheeldon, R. Ares, O.J. Arenas, V. Aimez, et al., Thermal test and simulation of alumina receiver with high efficiency multi-junction solar cell for concentrator systems, in: H.P. Schriemer, R.N. Kleiman (Eds.), Proc. SPIE 7750, Niagara Falls, Canada, 2010: pp. 775035–775035–8. doi:10.1117/12.872894.

[336]   C. Cancro, G. Ciniglio, G. Graditi, L. Mongibello, A. Pontecorvo, Design and optimization of a novel heat dissipation system developed for ecosole C-PV modules, in: 28th Eur. Photovolt. Sol. Energy Conf. Exhib., Paris, 2013: pp. 664–667.

doi:10.4229/28thEUPVSEC2013-1CV.6.46.

[337]   L. Micheli, N. Sarmah, X. Luo, K.S. Reddy, T.K. Mallick, Design of A 16-Cell Densely-packed Receiver for High Concentrating Photovoltaic Applications, Energy Procedia. 54 (2014) 185–198. doi:10.1016/j.egypro.2014.07.262.

[338]   J. King, Material Handbook for Hybrid Microelectronics, Artech House Publishers, 1988.

[339]   K.S. Reddy, S. Lokeswaran, P. Agarwal, T.K. Mallick, Numerical Investigation of Micro-channel based Active Module Cooling for Solar CPV System, Energy Procedia. 54 (2014) 400–416. doi:10.1016/j.egypro.2014.07.283.

[340]   I. Barducci, Trasmissione del calore, Masson, editoriale ESA, Roma (IT), 1995.

[341]   F.P. Incropera, D.P. DeWitt, T.L. Bergman, A.S. Lavine, Fundamentals of Heat and Mass Transfer, Wiley, 2007.

[342]   D. Kaplan, C. White, Hands-on electronics, Cambridge University Press, 2003.

[343]   T. Mallick, N. Sarmah, S. Banerjee, L. Micheli, K.S. Reddy, P. Ghosh, et al., Design concept and configuration of a hybrid renewable energy system for rural electrification in India through BioCPV project, in: 4th Int. Conf. Adv. Energy Res., Mumbai, 2013.

[344]   P. Sharma, A.W. Walker, J.F. Wheeldon, K. Hinzer, H. Schriemer, Enhanced Efficiencies for High-Concentration, Multijunction PV Systems by Optimizing Grid Spacing under Nonuniform Illumination, Int. J. Photoenergy. 2014 (2014) 1–7. doi:10.1155/2014/582083.

[345]   M. Muller, S. Kurtz, J. Rodriguez, Three years of observed failures and performance related issues associated with on-sun CPV module testing, in: AIP, 2012: pp. 143–147. doi:10.1063/1.4753854.

[346]   I. Aeby, D. Aiken, B. Clevenger, F. Newman, P. Patel, T. Varghese, et al., High Concentration CPV Reliability Progress at Emcore, Physics (College. Park. Md). 229 (2010) 229–232. doi:10.1063/1.3509198.

[347]   M. Schuetz, K. Shell, Design and construction of a~ 7× low-concentration photovoltaic system based on compound parabolic concentrators, IEEE J. Photovoltaics. 2 (2012) 382–386.

[348]   B. Fisher, K. Ghosal, D. Riley, C. Hansen, B. King, S. Burroughs, Field performance modeling

of Semprius CPV systems, 2014 IEEE 40th Photovolt. Spec. Conf. (2014) 0759–0765. doi:10.1109/PVSC.2014.6925030.

[349]   G.S. Kinsey, A. Nayak, M. Liu, V. Garboushian, Increasing Power and Energy in Amonix CPV Solar Power Plants, IEEE J. Photovoltaics. 1 (2011) 213–218. doi:10.1109/JPHOTOV.2011.2172775.

[350]   J. Nickelsen Jr, P. Je Sung, G. Pycroft, Concentrated photovoltaic receiver package with stacked internal support features, US Pat. 8,502,361. 1 (2013).

[351]   D. Fork, D. Duff, Solar concentrating photovoltaic device with resilient cell package assembly, 2007.

[352]   S. Hasin, R. Helfan, Photovoltaic Module Assembly, US 2013/0319507 A1, 2013.

[353]   K. Ghosal, D. Lilly, J. Gabriel, M. Whitehead, S. Seel, B. Fisher, et al., Semprius Field Results and Progress in System Development, IEEE J. Photovoltaics. 4 (2014) 703–708. doi:10.1109/JPHOTOV.2013.2288026.

[354]   G.S. Kinsey, K. Stone, J. Brown, V. Garboushian, Amonix CPV solar power plants, 2010 35th IEEE Photovolt. Spec. Conf. 3 (2010) 000820–000822. doi:10.1109/PVSC.2010.5617196.

[355]   Soitec CPV plant powers COP17 climate talks, Renew. Energy Focus. 12 (2011) 6. doi:10.1016/S1755-0084(11)70138-7.

[356]   K.A. McGowan, Semiconductors: From Book to Breadboard, 1st ed., Cengage Learning, 2012.

[357]   Ergonsolair, Ergonsolair HCPV modules - datasheet, (n.d.).

[358]   IPC - Association Connecting Electronics Industries, IPC-2221 Generic Standard on Printed Board Design, (1998) 123.

[359]   G.S. Kinsey, P. Hebert, K.E. Barbour, D.D. Krut, H.L. Cotal, R.A. Sherif, Concentrator multijunction solar cell characteristics under variable intensity and temperature, Prog. Photovoltaics Res. Appl. 16 (2008) 503–508. doi:10.1002/pip.834.

[360]   J. Shah, Estimating bond wire current-carrying capacity, Power Syst. Des. (2012) 22–25.

[361]   E.F. Fernández, F. Almonacid, Spectrally corrected direct normal irradiance based on

artificial neural networks for high concentrator photovoltaic applications, Energy. 74 (2014) 941–949. doi:10.1016/j.energy.2014.07.075.

[362]   E.F. Fernández, F. Almonacid, J. a. Ruiz-Arias, a. Soria-Moya, Analysis of the spectral variations on the performance of high concentrator photovoltaic modules operating under different real climate conditions, Sol. Energy Mater. Sol. Cells. 127 (2014) 179–187. doi:10.1016/j.solmat.2014.04.026.

[363]   E.F. Fernández, G. Siefer, F. Almonacid, a. J.G. Loureiro, P. Pérez-Higueras, A two subcell equivalent solar cell model for III–V triple junction solar cells under spectrum and temperature variations, Sol. Energy. 92 (2013) 221–229. doi:10.1016/j.solener.2013.03.012.

[364]   G. Peharz, G. Siefer, A.W. Bett, A simple method for quantifying spectral impacts on multi-junction solar cells, Sol. Energy. 83 (2009) 1588–1598. doi:10.1016/j.solener.2009.05.009.

[365]   IPC - The Institute for Interconnecting and Packaging Electronic Circuits, IPC-TM-650: Die Shear Strength (2.4.42.2), 1998.

[366]   Department of Defense, MIL-STD-883J: Method 2019.9, (2013).

[367]   Department of Defense, Test Method Standard Microcicuits (MIL-STD-883J), Columbus, OH, 2014.

[368]   IPC - The Institute for Interconnecting and Packaging Electronic Circuits, IPC-TM-650: Wire Bond Pull Strength Date (2.4.42.3), (1998).

[369]   Department of Defense, MIL-STD-883G: Method 2011.9, (2013).

[370]   I. Byun, R. Ueno, B. Kim, Micro-heaters embedded in PDMS fabricated using dry peel-off process, Microelectron. Eng. 121 (2014) 1–4. doi:10.1016/j.mee.2014.02.029.

[371]   E.F. Fernández, A.J.G. Loureiro, G.P. Smestad, Multijunction Concentrator Solar Cells: Analysis and Fundamentals, in: P. Pérez-Higueras, E.F. Fernández (Eds.), High Conc. Photovoltaics Fundam. Eng. Power Plants, Springer International Publishing, 2015. doi:10.1007/978-3-319-15039-0.

[372]   M. Data, T. Average, E. Data, Enhanced Fresnel Assembly - EFA Cell Type : Concentrator Triple Junction Solar Cell - 3C40A Application : Concentrating Photovoltaic COC Assembly, (2012) 3–6.

[373] C. Domínguez, I. Anton, G. Sala, I. Antón, G. Sala, Solar simulator for indoor characterization of large area high-concentration pv modules, Photovolt. Spec. Conf. 2008. PVSC '08. 33rd IEEE. (2008) 1–5. doi:10.1109/PVSC.2008.4922739.

[374] M. Bliss, Measurement System for Fast Power and Energy Rating of Photovoltaic Devices, Loughborough University, 2011.

[375] C. Domínguez, I. Antón, G. Sala, Solar simulator for concentrator photovoltaic systems, Opt. Express. 16 (2008) 14894–14901. doi:http://dx.doi.org/10.1364/OE.16.014894.

[376] N. Sarmah, B.S. Richards, T.K. Mallick, Design, development and indoor performance analysis of a low concentrating dielectric photovoltaic module, Sol. Energy. 103 (2014) 390–401. doi:10.1016/j.solener.2014.02.029.

[377] C. Domínguez, I. Antón, G. Sala, Solar simulator for concentrator photovoltaic systems., Opt. Express. 16 (2008) 14894–901.

[378] B. Prior, Roadmap for CPV Technology: A study conducted by GTM Research, 2011.

[379] IHS, Concentrated Photovoltaic Solar Installations Set to Boom in the Coming Years, IHS Press. (2013).

[380] A. Dayan, R. Kushnir, G. Mittelman, A. Ullmann, Laminar free convection underneath a downward facing hot fin array, Int. J. Heat Mass Transf. 47 (2004) 2849–2860. doi:10.1016/j.ijheatmasstransfer.2004.01.003.

[381] B. Govinda Rao, V. Dharma Rao, S.V. Naidu, K.V. Sharma, B. Sreenivasulu, Heat transfer from a vertical fin array by laminar natural convection and radiation-A quasi-3D approach, Heat Transf. Res. 40 (2011) 524–549. doi:10.1002/htj.20360.

[382] Y.K. Khor, Y.M. Hung, B.K. Lim, On the role of radiation view factor in thermal performance of straight-fin heat sinks, Int. Commun. Heat Mass Transf. 37 (2010) 1087–1095. doi:10.1016/j.icheatmasstransfer.2010.06.012.

[383] P. Razelos, A Critical Review of Extended Surface Heat Transfer, Heat Transf. Eng. 24 (2010) 11–28. doi:10.1080/714044411.

[384] J.S. Go, S.J. Kim, G. Lim, H. Yun, J. Lee, I. Song, et al., Heat transfer enhancement using flow-induced vibration of a microfin array, Sensors Actuators, A Phys. 90 (2001) 232–239. doi:10.1016/S0924-4247(01)00522-2.

[385]   IEC, IEC 62670-1 Photovoltaic concentrators (CPV) - Performance testing - Part 1: Standard conditions, (2013).

[386]   P. Blumenfeld, J. Foresi, Y. Lang, J. Nagyvary, Thermal Management and Engineering Economics in CPV Design, Emcore Corp., Albuquerque, NM (USA), 2010.

[387]   H. Ye, G. Zhang, A review of passive thermal management of LED module, J. Semicond. 32 (2011) 014008. doi:10.1088/1674-4926/32/1/014008.

[388]   C.-J. Weng, Advanced thermal enhancement and management of LED packages, Int. Commun. Heat Mass Transf. 36 (2009) 245–248. doi:10.1016/j.icheatmasstransfer.2008.11.015.

[389]   S.H. Yu, K.S. Lee, S.J. Yook, Optimum design of a radial heat sink under natural convection, Int. J. Heat Mass Transf. 54 (2011) 2499–2505. doi:10.1016/j.ijheatmasstransfer.2011.02.012.

[390]   H.H. Cheng, D.-S. Huang, M.-T. Lin, Heat dissipation design and analysis of high power LED array using the finite element method, Microelectron. Reliab. 52 (2012) 905–911. doi:10.1016/j.microrel.2011.05.009.

[391]   X. Luo, W. Xiong, T. Cheng, S. Liu, Design and optimization of horizontally-located plate fin heat sink for high power LED street lamps, Proc. - Electron. Components Technol. Conf. (2009) 854–859. doi:10.1109/ECTC.2009.5074112.